MEASUREMENT OF DEFORMATION IN ROLLING AND SLIDING CONTACTS

Yusuf Caner Taşan

This research project is financially supported by STW, the Dutch Technology Foundation.

Taşan, Yusuf Caner
MEASUREMENT OF DEFORMATION IN ROLLING AND SLIDING CONTACTS
Ph.D. Thesis, University of Twente, Enschede, the Netherlands
July 2005

ISBN: 90-365-2193-9

Keywords: Tribology, wear measurements, rolling contacts, sliding contacts, shakedown, running-in, contact mechanics.

Printed by PrintPartners Ipskamp B.V., Enschede.

MEASUREMENT OF DEFORMATION IN ROLLING AND SLIDING CONTACTS

PROEFSCHRIFT

ter verkrijging van
de graad van doctor aan de Universiteit Twente,
op gezag van de rector magnificus,
prof.dr. W.H.M. Zijm,
volgens besluit van het College voor Promoties
in het openbaar te verdedigen
op vrijdag 1 juli 2005 om 13.15 uur

door

Yusuf Caner Taşan
geboren op 6 oktober 1975
te Ankara, Turkije

Dit proefschrift is goedgekeurd door:

de promotor, prof. dr. ir. D.J. Schipper
en de assistant promotor, dr. ir. M.B. de Rooij

To my family

Summary

Wear and plastic deformation are two critical mechanisms that may lead to failure of the contacting mechanical components both in sliding and rolling contacts. With the improvements in the surface technology and the development of wear resistant materials, the amount of measurable wear and deformation reduces to a smaller scale or more precisely to the level of surface micro-geometry. As a result, the performance and lifetime of these components are related to the changes on the surface roughness level. An example is the running-in phenomenon where it is preferred to remove the highest asperities in a few plastic cycles, which is also known as shakedown. After this, an elastic steady state is obtained.

In this work, mechanisms behind micro-scale changes on the surfaces in rolling and sliding contacts are studied both experimentally and numerically. For the experimental study a wear and deformation measurement system is designed and produced. This system is composed of an interference microscope, a controllable rotating table and a friction device. The system allows measurement of the micro and nano-scale local changes on the surface micro-geometry during a wear or deformation experiment. The positioning inaccuracies caused by the components of the setup and the wear track formed are compensated using the developed numerical repositioning techniques. Friction measurements during the wear and deformation experiments are also carried out. With this setup, experimental studies on the roughness level deformation, wear and shakedown in rolling and dry sliding contacts are conducted.

In order to study the deformation mechanisms in rolling and sliding contacts, a numerical contact model is developed. With this model elastic and elastic-plastic normal contact of rough surfaces are simulated. Deformations, contact pressures and elastic sub-surface stresses are calculated. Surfaces measured by the produced test rig are directly used in the model without approximations such as summit models. Additionally, rolling contacts are simulated by multiple indentation of the deforming surface at different spots in the rolling direction.

Using the experimental and numerical tools, types of surface deformation in rolling contacts, namely asperity or bulk deformations, are studied. The experimentally obtained results are in general agreement with the numerical simulations. It is shown that a dominant asperity level deformation can be seen in the case of hard and rough surfaces. Different deformation modes are presented as a deformation map that can be used to predict the type of deformation of engineering surfaces.

Samenvatting

Slijtage en plastische deformatie zijn twee mechanismen die kunnen leiden tot falen van mechanische componenten in glijdende en rollende contacten. Door ontwikkelingen in de oppervlaktetechnologie en de ontwikkeling van slijtvaste materialen wordt de hoeveelheid te meten slijtage en deformatie steeds kleiner. De gewenste hoeveelheden te meten slijtage liggen op het niveau van de oppervlakteruwheid. Dit betekent dat de levensduur en prestatie van technische componenten samenhangen met verandering op het niveau van de oppervlakteruwheid. Een voorbeeld is het inloopproces, waar het wenselijk is om de hoogste ruwheidstoppen te verwijderen in een aantal passages. Als de hoogste ruwheidstoppen zijn verwijderd, wordt er een elastische contactsituatie bereikt.

In dit proefschrift worden de mechanismen die verantwoordelijk zijn voor veranderingen op het niveau van de oppervlakteruwheid bestudeerd met experimentele en numerieke technieken. Voor het experimentele deel van het onderzoek is er een opstelling ontworpen en gemaakt om slijtage en deformatie op deze kleine schaal te meten. Het systeem bestaat uit een interferentie meetmicroscoop, en rotatietafel en een meetarm voor de wrijvingskrachten. Het systeem is in staat om lokale veranderingen aan het oppervlak op micro- en nanoschaal gedurende een experiment te meten. De positioneringsonnauwkeurigheden die samenhangen met de opstelling worden gecompenseerd met numerieke repositioneringstechnieken, welke ontwikkeld zijn in het onderzoek. Met deze opstelling zijn experimenten uitgevoerd om deformatie op ruwheidsniveau en slijtage in rollende en glijdende contacten te meten.

Om de deformatiemechanismen in rollende en glijdende contacten verder te bestuderen, is er een numeriek contactmodel ontwikkeld Met dit model kan elastische en plastische deformatie van ruwe oppervlakken in normaal contact worden gesimuleerd. Met het model kunnen de contactdrukken, deformatie en spanningen onder het oppervlak worden berekend. Oppervlakken die gemeten zijn met de opstelling worden direct gebruikt in het contactmodel zonder dat benaderingen nodig zijn. Verder worden met het model rollende contacten gesimuleerd door een oppervlak meerdere malen te belastingen op verschillende posities in de rolrichting.

Door gebruik te maken van de ontwikkelde numerieke en experimentele gereedschappen kunnen verschillende typen oppervlaktedeformatie in rollende contacten worden bestudeerd. De twee belangrijkste typen deformatiemechanismen zijn deformatie van de ruwheidstoppen en bulk deformatie. De experimenteel verkregen resultaten zijn in het algemeen in overeenstemming met de numerieke resultaten. Het proefschrift laat bijvoorbeeld zien dat bijvoorbeeld deformatie van de ruwheidstoppen dominant is in het geval van ruwe en harde oppervlakken. De verschillende

typen oppervlaktedeformatie worden gepresenteerd in de vorm van een diagram dat kan worden gebruikt om het dominante deformatiemechanismen van technische oppervlakken te voorspellen.

Acknowledgement

This thesis is a result of a four year study on the STW project "Contactless detection of micro-wear". First of all I would like to thank them for their financial support that made this research possible.

I owe deep thanks to my supervisor Matthijn de Rooij from whom I learned a lot on the concept of Tribology. He supported me very well during my study and the preparation of this thesis.

I also want to thank my promotor Dik Schipper for his support and valuable comments.

Thanks to the other committee members of the graduation committee: Prof.dr.ir. H.J.Grootenboer, Prof.dr.ir. A. de Boer, Prof.dr.ing. D.H.A. Blank, Prof.dr.ir. P. de Baets and Prof.dr.ir. P.P.L. Regtien for participating in my promotion.

I also would like to thank to Erik de Vries and Willie Kerver for their helps in the design and production of the test rig and Walter Lette for his solutions on the problems related to computers and network. Many thanks to Belinda Bruinink for all the life saving arrangements she made on many bureaucratic difficulties I faced.

I enjoyed the nice working environment in the Tribology group very much. Apart from the working hours we had many nice organizations such as ski trips, barbeques, cakes… I want to thank the (ex-) staff members: Wijtze ten Napel, Dik Schipper, Kees Venner, Matthijn de Rooij, Erik de Vries, Walter Lette, Belinda Bruinink, Willie Kerver and the (former) PhD students: Ako, Bert, Bernd, Ellen, Emile, George, Gerrit, Irinel, Isaias, Jamari, Jan Willem, Loredana, Marc, Mark, Rihard and Qiang for these enjoyable moments.

I want to thank to Daniele, Pilar, Isaias, Agni, Mutlu, Deniz, Tolga, Konca, Esra, Koray, Deniz, Harald, Semih, Armağan, Çimen, Engin, Melis, Aygen, Can Ali, Eda, Hüseyin, Belgin, Çetin and Özlem for their friendship and support during my stay in the Netherlands.

Finally, I would like to thank to my family for their support, patience and presence. Without them nothing would be possible.

Contents

Nomenclature

Arabic symbols

a	[m]	Contact radius
A	[m^2]	Contact area
A_c	[m^2]	Area at the critical interference in elastic-perfectly plastic contacts
$A(\tau)$	[m]	Autocorrelation function
C_{ij}		Influence coefficients matrix
d_i	[m]	Displacement vector
d	[m]	Height differences of the transformed and reference images
E	[Pa]	Modulus of elasticity
E^*	[Pa]	Equivalent modulus of elasticity
F	[N]	Normal load
F_c	[N]	Load at the critical interference in elastic-perfectly plastic contacts
F_{wgt}		Weighed distance correlation function
H	[Pa]	Hardness
I		Interference intensity
J	[Pa]	von Mises and Tresca yield criteria
k	[Pa]	Shear yield strength
K		Hardness coefficient
L	[m]	Length
n		Fringe number
p	[Pa]	Contact pressure
p_m	[Pa]	Mean contact pressure
p_s	[Pa]	Shakedown pressure
p_0	[Pa]	Maximum contact pressure
p^*	[Pa]	Contact pressure when asperities are elastically flattened
Q	[N]	Friction force
R	[m]	Radius of surfaces
R_a	[m]	Centerline average
R_q	[m]	Root mean square
t	[m]	Air wedge thickness
u_z	[m]	Surface displacement
u_i, v_i		Search intervals in the global optimizer
v		Poisson's ratio
x, y	[m]	Space coordinates
z	[m]	Surface heights

Greek symbols

β	[1/m]	Correlation distance parameter
γ	[J]	Surface energy
γ_f		Fluctuation intensity
Γ	[J]	Work of adhesion
δ	[m]	Normal approach of the flat surface to the rough surface
δ_h	[m]	Normal deflection in Hertzian contacts
δ_p	[m]	Indentation depth in a perfectly plastic contact
δ_{int}	[m]	The best fitting degree of freedom in the re-positioning algorithm
Δ	[m]	Wave amplitude
Δ_x, Δ_y, Δ_z	[m]	Translation parameters in re-positioning
θ_x, θ_y, θ_z	[°]	Rotational parameters in re-positioning
λ	[m]	Wavelength
μ		Coefficient of friction
$\mu_{i,j}$		Local mean within a filter window
σ		Standard deviation
σ_1, σ_2, σ_3	[Pa]	Principal stresses
σ_r, σ_θ, σ_z	[Pa]	Stresses in radial coordinates
$\sigma_{i,j}$	[Pa]	Normal stress components
σ_y	[Pa]	Yield strength
τ	[m]	Spatial coordinate
$\tau_{i,j}$	[Pa]	Shear stress components
τ^*	[m]	Correlation distance
Φ		Probability density function
Φ_p		Phase in interference
ψ_s		Plasticity index
ω	[m]	Interference for elastic-perfectly plastic contacts
ω_c	[m]	Critical interference for elastic-perfectly plastic contacts

Abbreviations

2D	Two-dimensional
3D	Three-dimensional
AFM	Atomic force microscopy
B.E.M.	Boundary element method
CCD	Charge coupled device
D.O.F	Degree of freedom
F.E.M.	Finite element method
FFT	Fast Fourier Transform
PDF	Probability density function

PZT	Piezoelectric transducer
RMS	Root mean square

Chapter 1. Introduction

Mechanical components often involve contacting surfaces. The contact can be either in the form of a dry or a lubricated sliding contact (i.e. piston ring-cylinder liner, slider crank mechanisms, etc.) or a rolling contact (i.e. ball bearing: ball-ring, train: wheel-rail, etc.). Both in sliding and rolling contacts, wear (removal of material during contact of surfaces) and plastic deformation are the two critical mechanisms observed that may lead to failure of the contacting components. In the last decades, with the improvements in the wear resistant material technology, the amount of wear and deformation is reduced to a state where the changes are at the level of surface micro-geometry. As a result, the performance and lifetimes of today's mechanical components depend on the changes on the surface at the level of surface micro-geometry or more precisely the surface roughness change. An example is the running-in phenomenon where it is preferred to have more favorable run-in surfaces possessing an elastic steady state after a number of wear and plastic deformation cycles (also known as shakedown). In this thesis, micro-scale surface changes will be studied both experimentally as well as numerically (figure 1.1).

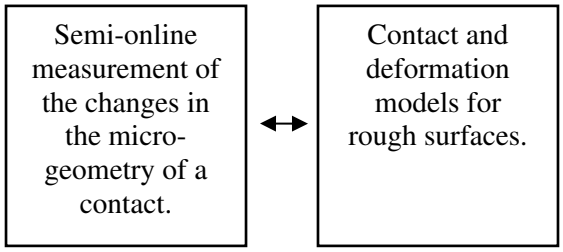

Figure 1.1. Scheme for modeling deformation in (rough) contacts.

Figure 1.2 shows an example of an original surface, the surface after passing of a ball and the result of a numerical rolling simulation. The final aim is to explain local deformation phenomena by coupling measurements of in-situ changes in the micro-geometry in the contact by numerical simulations.

1.1. Measurement of deformation and wear at the roughness level

Changes on a surface can be measured by different approaches. The available methods can be divided into on-line and off-line measurement techniques. In on-line techniques the roughness measurement and wear experiment are carried out simultaneously. As a necessity, therefore, these techniques are based on fast data acquisition methods combined with for instance capacitance [1], ultrasound [2] or scattered light [3] techniques, so that a measurement can be done on a moving surface. With these

techniques, the statistical surface parameters such as the centerline average (R_a) or the root mean square (R_q) are measured. A disadvantage is that local

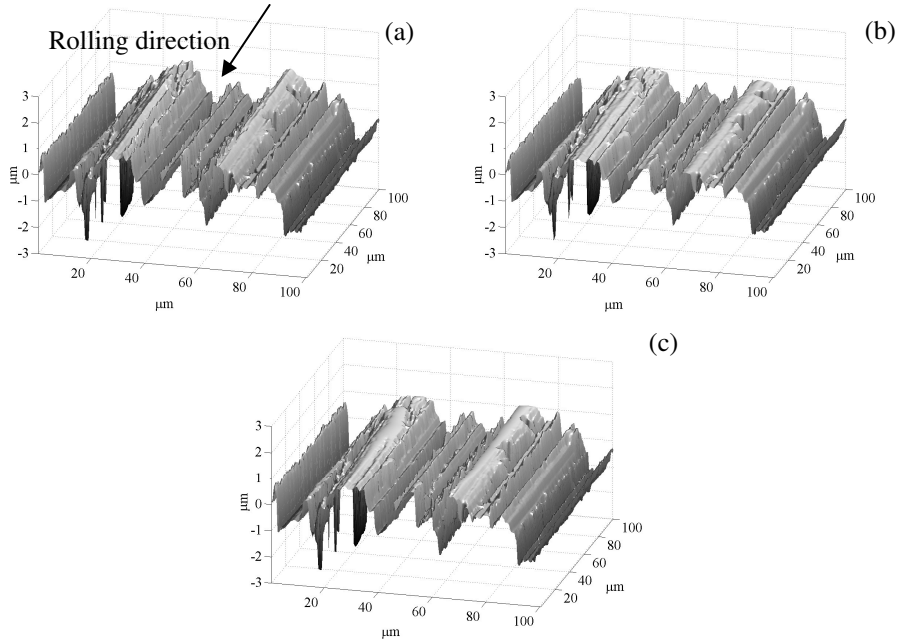

Figure 1.2. Steel surface (a) before a rolling contact experiment, (b) after a four cycle experiment and (c) surface after the numerical rolling simulation. The counter surface is a silicon carbide ball.

characteristics like 3D changes in the surface micro-geometry or the volumetric changes cannot be obtained. Local surface information is very much desired in many applications like running-in where the R_q is often constant, however changes in the micro-geometry are at the asperity level.

In off-line experimental techniques surface modification or wear measurements and wear experiments are separated. An example is measuring the weight of the specimen before and after a wear test and then calculating the volumetric change with the density of the material. Again, the major disadvantage is that local changes in the micro-geometry cannot be measured, and additionally the method is not very sensitive to low wear volumes. Besides this, the contact conditions change by removal of the specimen out of the tester and replacing it.

Hence, in this thesis a new method is developed in which local information is combined with semi-online measurements of the surface micro-geometry. This is done based on roughness measurements by interference microscopy techniques.

Interference microscopy technique (figure 1.3) is a commonly used technique that meets important criteria for measuring surface roughness like accuracy and repeatability. It is a non-contacting technique and applicable to many types of surfaces. Specifically, it is an optical technique and is applicable to surfaces with some reflectivity. The 3D surfaces are measured with a very high height and reasonable in-plane resolution of typically 1 nm and 1 μm respectively. The method is applicable to stationary surfaces only, so the sliding or rolling wear or deformation cycle should be stopped before a measurement. It can be used in a semi-online wear and deformation measurement setup where it is integrated with a wear tester.

In an experiment, it is very important that the surface micro-geometry of the same area before and after wear be measured at each cycle. The shifts and tilts in subsequently measured 3D surface topographies, due to the positioning inaccuracies caused by the components of a setup and the wear track formed, should be compensated for by using repositioning techniques [4], [5], [6]. The setup and the techniques will be presented in chapter 3.

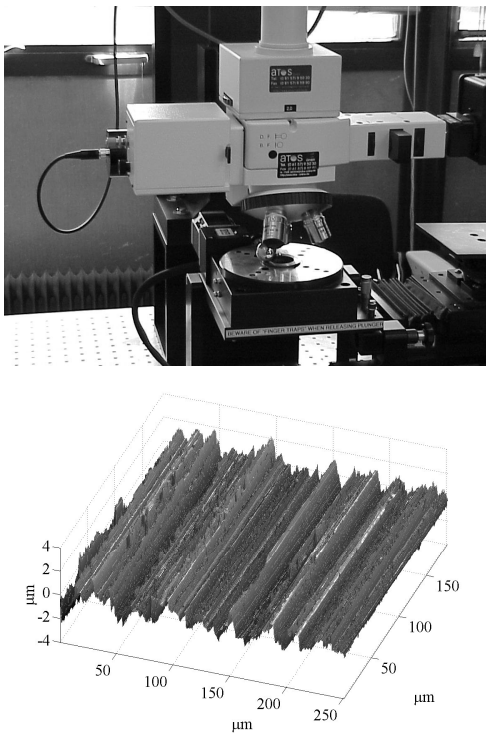

Figure 1.3. Interference microscope and a sample of a roughness measurement.

1.2. Modeling contact of rough surfaces

Contacting surfaces are never perfectly smooth, see for example figure 1.4 which shows a rough surface in contact with a rigid-smooth sphere and the

corresponding contact pressure distribution. In cyclic loaded contacts (i.e. surface is repeatedly loaded and unloaded) of ideally well designed surfaces, roughness details of the contacting surfaces may become smooth, hardened and less prone to a critical failure after a certain number of loading cycles. An application, running-in, can be seen as shearing of the asperity summits by wear or flattening due to a plastic normal deformation close to the surface. In this thesis, the focus is not on wear modeling as mentioned before. The focus will be on the elastic steady state obtained by the contacting surfaces after a number of cyclic plastic deformations. This phenomenon is also known as shakedown [7], [8]. For the contact of smooth surfaces, models for shakedown prediction are available and based on Melan`s shakedown theorem [9]. More details will be presented in chapter 2. Experimental verifications of shakedown models are strongly desired. Especially for rolling contacts, studies on changes in the micro-geometry are very limited.

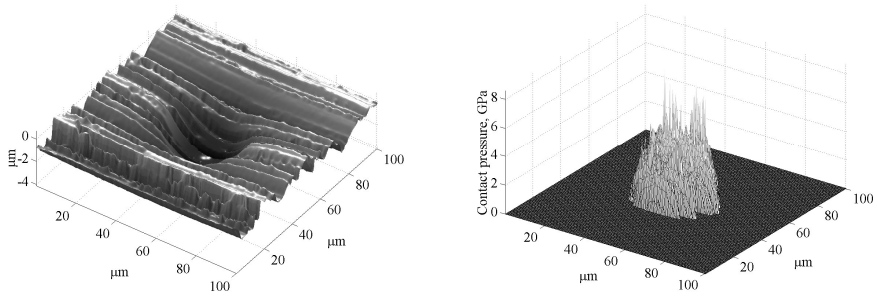

Figure 1.4. On the left, calculated changes on a rough deformable surface in elastic contact with a rigid sphere. On the right, calculated contact pressure distribution.

Elastic and elasto-plastic contact models based on finite elements are often not well suited for 3D contact calculations due to long calculation times. It is essential to introduce models that can be used together with high accuracy 3D topography measurements. Accurate measurements of the changes in the micro-geometry and a realistic contact model make it possible to study the effect of various parameters on the deformation and shakedown of surfaces.

Hence, within this thesis a three dimensional boundary element contact model is developed. The model is applicable to elastic and elastic-plastic contacts and can be used together with the experimental results obtained by the developed semi-online wear and deformation measurement method.

In the next section, based on the aforementioned factors, the objective of this thesis will be presented.

1.3. The objective of this research

Accurate measurement of the local changes on the surface micro-geometry during rolling and sliding contacts is very crucial to understand the wear and deformation mechanisms. Such techniques can be combined with numerical contact models to investigate the design parameters for running-in surfaces. In this thesis the objectives are:

- Design and production of a semi-online measurement system for the accurate measurement of deformation and wear on the level of surface micro-geometry or in other words on the level of the surface roughness. It is also aimed to include friction measurements during the wear and deformation experiments.

- Based on the previous studies, development of repositioning techniques necessary for measuring local surface differences.

- Experimental study on the roughness level deformation, wear and shakedown in rolling and dry sliding contacts, and investigation of the effects of material and geometrical properties on the deformation and wear in such contacts.

- Development of a numerical contact model in order to study the deformation mechanisms in rolling and sliding contacts. Wear modeling is not the scope of this thesis.

- Combining the experimental and the numerical techniques in order to study the types of surface deformation in rolling contacts.

1.4. Thesis layout

This thesis consists of eight chapters. Wear and deformation mechanisms in sliding and rolling contacts will be discussed in chapter 2. The discussion will start with the elastic contact of smooth bodies. This will be followed by plasticity effects, and the criteria defining the onset of yield in such contacts. Then cyclic contacts and the shakedown phenomena will be discussed. This will be extended to the contact of rough surfaces. At first, parameters related to surface roughness will be introduced. Then, analytical and numerical contact models available in the literature will be presented. The chapter will be closed by a general discussion on shakedown in rolling and sliding contacts and the wear mechanisms involved in sliding contacts. Next, in chapter 3, the developed semi-online wear and deformation measurement system and the improved repositioning techniques used in the experimental system will be presented. Several examples with the

measurement technique conducted will also be shown in this chapter. After this discussion, in chapter 4, a three-dimensional boundary element model (3D B.E.M.) will be introduced. This model will be tested for accuracy using an analytical model and a commercial finite element package (Ansys 5.7) and applied to the contact of rough surfaces. Rolling contact experiments performed with materials having different surface roughness, asperity layout and hardness will be presented in chapter 5. In order to understand the deformation mechanisms, 3D B.E.M. will be used for the calculation of pressure distributions and the elastic stresses under the contact in different cycles. Based on the results of the dry sliding contact experiments, deformation and wear in sliding contacts will be discussed in chapter 6. In these experiments, surfaces with different roughnesses will be used. Again, 3D B.E.M. will be incorporated in the deformation analysis, but this time including frictional effects. Next, in chapter 7, different modes of plastic deformation in rough surfaces will be analyzed using the experimental results, 3D B.E.M. and other approaches. These deformation modes will include, 1) solely deformation of the asperities, 2) bulk or subsurface deformation only, where the asperities do not change their shape and 3) a combination of asperity and bulk deformation. Finally, a parametric study will be presented using numerically generated surfaces, and an approach for the prediction of the deformation mode will be introduced. The conclusions and recommendations are given in chapter 8.

References

[1] B. Nowicki and A. Jarkiewicz, The in-process surface roughness measurement using fringe field capacitive (FFC) method, International Journal of Machine Tools and Manufacture 38 (1998), pp. 725-732.
[2] H. Ahn and D. Kim, In situ evaluation of wear surface by ultrasound, Wear 251 (2001), pp. 1193-1201.
[3] T.V. Vorburger and E.C. Teague, Optical techniques for on-line measurement of surface topography, Precision Engineering 3 (1981), pp. 61-83.
[4] Y.C. Taşan, M.B. de Rooij and D.J. Schipper, Measurement of wear on asperity level using image-processing techniques, Wear 258 (2005), pp. 83-91.
[5] M.B. De Rooij and D.J. Schipper, A wear measurement method based on the comparison of local surface heights, Wear 217 (1998), pp. 182-189.
[6] J.W. Sloetjes, D.J. Schipper, P.M. Lugt, and J.H. Tripp, The determination of changes in surface topography using image processing techniques, In Proceedings of the International Tribology Conference (2000), Nagasaki, pp. 241-246.
[7] A. Kapoor and K.L. Johnson, Effect of changes in contact geometry on shakedown of surfaces in rolling/sliding contact, Int. J. Mech. Sci. 34 (1992), pp. 223-239.
[8] A. Kapoor, J. A. Williams and K. L. Johnson, The steady state sliding of rough surfaces, Wear 175 (1994), pp. 81-92.
[9] E. Melan, Der Spannungsgudstand eines “Henky-Mises’schen” Kontinuums bei veranderlicher Belastung, Sitzungberichte der Ak. Wissenschaften Wien, Series 2A 147 (1938), pp. 73.

Chapter 2. Mechanisms of deformation and wear

2.1. Introduction

In this chapter fundamentals of deformation and wear mechanisms of contacting surfaces will be presented. The chapter starts with a description of the single contact of smooth bodies. At first, elastic contact of smooth bodies will be discussed in section 2.2.1. The pressure distribution, surface and subsurface stresses in a contact and initiation of yield as well as the effects of tangential loads (i.e. friction) on the stress distribution at the surface and subsurface will be presented. Secondly, effects of plasticity will be presented in section 2.2.2. In section 2.3, the discussion on single elastic and plastic contacts will be extended to cyclic loaded contacts. In this sub-section, the literature on shakedown phenomena will be introduced. Next, in section 2.4, we focus on the contact of rough surfaces. At first, in section 2.4.1, important surface roughness parameters will be explained and other statistical parameters that define a surface will be introduced. In section 2.4.2, a literature review on the contact between rough surfaces will be discussed. Next, in section 2.4.3, discussions on the cyclic loaded rolling and sliding contact between rough surfaces will be presented briefly. Shakedown in cyclic loaded rolling/sliding contact of rough surfaces and other geometrical effects will be discussed. Next, deformation and wear in sliding contacts will be presented.

2.2. Contact of smooth bodies

In the experimental setup used in this thesis, a ball is in contact with a flat surface. In the next section a case is considered in which an elastic ball is in contact with a rigid elastic half space.

2.2.1. Elasticity

When a load is applied to a body, the deformation of the body can be elastic or plastic. In figure 2.1, contact of two elastic bodies is shown. For the sake of explanation, it is assumed that the rectangular body has a very high modulus of elasticity (rigid) compared to the elasticity modulus of the sphere with radius R. A normal load F is applied for a contact pressure to develop. The developed pressure has a distribution according to Hertz [1]:

$$p(x) = p_0 \cdot \left\{ 1 - \left(\frac{x}{a} \right)^2 \right\}^{1/2} \qquad (2.1)$$

It can be seen that the pressure has a maximum at the center of the contact, where $x = 0$. At the center of the contact, the pressure $p(x) = p_0$ where p_0 represents the maximum contact pressure.

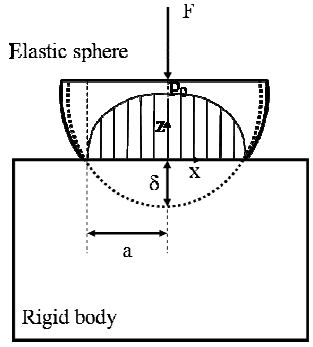

Figure 2.1. Normal contact of an elastic sphere and a rigid body.

According to Hertz, the contact radius (a), the deflection (δ_h), the maximum contact pressure (p_0) and the mean contact pressure (p_m) shown in figure 2.1 are defined by the equations:

$$a = \left(\frac{3 \cdot F \cdot R}{4 \cdot E^*} \right)^{1/3} \tag{2.2}$$

$$\delta_h = \left(\frac{9 \cdot F^2}{16 \cdot R \cdot E^{*2}} \right)^{1/3} \tag{2.3}$$

$$p_0 = \left(\frac{6 \cdot F \cdot E^{*2}}{\pi^3 \cdot R^2} \right)^{1/3} \tag{2.4}$$

$$p_m = \frac{2}{3} p_0 \tag{2.5}$$

where E^* represents the equivalent modulus of elasticity and 1/R is the relative curvature of the two surfaces. For a sphere and a flat surface in contact, R and E^* are defined by:

$$\frac{1}{R} = \frac{1}{R_1} + \frac{1}{R_2} \tag{2.6}$$

$$\frac{1}{E^*} = \frac{1-\nu_1^{\,2}}{E_1} + \frac{1-\nu_2^{\,2}}{E_2} \tag{2.7}$$

In the subsurface, a stress field will develop if a load is applied to two contacting bodies. Expressions for the stress field beneath a sliding spherical contact have been given by Hamilton [2]. These derivations will not be presented in this chapter, but are given in Appendix A.

In conditions like a sliding contact, besides a normal force, a tangential force also acts at the interface. As a consequence, the tangential force influences the subsurface stress field. In general, the coefficient of friction is much higher in a dry sliding contact than in lubricated sliding, rolling or a normally loaded contact. For steel-steel contact typical values are about 0.5 for dry sliding, 0.1 for lubricated sliding and 0.001 for rolling contacts.

If the applied load increases, onset of plasticity or initial yield is seen beneath the surface. For determining whether the stress distributions lead to an initiation of a plastic state or not, several criteria can be used. For ductile materials, a commonly used criterion is the von Mises yielding criterion. It is calculated from the principle stresses σ_1, σ_2, and σ_3 (see Appendix A) as in equation 2.8. These principal stresses can be found using the equations of Hamilton in Appendix A.

$$J = \sqrt{\frac{1}{6} \cdot \left\{ (\sigma_1 - \sigma_2)^2 + (\sigma_2 - \sigma_3)^2 + (\sigma_3 - \sigma_1)^2 \right\}} \tag{2.8}$$

Based on Hamilton's explicit equations, contour plots for the von Mises stress field in the subsurface are given in figure 2.2. Four plots in the figure represent stress distributions for different coefficients of friction ($\mu = 0$, $\mu = 0.1$, $\mu = 0.3$ and $\mu = 0.5$).

In figure 2.2 it is seen that the von Mises stress distribution is symmetric for the frictionless sliding case. The maximum von Mises stress is $0.358p_0$ at a subsurface location of $(0, 0.481a)$ in the center of the contact. From figure 2.2 it is also seen that the maximum of the von Mises stresses comes closer to the surface with increasing coefficient of friction. The maximum values for the von Mises (J) stresses and the locations of these maxima are presented in table 2.1 for different values of the coefficient of friction.

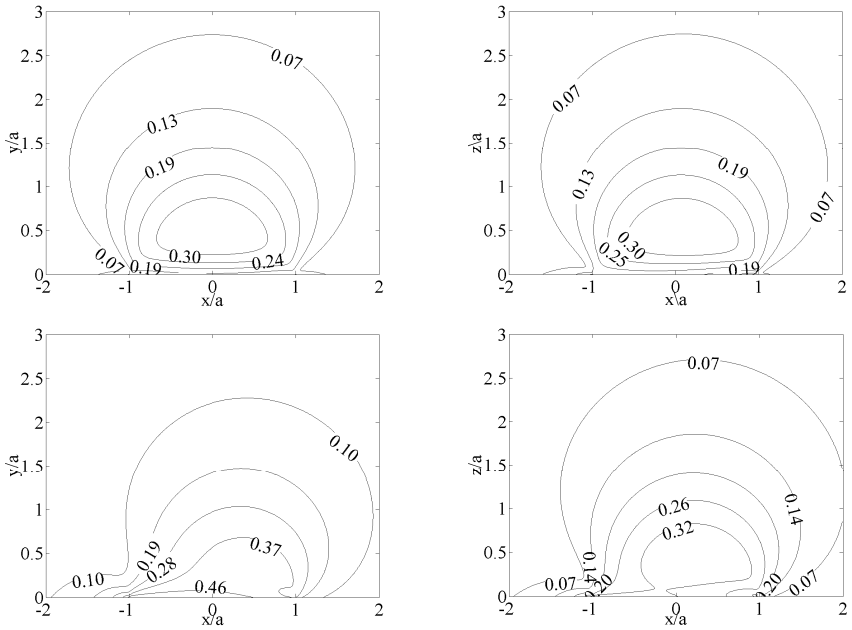

Figure 2.2. Subsurface von Mises stress (J/p_0) distribution for combined loading (normal+friction force) point contact. Clockwise from top left $\mu = 0$, $\mu = 0.1$, $\mu = 0.3$ and $\mu = 0.5$. The friction force acts to the left.

Table 2.1. von Mises stresses for different coefficients of friction

	J/p_0.	x/a	z/a
$\mu = 0$	0.358	0	0.481
$\mu = 0.1$	0.361	-0.112	0.475
$\mu = 0.3$	0.381	-0.319	0.428
$\mu = 0.5$	0.552	-0.550	0

As it can be noticed from table 2.1, the maximum of the von Mises stress increases with increasing coefficient of friction and shifts close to the surface. At the critical coefficient of friction of 0.3, Hamilton states that at $x = -a$ (trailing edge of the contact) and $y = 0$ (at the surface) there is a critical point with a sharp increase in the von Mises stress up to $0.334p_0$ leading to a failure prone tension zone at the trailing edge and a less critical compression zone in the front edge in the contact as indicated in figure 2.3 where Q is the friction force.

Obviously there are stress components on the surface as well. These stress components in and outside the contact region are given by Hamilton in the Cartesian coordinate system. In Appendix A, these stress components for a normal loaded contact without any tangential load (i.e. friction force) and a tangentially loaded contact are presented.

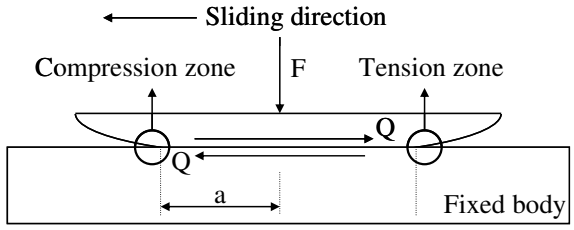

Figure 2.3. Sliding contact of elastic bodies where friction is involved.

For a Hertzian pressure distribution (without tangential load component), the plot of the stress component σ_x is shown in figure 2.4. In this plot the Poisson ratio is 0.3.

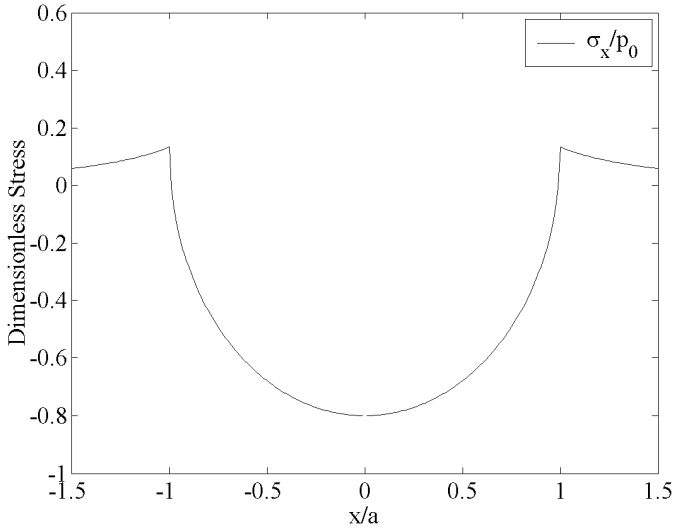

Figure 2.4. Surface normal stresses at the central plane (y/a = 0) of a circular area of contact, for Hertzian pressure distribution.

Note that around the edge of the contact ($x/a = \pm 1$) the stress component σ_x is tensile and the highest value of this tensile stress is just in the circumference region. It was reported by Johnson [3] that this region in a circular contact is more prone to failure especially for brittle materials.

Up to now, elastic material behavior was assumed. In the following sections effects of plasticity will also be included.

2.2.2. Plasticity effects

At a certain load, the subsurface stresses will become higher than the allowable stresses and plasticity will take place. The initiation of plasticity under a normally loaded contact was presented by Johnson [3]. For determining whether the stress distributions lead to an initiation of a plastic

state or not, several criteria can be used. For ductile materials, the most commonly used are the von Mises and the Tresca yielding criteria. The von Mises criterion was given in equation 2.8. The Tresca yield criterion is described as:

$$J = max\left\{\left|\frac{\sigma_1 - \sigma_2}{2}\right|, \left|\frac{\sigma_2 - \sigma_3}{2}\right|, \left|\frac{\sigma_3 - \sigma_1}{2}\right|\right\} \tag{2.9}$$

For the Tresca yield criterion, the allowable stress for the onset of initial yield is the shear yield strength of the material k (= $\sigma_y/2$), which is a material property. For the von Mises yield criterion this limit is $\sigma_y/\sqrt{3}$. If the stress field calculated by one of the two criteria, equations 2.8 or 2.9, exceeds the maximum allowable stress at a given location, then at that point initial yield occurs. At the contact, it was already shown in figure 2.2 that this initiation is generally in the subsurface and the location is dependent on the friction force.

For two spheres in contact, the explicit equations in Cartesian coordinates for the surface and subsurface stresses are given in Appendix A. At the symmetry axis of the contacting spheres the principal stresses can be defined in radial coordinates as σ_r, σ_θ, and σ_z for reasons of axisymmetry. If the Tresca criterion is used, at radius r the onset of yield will occur at a depth of $0.48a$ when:

$$J = \left|\frac{\sigma_z - \sigma_r}{2}\right| = k = \frac{\sigma_y}{2} \tag{2.10}$$

where:

$$\sigma_r = p_0\left[-(1+v)\left[1 - \left(\frac{z}{a}\right)tan^{-1}\left(\frac{a}{z}\right)\right] + \frac{1}{2}\left(1 + \frac{z^2}{a^2}\right)^{-1}\right] \tag{2.11}$$

and:

$$\sigma_z = -p_0\left(1 + \frac{z^2}{a^2}\right)^{-1} \tag{2.12}$$

Substituting the calculated equations 2.11 and 2.12 into 2.10 and assuming frictionless contact and $v = 0.3$ gives:

$$0.31p_0 = \frac{\sigma_y}{2} = k \tag{2.13}$$

and therefore:

$$p_0 = 1.61\sigma_y \tag{2.14}$$

If the mean pressure p_m is used, and considering $p_0 = 1.5p_m$:

$$p_m = 1.07\sigma_y \tag{2.15}$$

If the von Mises criterion is used the initial yield is calculated at a slightly higher contact pressure:

$$p_0 = 1.67\sigma_y \tag{2.16}$$

and with $p_0 = 1.5p_m$:

$$p_m = 1.11\sigma_y \tag{2.17}$$

Equations 2.15 and 2.17 show that, with the Tresca yield criterion, yield occurs a little earlier compared to the von Mises criterion. For metals the hardness is related to the yield strength of the material as $H \approx 2.8\sigma_y$. So, taking the von Mises criteria into consideration, the mean pressure required to start plastically deforming a surface during contact is 0.4 times the hardness of the soft contact partner.

Values obtained in the above equations hold for a frictionless sliding situation. Tangential loads cause a lower value of the pressure at the initial yield as in figure 2.5. In the figure it is seen that there is a drop in the contact pressure leading to an initial yield around a friction coefficient of 0.3. The initial yielding is in the subsurface below this value and comes rapidly closer to the surface when this value is exceeded. As the initial yield is exceeded, the deformation near the surface is plastic and is surrounded by an elastic deforming zone. As the deformation increases further, this plastic region gets wider and at a certain load it reaches the surface. In this transition, the contact pressures change from the initial Hertzian distribution to a constant distribution as shown in figure 2.6. When the contact is fully plastic, the contact pressure distribution is almost constant throughout the contact and is equal to the hardness of the materials in contact. In this state, the contact problem is similar to the contact of a perfectly plastic sphere and a rigid flat surface. In this state of full plasticity,

$$p_m = H \approx 2.8\sigma_y \tag{2.18}$$

As the contact pressure for the fully plastic regime and the applied load F are known, the contact radius can be calculated as:

$$p_m = \frac{F}{\pi a^2} \Rightarrow a = \sqrt{\frac{F}{\pi p_m}} \tag{2.19}$$

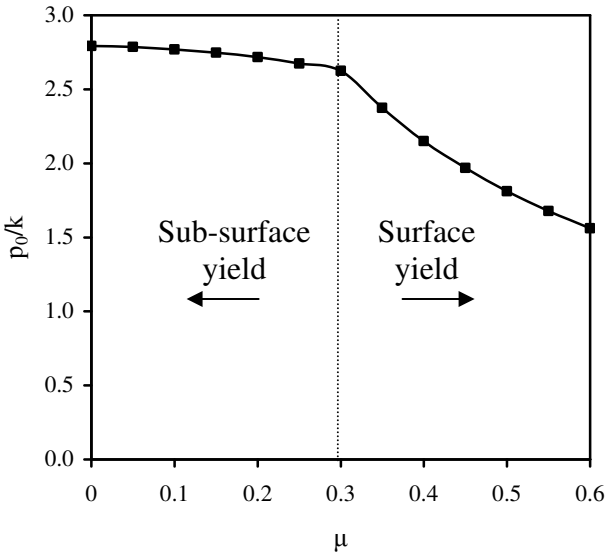

Figure 2.5. Pressures at yield for different coefficients of friction for a sphere sliding on a flat surface.

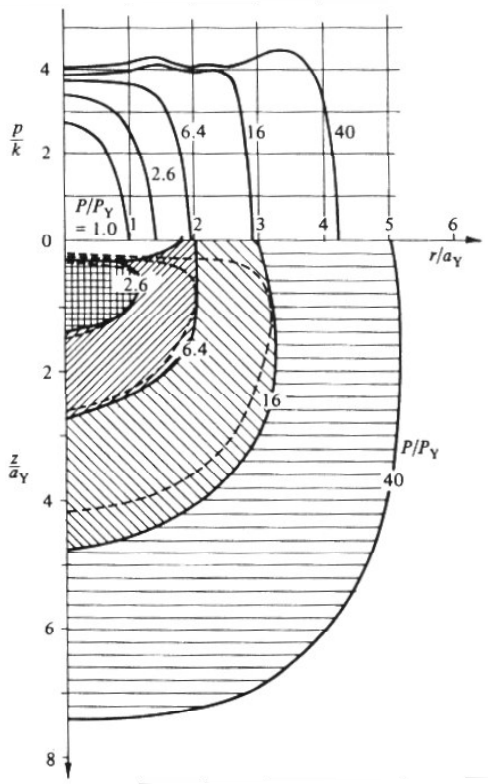

Figure 2.6. Pressure distribution in the contact with increasing plasticity. Taken from [3].

If a perfectly plastic sphere is in contact with a rigid flat surface, then on the basis of geometrical considerations the contact area should change linearly with the indentation depth. This relation can be presented as:

$$A = 2\pi R\delta_p \tag{2.20}$$

Representing F as the product of mean pressure (p_m) and contact area (A), equation 2.20 changes to:

$$F = 2\pi R\delta_p H \tag{2.21}$$

Equation 2.21 shows that the relation between the load during indentation and the indentation depth is also linear.

Up to now, elastically and plastically deforming bodies have been discussed. In cyclically loaded contacts other phenomena can be observed. The major focus in the next section will be on the cyclic contacts and *shakedown* phenomena, where contacting bodies confronting with plasticity can either reach an elastic steady state or keep on deforming in a repeated plastic manner. In the next section, the discussion will be on the first type of shakedown which is called the elastic shakedown.

2.3. Cyclically loaded contacts

In the experimental setup that will be introduced in the next chapter, the ball will be in cyclically loaded contact with a nominally flat disk. In such cyclically loaded contacts, the contacting surfaces are subjected to a series of deformation cycles. Examples are often seen in mechanical components or machine elements such as bearings and the contact between the rail and the wheels of a train.

Elastic shakedown [4] is the elastic steady state that a material reaches during a cyclic loaded contact above the elastic limit and it can be seen after a number of cyclic plastic deformations as seen in figure 2.7. For elastic shakedown to occur, the maximum load is called the *elastic-shakedown limit*. The phenomenon will be called shortly as *shakedown* during this thesis. Shakedown is described by Kapoor and co-workers [4] in four steps:

- As the contact stresses exceed the yield stress of the softer asperity, plastic deformation initiates.
- With the initialization of the plastic deformation protective subsurface residual stresses start to develop. At the same time the material eventually strain hardens.
- The contact area starts to increase so that the contact pressure decreases. As a result,

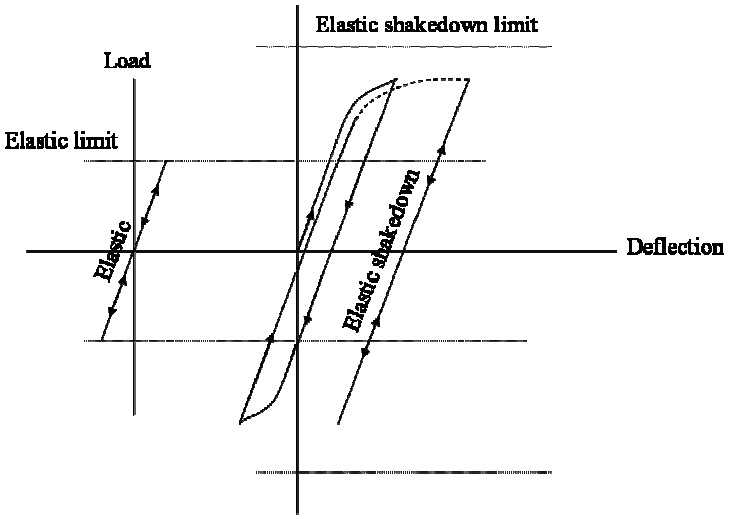

Figure 2.7. Material behavior up to elastic (left) and shakedown (right) limits. Re-illustrated from [5].

- Asperities come to a steady-state where the deformations are elastic, if the load is not too high.

The factors responsible for shakedown are:

1. *Residual stresses* being developed under the contacting surfaces.
2. *Geometrical changes* that lead to an increase in the conformity of the contacting bodies and decrease in the contact pressures.
3. *Strain hardening* that makes the material harder (increase in yield strength).

The first two factors are within the scope of this thesis but the strain hardening will not be included in the discussion. At first, the effect of residual stresses on shakedown in contacting surfaces will be presented. Upon exceeding the elastic limit, the onset of yield starts subsurface as a plastic deformation, provided that the coefficient of friction μ is sufficiently small as explained earlier. In repeated loading such as in a rolling/sliding contact, starting from the first cycle this plastic deformation leads to the development of residual stresses. After each loading event (or cycle), this field of residual stresses grows and forms a protective subsurface stress field with on-going plasticity. After a while, due to the combined effect of the normal pressure and the residual stresses, the system remains below the elastic limits of the contacting materials. This phenomenon is introduced in Melan`s [6] theorem for shakedown as "*If any time-independent distribution of residual stresses can be found which, together with the elastic stresses due to the load, constitutes a system of stresses within the elastic limit, then the system will shakedown. Conversely, if no such distribution of residual stresses can be found, then the system will not*

shakedown and plastic deformation will occur at every passage of the load".

For explanatory reasons, the rolling contact between a cylinder and a flat surface is described as a 2D contact problem. The contact situation is shown in figure 2.8. Below the center of the contact there is a compression zone, where compressive stresses act. These stresses both deform the element C in the subsurface in the compression direction and lateral direction (the element gets wider). After one cycle the compressive residual stresses increase as the element is pushed down. In cyclic loading, the residual stresses in this direction increase until no further deformation is allowed because of the built up protective residual stresses. In points B and D, the stresses are shear stresses, and change sign as the cylinder rolls along the disk surface. It is not possible for any residual stress distribution to build up due to this positive and negative alternation of the shear stresses. For this reason, cyclic plasticity can be expected at B and D and hence, the shear stress states at B and D determine whether or not there will be a shakedown in the system.

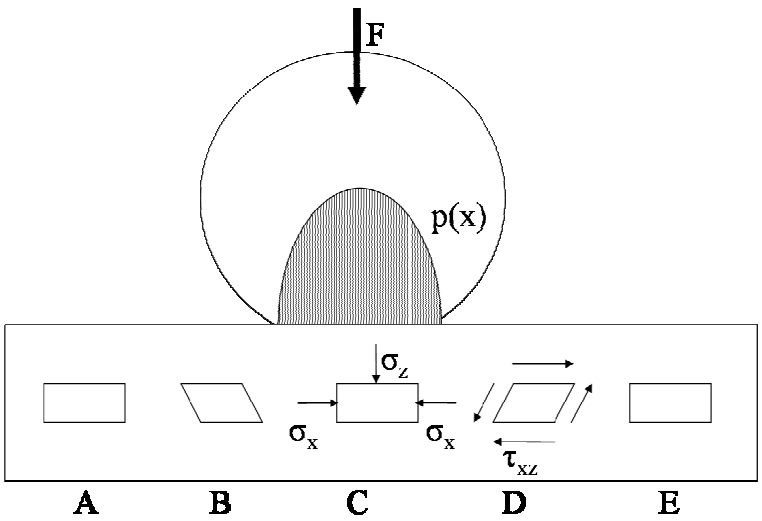

Figure 2.8. Cylinder and flat in contact. Taken from [3].

The focus of this thesis is on the (local) contact of a sphere and a flat. Johnson [3] presented the shakedown limit of a sphere in contact with a flat surface. In these calculations, the reduction in the contact pressure due to geometrical effects (i.e. increase in the conformity) is not taken into account. As a sphere is a symmetric 3D body, simplifications in the stress states can be made. If the plane $y = 0$ is taken, then at the center of the contact the two shear stress components are zero for reasons of symmetry. The shear stresses are zero on this plane in the contact:

$$\left(\tau_{xy}\right)_r = 0 \tag{2.22}$$

$$\left(\tau_{yz}\right)_r = 0 \tag{2.23}$$

However, in this plane the τ_{xz} has positive and negative peaks on the leading and trailing edges of the contact. It is not possible to preserve the development of residual stresses $(\tau_{xz})_r$ of this form due to this alternating behavior. Hence, referring to Melan's theorem, the maximum value of τ_{xz} (see figure 2.9) determines the shakedown limit. From Hamilton's equation, and for $\mu = 0$ this value can be calculated as:

$$\left(\tau_{zx}\right)_{\max} = 0.214\, p_0 \tag{2.24}$$

and is located at $(0.85a, 0.35a)$.

Hence, at the limit of shakedown this maximum value of the shear strength ($(\tau_{zx})_{max}$) should be equal to the shear yield strength (k). With this information, equation 2.24 can be re-written as:

$$p_0 \le 4.7k \tag{2.25}$$

Recalling that initial yield for contacting spheres occur when:

$$p_0 \ge 1.67\sigma_y \tag{2.26}$$

and:

$$\sigma_y = \sqrt{3}k \tag{2.27}$$

then:

$$p_0 \ge 2.8k \tag{2.28}$$

Shakedown is expected above the initial yield pressure and below the shakedown pressure. Then, for a sphere in contact with a plane, this region can be defined as:

$$2.8k \le p_0 \le 4.7k \tag{2.29}$$

Compared to the shakedown behavior of spheres, cylinders in contact have a smaller pressure interval between the initial yield and shakedown as was demonstrated from the rolling contact of cylinders for which this interval was calculated in [3] as:

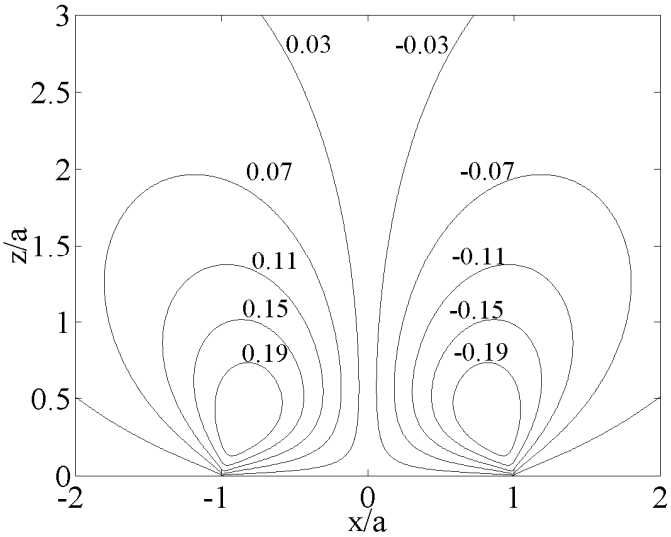

Figure 2.9. Distribution of τ_{xz} in $y = 0$ plane.

$$3.1k \le p_0 \le 4k \tag{2.30}$$

For both the spherical and cylindrical contacts, these limits are dependent on the coefficient of friction. For instance, for point contact, these limits can be calculated as $4.1k$ (for $\mu = 0.1$) and $2.0k$ (for $\mu = 0.5$). The increasing coefficient of friction reduces both the pressure at the initial yield and at shakedown.

For a sliding point contact, a sample shakedown map is shown in figure 2.10. The shakedown pressure values are calculated in the same way as done for obtaining the interval in equation 2.29. For a better understanding, the initial yield pressures shown previously in figure 2.5 are also plotted together with the shakedown pressures. As can be seen, the shakedown region is in-between the solid line representing the elastic shakedown limit and above the dashed line representing the limit of the elastic region. Above the shakedown limit material experiences cyclic plasticity termed "ratchetting". This is further discussed in [7].

In this section an introduction to the shakedown phenomenon has been given and effects of residual stresses on the elastic shakedown of contacting materials have been discussed. Further discussions on the second factor, the geometric factors, will be presented later in section 2.4.

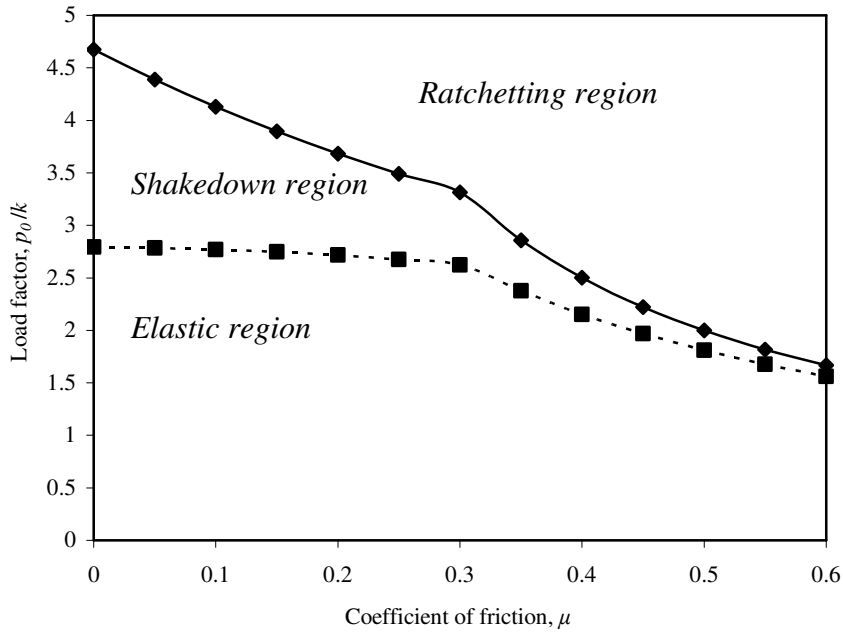

2.10. Shakedown map for point contact plotted for different coefficients of friction. The solid and dashed lines represent the shakedown and elastic limits respectively.

2.4. Rough surfaces

Up to now, the contacting surfaces were considered to be smooth. In reality surfaces are not smooth and possess a roughness. The roughness will be of influence on both single contacts which will be described in section 2.4.2 as well as on cyclically loaded contacts that will be described in section 2.4.3. Before discussing the effect of the micro-geometry or roughness and the contact of rough surfaces, it is appropriate to introduce parameters defining roughness in the following section.

2.4.1. Surface roughness

In tribological problems various parameters are used for describing a surface. Depending on the machining process used for the generation of the surface, the texture or marks created by the machine tool on the surface of the material may vary. These marks on the surface form the roughness of the surface. One can assume that a perfectly smooth surface has zero roughness. If the surface of interest is a sphere, or a cylinder, or another wavy surface, roughness is the variations of the surface when these underlying topographies are subtracted from it (figure 2.11).

The two common parameters used for defining how "rough" a surface is are the root mean square (R_q, or RMS) and the centerline average (R_a). These parameters are defined in the following way:

$$R_q{}^2 = \sigma^2 = \frac{1}{L}\int_0^L z^2 dx \tag{2.31}$$

$$R_a = \frac{1}{L}\int_0^L |z| dx \tag{2.32}$$

where L is the total number of points or length and z is the height value.

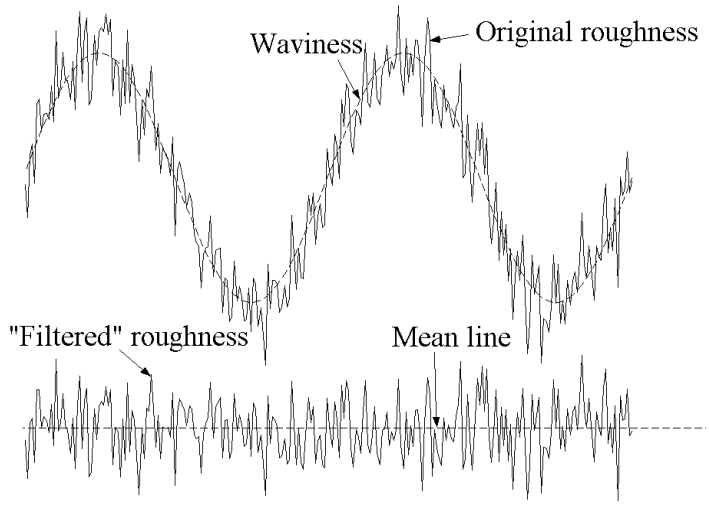

Figure 2.11. Roughness and waviness.

R_a and R_q give only a value of the deviation of heights from a calculated average or mean. They are not sufficient for fully defining how the distribution of the heights is throughout the surface. The distribution of heights is often described by using the probability density function (PDF). This function determines the probability that a certain height is present within the surface height data. With this function, all the height data is divided into equal height intervals, and heights are classified accordingly. Many surfaces have height distributions close to a Gaussian height distribution. For a Gaussian distribution of heights, the probability density function is defined as:

$$\phi(z) = \frac{1}{\sqrt{2\pi\sigma}} \cdot e^{\left(-\frac{z^2}{2\sigma^2}\right)} \tag{2.33}$$

Where z represents the surface heights and σ is the standard deviation of the surface which is the same as the R_q value. In figure 2.12 a measured probability density is compared with an equivalent Gaussian distribution.

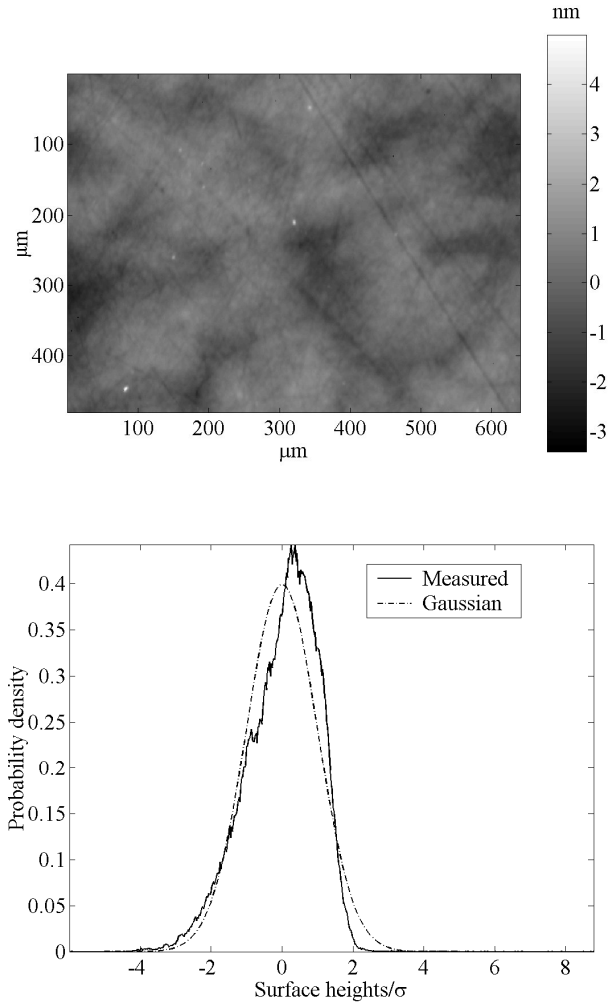

Figure 2.12. (a) Polished steel surface (b) PDF for measured and Gaussian surfaces.

The shape of the probability density function is dependent on the surface forming contact conditions or machining operations. As an example, flattening of the highest asperities on the surface to a single height would be seen as a pulse to the right side of the function.

For describing spatial characteristics of surfaces, parameters like R_q and R_a or a distribution function are not sufficient, as they give single values for the height distribution or distribution of heights only in the vertical or normal direction. They do not give spatial information about how the height

varies in the lateral direction. A commonly used function for characterization in the spatial direction is called the autocorrelation function. The autocorrelation function can be calculated for 3D data, however for the sake of simplicity, a one-dimensional autocorrelation function will be presented here. The autocorrelation function is defined as the expected product of a height $z(x)$ and a height $z(x+\tau)$ which is placed close to the $z(x)$. This expected product ($E(z(x)\, z(x+\tau))$) is expressed as:

$$E(z(x)z(x+\tau)) = A(\tau) = \frac{1}{L}\int_0^L z(x)z(x+\tau)dx \qquad (2.34)$$

In equation 2.34, $A(\tau)$ is the autocorrelation function, L is the length and τ is the spatial coordinate. The spatial comparison measure of the neighboring heights is obtained by multiplication of a height at a spot by the height τ away from it within the integral. When $\tau = 0$, the autocorrelation function is equal to the square of root mean square (R_q), which is the variance of the surface heights.

As many surfaces have a Gaussian height distribution, they show an exponentially decaying autocorrelation function. This characteristics can be seen in a decaying function that can be represented as:

$$A(\tau) = \sigma^2 e^{-\beta x} \qquad (2.35)$$

Where $\tau = \beta^{-1}$. In equation 2.35, β is a parameter that can be related to the correlation distance of a surface. The surface correlation distance can be defined as the distance at which surface heights are still comparable. The correlation distance corresponds to an auto-correlation value of 1/e or 37% for the normalized autocorrelation function. The correlation distance can be calculated as:

$$\tau^* = \frac{1}{\beta} = \frac{1}{A(0)}\int_0^\infty |A(\tau)|d\tau \qquad (2.36)$$

In figure 2.13 the autocorrelation function for the polished steel surface (see figure 2.12.a) is presented together with the generated correlation function. The 2D plot is for the y-direction. It can be seen in the figure that the correlation function has a decreasing behavior and fits well with equation 2.35. For periodic surfaces such as a turned or a ground surface, the correlation has a periodic appearance.

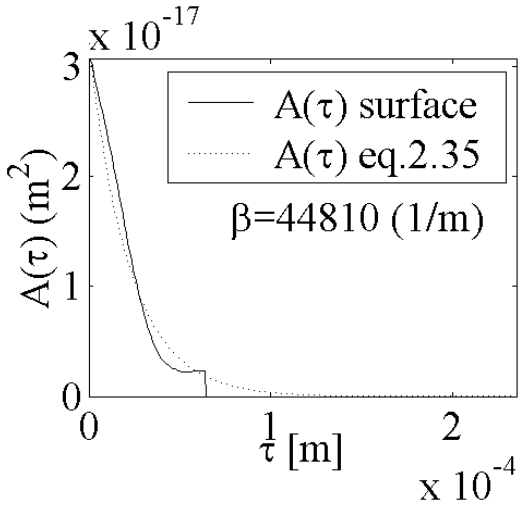

Figure 2.13. Autocorrelation function for a polished surface.

As an example, the autocorrelation function for a ground surface is presented in figure 2.14. The correlation is calculated in the *x*-direction, which is perpendicular to the machining grooves generated by the grinding process.

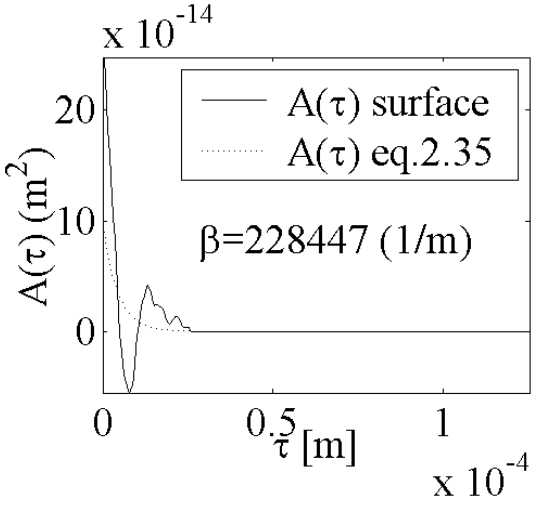

Figure 2.14. Autocorrelation function for a ground surface.

After this brief discussion on the parameters describing a surface, in the next section the contact of rough surfaces will be discussed.

2.4.2. Contact between rough surfaces

Contacting surfaces are never perfectly smooth. The roughness is caused by the finishing processes used for generating them. Additionally, cracks, defects and other factors can be involved. Thus, the physical phenomenon

discussed in sections 2.2 and 2.3 does not hold for the contact of rough surfaces directly. The information presented in the aforementioned sections is often used for comparison purposes or modeling contact of rough surfaces deterministically as was done by Johnson [3], Sayles [8], Chang et al. [9] and many other researchers. Valuable statistical models are also available for the contact of rough surfaces by for instance Greenwood and Williamson [10].

When two rough surfaces are in contact, the contact is between the *asperities* of the two surfaces as seen in figure 2.15. Asperities are spots which are higher than the neighboring points. The area of contact between these asperities is called the *real area of contact*. The real area of contact is often very small compared to the *nominal contact area*, the area over which the two surfaces are apparently making contact. In contrast to the smooth surfaces that have been discussed before, concentrated high contact pressures occur in these local contacts. This can be seen in figure 2.16, where calculations for contact pressures for an aluminum flat and a steel sphere in elastic contact are shown. In figure 2.16.a, the contacting couple is smooth, and in 2.16.b the pressure distribution is shown when roughness (0.5 μm) is involved. The load in both cases is the same. Note that the smooth couple has a Hertzian contact pressure distribution with a maximum pressure of 0.6 GPa whereas if roughness is included the maximum pressures rise up to 20 GPa. In this state, it is expected that subsurface stress distributions deviate strongly from the situation where smooth surfaces are in contact.

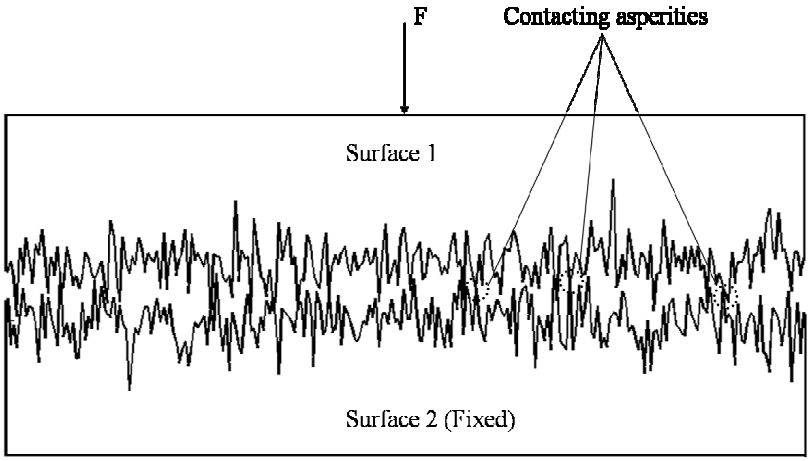

Figure 2.15. Rough surfaces in contact

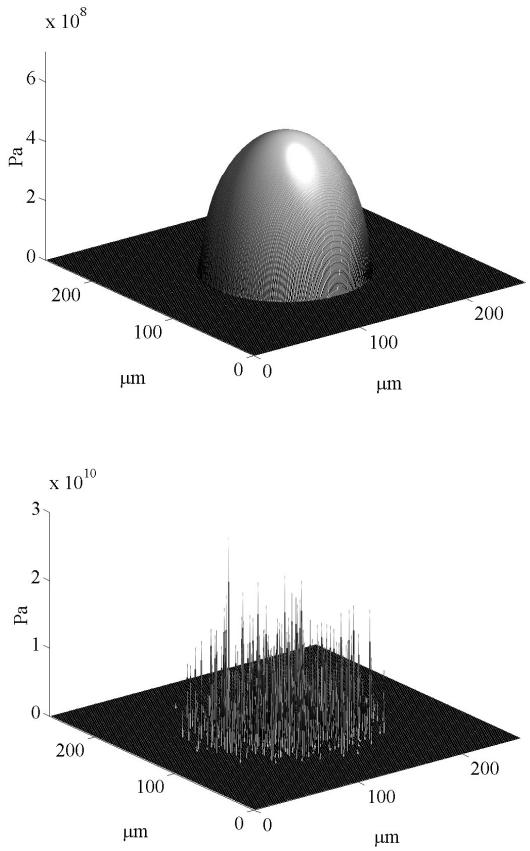

Figure 2.16. Contact pressures for an elastic contact of a flat (aluminum)-sphere (steel) couple. In (a) the contacting surfaces are smooth, in (b) the flat surface is rough.

There have been different approaches for modeling the contact of two rough surfaces. Johnson [3] modeled the contact of a flat elastic half-space (see figure 2.17) with an elastic wavy surface (in one direction) of the form:

$$y = \Delta \cos\left(\frac{2 \cdot \pi \cdot x}{\lambda}\right) \tag{2.37}$$

where Δ is the amplitude of the wave and λ is the wavelength.

Johnson used the equations derived by Westergaard [11] for the surface displacements (u_z) of an elastic-half space under the influence of a normal pressure distribution $p(x)$.

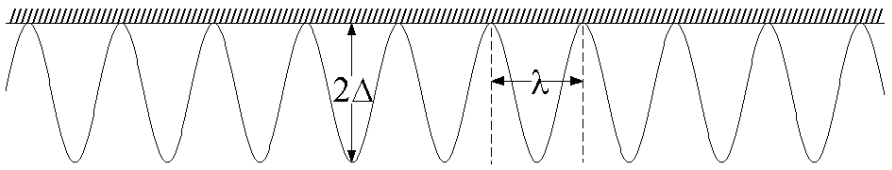

Figure 2.17. Elastic contact between a flat surface and rough surface.

Johnson additionally introduces the ratio of the real to the nominal area of contact for the contact of such surfaces as:

$$\frac{2 \cdot a}{\lambda} = \left(\frac{2}{\pi}\right) \cdot \sin^{-1}\left(\frac{p_m}{p^*}\right)^{1/2} \tag{2.38}$$

where $p^*=\pi E^* \Delta/\lambda$ and a is the contact radius. The real to nominal area of contact ratio is plotted in [3] and represented in figure 2.18. Note that it is possible to elastically flatten all the asperities ($2a/\lambda$ = 1) according to this model. However, high pressures are required at high Δ and low λ.

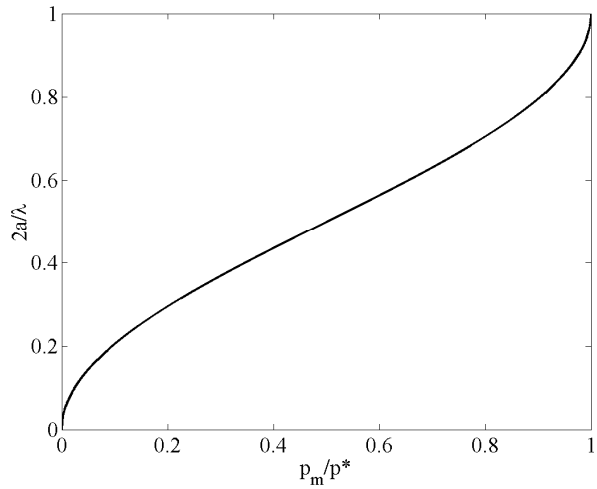

Figure 2.18. Change of real to nominal area of contact with respect to the nominal pressure [3].

Numerical approaches, such as presented by Sayles [8] and later Chang et al. [9], are suitable for elastic normal contact of rough surfaces. Both techniques are based on the integral presented in [3] which defines the deformation, d, of an elastic half-space under the influence of a pressure distribution $p(\xi, \eta)$. This integral is presented as:

$$d(x, y) = \iint_A p(\xi,\eta) \cdot k(x, y, \xi, \eta) \cdot d\xi \cdot d\eta \tag{2.39}$$

In which k is the stiffness component. Sayles and then Chang et al. numerically discretized the integral in equation 2.39 as:

$$d_i = \sum_{j=1}^{N} C_{ij} \cdot p_j \qquad i = 1, 2, ..., N \text{ or } \quad \{d\} = [C]\{p\} \qquad (2.40)$$

In equation 2.40, d is the displacement vector, C is the influence coefficients matrix and p is the contact pressure vector. More focus on these numerical approaches will be given in Chapter 4.

2.4.3 Rolling and sliding

Rolling is defined as a relative angular velocity between the two bodies in contact about an axis parallel to their common tangent plane [3]. A percentage of sliding can also be involved, and introduce differences in rotational speeds of the contacting bodies. This phenomenon is called (partial) slip. If no torque is applied on the rolling element, the contact situation is called free rolling. Apart from slip on a micro-scale, free rolling contacts will involve almost no macro-slip. The situation in which one of the rolling elements is driven is called tractive rolling. Tractive rolling may result in fairly large amounts of slip. So the increase in the sliding percentage or slip of the motion is related to the change of the contact from an ideal rolling situation to a state in which a percentage of tangential components are introduced.

Well designed rolling contacts only fail after many cyclically loaded contacts. However, in the initial stages localized plastic deformation may occur in rolling contacts. Running-in is an example where initial small scale plastic deformation of the asperities is having the effect of generating more favorable running surfaces. If certain conditions are satisfied, initial plastic deformation in rolling contacts may result in an elastic steady state situation after a certain number of rotations. Work has been done to model these phenomena and has resulted in the formulation of shakedown models as discussed before. Some background can be found in [3], [4], [5] and [12].

As discussed in section 2.2.1, subsurface stresses under sliding or rolling contacts are dependent on the coefficient of friction. Roughness will also influence the subsurface stress and therefore also have an effect on the transition from an initially plastic to an elastic steady state in rolling. These initial plastic deformation effects, which result in a certain number of rotations in an elastic steady state can, both at the level of the micro-geometry as well as on the scale of a whole micro-contact, be described by shakedown models, see for example [4]. A steady state situation in the contact can be obtained after the first rotation or after a certain number of rotations. One of the shakedown mechanisms which is the effect of residual

stresses was introduced in section 2.3 with Melan's theorem. A sample shakedown map has been plotted for point contacts. Those calculations neglect the formation of a groove i.e. a change in the macro-geometry, and the changes in the micro-geometry that affect the contact pressure. It is therefore not more than an approximation for rough surfaces as the changes in the geometry of the contact will affect the contact behavior in cyclically loaded rolling. A more realistic case is the case of contacting rough surfaces. In such a contact a deviation from the assumed pressure distributions for flat bodies could be expected as micro-contacts lead to higher local pressures [13]. The increasing conformity introduces new asperities to the contact and the reduced pressure leads to a state in which no plastic deformation exists [14] (figure 2.19).

During the rolling contact of a hard and smooth ball against a softer rough surface, considering the asperities only in the wear track, the asperities have approximately the same height after the truncation of their tops and/or the subsurface plasticity has occurred. This leads to larger plateaus and thus an increase in the number of asperities with the same height.

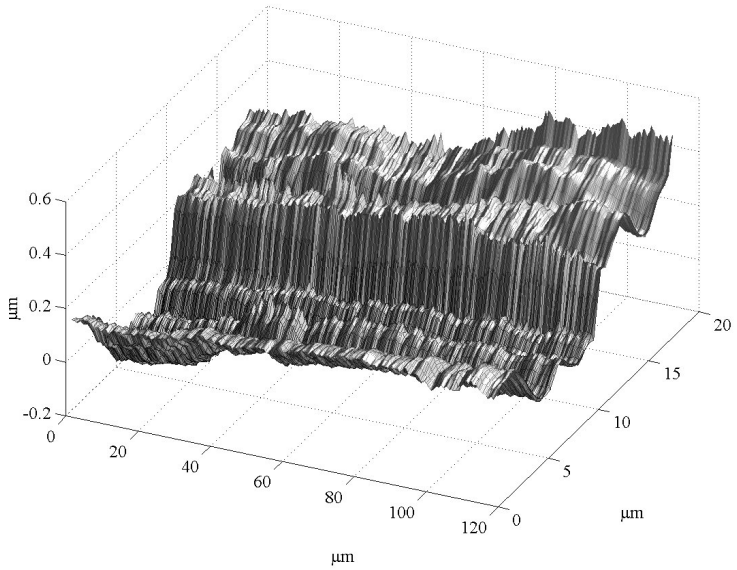

(a)

Figure 2.19. Increasing conformity in a rolling contact. (a) Before contact, (b) after 1st cycle and (c) after 20 cycles. Groove formed is on ground mild steel surface in rolling contact with a SiC ball [14].

(continued)

(continued)

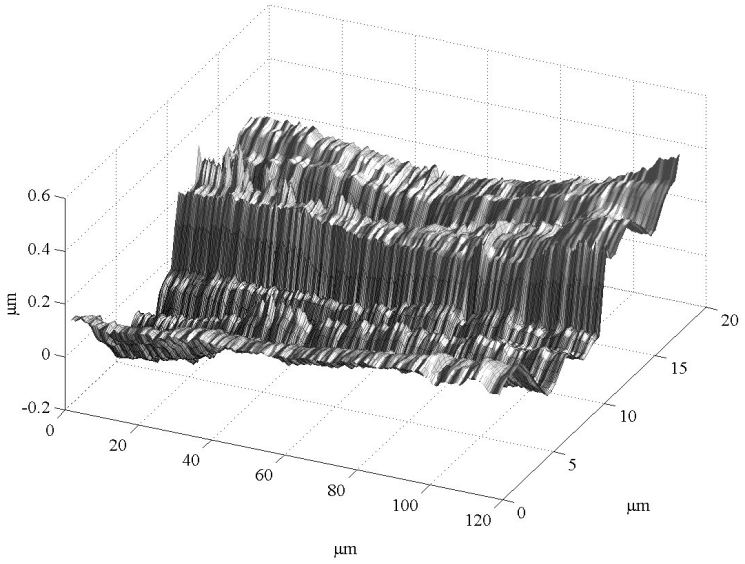

(b)

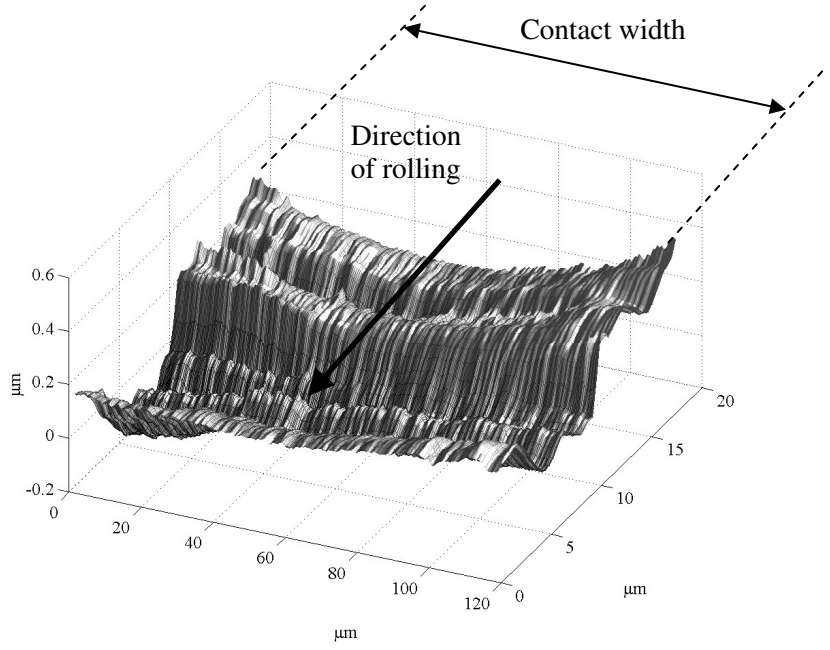

(c)

Figure 2.19. Increasing conformity in a rolling contact: (a) before contact, (b) after 1st cycle and (c) after 20 cycles. Groove formed is on ground mild steel surface in rolling contact with a SiC ball [14].

Not only the roughness of the surface, but also the type of roughness affects shakedown. Shakedown pressures in sliding contacts for different values for the coefficient of friction and asperity configurations were analyzed by Johnson for longitudinal asperities (parallel to the sliding/rolling direction) and lateral asperities (perpendicular to the sliding/rolling direction) (see figure 2.20) [15]. The results of this study revealed that an increasing coefficient of friction in sliding makes the shakedown pressures for longitudinal and lateral asperities approximately the same (see figure 2.20). In rolling, the coefficient of friction is low. In such a case there will be a deviation between the shakedown pressures of the two roughness types and the shakedown pressure for longitudinal asperities is higher than those for the lateral asperities. In other terms, lateral asperities would behave elastically under certain loading conditions where cyclic plastic deformation is observed for the longitudinal asperities.

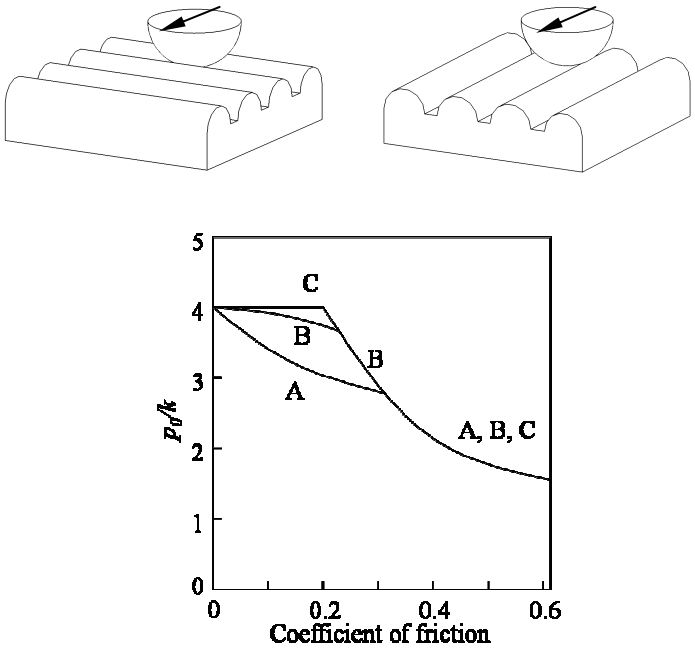

Figure 2.20. Asperity layout, lateral (top left) and longitudinal (top right) asperities. On the bottom, shakedown limits for lubricated sliding of (A) lateral asperities, (B) longitudinal asperities, (C) kinematic hardening of lateral and longitudinal asperities. Figures are re-illustrated from [15].

Unlike the case of lubricated sliding, dry sliding contacts involve higher coefficients of friction and the tangential components introduced are larger. In both cases it is possible that a steady state be achieved after a number of cycles of plastic deformation or wear. By wear mechanisms, material is removed from the contacting surfaces so that there are severe changes in

their topography. In contrast to plastic deformation of surfaces where roughness details do not completely change, surface topography or roughness details may completely change due to wear. There are several types of wear mechanisms, and some of them will be briefly explained in this section. However, at first the shakedown in sliding contacts will be briefly discussed.

In [12], a shakedown map is presented for two rough surfaces in sliding contact. The hard surface is modeled by spherical asperities with the same radii and Gaussian height distribution. The soft surface is modeled so that it can have any type of height distribution and spheres with different radii. The plots in figure 2.21 are taken from this study. In these plots, ψ_s is the plasticity index for repeated sliding and is defined by the authors as:

$$\Psi_s = \left(\frac{E^*}{p_s}\right) \cdot \left(\frac{\sigma_1}{R_1}\right)^{1/2} \tag{2.41}$$

where p_s is the limiting shakedown pressure calculated as defined in section 2.3, E^* is the equivalent modulus, R_1 is the average radius of the soft asperities and σ_1 is the R_q of the hard surface. Note that, as by definition, a plasticity index lower than 0.6 represents elastic contact of the asperities, whereas higher than 1 represents a plastic contact. A small plasticity index means smooth surfaces in contact so that there are not steep asperities that can be crashed plastically, as contact pressures are low. In figure 2.21 the shakedown map for cylindrical asperities are presented. As the plasticity index increases above 1, there is a sudden drop in the shakedown pressures which means that at even low pressures, instead of an elastic steady state, cyclic plasticity will be observed.

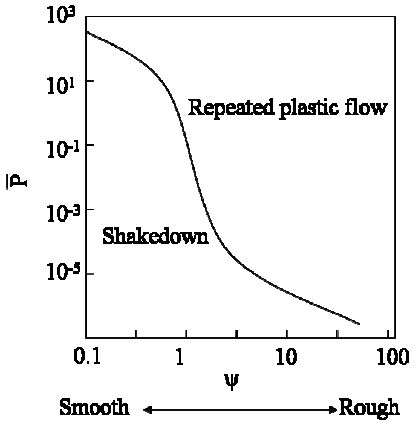

Figure 2.21. Shakedown map for sliding contact of rough surfaces. The asperities are cylindrical. $\bar{P}$ is the normalized nominal pressure. The figure is re-illustrated from [12].

In the following sections, two wear mechanisms, namely adhesion and abrasion, often observed in sliding contacts will be presented.

Adhesion

Considering two bodies in a sliding contact, adhesive wear may occur in which material transfer from one surface to the other takes place (see figure 2.22). The mechanism of this transfer is at the level of atomic bonds between the two contacting bodies. If these atomic bonds are stronger than one of the materials, the weak material is removed and is transferred to the material with stronger bonds.

Different bond types were presented in [16] and named strong and weak bonds. Examples of strong bonds are ionic bonds (based on the attraction of the oppositely charged ions), covalent bonds (formed when there are shared electrons, i.e. a diamond crystal) and metallic bonds (based on the free electrons moving in-between positive ions of metals and metal alloys). There are also weak bonds within materials. Weak bonds can be hydrogen bonds (bonding of two molecules by a hydrogen atom), van der Waals forces (electromagnetic interactions between the electrons), etc.

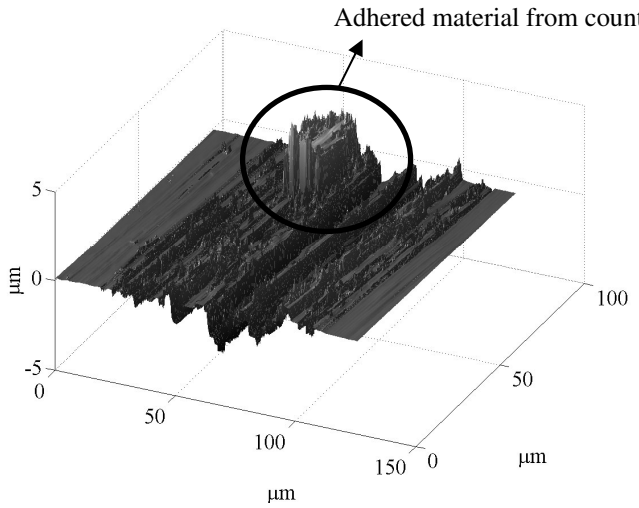

Figure 2.22. Adhesion in a steel-steel contact.

The adhesion mechanism is presented in figure 2.23. On the left, as the two surfaces are far away from each other, there are only atomic interactions between the atoms within the solids. As the upper surface approaches the lower surface, the atoms on the surface have a higher surface energy (γ) compared to the atoms in the bulk, as they are under the effect of both the atomic forces within the body and between the surfaces as discussed in the previous paragraphs. If at this moment adhesion takes place, then the work

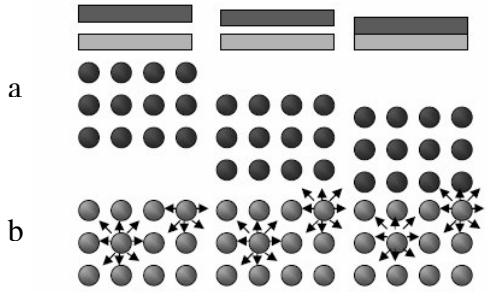

Figure 2.23. Mechanism of adhesion. Taken from [16].

done by the surface atoms on the upper body is called *work of adhesion*, denoted by Γ. If the materials are similar, than as the surfaces touch, the atoms on the surface of the two bodies have bonds such that they are in a steady state as are the atoms in the bulk material. If the materials are different, there is still energy on the surfaces, called the interfacial energy (γ_{ab}). Then the adhesive work that has to be done to separate material from the surfaces can be represented by the equation:

$$\Gamma_{ab} = \Delta\gamma = \gamma_a + \gamma_b - \gamma_{ab} \tag{2.42}$$

where γ_a and γ_b are the energies required to create the two surfaces and γ_{ab} is the interfacial energy. With similar solids this equation reduces to:

$$\Gamma_{ab} = \Delta\gamma = 2\gamma \tag{2.43}$$

Abrasion

Abrasive wear is caused by hard abrasive particles between contacting bodies. This type of abrasion is called *three-body abrasion*. In three-body abrasion, the hard particles can slide or rotate between the two surfaces, causing wear of the surfaces. However, in a more idealized situation, abrasive wear can be described as a formation of a groove and side ridges (called ploughing), when a hard asperity slides against a softer flat surface (see Figure 2.24). This can be analyzed on the macro-scale, by simply using a smooth relatively hard sphere sliding on a smooth and soft surface. As there are two contacting bodies this time, this type of abrasion is called *two-body abrasion*. Kato and Hokkirigawa defined a wear map for such a single asperity contact situation [17], where the type of the abrasion can be ploughing, wedge formation or cutting depending on the penetration of the sphere into the material and the interfacial shear strength in relation with shear strength of the softer surface.

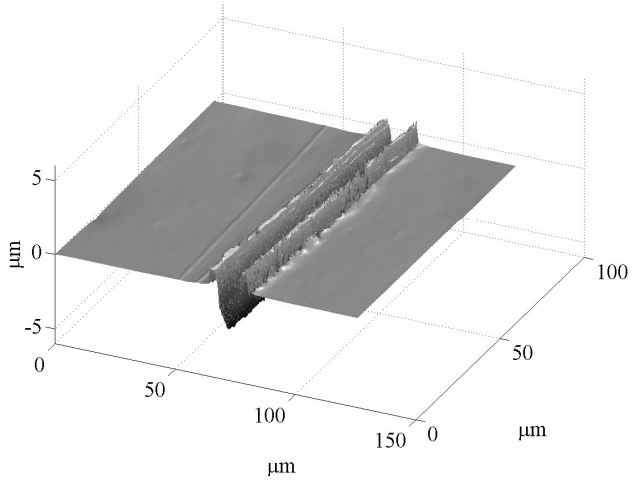

Figure 2.24. Two-body abrasion in a ceramic-steel contact

According to Kato [17], in the cutting mode long particles are formed at the leading edge of the sliding contact and the coefficient of friction is low in this type of abrasion. In the wedge formation mode, the removed material is in the form of a wedge which gets larger in time, and during sliding of the wedge there is also adhesion of material from the surface to the wedge. The ploughing mode is different to cutting and wedge forming because no material is removed as chips, however, as the abrasive moves along the soft surface, a shallow groove is formed and the abrasive material ploughs through the surface.

2.5. Summary

In this chapter, mechanisms of deformation and wear in rolling and sliding contacts for smooth and rough surfaces were discussed. The literature on elastic and plastic contacts for smooth and rough surfaces as well as wear and deformation mechanisms were described. The two models (analytical and numerical) that were referred to in section 2.4.2 will be further discussed in chapter 4 and used in the analysis.

References

[1] H. Hertz, Ueber die berührung fester elasticher körper, J. Reine Angew. Math. 92 (1881), pp. 156-171.
[2] G.M. Hamilton, Explicit equations for the stresses beneath a sliding spherical contact, Proc. Instn. Mech. Engnrs. 197C (1983), pp. 53-59.
[3] K.L. Johnson, Contact Mechanics, Cambdridge University Press, Cambridge, 1985.
[4] A. Kapoor and K.L. Johnson, Effect of changes in contact geometry on shakedown of surfaces in rolling/sliding contact, Int. J. Mech. Sci. 34 (1992), pp. 223-239.
[5] A. Kapoor and J.A. Williams, Shakedown limits in sliding contacts on a surface-hardened half-space, Wear 172 (1994), pp. 197-206.
[6] E. Melan, Der Spannungsgudstand eines Henky-Mises schen Kontinuums bei verlandicher Belastung, Sitzungberichte der Ak. Wissenschaften Wien, Series 2A 147 (1938), pp. 73.
[7] A. Kapoor, K.L. Johnson and J.A. Williams, A model for the mild ratchetting wear of metals, Wear 200 (1996), pp. 38-44.
[8] R.S. Sayles, Basic principles of rough surface contact analysis using numerical methods, Tribology International 29 (1996), pp. 639-650.
[9] L. Chang and Y. Gao, A simple numerical method for contact analysis of rough surfaces, Journal of Tribology 121 (1999), pp. 425-432.
[10] J.A. Greenwood and J.B.P. Williamson, Contact of nominally flat surfaces, Proc. Roy. Soc. A295 (1966), pp. 300-319.
[11] H.M. Westergaard, Bearing pressures and cracks, Trans. ASME, Journal of Applied Mechanics 6, 49 (1939), pp. 399.
[12] A. Kapoor, J. A. Williams and K. L. Johnson, The steady state sliding of rough surfaces, Wear 175 (1994), pp. 81-92.
[13] A. Kapoor, F. J. Franklin, S. K. Wong and M. Ishida, Surface roughness and plastic flow in rail wheel contact, Wear 253 (2002), pp. 257-264.
[14] Y.C. Taşan, M.B. de Rooij and D.J. Schipper, Changes in the micro-geometry of a rolling contact, In Proceedings of the 11th Nordic Symposium on Tribology (2004), pp. 33-44.
[15] K.L. Johnson and H.R. Shercliff, Shakedown of two-dimensional asperities in sliding contact, Int. J. Mech. Sci. 34 (1992), pp. 375-394.
[16] M.B. de Rooij, Solid and Surfaces Handouts, Laboratory of Surface Technology and Tribology, University of Twente (2003).
[17] K. Kato, Wear mechanisms, In Proceedings of the 1st World Tribology Congress (1997), London, pp. 39-56.

Chapter 3. Measurement of changes in the surface micro-geometry

3.1. Introduction

In chapter 2 mechanisms of wear and deformation in rolling and sliding contacts were introduced. In chapter 3 the focus will be on the techniques developed for measurement of changes in the surface micro-geometry during wear experiments. These techniques include the semi-online wear measurement system that can be used for sliding and rolling contact experiments, and a repositioning algorithm for processing the data acquired by the interference microscope.

Depending on the way the data is acquired during an experiment, wear measurement techniques can be classified as on-line and off-line methods. On-line micro-wear methods are almost always based on fast data acquisition techniques and basic principles for the measurement of the changes in statistical surface parameters like centerline average (R_a) or root mean square (R_q) during the wear test. These measurements on selected areas or cross-sections are performed using a variety of measurement tools and approaches like capacitance [1], ultrasound [2], or scattered light [3]. They are mostly used in in-situ tool monitoring systems or roughness control for crucial processes like finishing operations. On-line micro-wear methods applied to wear tests have the advantage of applying the wear test and obtaining the data simultaneously. However, the major drawbacks are that global changes (i.e. R_q change) rather than the local topographical changes on the surface are measured. Furthermore, volumetric changes cannot be obtained.

On the other hand, in off-line experiments, the wear test and the measurement of wear are separated. For example, the weight of the specimen before and after a wear experiment is measured using weight measuring equipment. Weight loss gives information about the mass (and with density, volume) that is worn away. The method is quantitative, and simple. The resolution of this method is limited, and secondly, local surface changes cannot be measured. Moreover, the mass change measured represents the net amount of material removed and adhered to the contacting surfaces.

Using roughness measurement systems like AFM and the interference microscope, 3D surface height information can be obtained. Such equipment can be used to measure wear by dismounting the specimen from the wear tester after a wear test and performing a roughness measurement. In this way, accurate measurement of the changes in the surface topography is made possible by comparing a roughness measurement before and after

the experiment. However, two problems arise during off-line experiments. At first, there is the problem of inaccurate repositioning of the specimen under the measurement setup after a cycle (or remounting). This problem necessitates the use of precise sample holders and accurate positioning tools to measure the topography of the same area after each cycle. Secondly, after remounting, contacting pairs of micro-asperities change. This leads to new contact conditions at the start of each cycle and hence an interrupted progress of wear.

Thus, a semi-online method is proposed where roughness measurement equipment is integrated with a wear tester [4]. With this technique the changes in surface topography can be measured locally at the asperity level and progressively in, for example, a wear tester combined with a roughness measurement system. In our case this will be a pin-on-disk tester combined with a white-light interference microscope. The applicability of the method is for both mild and severe wear cases. Also, locally removed and adhered material at the surface can be measured with the assumption that these two do not take place at the same spot. These characteristics make the measurement technique suitable for wear processes like erosion and abrasion, as side ridges, abrasion grooves (see figure 3.1) and erosion craters can be measured independently. The repositioning errors due to the in-situ positioning inaccuracies of the positioning system can be solved using a repositioning algorithm. Such an algorithm was introduced in [5] and improved and optimized in [6] and [7]. The setup also gives the possibility to simultaneously measure the friction force that can later be correlated to the wear of the contacting materials.

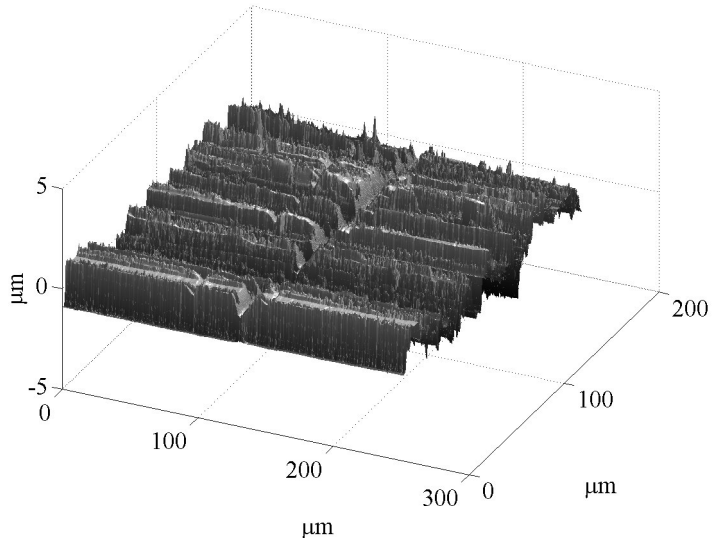

Figure 3.1. Abrasion grooves formed by a wedge shaped tool.

In the next section the developed measurement setup and operating principles will be introduced. Following that, in section 3.3 the pre-processing operations done on the raw data will be discussed. The developed repositioning algorithms termed *matching* and *stitching* will be discussed in sections 3.4 and 3.5 and later focused in detail in section 3.6.

3.2. Semi-online measurement of wear

The measurement technique is based on measuring the changes in the surface topography or in this case a certain spot on a disk surface which is in contact with a bearing ball specimen. Figure 3.2 shows the steps in such an experiment. Roughness measurements done by an interference microscope before and after wear are stored for this measured spot on the disk surface. In order to obtain the progressive three-dimensional changes in this area of interest, these images are relocated using dedicated algorithms. The resulting difference image shows the local net change of the surface. These steps and the components being used will be the subject of the following sections.

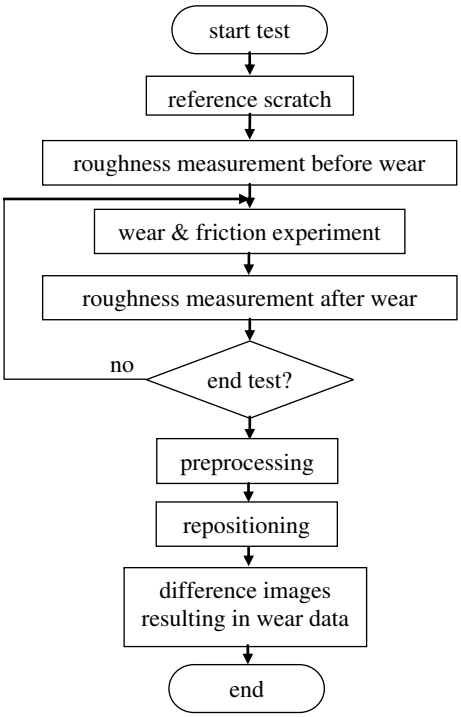

Figure 3.2. Operation diagram for the measurement system.

In the following section basics of the interference microscopy technique and surface roughness measurements with the interference microscopy

technique will be presented. In section 3.2.2, the wear and friction tester will be introduced and wear experiment procedures will be discussed. In section 3.2.3 the rolling contact adaptor of the setup used in the rolling contact experiments will be described.

3.2.1. Measurement of surface roughness

Roughness measurements were carried out using a Mirau type white-light type interference microscope called Micromap. Interference microscopes are non-contact measurement instruments that can measure roughness not only in profiles but also in three dimensions in a single measurement. They are faster than other measurement tools and thus suited well for semi-online measurements of surface roughness.

An interference microscope utilizes the interference patterns formed during a measurement to calculate the surface heights and re-construct a surface. These interference patterns are called fringes and are presented in figure 3.3 of an alumina (Al_2O_3) sphere surface of radius 5 mm. As can be seen, the fringes have dark and light bands positioned next to each other. These bands are at a distance of half the wavelength of the applied light (as will be derived later in this section) and they form isometric lines along the areas of the surface of equal height.

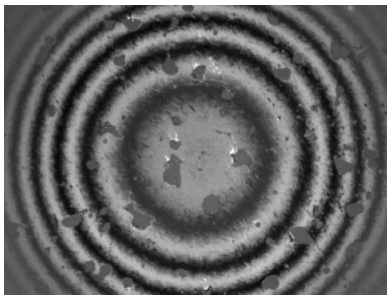

Figure 3.3. The interference fringes from Al_2O_3 sphere surface.

A basic setup for a better understanding of how fringes can be used to obtain height data can be seen in figure 3.4. This setup is called an air wedge setup [8] and is composed of two glass plates positioned at an angle to each other forming the shape of a wedge. The medium of the setup is air. When a light beam from a light source is reflected from the first glass plate, a percentage of light will continue its path at a diffraction angle. This beam then reflects from the second glass plate and leaves the wedge again at a diffraction angle. The initially reflected beam follows a path that is shorter than the ray reflected from the second glass plate. Considering that the light motion is in the form of a wave, this optical path difference causes a shift in the positions of the highest and lowest amplitude of the light wave with respect to the initial wave. Thus, light and dark interference patterns form

because of the match of the highest versus highest and highest versus lowest points in the wave. The former case leads to light fringes (constructive interference) and the latter to dark fringes (destructive interference) respectively.

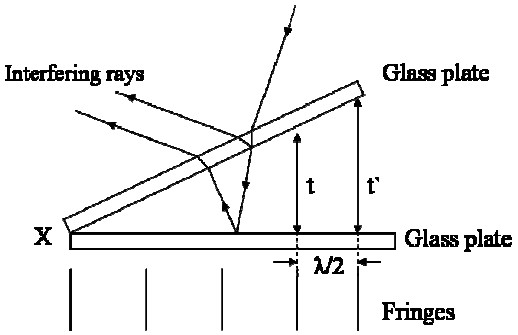

Figure 3.4. Air wedge forming interference fringes (re-illustrated from [8]).

As explained, in the air wedge setup, the interfering rays are reflected (a) from the first glass plate and (b) from the second glass plate. If the number of fringes formed in an air wedge setup is represented as n (where n = 0,1,2…), considering that at x = 0 the phase change is $\lambda/2$ (due to reflection of light from air to glass) and the path followed in-between the two plates is equal to $2t$ (due to very small wedge angle), then the path difference at the n^{th} fringe (constructive interference) at thickness t can be represented as:

$$n\lambda = 2t + \frac{\lambda}{2} \tag{3.1}$$

and for $n+1^{th}$ fringe (destructive interference) it is:

$$(n+1)\lambda = 2t` + \frac{\lambda}{2} \tag{3.2}$$

Using equation 3.1 and equation 3.2, the thickness difference between the points of neighboring dark and light fringes is given by:

$$t - t` = \frac{\lambda}{2} \tag{3.3}$$

Knowing the wavelength of the applied light, one can calculate the thickness of a point by counting the light fringes placed between x = 0 and the measurement position. Then equation 3.1 can be used for calculating the heights. The same procedure can be done for the dark fringes, this time with equation 3.2.

Similarly, for a Mirau interference microscope the lower glass plate in the wedge problem is the surface of interest where a measurement is conducted and the top glass plate is the reference surface which is a mirror. The fringes are established upon interference of the rays reflected from these two surfaces as explained in the air wedge example. The operating principle of a basic two-beam Mirau interference microscopy system is shown in figure 3.5 on the left. A beam splitter is used to split the light from a light source to the surface of interest. Light reflected from the measurement surface and the reference surface within the objective of the microscope in figure 3.5 (right) forms the fringes as the system is focused on the specimen.

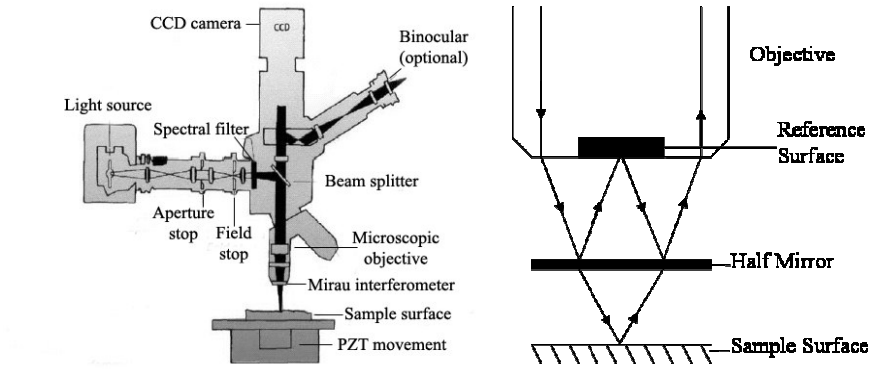

Figure 3.5. Mirau type interference microscope (left), lenses used (right). Left image is taken from [9].

For a two-beam interference at a point, the basic equation for the calculation of the surface height at a phase of Φ_p is given in [10] as:

$$z(x,y) = \left(\frac{\lambda}{4}\right)\Phi_p(x,y) \tag{3.4}$$

For the calculation of phase within the interference field, the equation for the intensity of the interference fringes (I) is used. This equation, where γ_f is the fluctuation of the intensity ($0 < \gamma_f < 1$) is defined as:

$$I(x,y) = I'(x,y)\left[1 + \gamma_f(x,y)\cdot cos\Phi_p(x,y)\right] \tag{3.5}$$

Using equation 3.5 it is possible to calculate the interference intensity at the four phase shifts of 0, π/2, π and 3π/2. These intensities I_1, I_2, I_3, I_4 then can be represented as:

$$I_1 = I'\left[1 + \gamma_f cos(\Phi_p + 0)\right] = I'\left(1 + \gamma_f cos\Phi_p\right) \tag{3.6}$$

$$I_2 = I'\left[1 + \gamma_f cos\left(\Phi_p + \frac{\pi}{2}\right)\right] = I'\left(1 - \gamma_f sin\Phi_p\right) \quad (3.7)$$

$$I_3 = I'\left[1 + \gamma_f cos\left(\Phi_p + \pi\right)\right] = I'\left(1 - \gamma_f cos\Phi_p\right) \quad (3.8)$$

$$I_4 = I'\left[1 + \gamma_f cos\left(\Phi_p + \frac{3\pi}{2}\right)\right] = I'\left(1 + \gamma_f sin\Phi_p\right) \quad (3.9)$$

Then equations 3.6 to 3.9 can be used to calculate the phase at each point as:

$$\Phi_p(x, y) = tan^{-1}\left(\frac{I_4 - I_2}{I_1 - I_3}\right) \quad (3.10)$$

Substituting Φ_p into equation 3.4 one can calculate the surface heights.

In a Mirau type interference microscope the phase shifts in equations 3.6 to 3.9 are done by means of the PZT movement of the focus and the algebra for the surface reconstruction is as discussed earlier.

The Micromap interference microscope measures 3D surfaces with height resolutions of approximately 1 nm and an in-plane resolution of less than 1 μm depending on the magnification used. The areas that can be measured are presented in table 3.1 for a variety of magnification options. By increasing the magnification, more detail on surface features (such as a wear track geometry) can be obtained.

Table 3.1. Sampling interval options for the interference microscope

Magnification	Pixel size (μm)	Measurement area (for 307200 pixels)
10	0.98	627.20 μm x 470.40 μm
20	0.49	313.60 μm x 235.20 μm
25	0.39	250.88 μm x 188.16 μm
50	0.20	125.44 μm x 94.08 μm
75	0.13	83.63 μm x 62.72 μm
100	0.09	55.75 μm x 41.81 μm

As the principle of measurement is based on the light reflected from a surface and its intensity, the specimen on which a topography measurement is done should have reasonable reflectivity. For the described interferometer the required minimum reflectivity of the sample was approximately 1%.

The height resolution is independent of the magnification. For rough surfaces, the maximum possible slope that can be measured are dependent

on the magnification. For 20 times magnification the maximum slope that can be measured is 0.3 radians. At higher magnifications i.e. 50 or 100 times, measurements on larger slopes are possible. However, for slopes that are higher than the maximum permissible slope then light is not reflected back to the lens and these spots with high slopes are represented as missing points in the measured surface. A sample measurement which was not processed is presented in figure 3.6. The measurement was conducted with a 75 times magnification. The white spots show the regions where no valid measurement points were obtained. The data could also involve outliers and measurement noise which should be removed. Methods and procedures for these purposes will be discussed later in this chapter.

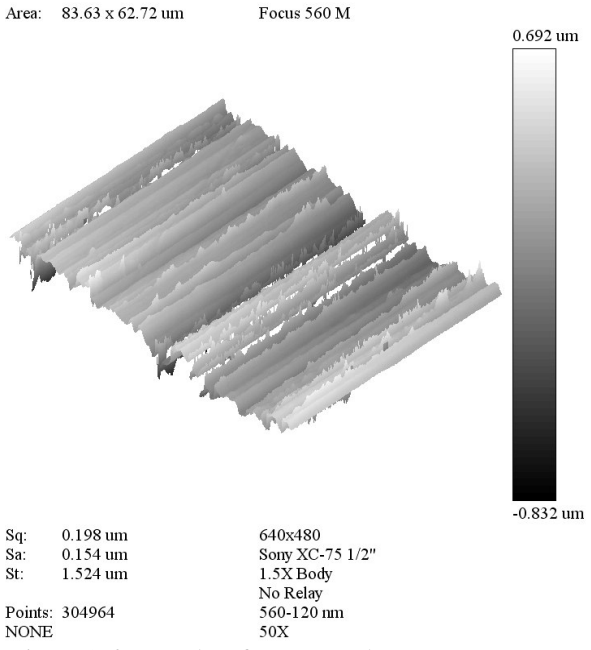

Figure 3.6. Raw data from a roughness measurement.

3.2.2. The wear and friction tester

The pictures of the measurement setup can be found in Appendix B. The setup introduced in [4] consists of 3 main components (see figure 3.7), namely an interference microscope, a friction device and a controllable positioning table. The friction device is mounted on the controllable table so that they can move together. Roughness measurements are done by white light interference microscopy based on the principles described in the previous section. In a wear experiment, the contacting surfaces are a ball and a disk mounted on a rotating table. The ball is connected to the friction device. The ball is restricted to rotate or move. The adaptor can be a rolling adaptor or a sliding adaptor (i.e. the ball is fixed). The rolling adaptor will be further described in section 3.2.3.

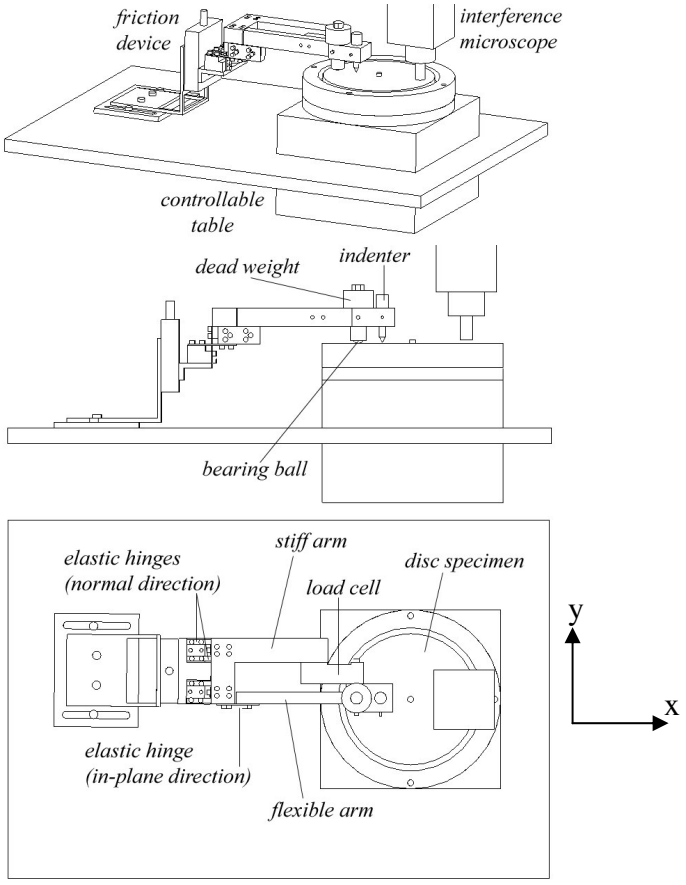

Figure 3.7. Views from the setup.

The relative sliding motion between the disk and the ball is obtained by the rotation of the controllable table, which is step motor driven. Accuracy and repeatability in the rotational direction are $2.9.10^{-3}$ and $1.4.10^{-4}$ radians respectively. This repeatability accounts for approximately $2.4.10^{-4}$ μm in the *x* and 3.5 μm in *y*-directions at a wear track diameter of 50 mm. The *x* and *y* stepper motors are used for positioning the disc specimen before the experiment. The friction device is illustrated in the same figure.

During the wear experiments, a bending type load cell is used for friction force measurements. The system flexibility in the in-plane rotational direction (friction force direction) is achieved by means of a steel elastic hinge of 0.2 mm thickness in the direction of the friction force. The normal load is applied by dead weights and the flexibility in the direction normal to the plane of contact is also achieved by means of elastic hinges. These hinges are stiff in the direction of the friction force so that flexibility is only in the direction of sliding. With the use of the hinges the parasitic frictional losses in the system are eliminated. A vertical micrometer table is used for adjusting the level of the ball so that it just touches the surface and applies

zero load without the dead weights. The measurement resolution of the friction measurements is 0.01 N.

The result of the contact between the ball and the disk is a wear scratch that develops in the tangential direction as a function of the number of revolutions. Because it is not known in advance where the wear track is going to be formed, a reference position is required. For this, an indenter is positioned close to the ball adaptor for forming a reference scratch on the disk surface. As the distance between the indenter center and the ball is known in advance, the *x-y* table can be used for first centering the indentation on the video output of the computer screen. Then again the *x-y* table is used to move the table a predetermined amount. In this way, the reference scratch is used for positioning the area of interest where the roughness measurements will take place.

The operation of the test rig shown in figure 3.2 includes wear and friction measurements at the same time. The first step in the experiment is scratching the disk with the indenter forming a reference scratch. The candidate area of the wear track is then found with the help of the *x-y* table and a roughness measurement is made on the spot where the wear track will be formed, with the interference microscope. After a certain number of rotations the table is stopped and another roughness measurement is performed. In this way, successive rotations allow a wear track to be formed. During the experiment, after each rotation, three-dimensional images of the spot are stored. Simultaneously, the friction force signal is recorded for correlation purposes.

3.2.3. Rolling contact adaptor

In addition to sliding, rolling contact experiments can also be made with the wear and friction tester. Images of the 35 mm height adaptor can be found in Appendix B. The adaptor was introduced in [11] and as is seen in figure 3.8 consists of three major parts: miniature ball bearings, a clamping unit and a horizontal slider. The miniature ball bearings have an outer diameter of 3 mm and bore diameter of 1 mm. The bearings can withstand a maximum load of 7 N and they are mounted on the unit which is used to clamp the ball specimen. The clamping unit and the slider allow different diameters of balls to be used in rolling experiments, ranging from 6 mm to 12 mm. After clamping there is an offset between the center of contact and the applied load for different diameters of balls used. The horizontal slider is used to eliminate this offset so that the applied load and the center of contact are in the same plane.

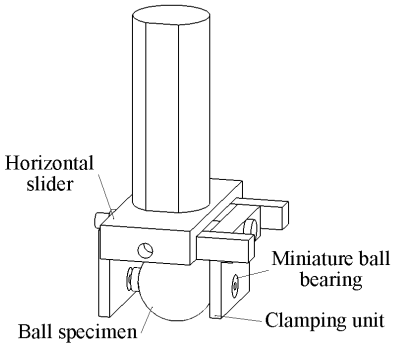

Figure 3.8. Adaptor for free-rolling contact experiments.

The rolling and sliding contact experiments were performed considering the specifications of the measurement setup. These specifications are presented in table 3.2.

Table 3.2. Technical specifications of the measurement setup.

Maximum normal load (N)	10 (Sliding)
	5 (Rolling)
Disk specimen diameter (mm)	100
Ball specimen diameter (mm)	Sliding: 10 (max)
	Sliding: 3 (min)
	Rolling: 12 (max)
	Rolling: 6 (min)
Maximum speed (mm/s)	9

The raw data from the sliding and rolling contact experiments require pre-processing before matching and stitching. In the following sections the pre-processing algorithms of the measured roughness data will be discussed.

3.3. Pre-processing the measurement data

The 3D images from the measurements have three types of problems. There are outliers, missing points and measurement noise. Outliers are erroneously measured extremely high/low local points or spikes due to the measurement systems limitations. Secondly, there can be missing points in the data on account of the high local slopes of the surface. Measurement noise can be the third factor introduced by the measurement system and/or the vibrations from the surrounding. Repositioning the measurement data without an initial step that deals with these measurement errors is problematic and leads to inefficient use of the matching and stitching procedures.

3.3.1. Noise removal

Measured 3D images include measurement noise (see figure 3.9), especially with increasing roughness. The noise has a high frequency and disturbs the image and the effectiveness of the repositioning algorithm. This noise can be either of a Gaussian or a non-Gaussian type. The elimination of the latter type requires several techniques that are not included in this section. For the Gaussian noise different filters are available. One is the Wiener adaptive filter [12], which is generally suitable for this type of noise.

The Wiener filter is a linear adaptive filter. The variance in the filtering window is calculated during filtering. If the variance in a region in the image is large, then less smoothing is applied than the case where the variance is small. In this way edges and some important high frequency features are preserved during filtering.

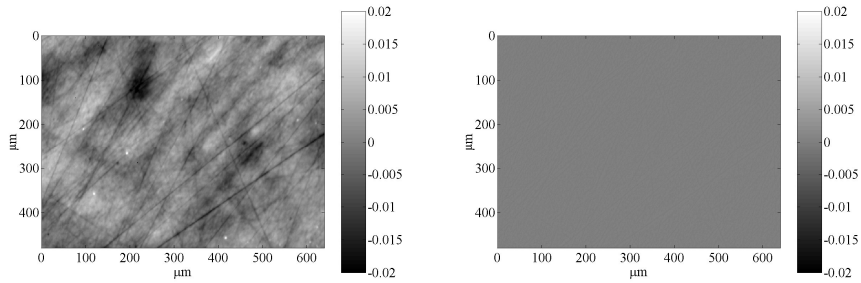

Figure 3.9. 3D image with noise (left). The removed noise is on the right.

At a given pixel, filtering is achieved using the neighboring pixels. The pixel of interest and the neighboring pixels form the filtering window size which can be determined by the user in advance. In this way, for each pixel the local mean (μ) within the filter window size and the variance (σ^2) are calculated according to the equations:

$$\mu_{i,j} = \frac{1}{NM}\sum_{i=1}^{N}\sum_{j=1}^{M} z(i,j) \tag{3.11}$$

$$\sigma_{i,j}{}^2 = \frac{1}{NM}\sum_{i=1}^{N}\sum_{j=1}^{M} (z(i,j) - \mu_{i,j})^2 \tag{3.12}$$

Then a new surface is generated using:

$$z_{new}(i,j) = \mu_{i,j} + \frac{\sigma_{i,j}{}^2 - \upsilon^2}{\sigma_{i,j}{}^2}(z(i,j) - \mu_{i,j}) \tag{3.13}$$

In equation 3.13, v^2 is the noise variance which is the average of all local estimated means $\mu_{i,j}$. Compared to standard low-pass filters with a non-changing averaging window, the order of the noise estimated by the filter is generally low and the effect of the surface features and edges do not affect neighboring pixels. In figure 3.9, the surface on the left with noise has a roughness of 4.3 nm which is very smooth. Standard deviation of the removed noise on the right is 0.2 nm, which is the noise level of the interference microscope. For rougher surfaces, this percentage is less.

The noise removal is only used for the images required for the repositioning stage. After the transformation parameters are obtained, noise removal is not applied to the original images as important high frequency information can be eliminated as well. In that sense, this step is only used for reducing the effects of noise in the solution stage as will be discussed in section 3.4. The noise removal is followed by the filling-in of missing points on the surface and this will be discussed in the following section.

3.3.2. Missing points

Missing points, for example caused by high local slopes as illustrated in figure 3.10, are marked as NaN (not a number) in the surface matrix. The elimination of the missing points is performed with a neighborhood operation. The heights at the missing points are calculated as a weighted sum of linear interpolations from the nearest available points as follows:

$$z_{i,j} = \frac{1}{4}\left[z_{i+1,j} + z_{i,j-1} + z_{i,j+1} + z_{i-1,j}\right] \tag{3.14}$$

3.3.3. Outliers

Outliers are also errors introduced by the measurement system. They are extremely high or low artificial points with respect to the general distribution. One way to eliminate them is to assume a Gaussian distribution throughout the surface. The values outside the interval are counted as outliers and replaced by NaN. In equation 3.15, z is the height data, μ is the mean and σ is the standard deviation of the data points. Then these values are re-estimated using the procedure for missing points described above:

$$\mu - 6\sigma < z < \mu + 6\sigma \tag{3.15}$$

However, for the case of wear and outliers it is not possible to obtain a reliable value for the mean of a surface because the surface can have heights with a higher deviation from the mean than 3σ. For this reason, to eliminate outliers, median filtering is used instead.

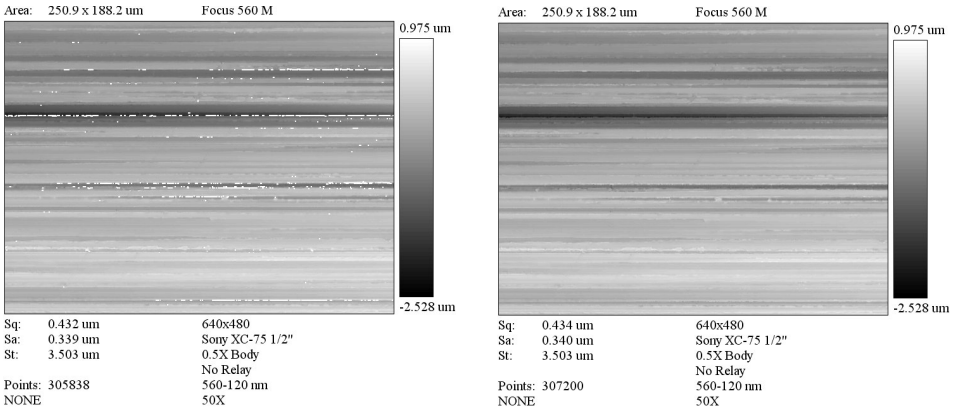

Figure 3.10. Missing points (left) are filled (right).

Similar to the noise removal stage, outlier removal is also applied at the solution stage (repositioning) to speed up the solution process as in [4]. With the known transformation parameters, original images are then repositioned. In the next section the repositioning stage will be explained.

3.4. Repositioning the roughness data

The series of images obtained during an experiment is post-processed as the experiment is finished (see figure 3.2). The main objective of this step is to obtain the local changes on the surface from the differences of the measured successive surfaces. At first the positioning errors related to the rotational accuracy of the controllable table should be corrected. Although the table is stopped approximately at the same spot in each step, positioning accuracy of the table leads to a slightly rotated worn image. Before comparing two surfaces, it is necessary to compensate this positioning error in the image. This results in a required compensation for θ_z, Δ_x and Δ_y (see figure 3.11).

Secondly, due to the generated wear track which results in a tilted and vertically shifted reference plane, mean lines of the images before and after wear are different as seen in Figure 3.12. The differences in the reference

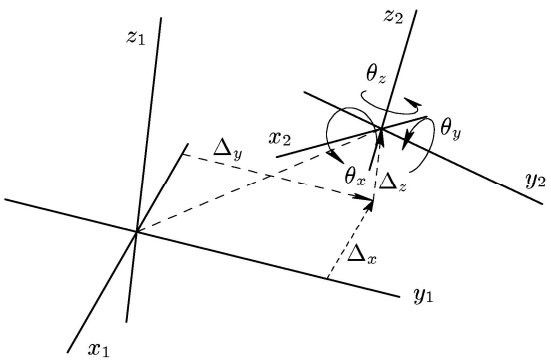

Figure 3.11. Coordinate systems and degrees of freedom.

planes are the tilts and shift represented as: Δ_z, θ_x and θ_y. In short, this means that the surfaces need to be repositioned in all six degrees of freedom. Distortions are not taken into account and rigid body transformation is applied.

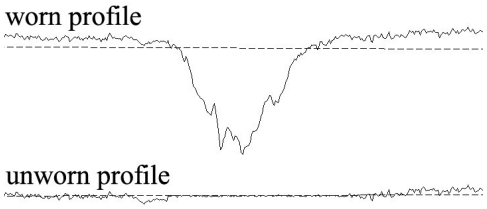

Figure 3.12. Worn and unworn surface profiles. Dashed lines represent the mean lines.

To solve this problem, a repositioning algorithm [4] and [6] is developed. This algorithm is used for two purposes:

1. Repositioning of the two measurements on the same area. This will be called *matching* in the remainder of this thesis.
2. Repositioning of a series of partly overlapping images. This will be called *stitching* in the remainder of this thesis.

Successive surface topography measurements result in images which possess a certain amount of similarity. The images are matched in order to obtain the difference image representing the local changes. For this purpose, the images obtained before and after wear are repositioned relative to each other before subtracting the two, so as to compensate the positioning errors developed through the test. In the 3D space there are 6 parameters that should be considered, i.e. 3 translations (Δ_x, Δ_y and Δ_z) and 3 rotations (θ_x, θ_y and θ_z) (see figure 3.11). Determination of these correct shifts and rotations can be done by optimizing a cost function, which is a function of these 6 parameters. In this study the weighted distance function introduced in [6] is used. This function is represented as:

$$cost_i(\Delta_x, \Delta_y, \Delta_z, \theta_x, \theta_y, \theta_z) = \frac{1}{N} \sum F_{wgt}(d) \tag{3.16}$$

where N is the number of pixels and

$$d = z_2^t(x_2^t, y_2^t) - z_1(x_1, y_1) \tag{3.17}$$

In equation 3.17, d denotes the height differences of the transformed (z_2^t) and the reference (z_1) images. The weighted distance correlation function F_{wgt} is defined as:

$$F_{wgt}(d) = exp\left[-\frac{1}{2} \cdot \left(\frac{d}{R_q} \right)^2 \right] \tag{3.18}$$

where R_q is the roughness of the difference image. Such normalization is necessary in particular for the case of matching two images having particular differences like a wear track. Outliers have a small contribution to the overall sum as proven in [6]. The function (3.18) has the maximum value for the case of best fit as the sum of the distances between the corresponding points in two surfaces gets closer to zero.

The solution of such a nonlinear minimization/maximization problem with a number of unknowns requires the use of efficient solvers. A number of solvers were tested in [7]. In this work, the solver used to get the maximum value of the cost function is the global optimizer introduced in [13]. This global solver is efficient at finding the global minimum among a number of local minima (figure 3.13). It is based on windowing the search space and it uses a combination of local and global searches initialized with a line search method as default. With the global search candidate points that are possible minima are put in a "shopping basket" and subsequently a local search is carried out around these points. The solver also requires initial search intervals for the unknowns (Δ_x, Δ_y, Δ_z, θ_x, θ_y and θ_z), assuming that the solution is within the intervals. Detailed information on the solver and the windowing technique can be found in Appendix C.

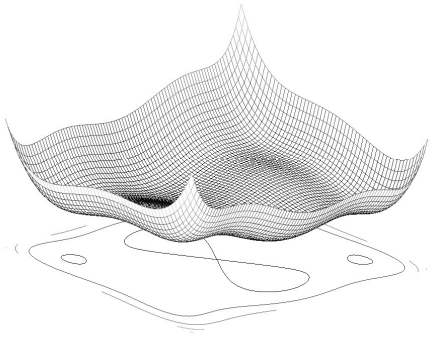

Figure 3.13. Function with multiple local minima.

Taking the solver as the cost function optimizer, an algorithm is developed. Due to the complexity of the current problem with 6 unknowns and a risk of local minima, a level structure is used as shown in figure 3.14 to allow for larger search intervals. Also, using an initial coarse grid is a second measure to avoid local minima. In other words, the initial searches (Δ_x, Δ_y, Δ_z, θ_x, θ_y and θ_z) are done at a coarse level, which makes the process faster and

avoids the problem of getting stuck in local minima because the coarse grid contains low frequency information and it has less local minima. In this structure, taking i as the level number, at first an interpolation factor l for generating a coarser surface is determined as:

$$l = \frac{1}{2^i} \tag{3.19}$$

l is used at each level for reconstructing a new surface. The points where the new surface heights will be calculated are determined by generating a new grid on the x-y plane of the surface. l is used as a step size in the construction of this mesh as $[(1..l..x_{size}), (1..l..y_{size})]$, where x_{size} and y_{size} are the size of the surface in the x- and y-directions respectively. In this mesh the new height at a new mesh point is interpolated among the surrounding points on the original image using a bilinear interpolation.

In figure 3.15 the repositioning algorithm is presented. To speed up the repositioning process, initial values for the search of in-plane shifts and rotations (Δ_x, Δ_y and θ_z) are required. This can easily be done by means of a manual check of the pre-processed images or are known in the stitching case beforehand. These initial guesses for the in-plane D.O.F' s (Δ_x, Δ_y and θ_z) are used in a fast least squares plane fit of a plane $z = ax+by+c$ to the corresponding difference image, in order to obtain the initial values for the out-of-plane D.O.F' s (Δ_z, θ_x and θ_y). The function used for the least squares fit is:

$$f = \left[z_2(x,y) - z_1(x,y)\right] - \left(a(x-\Delta x) + b(y-\Delta y) + (c-\Delta z)\right) \tag{3.20}$$

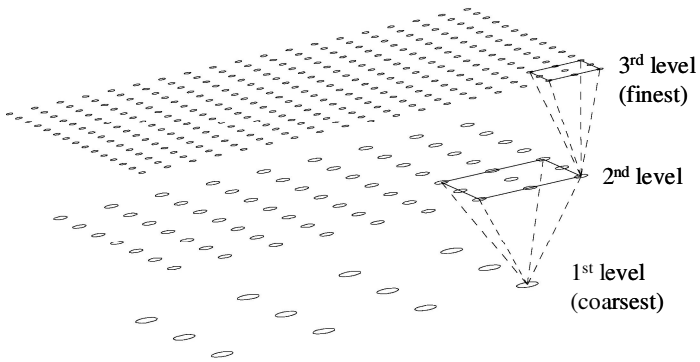

Figure 3.14. Grid structure used in the solution procedure.

The best values of *a*, *b* and *c* (for the minimum difference between the difference of surfaces z_1 and z_2 and the fitted plane) are obtained by a least squares minimization procedure.

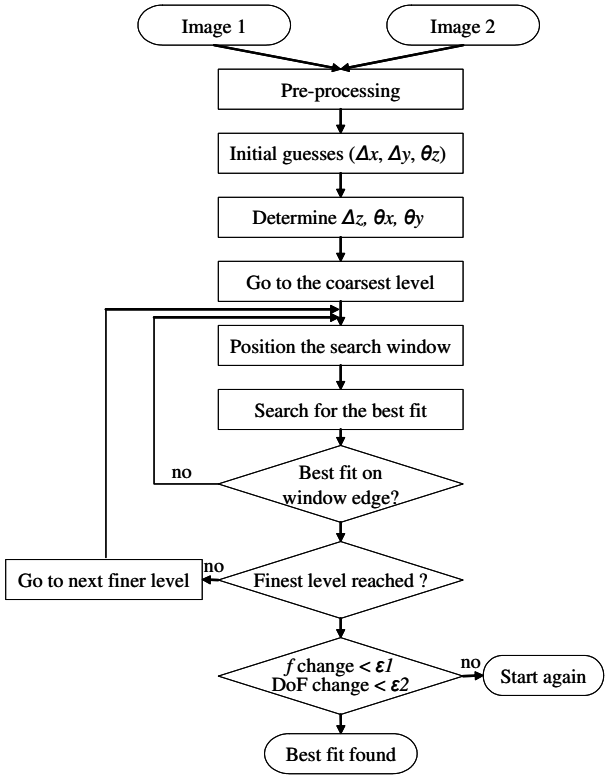

Figure 3.15. Repositioning procedure.

The search of the best-fit starts with large search windows for each degree of freedom at the coarsest level, taking the initial values as starting values. Next, the solution at that level is used to build a new and smaller search window at a finer level that has higher frequency information. The size of the window at the new finer level is calculated as:

$$\Delta\delta_{int} = 0.001 \cdot \left|\delta_{int}\right| + \varepsilon \tag{3.21}$$

$$d_{int+1} = \delta_{int} \pm \Delta\delta_{int} \tag{3.22}$$

In equation 3.21, the search interval ($\Delta\delta_{int}$) is calculated from the best fit (δ_{int}) at a level. The new search interval (d_{int+1}) is calculated around this best fitting D.O.F as in equation 3.22. For large shifts, a large interval is used.

When a solution is found just at the edge of the window frame, the search is repeated at that level, repositioning the new window with that particular

solution at the center. In every window search at a given level, the solver searches for the D.O.F giving the maximum function value for equation 3.18. At the finest level, finally, a last solution is found for Δ_x, Δ_y, Δ_z, θ_x, θ_y and θ_z. If there is no convergence, the search should be started with new search windows or initial guesses. However, in all cases tested up to now, accurate solutions were found.

In this scheme, the transformation of point coordinates in one image to the reference image coordinates is obtained by means of the equation:

$$\begin{bmatrix} x2 \\ y2 \\ z2 \end{bmatrix} = R_{xyz} \cdot \begin{bmatrix} x1 \\ y1 \\ z1 \end{bmatrix} + \begin{bmatrix} \Delta_x \\ \Delta_y \\ \Delta_z \end{bmatrix} \tag{3.23}$$

where:

$$R_{xyz} = R_z \cdot R_x \cdot R_y \tag{3.24}$$

with:

$$R_x = \begin{bmatrix} 1 & 0 & 0 \\ 0 & cos(\theta_x) & -sin(\theta_x) \\ 0 & sin(\theta_x) & cos(\theta_x) \end{bmatrix} \tag{3.25}$$

$$R_y = \begin{bmatrix} cos(\theta_y) & 0 & sin(\theta_y) \\ 0 & 1 & 0 \\ -sin(\theta_y) & 0 & cos(\theta_y) \end{bmatrix} \tag{3.26}$$

$$R_z = \begin{bmatrix} cos(\theta_z) & -sin(\theta_z) & 0 \\ sin(\theta_z) & cos(\theta_z) & 0 \\ 0 & 0 & 1 \end{bmatrix} \tag{3.27}$$

The corresponding coordinates for the grid of the second image were obtained using a bilinear interpolation followed by the calculation of the difference d in equation 3.17 in order to obtain sub-pixel accuracy for the D.O.F's

3.5. Stitching

The wear track may be larger than the measured area. In this case, adjacent images need to be stitched together so that the measured images before and after a wear test cycle can be subtracted to calculate wear. The procedure for stitching is very similar to the one for the matching except that the resulting image is not a difference of two images at the same spot but a series of stitched images. Wear can be calculated by matching two groups of stitched images before and after a number of wear cycles. Two factors are important in stitching. At first, reasonable initial guesses are again required for the solution procedure to speed up the convergence and to avoid the risk of getting stuck in local minima. The initial values can easily be determined from the known amount of overlap of the two images. Secondly, the amount of overlap should not be less than 50% as recommended in [7]. In figure 3.16, a steel surface worn against a SiC ball is shown. In this example two images with a percentage of overlap of 50% are stitched together before wear so as to include the entire wear track within a single image after the first cycle. The dashed frame in the image represents the overlapping region of the two images.

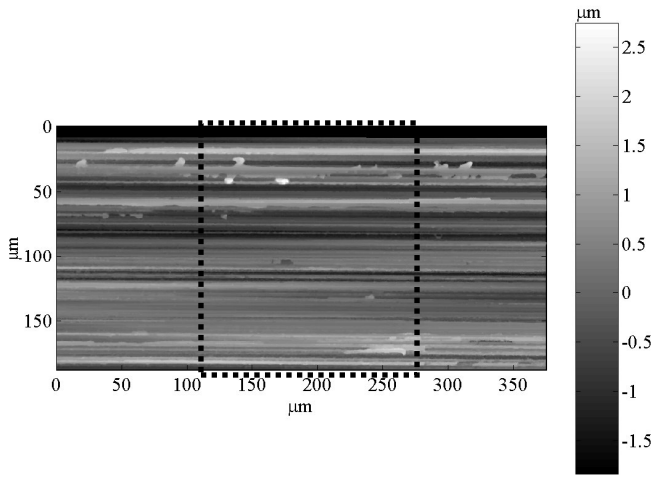

Figure 3.16. Stitching example with two images of 188.16x250.88 µm stitched together with approximately 50 % overlap.

3.6. Examples

In this section, six examples will be introduced. In the first example, an artificially generated surface with noise is used for checking the accuracy and efficiency of the repositioning algorithm used. In the second example, ground surfaces will be matched and effects of local minima will be discussed. The third example will be on the effects of wear track and

outliers on matching accuracy. In the fourth example sliding experiment and in the fifth example rolling contact experiment data will be used. Finally in the last example, a stitching example will be presented.

3.6.1. Example 1: Matching of noisy images

For testing the accuracy of the repositioning algorithm, artificially generated surfaces with known translation and rotation values were used (see figure 3.17). The surfaces had a roughness (R_q) of 100 nm. The second image had an additional Gaussian noise with a roughness of 10 nm. The known translation and rotation values were as in table 3.3. For the two images, the pixel size was 1 µm and area is 360 µm x 490 µm. For repositioning, the algorithm introduced by [7] and discussed in [4] was used.

Table 3.3. Translation and rotation parameters for the images.

D.o.F	Value
Δ_x	160 μm
Δ_y	-10 μm
Δ_z	1.5 μm
θ_x	-0.2˚
θ_y	0.1˚
θ_z	2˚

The criterion for the selection of initial search intervals is important as it affects the size of the search space and therefore the convergence time for the best solution. For this reason, an initial guess for the translation in x (Δ_x), y (Δ_y) and in-plane rotation (θ_z) can be made manually by eye, comparing the positions of the common features in the two images. For this particular problem whose solution is known in advance the initial guesses for these three in-plane degrees of freedom were selected to be; Δ_x = 165 μm, Δ_y = -10 μm and θ_z = 0˚ with window sizes of ±10 μm for Δ_x and Δ_y and ±2˚ for the θ_z. The initial guesses for θ_y, θ_z and Δ_z were calculated from these values. The difference image has a roughness (R_q) of 12 nm which is consistent with the applied Gaussian noise.

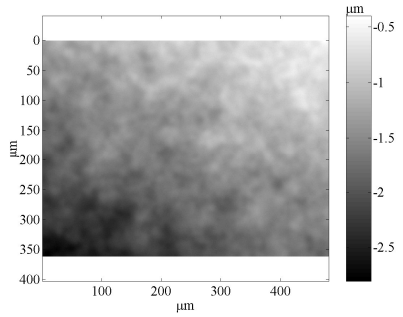

(a)

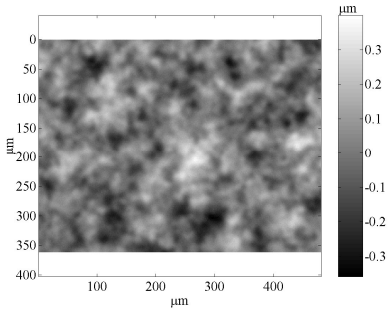

(b) (Continued)

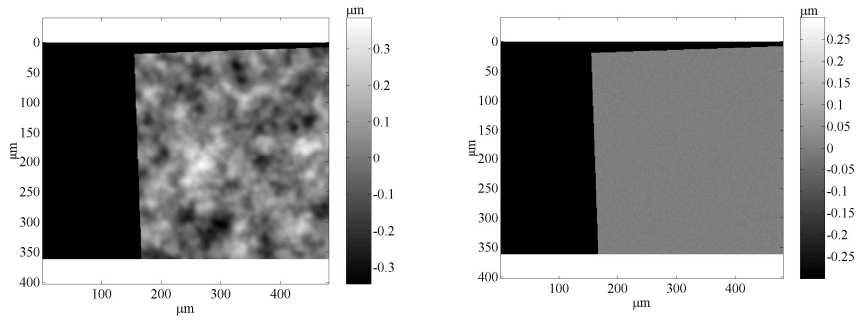

(c) (d)

Figure 3.17. Generated artificial surfaces (a) and (b), translation of (a) in (c) and the difference of (b) and (c) in (d).

In table 3.4 the number of function evaluations and the deviation from the applied transformation values are presented. The errors found in the in-plane translations Δ_x and Δ_y are on a sub-pixel scale, which shows that the interpolation method is working well. The other deviation values are also consistent with the known transformation parameters.

Table 3.4. Translation and rotation parameters for the images.

number of function evaluations	414
Δ_x, 10^{-2} [μm]	-1.01
Δ_y, 10^{-2} [μm]	1.11
Δ_z, 10^{-4} [μm]	0.51
θ_x, 10^{-4} [°]	-0.41
θ_y, 10^{-4} [°]	0.50
θ_z, 10^{-2} [°]	0.59

3.6.2. Example 2: Ground surfaces

In the repositioning algorithm, a good solution is found by finding the minimum of a correlation function as explained in section 3.4. However, in particular cases, there can be other spots or large areas that have close values to this real minimum. These values can be positioned close to this real minimum as will be discussed for the case of a ground surface that is characterized by periodicity of asperity profiles in one direction but with dissimilar valley heights and shapes. The correlation function might be periodic throughout the search interval, as that is the case in turned surfaces (periodicity in the asperity profiles and similar valley heights). In the former case there is isotropy in a certain direction where the translation parameter in that direction does not have as dominant effect on the correlation function as the translation in the anisotropic direction. The latter case will not be analyzed in this chapter.

The accuracy of local search algorithms is always affected by the multiple local minima case, as soon as the solver gets stuck in such an erroneous interval. For global optimizers such as the solver used in this study this effect is reduced. In this section these effects will be analyzed with an example.

In this example a milled steel disk (DIN 100MnCrW4) with an R_q of 0.2 µm was used. As seen in figure 3.18 two spots were measured with a sampling area of 84 µm x 63 µm and a pixel size of 0.13 µm with x75 magnification. At first, a measurement was performed on a certain spot and then the disk was moved in the x- and y-directions. Then the second measurement was performed. The R_q's of the two measured surfaces are close but not the same as new points are introduced in the second measurement after the movement of the table.

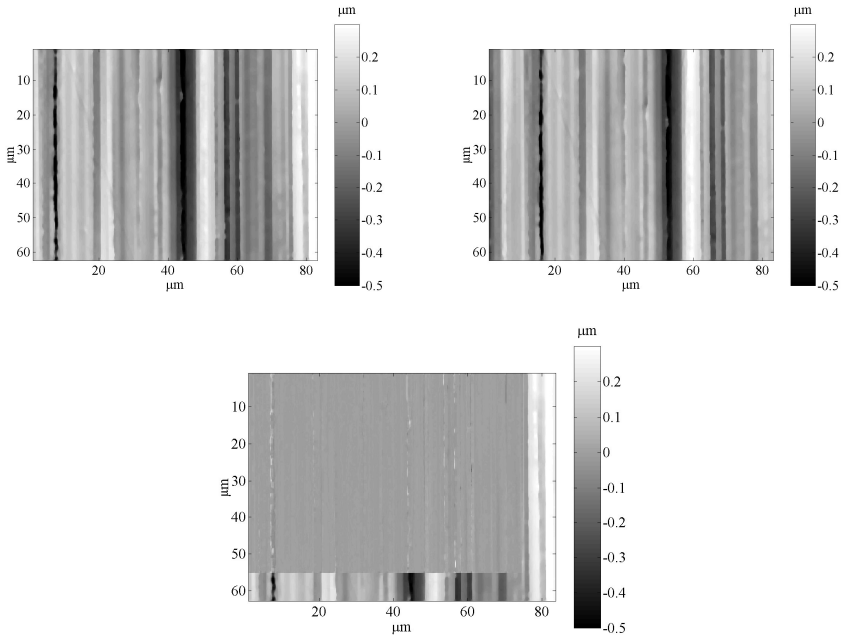

Figure 3.18. Steel disk surface topographies measured (top left and right) and their difference after translation (bottom).

In the first step, in order to check the shape of the cost function the correlation function is calculated using only the two parameters of interest namely the translations in the x- (Δ_x) and y-(Δ_y) directions. A search interval of 10 µm is used for Δ_x and Δ_y around the initial guesses made by zooming into the common distinguishable features on the two surfaces. These initial guesses were Δ_x = -9 µm and Δ_y = 8 µm. The calculated correlation function is plotted with respect to Δ_x and Δ_y in figure 3.19 (left). From this figure it is clear that the function is much sensitive to the changes in Δ_x compared to the changes with respect to Δ_y. The bottom minimum part of the function

which looks flat is zoomed in and then replotted in figure 3.19 on the right. The real minimum (Δ_x= -8.75 µm, Δ_y = 7.80 µm) is a spot surrounded by a smooth region. In the second step the repositioning algorithm is used for finding the best fit. The same initial guesses and search intervals were used for the solution. The calculated values were Δ_x=-8.75 µm and Δ_y=7.79 µm which were about the same as the values used for translation. The difference image has an approximate roughness of 10 nm which is mainly caused by the limited repeatability of interference microscopes, at spots with high slopes on the surfaces. This is visible as lines in the difference image shown in figure 3.18.

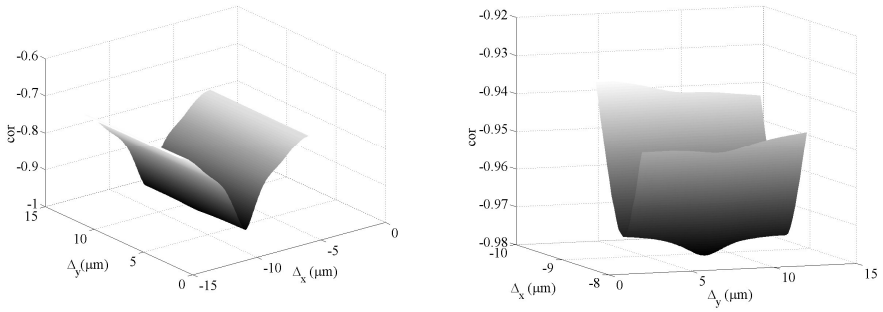

Figure 3.19. Cost function plotted with respect to Δ_x and Δ_y on large scale (left) and zoomed at the global minimum (right).

3.6.3. Example 3: Effects of wear track and outliers

Outliers are introduced due to measurement system limitations. The extremely high and low outliers are removed during median filtering as explained in section 3.3.3. However, because of the remaining spikes there is still a dissimilarity between the surfaces to be repositioned.

For accurate matching, there should be a percentage of unworn region on the worn surface that is similar to the unworn surface. However, as illustrated in figure 3.12 and discussed in section 3.4, a major problem could arise as the mean planes of the surfaces are no longer coincident. This could lead to a misfit of the out of plane D.O.F.'s (Δ_z, θ_x and θ_y). Before discussing a case with a wear track where this problem might occur, an artificial case will be studied first.

In this example two artificial surfaces that can be seen in figure 3.20 are used. For the z_0 = 1 µm height bump, an exponential function is used as follows:

$$z = z_0 e^{-\frac{7}{2}\left(x^2+y^2\right)} \tag{3.28}$$

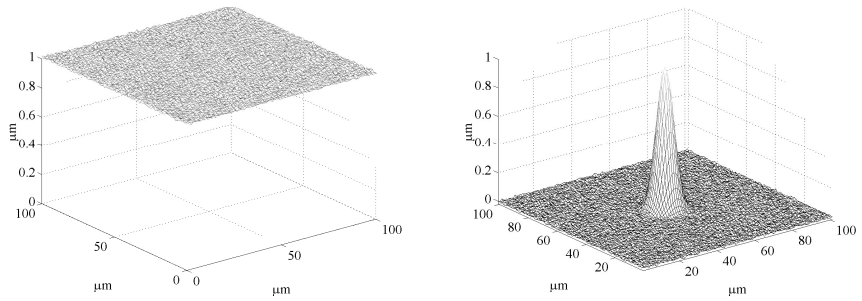

Figure 3.20. Noisy surfaces without and with bump (right).

For the surfaces two different random Gaussian noises with a standard deviation of 5 nm are added. The intervals for Δ_x, Δ_y and θ_z are kept very small for checking the variation of the tilts only as there is no best fit available. For an initial guess of 0 μm and a search interval of ±0.5 μm the solution is obtained at Δ_z =-0.9993. This value is the approach of the flat surface to the surface with bump. This means that the mean of the flat surface is as close as 0.7 nm to the flat region of the surface with bump of 1 μm height.

Having checked the effect of a single bump on the solution, in the following sections results of real wear experiments will be presented and discussed.

3.6.4. Example 4: A sliding contact experiment with low wear volume

In this experiment the contacting bodies are an alumina ball sliding on a very smooth polished mild steel disk with an R_q of 7 nm. The ball and the disk have a hardness of 22 GPa and 1 GPa respectively. Additionally, friction force measurements were also carried out. The measured area was 627.2x470.4 μm^2 and the pixel size was 0.98 μm for each measurement. As load, a normal load of 3 N was applied. The average contact pressure for this case was calculated as 0.52 GPa assuming an elastic Hertzian contact. The calculated contact radius was 43 μm. An elastic-plastic behavior was expected, as the average contact pressure was close to 0.4H (see for details Chapter 2). The sliding distance throughout the experiment was 3.75 m, equal to a total of 15 revolutions. During the rotations, the sliding velocity was constant at 1.3 mm/s. After the first rotation, the table was stopped and a roughness measurement was performed. The following roughness measurements were done at the end of the 6^{th}, 11^{th}, 13^{th} and 15^{th} revolutions. During the operation of the rotating table the friction force measurement was carried out at a sampling rate of 50 Hz. In figure 3.21 the net change in the surface geometry after 1 revolution is shown.

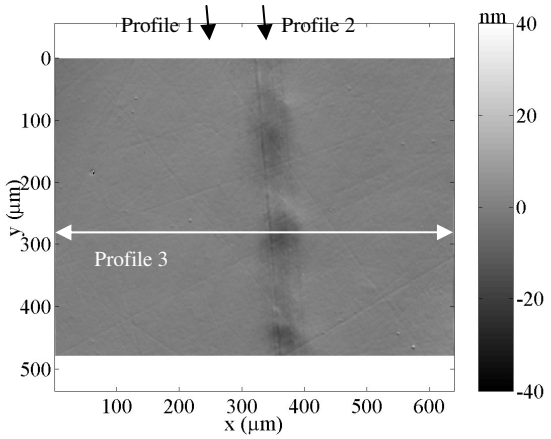

Figure 3.21. Difference image after the first rotation.

The region outside the contact in the difference image has an R_q of approximately 1 nm. At the center of the figure, the wear track is clearly visible. The darker areas along the track represent the spots that have relatively higher height differences. The wear track has a periodic appearance which can be explained by dynamic effects such as stiffness of the machine and the dynamic friction effects in the contact. Along the wear track three profiles are marked. The first two are outside (profile 1) and in (profile 2) the wear track, in the images before and after the wear cycle. Profile 3 is across the wear track and was obtained from the difference image itself. Profiles 1 and 2 (see figure 3.21) are in figure 3.22.

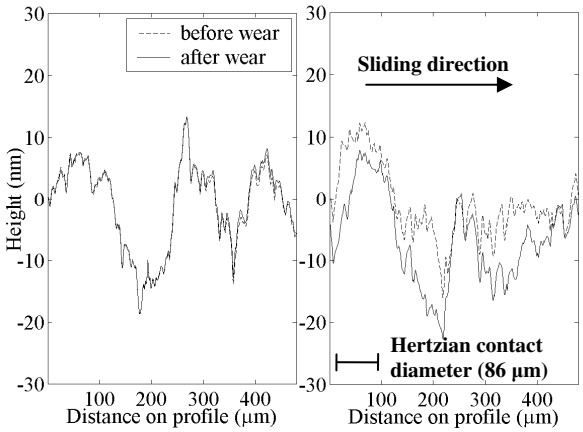

Figure 3.22. Profiles of the surface along the wear track before and after the first rotation. The left (profile 1) and right (profile 2) profiles are along the marked lines in figure 3.21.

Profile 1 shows that the tilts and shifts were calculated correctly. In profile 2, the high frequency roughness details are still present while the profile looks "pushed down". Across the wear track, the profile of the difference image is represented in figure 3.23. It can be observed that there is a very small scale ploughing of the micro-asperities. The depth and width of the track are 15 nm and 95 μm respectively.

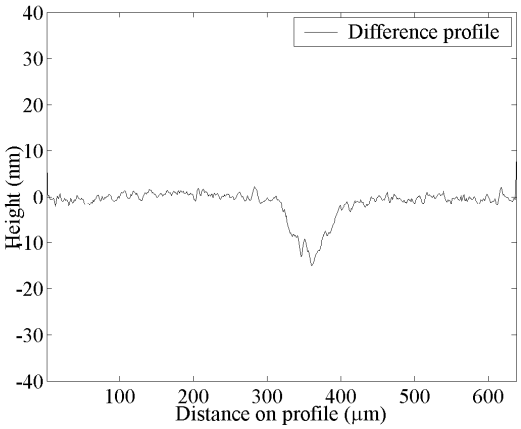

Figure 3.23. Profile of the difference image along profile 3 in figure 3.21.

The coefficient of friction for this specific position in the first cycle was approximately 0.1 (see figure 3.24) and could have resulted from the existence of a boundary layer. The contact radius was 48 μm which is a bit larger than the Hertzian contact radius of 43 μm. From figure 3.24 it is observed that there is a linear increase in the coefficient of friction up to the sixth revolution (a sliding distance of 1.5 m). The nearly linear increase of friction as a function of number of revolutions changes in the 7^{th} revolution and is followed by a major increase (up to 0.4) which could be due to major changes in the surface topography. At the end of revolution no. 11 and 13 the coefficient of friction is approximately 0.25. Analyzing the profiles of the differences at these two positions presented in figure 3.25, it is observed that there are also changes in the profile. In the last two rotations the wear track gets wider, which results in an increase in the coefficient of friction in the 15^{th} rotation.

Finally, using the difference images at the measurement locations it is also possible to calculate the volume change during a test. Figure 3.26 represents the volume change per unit normal load and per unit sliding distance with respect to the number of revolutions. The slope of this line is comparable to Archard's wear coefficient *k*. It is seen that the amount of wear increased

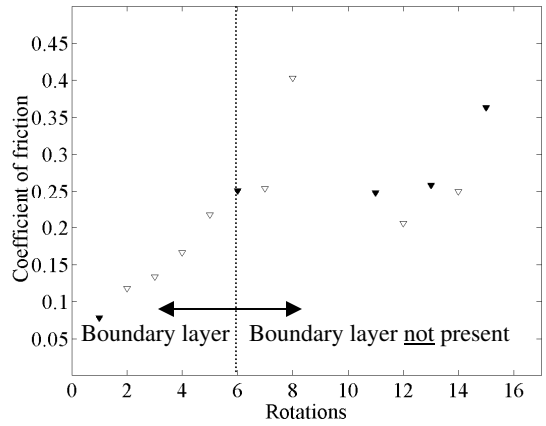

Figure 3.24. Coefficient of friction measured in the roughness measurement position. Dark triangles represent the rotations where roughness measurements were carried out.

approximately linearly throughout the number of rotations. This example makes it clear that using this technique one is able to study wear locally. The mechanisms during running-in can be unrevealed by this method.

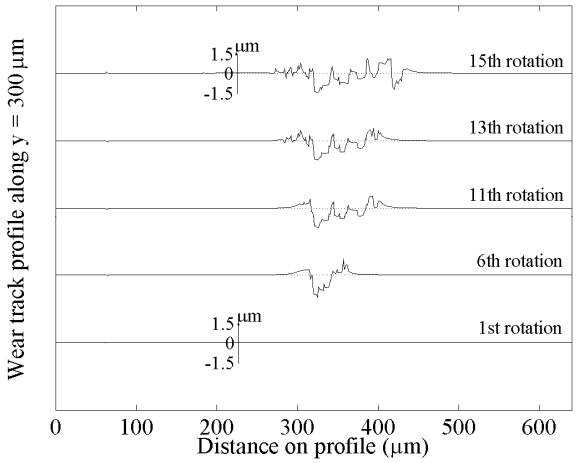

Figure 3.25. Profiles of the difference image at specified rotations where roughness measurements were carried out. The profile after the first rotation is plotted in greater detail in figure 3.23.

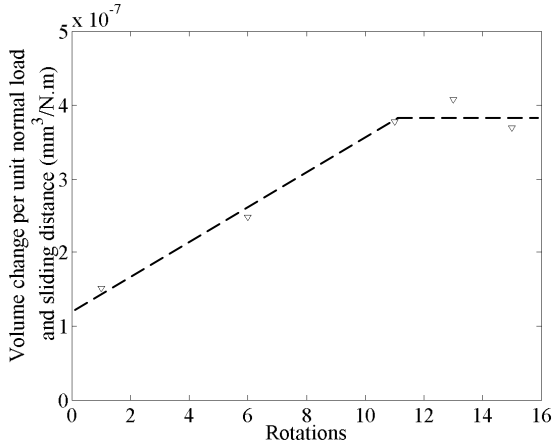

Figure 3.26. Change of volume per unit normal load and sliding distance (specific wear rate) during the experiment for the alumina-steel contact. The normal load is 3 N, the sliding velocity is 1.3 mm/s and the ball diameter is 10 mm.

3.6.5. Example 5: A rolling contact experiment

In this example, a silicon carbide (SiC) ball with diameter of 10 mm and hardness of 28 GPa is in free rolling contact with a mild steel disk of hardness 1 GPa. The calculated mean Hertzian contact pressure is 0.6 GPa with the applied 4 N load. Elastic-plastic behavior can be expected as mentioned in the previous section, as the contact pressure is larger than 0.4 times the hardness of the surface [14].

The ball and disk are very smooth with roughness values of 5 nm and 6.5 nm respectively. During the experiments, the velocity is kept constant at 1.75 mm/s for 15 revolutions (4.7 meters). The measured area in the roughness measurements was 470.4 μm x 627.2 μm with 10 times magnification. The measurements were carried out before the experiment, and at the 1st, 9^{th} and 15^{th} rotations.

In figure 3.27 these roughness measurements on the measurement location are presented. In the top left figure, the topography before wear is seen. In the clockwise direction, deformation progress in the order of nanometers can be seen. The change in the profile along the marked profile in the same figure is presented in figure 3.28. It is seen that, starting from the initial deformation in the first encounter of the contacting bodies, there is no change in the high frequency roughness throughout the rotations. In the first cycle there is bulk deformation in the order of 5 nm. As the deformation mechanism progresses, the conformity increases and the contact pressure decreases. Maximum conformity is reached at the 15^{th} cycle where an elastic steady state, or in other words *shakedown*, occurs. At this moment the depth of the deformation band is approximately 10 nm.

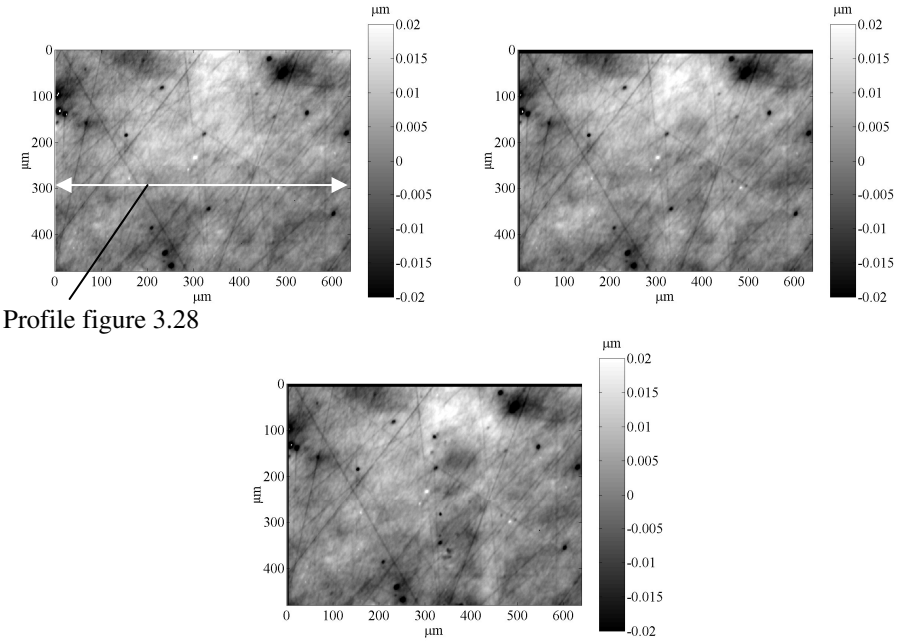

Profile figure 3.28

Figure 3.27. Roughness measurements on the same location during the rolling contact experiment. Clockwise from top left, initial, 1st and 15th cycles.

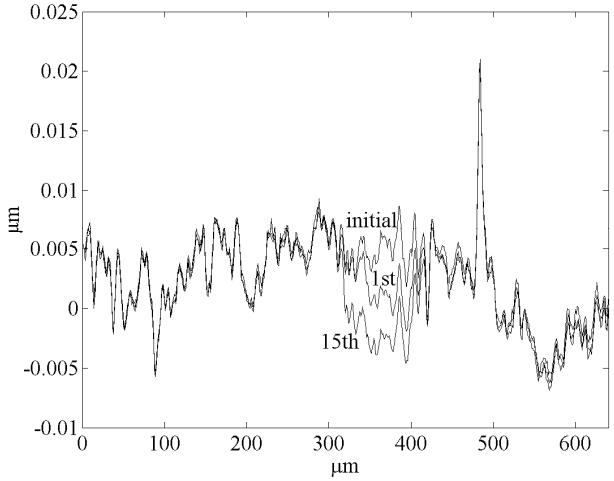

Figure 3.28. Changes in the topography across the track.

3.6.6. Example 6: Stitching

As discussed before the percentage of similarity in stitching depends on the overlap percentage of the stitched images. In [7] the effect of overlap percentage on the solution accuracy was analyzed.

In this example an overlap percentage of approximately 2/3 was used. The surfaces to be stitched are presented in figures 3.29 (a) and (b). The measurements were done with the interference microscope with a pixel size of 0.2 µm, and a measurement area of 125.44 µm x 94.08 µm. Initially a repeatability test at a certain position was made before the measurement. The repeatability was found to be around 0.5 nm. A positioning table was used for translations in the *x*- and *y*-directions.

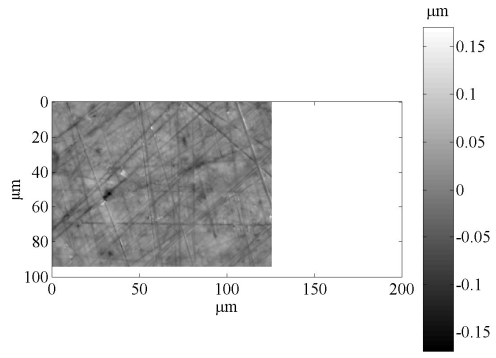

(a)

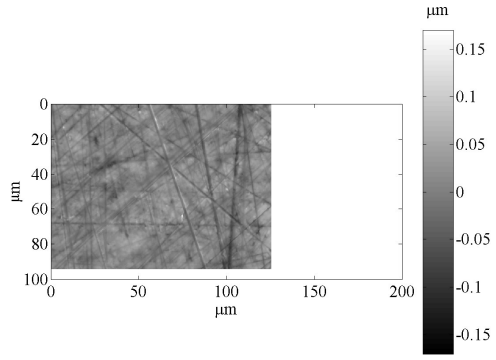

(b)

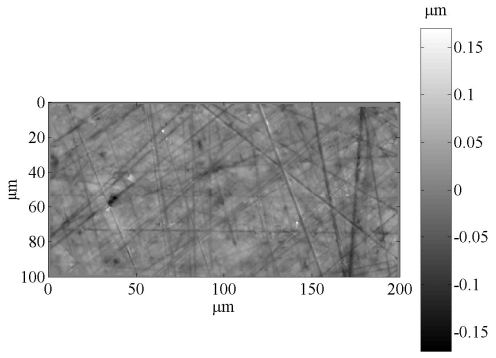

(c)

Figure 3.29. (a) and (b) images with partial similarity are stitched (c).

The stitched images are presented in figure 3.29 (c). A good measure to check whether the stitching is correct is to check profiles of the transformed image and the original image. This was done along the y = 40 μm line and the resulting profile of left and right images is presented in figure 3.30. In the stitched region there is a deviation at the 1.5 nm level. The difference of the surfaces in that region also has an R_q of 1.5 nm which is close to the measurement resolution. Thus the stitching process has been successfully performed.

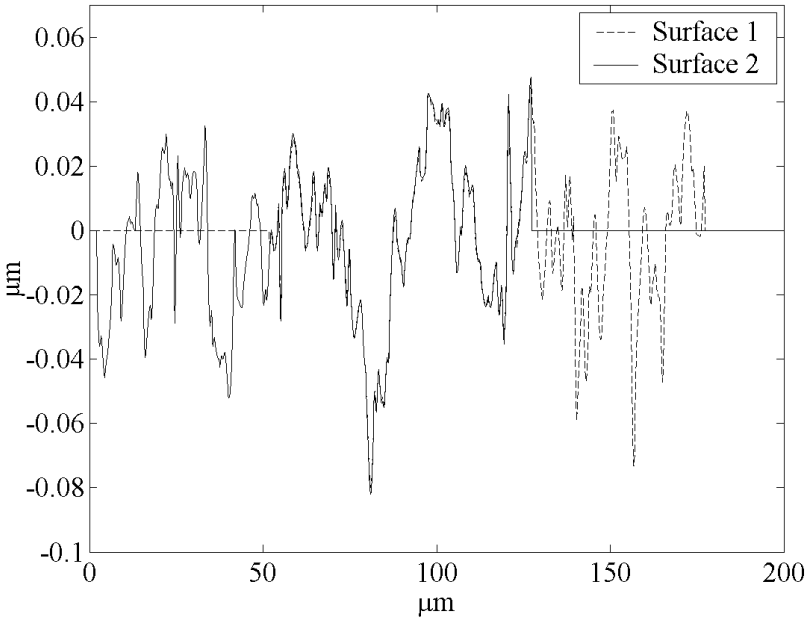

Figure 3.30. Profile on y=40 *μm* line for the left image and the right (translated state) image.

3.7. Summary

- A measurement setup for measuring the nano-scale local 3D changes in the surface topography was developed. With this setup, in a semi-online manner, 3D roughness measurements can be carried out accurately on a certain area of a disk in contact with a sliding or rolling ball specimen. The method makes it possible to simulate a variety of wear and deformation situations and asperity and bulk deformation of a material can be measured. This offers the possibility to study phenomena like running-in or deformation in repeating contacts.

- A repositioning algorithm based on the previous studies of [5] and [6] is developed. This algorithm is a very accurate repositioning tool that can compensate for the repositioning inaccuracies of the

positioning system and the effects of wear track and outliers. With the presented examples it is shown that the technique is even accurate for noisy images and in the existence of wear track and outliers. A series of overlapping images with a percentage of similarity can also be stitched together for the case where larger areas are of interest. The accuracy of the stitching was tested with a measured surface and the results show that the algorithm works accurately.

References

[1] B. Nowicki, A. Jarkiewicz, The in-process surface roughness measurement using fringe field capacitive (FFC) method, International Journal of Machine Tools and Manufacture 38 (1998), pp. 725-732.
[2] H. Ahn, D. Kim, In situ evaluation of wear surface by ultrasound, Wear 251 (2001), pp. 1193-1201.
[3] T.V. Vorburger, E.C. Teague, Optical techniques for on-line measurement of surface topography, Precision Engineering 3 (1981), pp. 61-83.
[4] Y.C. Taşan, M.B. de Rooij and D.J. Schipper, Measurement of wear on asperity level using image-processing techniques, Wear 258 (2005), pp. 83-91.
[5] M.B. De Rooij, D.J. Schipper, A wear measurement method based on the comparison of local surface heights, Wear 217 (1998), pp. 182-189.
[6] J.W. Sloetjes, D.J. Schipper, P.M. Lugt, and J.H. Tripp, The determination of changes in surface topography using image processing techniques, In Proceedings of the International Tribology Conference (2000), Nagasaki, pp. 241-246.
[7] J.W. Sloetjes, Y.C. Taşan, M.B. De Rooij, and D.J. Schipper, Algorithm for determining changes in micro-geometry using image processing techniques, In Proceedings of the 2nd Asia International Conference on Tribology (2002), ASIATRIB '02, Cheju Island.
[8] H.S. Fricker, Teaching air wedge interference, Phys. Educ. 21 (1986), pp. 48-52.
[9] ATOS GmbH Micromap series catalogue, http://www.atos-online.de.
[10] K. Miyamoto, Measurement of surface roughness, Japanese Journal of Tribology 43 (1998), pp. 1355-1365.
[11] Y.C. Taşan, M.B. de Rooij and D.J. Schipper, Changes in the micro-geometry of a rolling contact, In Proceedings of the 11th Nordic Symposium on Tribology (2004), pp. 33-44.
[12] J.S. Lim, Two-Dimensional Signal and Image Processing, Prentice Hall, Englewood Cliffs NJ, 1990.
[13] W. Huyer, A. Neumaier, Global optimization by multilevel coordinate search, Journal of Global Optimization 14 (1999), 331-355.
[14] D. Tabor, The Hardness of Metals, Oxford University Press, Oxford, 1951.

Chapter 4. Modeling contact of rough surfaces

4.1. Introduction

The wear measurement setup introduced in the previous chapter allows measurement of wear and deformation at nanometer and micrometer scales. In other words, the setup makes it possible to measure changes in the surface topography of a rough surface at the level of its roughness. The main objective in this chapter is to introduce models that can help understand the mechanisms of surface deformation in the contact of rough surfaces. Some of the basic mechanisms were introduced in chapter 2. The comparisons for these models and experiments will later be done in chapters 5, 6 and 7.

In section 4.2, a three dimensional boundary elements model (3D B.E.M.) based on the works of Sayles [1] and Chang et al. [2] as introduced in section 2.4.2 will be presented. Elastic and elastic-plastic contact algorithms will be discussed. In section 4.3, a two-dimensional finite element model (2D F.E.M.) of a cosine surface will be introduced. Here, elastic and elastic-perfectly plastic validations will be given. In this analysis 2D plane strain and 2D axisymmetric solid elements of the commercial program ANSYS 5.7 will be used. In section 4.4, a simplified roughness model will be introduced. In this simplified approach, roughness will be regarded as a cosine wave. Analysis with cosine waves will be presented in section 4.5. In this section, the introduced models will be compared. In section 4.6, surface roughness will be regarded as a combination of multiple cosine waves and elastic and elastic-plastic deformation mechanisms will be discussed. Finally in section 4.7, an elastic and elastic-plastic 3D B.E.M. analysis with a Gaussian surface will be presented.

4.2. A three-dimensional boundary element model

The first model that will be introduced will be called a three-dimensional boundary element model (3D B.E.M.) throughout this thesis, as it uses a surface mesh and solves equations for the deformation of the surface grid only. This is in contrast with the generally used three-dimensional solid finite elements in which the bulk deformation of the material is also modeled. As a disadvantage, calculation times are long for the finite element method especially for the three-dimensional contact analysis of rough surfaces. Additionally, for very rough surfaces finite element meshes contain geometrically degenerated elements which affect the accuracy of the solution.

The method that will be presented in the following sections is based on the analytical formulation of Love [3]. Love analyzed the case where a

rectangular area (or a grid point) of size *2a* x *2b* is under the influence of uniform pressure *p* as illustrated in figure 4.1.

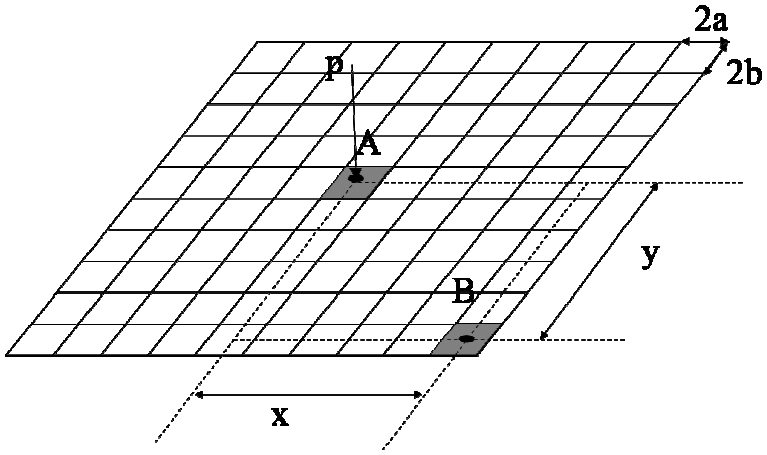

Figure 4.1. Point loading of an infinite half-space.

In Cartesian coordinates the deformation of a point on the surface is given by the equation:

$$\begin{aligned}\overline{u_z} = \frac{p(1-\nu^2)}{\pi E}&(x+a)ln\left[\frac{(y+b)+\{(y+b)^2+(x+a)^2\}^{1/2}}{(y-b)+\{(y-b)^2+(x+a)^2\}^{1/2}}\right]\\&+(y+b)ln\left[\frac{(x+a)+\{(y+b)^2+(x+a)^2\}^{1/2}}{(x-a)+\{(y+b)^2+(x-a)^2\}^{1/2}}\right]\\&+(x-a)ln\left[\frac{(y-b)+\{(y-b)^2+(x-a)^2\}^{1/2}}{(y+b)+\{(y+b)^2+(x-a)^2\}^{1/2}}\right]\\&+(y-b)ln\left[\frac{(x-a)+\{(y-b)^2+(x-a)^2\}^{1/2}}{(x+a)+\{(y-b)^2+(x+a)^2\}^{1/2}}\right]\end{aligned} \quad (4.1)$$

where *p* is the uniform pressure effecting on the grid point, *v* and *E* are the Poisson's ratio and elastic modulus respectively. *x* and *y* are the distances between the point at which the deformations are calculated and the center of the loaded patch.

A rough surface can be visualized as a combination of very small rectangular elements forming the grid points. If these elements are sufficiently small and the pressures on each element can be calculated, then the deformations at each point of the rough surface can be calculated with equation 4.1. An approach for modeling elastic contact of rough surfaces has been introduced in section 2.4.2 with equation 2.40. Equation 4.1 can

easily be re-written in terms of the parameters in 2.40 for having the "surface compliance matrix" [2] C_{ij} for the calculation of deformations.

Now consider a rigid flat surface that is in contact with an elastic rough surface. A 2D profile of such a contact is schematically shown in figure 4.2. If the *x*-*y* plane is assumed to be the plane in which the flat-rigid surface lies and *z* is the direction normal to the plane, then the numerical penetration ($z(x, y) > 0$) or separation ($z(x, y) < 0$) between the two surfaces (upon convergence $z(x, y) = 0$) in the *z*-direction can be defined as:

$$z(x,y) = -\delta + g(x,y) + r(x,y) + d(x,y) \tag{4.2}$$

as introduced in [2]. In equation 4.2, δ is the normal approach of the flat surface to the rough surface, *g(x, y)* is the underlying geometry of the nominally flat surface (i.e. sphere, cylinder etc.), *r(x, y)* is the surface roughness and *d(x, y)* is the deformation of the rough surface. The approach is defined as the distance from the flat surface to a specific point on the rough surface. In [2], the deformation of the rough surface is calculated from the contact pressures by:

$$d_i = \sum_{j=1}^{N} C_{ij}\, p_i \qquad i = 1,2,...,N \tag{4.3}$$

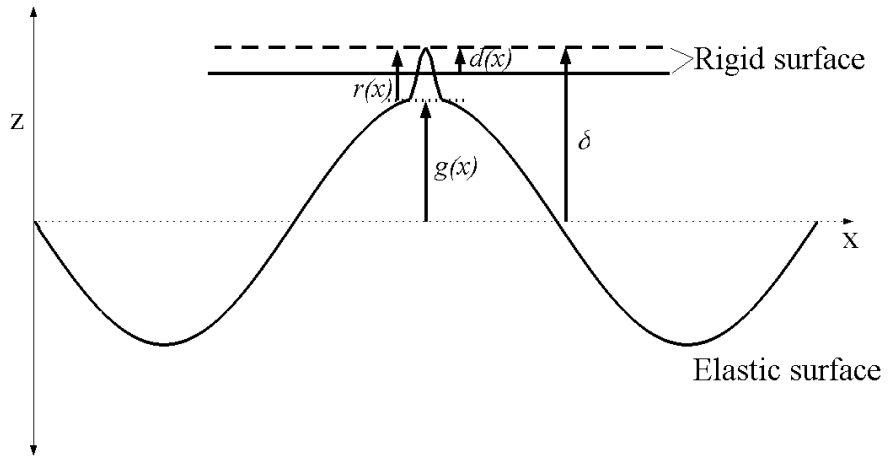

Figure 4.2. Contact between a rigid flat and a rough elastic surface.

where d_i is the deformation of each surface patch, C_{ij} is the surface compliance matrix and is a function of the distances between points *i* and *j*, p_i is the pressure at each element and *N* is the total number of surface patches on the surface. So a deformation of a certain point *i* is influenced by all pressures acting on the surface. The surface compliance matrix C_{ij}

represents the influence of pressure p_i on the deformation d_i. Chang et al. pointed out that in a 3D problem the use of a uniform grid for the surface reduces the size of the surface compliance matrix C_{ij} from NxN to N as C_{ij} is a function of the distances between points i and j. Equation 4.2 can be re-written in the same numerical form as:

$$z_i = -\delta + g_i + r_i + d_i \qquad i = 1,2,...,N \tag{4.4}$$

Because neither the pressures nor the deformations are known beforehand, an iterative procedure must be used. The flow diagram of the method is shown in figure 4.3.

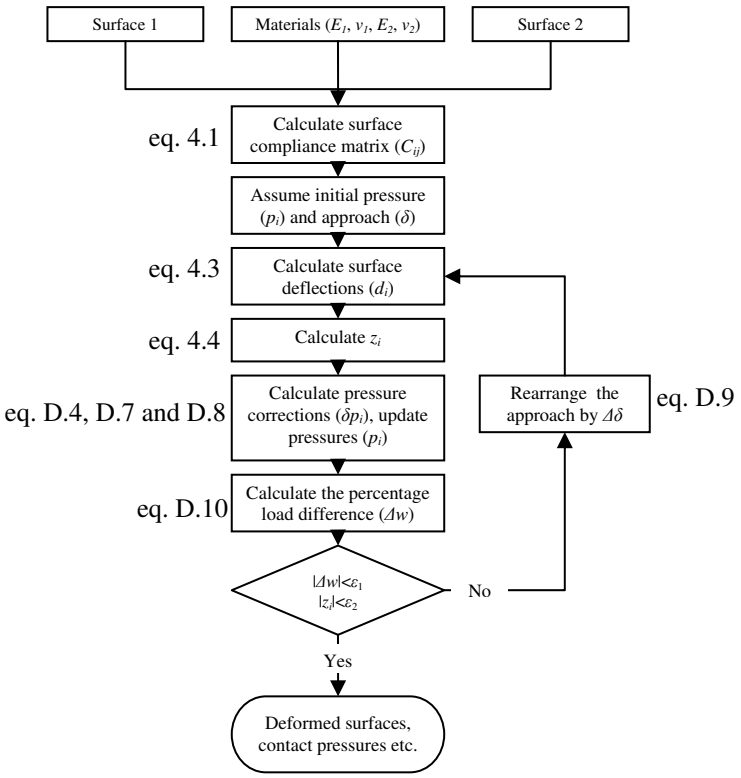

Figure 4.3. Elastic contact algorithm.

The details of this iterative approach can be found in Appendix D.

In order to obtain a faster convergence, the problem is solved in levels with the criteria presented in equation D.11. The surface compliance matrix is calculated only once before the calculations, at each level. However, the time consuming part of the algorithm is the solution of equation 4.3, where

deflections are calculated with the pre-calculated surface compliance matrix (C_{ij}) and contact pressure vector (p_i). This calculation is repeated for each iteration.

Reng and Lee [4], proposed a technique to reduce the storage space and calculation time, called the moving grid technique. Here, at first a new grid called the calculation surface is formed. This calculation grid is almost twice the size of the original grid (with the same grid spacing). For instance, if the original grid is of size 5 x 5 grid points then the calculation surface is of size 9 x 9 grid points (see figure 4.4). The original grid (shaded portion) is placed within the calculation surface and the calculation surface is "moved" onto the original grid. The surface deformations are always calculated at the center of the calculation surface so that the surface compliance matrix elements are always the same at each position of the calculation surface. Note that the contact pressures in the region outside the original grid are always equal to zero, as there is no pressure acting on that region. Calculated deformations of this "moving point" at all surface points then gives the whole surface deformation of the surface of interest. The storage space is reduced significantly with this method. As an example [4], a 200 x 200 grid system in double precision numbers requires a memory of 320 kilobytes with this technique, rather than 12.8 gigabytes for storing the surface compliance matrix as it is.

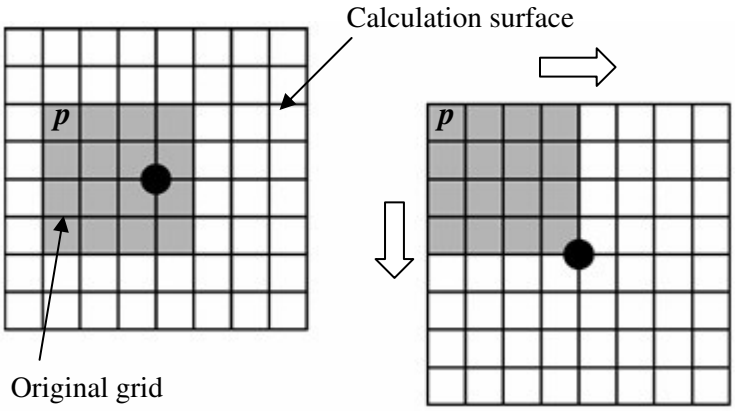

Figure 4.4. The moving grid technique. Re-illustrated from [4].

The principle that was presented in the previous section and illustrated in figure 4.4 can also be visualized as a two-dimensional convolution with a digital filter. The moving grid of pressures (p_i) can be used as the filter for the surface compliance matrix (C_{ij}) where the result of this filtering operation is the deformation vector (d_i). Then, deformations are calculated by filtering the pressure matrix with a digital filter equal to the surface compliance matrix (C_{ij}). As a convolution in the spatial domain is equal to

multiplication in the frequency domain, Fast Fourier Transformation (FFT) is used to perform the digital filtering in the frequency domain.

So far, an algorithm for determining the deformations and contact pressures for three-dimensional bodies in an elastic contact has been discussed. Elastic subsurface stresses can easily be calculated with the pressure distribution on the surface grid. The subsurface stresses can be calculated with the equations presented in [5]. These equations can also be found in Appendix A. In the following section, the model will be extended to plasticity effects.

4.2.1. Plastic deformation

In chapter 2, it has already been shown that the contact is fully plastic when:

$$p_m = H \approx 2.8\sigma_y \tag{4.5}$$

Equation 4.5 can be considered as an upper limit for the contact pressures. Based on this observation of Tabor [6], West and Sayles [7] extended their elastic model to an elastic-perfectly plastic model. According to this approach (see figure 4.5), if the calculated grid pressures extend the value in 4.5 then the shape of the original undeformed surface is modified by a reduction in height at that specific grid point. The elastic equations are solved again for the new shape. The algorithm runs until a convergence is obtained with no grid pressures larger than the hardness (or $2.8\sigma_y$). The same approach is used in this thesis. Note that with this approach, the effect of the subsurface plasticity is represented only by a constant hardness value, and hence effects of strain hardening and residual stresses are not taken into account. However, it is possible to compare the effects of such an approach with the finite element technique, where mechanisms in the subsurface can also be analyzed with the elasto-plastic elements.

4.3. Finite element models

A recent study on elastic-perfectly plastic contacts with finite elements was introduced by Kogut and Etsion [8]. The authors analyzed the contact of a deformable sphere and a rigid flat surface, where the sphere surface was in normal contact with the flat rigid surface. Calculations were performed using the commercial package ANSYS 5.7. The same analysis will be repeated in this study for the validation of the elastic and elastic-plastic models. Due to the rotational symmetry of the problem at hand, the sphere and flat surface can be represented as a quarter circle and a line respectively as can be seen figure 4.6. The material of the sphere is taken to be elastic-perfectly plastic (see figure 4.7 for the stress-strain relation). The material

properties are: σ_y = 200 MPa, E = 200 GPa, ν = 0.3. In total, 1200 PLANE82 axi-symmetric elements were used in the analysis, and over 80% of these elements were accommodated in zone 1 marked in figure 4.6. For modeling the rigid surface a single target element was used, and for a good approximation of the pressure distribution the sphere surface had more than 130 contact elements near zone 1.

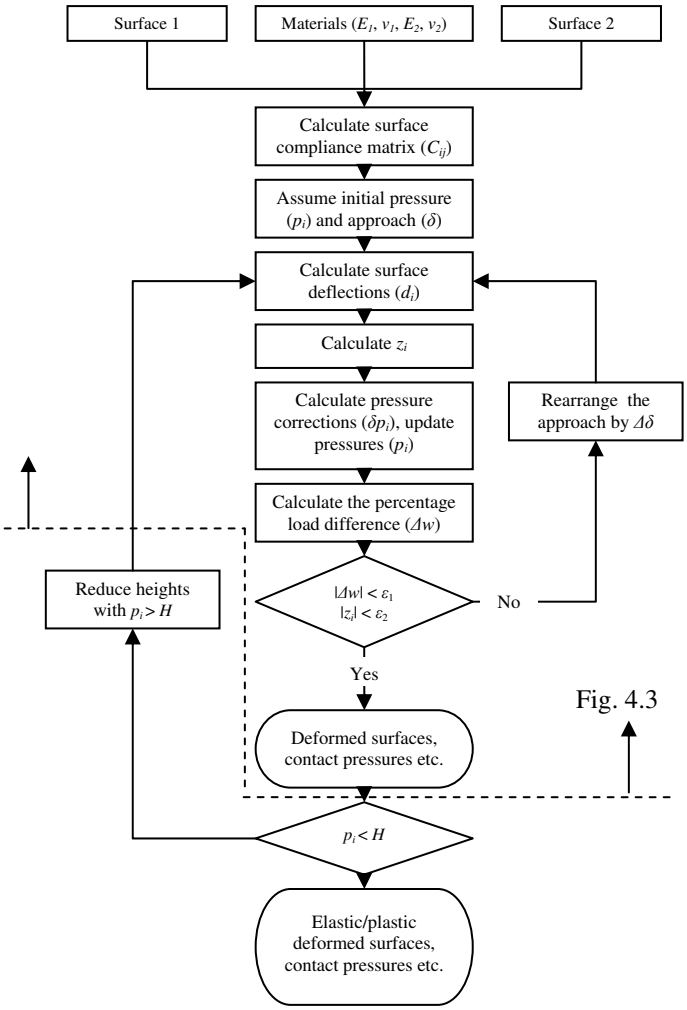

Fig. 4.3

Figure 4.5. Elastic-perfectly plastic contact algorithm.

The boundary conditions are so that, at the symmetry axis the nodes cannot move in the radial direction, whereas on the bottom the nodes cannot move in the axial direction. Before discussing the elastic-plastic material models, it would be appropriate to compare the finite element and 3D B.E.M. in the

elastic regime. As a test calculation, the two models were run in the elastic mode and a Hertzian contact was calculated. In the calculation, a rigid flat and a deformable ball of 1 mm radius are in contact with a normal load of 0.5 kN. The analytical solution for a Hertzian contact is known and given

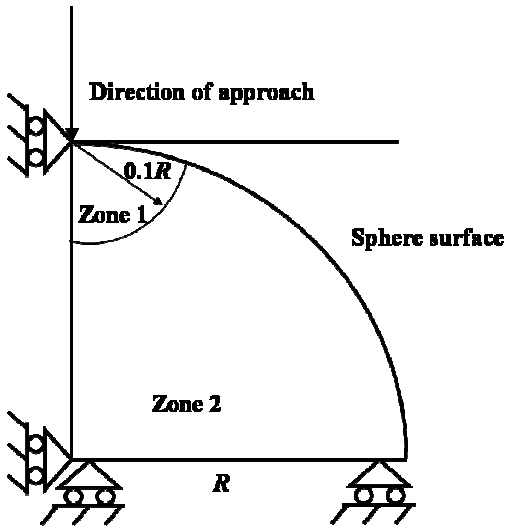

Figure 4.6. Contact of a rigid flat and a deformable sphere. Re-illustrated from [8].

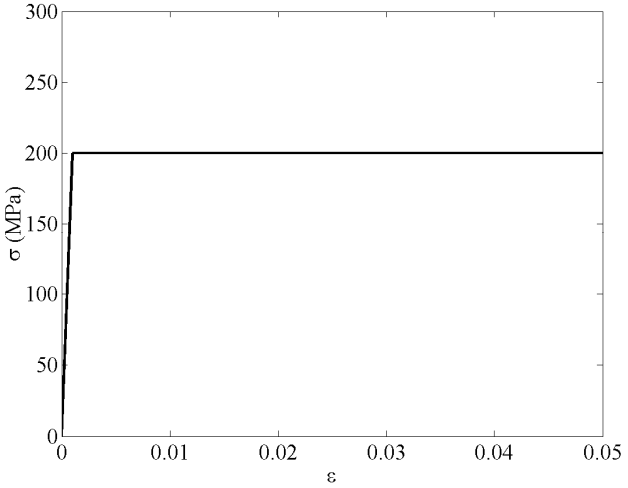

Figure 4.7. Elastic-perfectly plastic material model used by [8].

by equations 2.1 to 2.5. The input for the 3D B.E.M. is the normal load. However, the finite element package is displacement driven, so the approach of bodies is used as an input. For this reason the analytically calculated approach is used as an input for the finite element package. The contact geometries and pressures are presented in figures 4.8.a and 4.8.b

respectively. For the 3D B.E.M., a grid of 256 x 256 was used in the calculations.

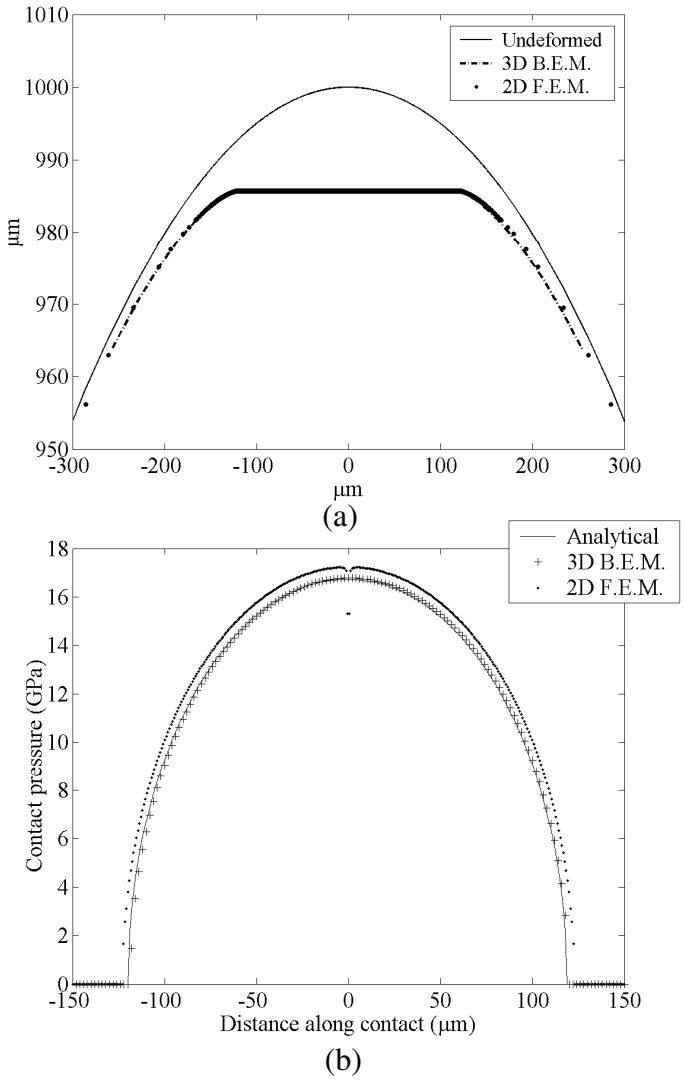

Figure 4.8. Deformed profiles (a) and contact pressures (b) for a Hertzian contact.

Figure 4.8 shows that the 3D B.E.M. agrees well with both the analytical and the finite element models, both in the calculation of deformations, contact radius and the contact pressures. The largest error seen in the calculation of contact pressures was approximately 4% for the finite element package, but it could be improved by increasing the mesh density as remarked by Kogut and Etsion [8].

4.3.1. Elastic-plastic calculations

For the elastic-plastic analysis the same contact situation was used. The material model in figure 4.7 was used for simulating an elastic-perfectly plastic material behavior for the finite element calculation. For this analysis, the critical interference (ω_c) given by Chang et al. [9] is be used. The critical interference is defined as the approach of bodies where the transition from elastic to elastic-plastic deformation regime starts, and it is described as:

$$\omega_c = \left(\frac{\pi K H}{2E}\right)^2 R \tag{4.6}$$

Here, H is the hardness of the sphere ($H \approx 2.8\sigma_y$), E is the elastic modulus, R is the radius of the sphere and $K = 0.454 + 0.41\nu$ [10]. The critical interference for this case was calculated as 6.44 nm and the maximum interference was 200 times of it which is equal to 1.29 μm. In figure 4.9, the dimensionless mean contact pressure (p_m/σ_y) is plotted with respect to the dimensionless interference defined as ω/ω_c. As the approach of the bodies increases, the contact pressure increases and becomes constant at about an interference of 110, which is the same value obtained by Kogut and Etsion [8]. In this thesis, the focus will not be on the elasto-plastic region which is seen in the plot. However, the relation plotted in figure 4.9 indicates that the value $2.8\sigma_y$ can be used as a limit beyond which the contact is fully plastic.

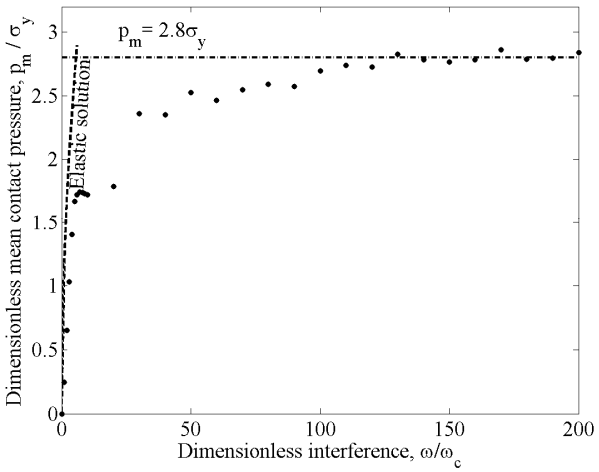

Figure 4.9. Dimensionless mean contact pressure.

4.4. Deformation of cosine waves

Trigonometric functions such as cosine waves are simple models for representing roughness in contacts. The primary reason is that a cosine can

be defined by a wavelength and amplitude only. The wavelength can define the distance between the neighboring asperities and, together with amplitude, the slope of the asperity is also defined. In this chapter cosine waves will be studied in two dimensions. Such an approximation is a suitable description for surfaces generated by certain machining operations such as grinding, turning, and milling where there is a periodic component in the roughness.

In figure 4.10, a cosine wave that represents an elastic half-space and that is in contact with a rigid flat surface is presented. In figure 2.18, the relations between the real to nominal contact area and dimensionless mean pressure ($2a/\lambda$ and p_m/p^*) have been given. This plot can be compared with the results of the aforementioned elastic numerical models in order to validate the numerical results.

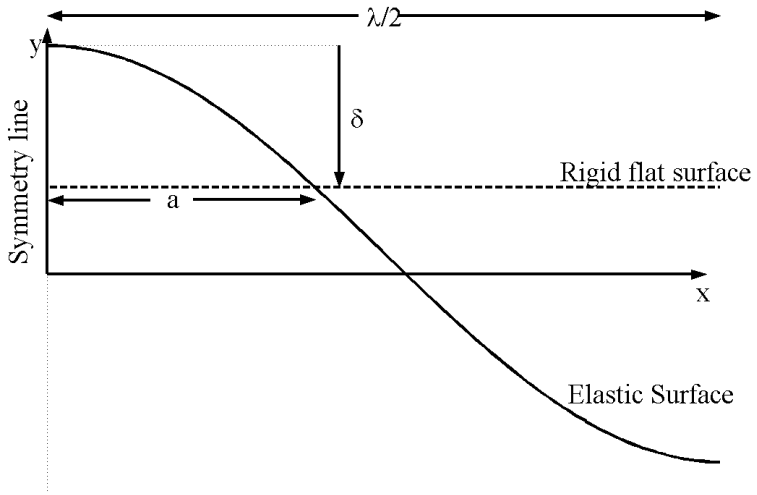

Figure 4.10. Rigid flat against an elastic cosine surface.

The contact situation is shown in figure 4.10. Here, it can be seen that the rigid flat surface has an approach of δ towards the elastic cosine surface. The contact pressure in the contact and deformation per wave inside and outside the contact were defined by Johnson as:

$$p(x) = \frac{2 \cdot p_m \cdot cos\left(\frac{\pi \cdot x}{\lambda}\right)}{sin^2\left(\frac{\pi \cdot a}{\lambda}\right)} \cdot \left\{ sin^2\left(\frac{\pi \cdot a}{\lambda}\right) - sin^2\left(\frac{\pi \cdot x}{\lambda}\right) \right\}^{1/2} \tag{4.7}$$

$$u_z(x) = \frac{\left(1-\nu^2\right) \cdot p_m \cdot \lambda}{\pi \cdot E \cdot \sin^2\left(\psi_a\right)} \cdot \cos\left(2 \cdot \psi\right) + C, \quad 0 \le |x| \le a \tag{4.8a}$$

$$u_z(x) = \frac{(1-\nu^2)\cdot p_m \cdot \lambda}{\pi \cdot E \cdot \sin^2(\psi_a)}\left[\cos(2\cdot\psi) + 2\cdot\sin\psi\cdot\left(\sin^2(\psi)-\sin^2(\psi_a)\right)^{1/2}\right.$$
$$\left. - 2\cdot\sin^2(\psi_a)\cdot\ln\left\{\frac{\sin(\psi)+\left(\sin^2(\psi)-\sin^2(\psi_a)\right)^{1/2}}{\sin(\psi_a)}\right\}\right] \qquad (4.8b)$$
$$+ C, \quad a \le |x| \le \frac{\lambda}{2}$$

In equations 4.7 and 4.8, p_m is the mean pressure, $\psi = nx / \lambda$, $\psi_a = na / \lambda$, C is a constant and a is the contact radius.

4.5. Analysis of cosine waves

Now that the two modeling tools have been tested for single asperity contacts for the case of elasticity and plasticity the models are analyzed with the use of finite elements. In the following paragraphs, a comparison between this elastic analytical solution and the two numerical models will be given.

The analytical solution for the problem of a cosine wave pushed normally by a flat surface has been defined by equations 4.7 to 4.8. It can be seen from these equations that the input for the analytical model is the contact radius. So, knowing the contact radius, contact pressure distributions and displacements can be calculated. It has been mentioned that the 3D B.E.M. has an input of normal load and the 2D F.E.M. has the approach of the two surfaces as the input parameter. This problem was first solved by the 3D B.E.M. with a chosen value for the load. Then the calculated contact radius was used as an input for the analytical solution. The output of the analytical solution is the normal displacement, which is used as an approach input for the finite element technique. In this way, it is possible to compare the pressure distributions and deformed profiles calculated by each technique.

In this analysis, a single wave (see figure 4.11) will be analyzed. In 2D, the sphere is elastically deformable with E = 200 GPa and ν = 0.3. The contacting flat surface is rigid. The amplitude (Δ) and wavelength (λ) that define the cosine wave are given as; $\Delta = \pi$ μm and $\lambda = 256\pi$ μm. For the 2D F.E.M., a total of 2700 PLANE82 elements were used. 93% of these elements were near the surface, in order to model the deformation and contact pressures in the contact accurately. The depth of the material (or bulk) was taken as 400 μm which is approximately one-half of the wavelength. Compared to the amplitude of the wave, this bulk depth is approximately equal to 130Δ. A single target element was used for modeling the rigid flat line. The total number of contact elements on the cosine surface was 225. With the 3D B.E.M., the problem was solved in 3D

with a surface grid of 256 x 256 and grid size of π μm. The input load was 100 N for the 3D B.E.M.. The calculated contact radius was 56.55 μm.

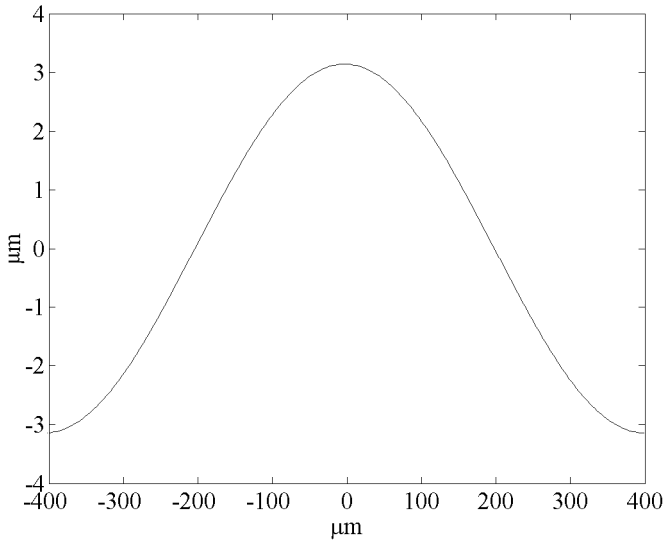

Figure 4.11. Cosine curve used for numerical models.

In figure 4.12 pressure distributions calculated by the three different models are presented. It can be seen that that there is a fairly good approximation of the pressure distribution by both the boundary element technique and the finite element model. Note that the distribution resembles a Hertzian contact pressure distribution and the pressure distribution outside the contact is zero.

Figure 4.13. shows the deformed profiles calculated by the three models. The finite element model and analytical approach have the same normal deformation. The reason for this is that the deformation which is the output of the analytical solution is used as an input for the finite element approach. The boundary element technique also gave a fairly good approximation with 256 elements on the profile, compared to the 2600 finite elements of the 2D F.E.M.

The same analysis was repeated for other loads in order to plot figure 2.18, so that the ratio of the real to nominal contact area changes from 0 to 1. Analytically p^* was defined as the contact pressure at the moment when this ratio ($2a/\lambda$) is equal to 1. The values obtained for p^* by 3D B.E.M. and 2D F.E.M. are within a 3% error accuracy of the calculated analytical result ($p^* = 2697$ N).

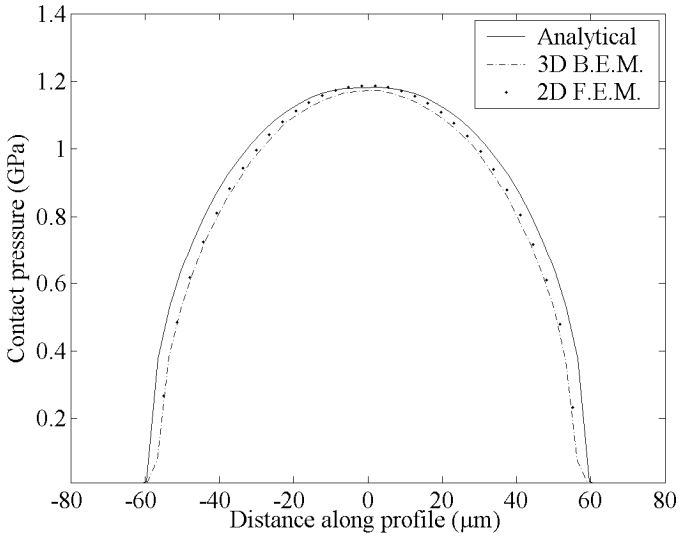

Figure 4.12. Pressure distributions for the cosine wave problem.

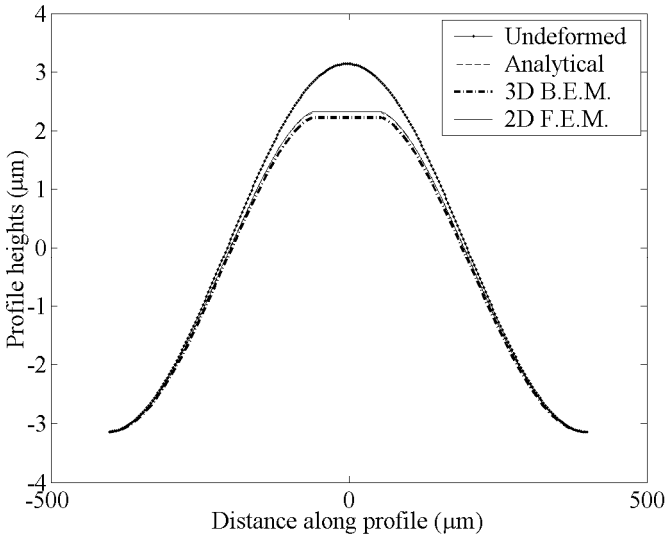

Figure 4.13. Calculated deformed cosine profiles.

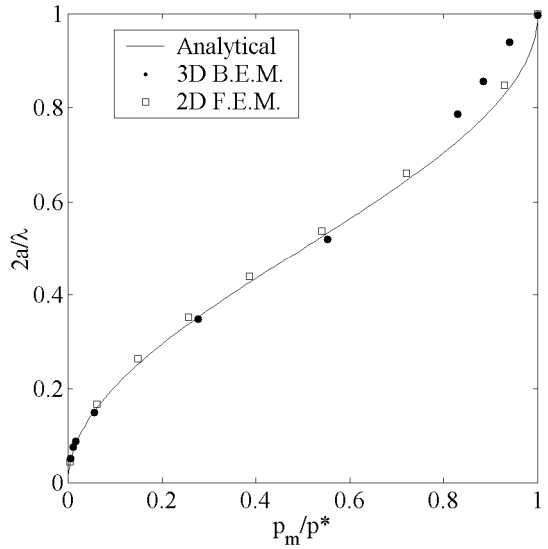

Figure 4.14. Ratio of real to nominal contact area as a function of dimensionless mean pressure.

Figure 4.14 shows that the 2D F.E.M. results agree very well with the analytical solution for the whole range. The boundary element solution has a good fit up to $2a/\lambda = 0.5$, and beyond this point there is a deviation from both the analytical and the finite element solutions. This can be explained as follows: the 2D finite elements can deform both in the direction of approach and in-plane. In contrast, the 3D boundary elements have deformation in the direction of the applied load only. When deformation is "small scale" the difference between these two deformation mechanisms are negligible. However, when the deformation is on a larger scale, these different deformation assumptions affect the calculated contact radii. A finer boundary element mesh might reduce this effect, however, at the same time it would increase the calculation time. The results can still be considered as a fairly good approximation.

In this section, a single cosine model for a rough surface approximation was introduced. An analytical model and two numerical models, namely a 3D B.E.M. and a 2D F.E.M. were described and validated firstly with a known analytical situation, namely the Hertzian contact. Subsequently, a cosine wave was studied. In the next section, a study on roughness will be presented. At first, the cosine surface that was introduced earlier will be upgraded to a model where the geometry is composed of a combination of two cosine waves, one (long wavelength) representing the waviness and the other (short wavelength) the roughness. After the validations with these examples, the boundary element technique will be used for the contact of a flat rigid surface against a randomly rough surface, which is most frequently the case in real surfaces.

4.6. Study of roughness

Consider a surface composed of a combination of two cosine waves in the following way:

$$y = \Delta_1 cos\left(\frac{2 \cdot \pi \cdot x}{\lambda_1}\right) + \Delta_2 cos\left(\frac{2 \cdot \pi \cdot x}{\lambda_2}\right) \tag{4.9}$$

where Δ_1 and Δ_2 are the amplitudes and λ_1 and λ_2 are the wavelengths of the two waves so that:

$$\Delta_1 >> \Delta_2 \text{ and } \lambda_1 >> \lambda_2 \tag{4.10}$$

An example would be the plot in figure 4.15. Note that the scale in figure 4.15 is exaggerated for explanatory reasons.

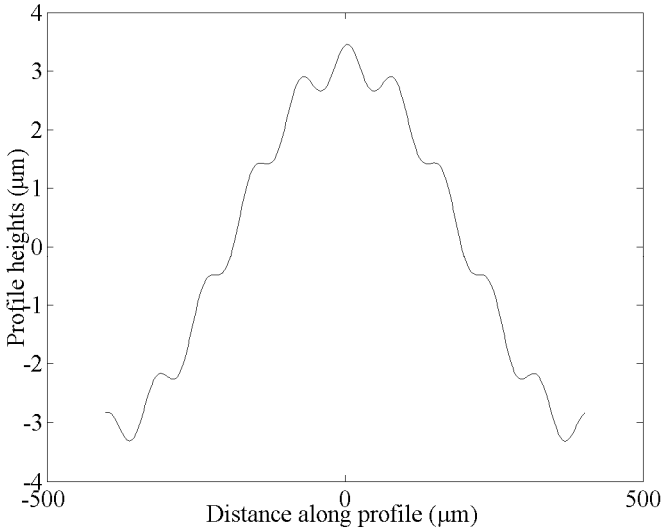

Figure 4.15. A combination of two cosine waves.

This example will be used in the analysis of this section. The geometry of the surface is defined as: $\Delta_1 = \pi$ μm, $\Delta_2 = 0.1\pi$ μm, $\lambda_1 = 256\pi$ μm and $\lambda_2 = 25.6\pi$ μm.

Consider that a flat rigid surface is in contact with the rough surface defined by equation 4.9 and illustrated in figure 4.15. It is not possible to solve this problem analytically. For this reason the contact problem has to be solved by the numerical models introduced in the previous section. At first, the 2D F.E.M. approach will be used. For a two-dimensional representation, a profile as seen in figure 4.15 will be used as the deformable rough surface and a rigid line will be used as counter surface. It is of interest to determine

the behavior of contact for elastic and elastic-plastic contact cases. For this reason two analyses are performed. In the first part, solely elastic solid elements (PLANE82) are used with material properties E = 200 GPa and v = 0.3. The approach of the rigid body is set to 1 μm. In the second case, the material model presented in figure 4.7 is used. Recall that in this model the yield strength is 200 MPa. For this case, using the elastic-perfectly plastic material model, the approach is set equal to 1 μm as for the elastic case. The bulk thickness is selected as $130\Delta_1$ as for the single cosine surface in the previous section. For both the elastic and elastic-perfectly plastic cases, the same mesh is used where the total number of solid elements is equal to 3100 elements. 94% of these elements are close to the contact zone, in order to simulate the deformations and pressure distributions with high accuracy. A single target element is used for the rigid line, and 400 contact elements are used for the cosine surface. The resulting profiles for these two cases, along with the original profile are plotted in figure 4.16. It can be seen from the figure that, at an approach of 1 μm the highest three asperities are

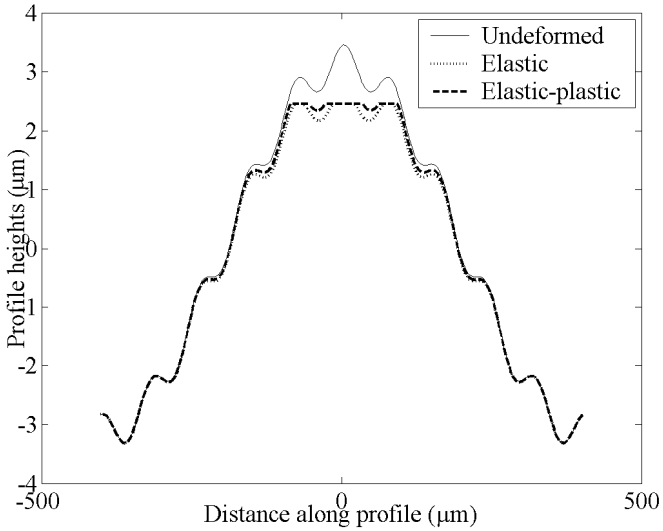

Figure 4.16. Rough surface deformed elastically and elastic-perfectly plastic.

already in contact. For the elastic case, the deformation is the total deformation of the roughness details and the bulk. When an elastic-perfectly plastic contact is assumed, the major deformation is in the asperities. Note that in an elastic-perfectly plastic calculation, the asperities enlarge laterally. A conclusion is that during contact, when stresses are elastic it is more difficult to fully flatten them compared to an elastic-perfectly plastic contact situation. Also, recall that a high amplitude (Δ) and short wavelength (λ) of the cosine wave (or sharp asperities) increase the value of p^* which is the pressure when asperities are fully flattened (see chapter 2).

The same problem was solved by the 3D B.E.M., with the elastic-plastic assumption. Note that with this assumption, a grid point either deforms elastically or plastically, depending on whether or not the pressure element acting on it is larger than the material hardness H (or $2.8\sigma_y$). A grid of 256 x 256 is used for modeling the surface, with a grid size of π μm. The deformed profile results are presented in figure 4.17 together with the undeformed profile and the finite element solution that was presented in figure 4.16. The first observation is that for the finite element results, material motion is not only axial in the direction of the approach, but also lateral, hence making a wider asperity. It is also observed from figure 4.17 that the approach is overestimated with an error of 4% by the boundary element model. This overestimation can be the result of the interaction of the stress fields beneath the asperities which are not taken into account. As a result, pressures higher than $2.8\sigma_y$ can be carried, which was the value assumed in the calculation. In order to understand the mechanism further it is worthwhile having a look at the pressure calculations as well. These results are presented in figure 4.18.

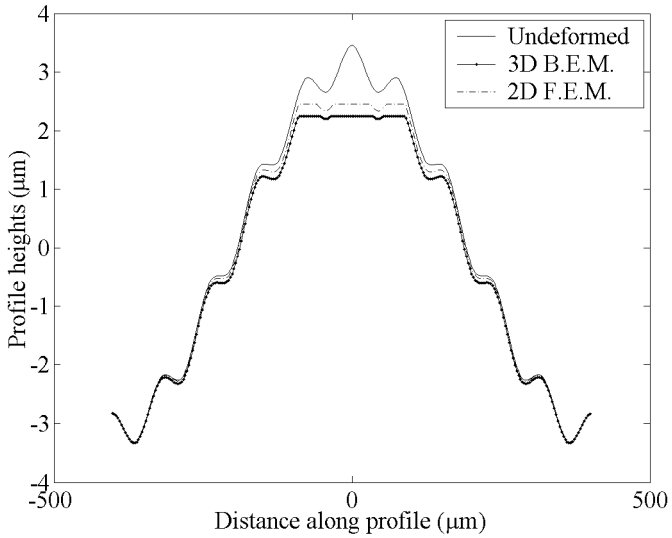

Figure 4.17. Rough surface deformed elastic-plastically with two different models.

The dashed line in this plot represents the critical pressure value (p_m = $2.8\sigma_y$) which is the mean contact pressure when the contact is fully plastic. Recall that this value was obtained for a single elastic-perfectly plastic sphere in contact with a rigid flat surface (see figure 4.9). From figure 4.18, it is seen that all the contact pressures in the contact are approximately equal to this value ($2.8\sigma_y$) for the boundary element technique. This is not a surprise, as it is the criterion for plasticity for the boundary element method. However, the finite element solution shows that the pressure on the central asperity is significantly larger ($\approx 3\sigma_y$) than the surrounding two asperities. This means that the introduction of new neighboring asperities to the

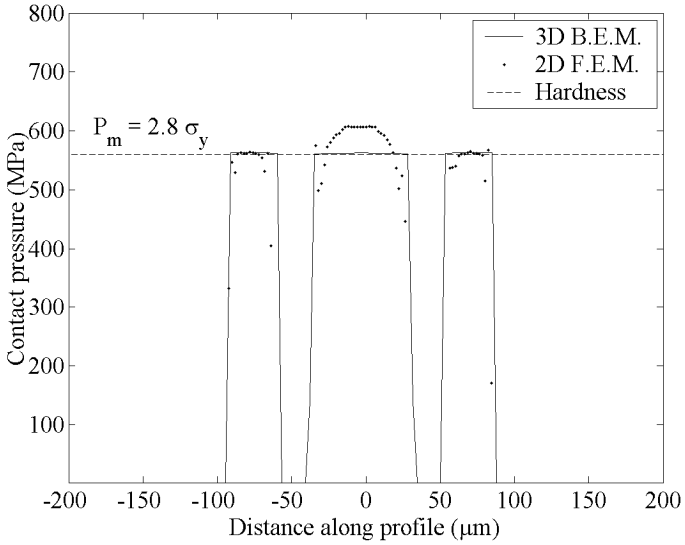

Figure 4.18. Contact pressures on the rough surface calculated with two different models.

contact affects the deformability of an asperity. This can be caused by interaction of stress fields so that the material flow is prevented for the central asperity compared to the case that it is deformed individually. For this reason, it can be said that the assumption for the 3D B.E.M. at a pressure of $2.8\sigma_y$ will overestimate the deformation in the plasticity calculations.

Before going into an analysis with a randomly rough surface, the analysis is finalized by deforming the same cosine surface with the finite element model, however, this time stepwise in order to investigate the effect of neighboring asperities. The same analysis that was presented in figure 4.16 was performed again with finite elements. All the material properties, plasticity model and mesh geometries were the same. The approach was set to 0.6 μm, 1 μm, 2.1 μm, 2.5 μm and 3 μm. These values were selected such that the behavior of an individual asperity and new neighboring asperities in contact could be analyzed. The deformed profiles based on the aforementioned approaches are presented in figure 4.19. In the first approach step (δ = 0.6 μm), the highest central asperity is the only contacting asperity. Actually this is the step just before the contact with the two neighboring asperities. From figure 4.20 it is seen that the mean contact pressure is still below $2.8\sigma_y$, at a value of around $2.6\sigma_y$, which means that the contact is not fully plastic. When δ = 1 μm three asperities start to carry the load, as discussed in the previous example. Here, the two new asperities have a contact pressure of $2.8\sigma_y$ and the mean contact pressure on the central asperity starts to increase ($3\sigma_y$). Just before the next two asperities that will be included in the contact, the pressure increases to $3\sigma_y$ for the

neighboring asperities and $3.2\sigma_y$ for the central asperity. The same sequence is seen for the new asperities included in the contact and the final pressure remains constant around a pressure of $3.2\sigma_y$ at the points of asperity contact. Then it can be concluded that multiple asperities at small lateral distances can carry higher loads than the asperities individually. This effect possibly results from the interaction of the stress components in the subsurface of the asperities. As a result, with rough surfaces it is possible to end up pressures higher than $2.8\sigma_y$.

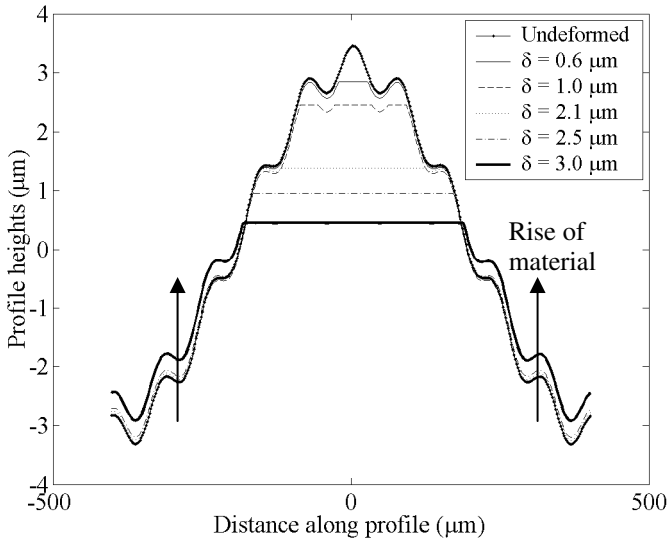

Figure 4.19. Deformed profile with increasing approach.

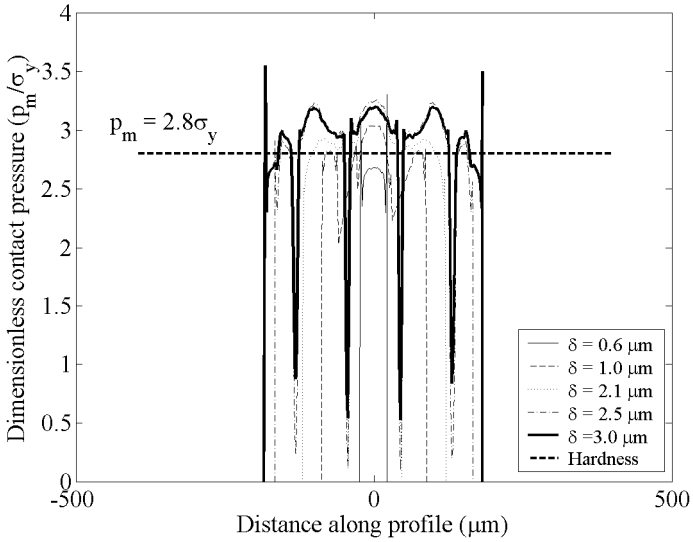

Figure 4.20. Contact pressures with increasing approach.

From figure 4.19 it is also seen that up to a certain ratio of real to nominal area of contact (for this case around 0.45), the deformation is on the surface. As the deformation continues, material starts to rise on the sides, as can be seen for δ = 3 μm in the same figure. This shows the tendency for volume conservation in this plastic deformation situation.

4.7. Rough surface

As a final discussion, a randomly rough surface was analyzed. In this analysis a numerically generated Gaussian surface (E = 200 GPa, ν = 0.3) was used (several measured real surface analysis will later be presented in chapter 7). The surface with a roughness of 1 μm is presented in figure 4.21. The surface is isotropic, and in the x- and y-directions an autocorrelation length of 20 μm was used (for details on autocorrelation the reader is referred to chapter 2). The hardness of the surface was 1 GPa and the grid used was 256 x 256 with a grid element size of 1 μm. The 3D B.E.M. is used as it is very fast compared to finite element calculations. The counter-surface was a rigid sphere with a diameter of 2 mm. Two analyses were performed. At first, the problem was solved assuming the contact was elastic. This gave a possibility to see the initial contact pressures. The sub-surface stress distributions can also be plotted as explained in section 4.2.

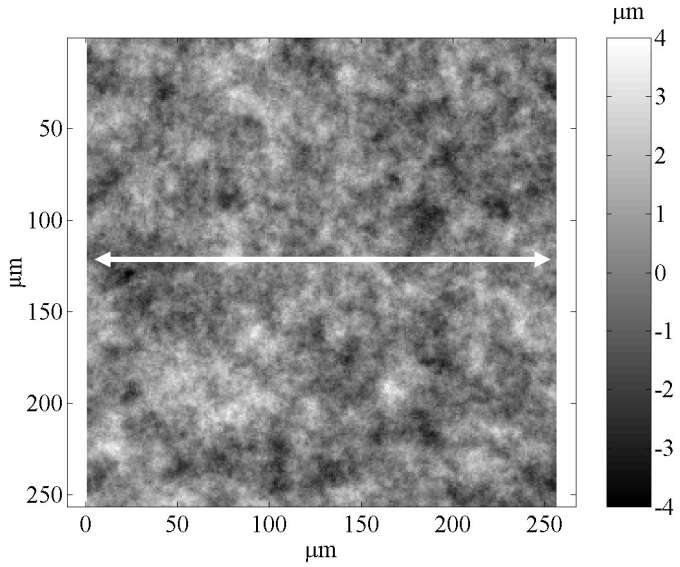

Figure 4.21. Rough surface with Gaussian height distribution. The marked profile is referred to in figures 4.23, 4.24 and 4.26.

In figure 4.22, the elastic pressure distribution is presented. The effect of roughness details on the pressure distribution is clearly seen. If such a contact would have been between an elastic smooth flat surface and a rigid smooth sphere with the same properties, then the maximum contact pressure would have been 3.6 GPa. Note that the maximum pressure

calculated for the rough surface is more than 200 GPa. This is an extremely high value and at such pressures naturally elasticity cannot be retained. However, this result can give some insights of how roughness effects the initial pressure distributions.

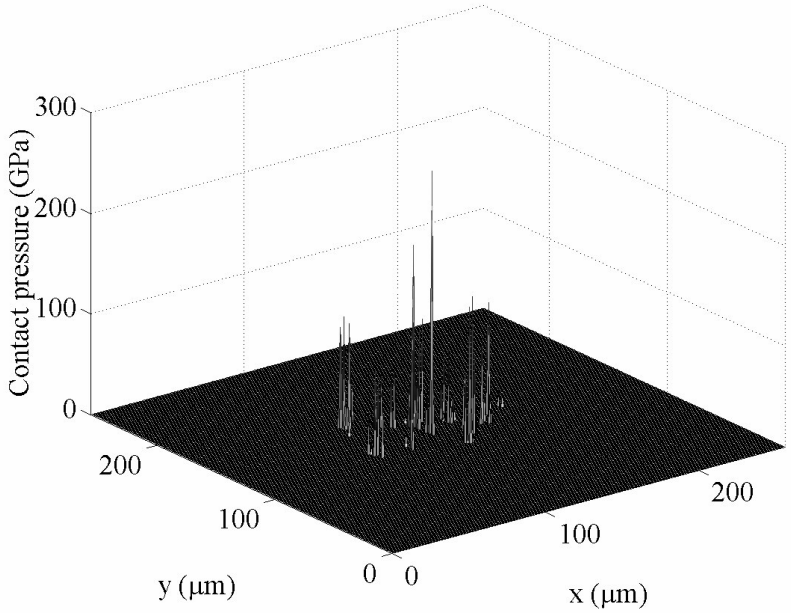

Figure 4.22. Contact pressures if the contact is assumed to be elastic.

In the next step, the elastic deformations will be discussed. This can be seen in figure 4.23 where the elastically deformed profile is presented with the original undeformed profile. This profile is taken at y = 128 μm which is the central profile of the surface. It is observed that the roughness details still exist in the deformed profile and the deformation is more like a global deformation of the asperities in the loading direction. This behavior is very similar to the case of the finite element calculation performed for the cosine rough surface presented in figure 4.16, where roughness details were preserved. The subsurface von Mises stresses were also calculated for the elastic problem. The resulting distribution under the profile presented in figure 4.23 is shown in figure 4.24. The calculation was performed for a depth of 9 μm which is exactly nine times the roughness of the surface. The maximum von Mises stress value is under the central sharp asperity, and this value goes up to 55 GPa near the surface. 55 GPa is an extremely high value and is generated by a very high concentrated pressure acting on the grid element.

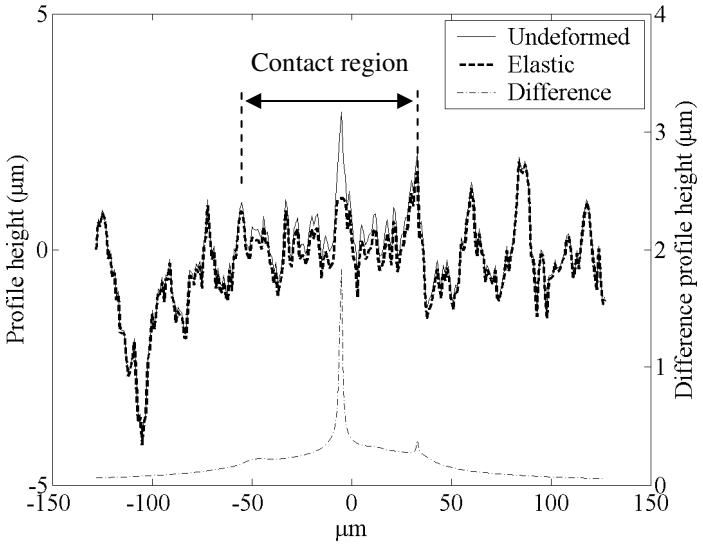

Figure 4.23. Profiles from the undeformed and elastically deformed surfaces.

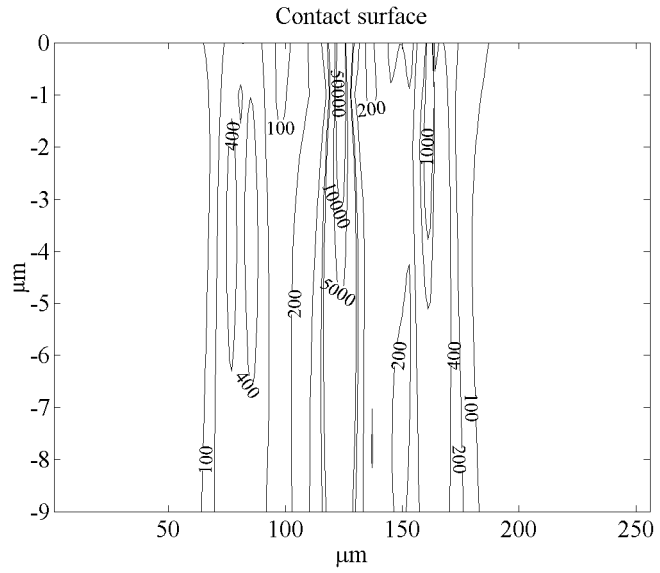

Figure 4.24. Subsurface von Mises stresses in MPa beneath the contact.

Finally, the same problem was solved with the elastic-plastic model. The pressure distribution obtained with this assumption is presented in figure 4.25. The pressure distribution is flat at the value of the hardness (1 GPa) according to the model. The contact diameter is approximately 100 μm. The central profile of the deformed three-dimensional roughness data is plotted together with the undeformed profile in figure 4.26. Note that the deformed profile in figure 4.26 is the unloaded state of the surface, so the calculated

elastic deformation is “subtracted” from the overall deformation. With the introduced model, the roughness details are completely flattened in the contact region. Conformity of the contact is obtained in the shape of the rigid sphere counter surface. This model will be used in chapter 7 in comparison with the experimental results.

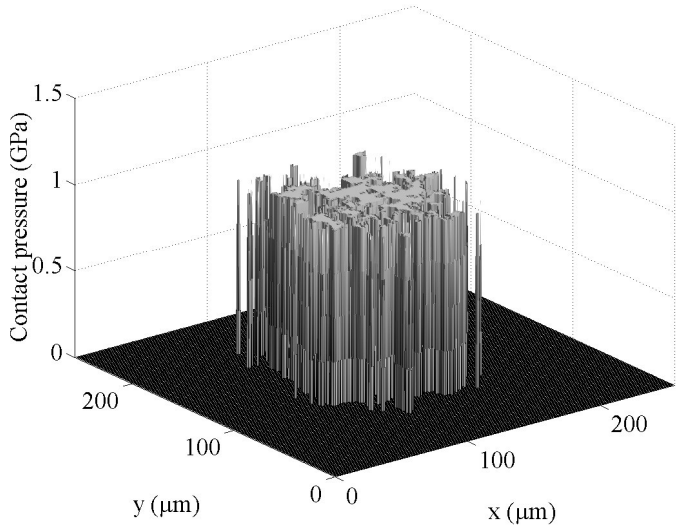

Figure 4.25. Contact pressures if the contact is assumed to be elastic-plastic.

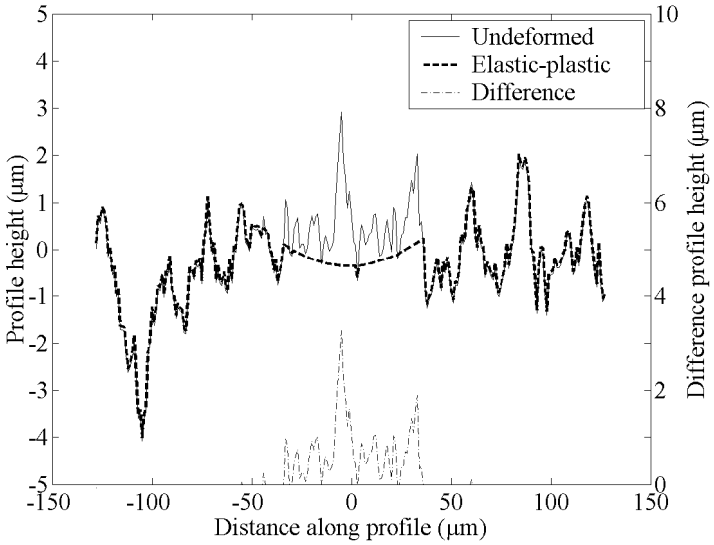

Figure 4.26. Profiles from the undeformed and deformed (elastic-plastic) surfaces.

4.8. Summary and Conclusions

- A 2D F.E.M. and a 3D B.E.M. were introduced. These models were validated with the numerical and the analytical approaches presented in the literature. The results show that the 3D B.E.M. can be used for 3D elastic-plastic contact problems and offers a fairly good approximation and is faster than the finite element technique. This tool will be used later in chapters 5, 6 and 7, for a better understanding of the experimental results measured by the wear and deformation measurement technique introduced in this thesis (see chapter 3).

- It is shown that the general material assumption of having the fully plastic regime with a mean pressure is equal to 2.8 times the yield strength holds very well for the single asperity case. However, when rough surfaces are considered, this value increases due to the interaction of the asperities.

- When a rough surface is in contact with a flat rigid surface, it is observed that the deformation mechanism of the asperities is related to whether the contact is elastic or elastic-plastic. If the contact is elastic, asperities are pressed down together and they nearly change their shapes. If the contact is elastic-plastic, then the change in shape of the asperities is considerable.

References

[1] R.S. Sayles, Basic principles of rough surface contact analysis using numerical methods, Tribology International 29 (1996), pp. 639-650.
[2] L. Chang and Y. Gao, A simple numerical method for contact analysis of rough surfaces, Journal of Tribology 121 (1999), pp. 425-432.
[3] A.E.H. Love, The stress produced in a semi-infinite solid by pressure on part of the boundary, Philosophical Transactions of the Royal Society of London, Series A, 228 (1929), pp. 377-420.
[4] N. Ren and S.C. Lee, Contact simulation of three-dimensional rough surfaces using moving grid method, Journal of Tribology 115 (1993), pp. 597-601.
[5] E. Sourty, J.L. Sullivan and M.D. Bijker, Numerical modeling of sub-surface stress in magnetic data tape heads due to dynamic contact with a tape, Tribology International 35 (2002), pp. 171-184.
[6] D. Tabor, The Hardness of Metals, Oxford University Press, Oxford, 1951.
[7] M.A. West and R.S. Sayles, A 3-dimensional method of studying 3-body contact geometry and stress on real rough surfaces, 14th Leeds-Lyon Symp. (1987), Lyon, pp. 195-200.
[8] L. Kogut and I. Etsion, Elastic-plastic contact analysis of a sphere and a rigid flat, Journal of Applied Mechanics 69 (2002), pp. 657-662.
[9] W.R. Chang, I. Etsion and D.B. Bogy, An elastic-plastic model for the contact of rough surfaces, ASME J. Tribol. 109 (1987), pp. 257-263.
[10] W.R. Chang, I. Etsion, and D.B. Bogy, Static friction coefficient model for metallic rough surfaces, ASME J. Tribol. 110 (1988), pp. 57-63.

Chapter 5. Changes in the micro-geometry of rolling contacts

5.1. Introduction

In this chapter, rolling contact experiments will be presented. These experiments cover the effects of geometric properties of surfaces (such as roughness, R_q) and material properties (such as hardness, H) on deformation mechanisms taking place in a rolling contact. Both the single loaded and cyclically loaded rolling contacts will be studied.

In section 5.2, deformation and shakedown [1] in a rolling contact between smooth bodies will be discussed. By the model presented in chapter 4, it has already been shown that pressures and subsurface stresses are much higher in rough surfaces than in the case of smooth surfaces in contact. For a better understanding, in section 5.3.1 the rolling contact between a smooth rigid sphere against a rough surface will be studied. This discussion will be followed by experiments with surfaces with a lower roughness. In section 5.3.2, the shakedown behavior of surfaces with different asperity layouts such as lateral and longitudinal asperities will be discussed.

After these discussions based on geometrical effects, the effects of material properties on deformation and shakedown will be discussed in sections 5.3.3 and 5.3.4. Experiments with a rigid sphere against hardened rough disks will be shown in section 5.3.3. In section 5.3.4, deformation of a non-work hardening rough surface will be illustrated with an example. In all the experiments, the experimental conditions are as presented in table 5.1. Any deviation from these conditions will be mentioned in the text.

Table 5.1. Standard experimental conditions.

Number of cycles	50
Normal load	4 N
Rolling velocity	7 mm/s
Track radius	40 mm
Temperature	24 °C
Relative humidity	50 %
Lubrication	None

5.2. Rolling contact of a smooth sphere against smooth disk

In this experiment a smooth silicon carbide (SiC) sphere was in rolling contact with a smooth steel (EN1.2510) disk. The geometrical and material properties of the two contacting bodies are presented in table 5.2. In addition, the corresponding Hertzian contact properties are given in table 5.3.

Table 5.2. Properties of the contacting surfaces.

Material	EN1.2510 flat disk	SiC sphere
Radius (mm)	-	3.2
R_q (μm)	0.03	0.01
E (GPa)	210	430
v	0.3	0.17
H (GPa)	2.9 (z = 2.5 μm)	22
	2.3 (z = 6 μm)	
σ_y (GPa)	0.82	3.5 (tensile strength)
k (GPa)	0.47	-
p_0 (initial yield) (GPa)	1.38	
p_0 (shakedown) (GPa)	2.22	

Table 5.3. Hertzian contact properties.

Contact radius	40 μm
Contact approach	0.5 μm
Mean contact pressure (p_m)	0.8 GPa
Maximum contact pressure (p_0)	1.2 GPa

The yield strength of the disk can be calculated from a measured hardness value according to the relation $\sigma_y = H/2.8$ [2] as 0.82. This hardness is measured with a Vickers micro-indenter at a load of 0.05 N. The indentation depth was 6 μm. The shear yield strength of the material is calculated to be 0.47 GPa using the expression:

$$k = \frac{\sigma_y}{\sqrt{3}} \tag{5.1}$$

The standard experimental conditions are described in table 5.1. In the experiment, the rotational velocity of the freely rolling ball (running at a track radius of approximately 40 mm) was approximately 7 mm/sec. The applied normal load was 4 N. At this load, the calculated mean contact pressure (if the contact is assumed to be perfectly smooth and elastic) was 0.8 GPa and the maximum contact pressure was 1.2 GPa using the Hertzian equation. With the same assumption, the contact radius and approach of the two bodies can be calculated as 40 μm and 0.5 μm respectively. Also, from equation 2.29, initial yield occurs when the maximum contact pressure is larger than 1.38 GPa (or $p_m > 0.92$ GPa). This value is slightly higher than the maximum contact pressure of 1.2 GPa calculated for contact between a ball and a flat. Shakedown is expected below a maximum contact pressure of 2.22 GPa (or $p_m < 1.48$ GPa). From equation 2.24, the calculated maximum shear stress (τ_{xz}) value is equal to 0.26 GPa.

The experiment takes place over 50 load cycles for the disk. In figure 5.1 the steel disk surfaces before and after the first cycle are presented. The rolling direction was as marked. The heights along the marked profile before and after the first cycle are shown figure 5.2. Here, the dotted profile is from the initial (undeformed) surface in figure 5.1. The solid line is the profile of the surface after the first deformation cycle (first contact), see figure 5.1. The direction of rolling in figure 5.2 points out of the page.

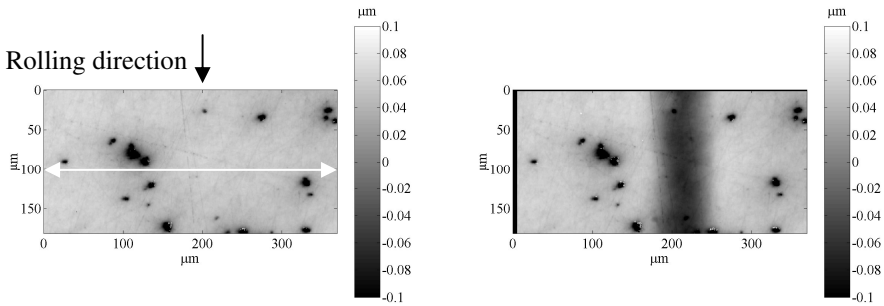

Figure 5.1. Disk surface before (left) and after the first cycle (right).

From figure 5.2 it is seen that the contact diameter is approximately 90 µm. This value is of the order of the Hertzian contact diameter of 80 µm as expected. After the first cycle, the change in the profile is shown in figure 5.3. It is seen that there is continuing plastic deformation during the first 30 cycles. The deformation is in the form of bulk deformation. While the conformity increases, the amount of deformation per cycle decreases and finally a shakedown state is achieved. It is also seen that, after the first cycle, the surface starts to rise on the sides to form ridges.

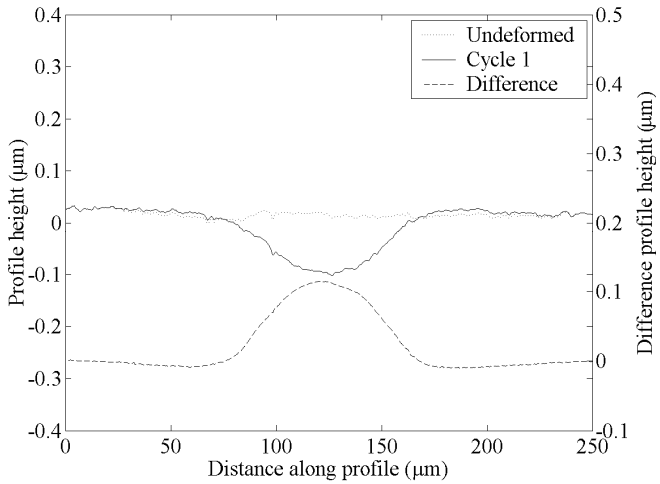

Figure 5.2. Profiles along the rough steel disk surface as marked in figure 5.1 for a single contact.

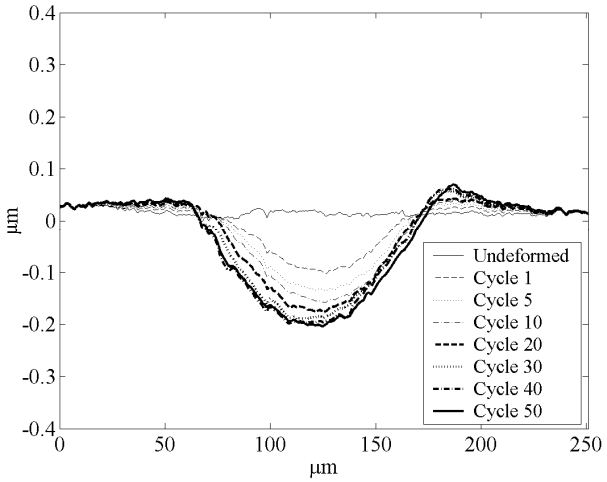

Figure 5.3. Profiles along the steel disk (R_q = 0.03 µm) surface for 50 cycles.

Obviously, the contact is not elastic in the first cycle. However for a better understanding, the subsurface von Mises and shear stress component (τ_{xz}) governing the shakedown criteria in a smooth ball-flat configuration were calculated using the elastic contact algorithm presented in Chapter 4. For details the reader is referred to chapter 2. These stress distributions are shown in figure 5.4. For this analysis, the surfaces were normally loaded.

The distribution of the von Mises stresses in figure 5.4.a is similar to the distribution of the von Mises stresses in the case of an ideally smooth ball against the disk, see figure 5.4.b. The low sloped roughness details do not introduce high stress concentrations near the surface. The maximum von Mises stress is 435 MPa at a depth of 20 µm which is very close to the value in figure 5.4.b for the smooth surface solution. In figure 5.4.c, it is seen that the shear stress component τ_{xz} is below the yield shear strength (k) of the material which is 470 MPa. This ensures that the residual stresses develop for a shakedown state as discussed in section 2.3.

In figure 5.5, the pressure distributions in the contact for the 1st and 50th cycles are presented. The distribution in the 50th cycle was calculated by centering the normally loaded sphere against the deformed surface. It is seen that, as the contact is conforming, the circular contact area changes to an elliptically shaped contact region. In this state, the contact pressures are closer to a Kunert type pressure distribution [1]. In the first cycle, the numerically calculated average pressure on the asperities is 0.84 GPa. This value is close to the mean pressure required for the initial yield in a smooth ball-flat contact, which is 0.92 GPa. Thus, the contact is expected to be in a transition from elastic to an elasto-plastic deformation regime.

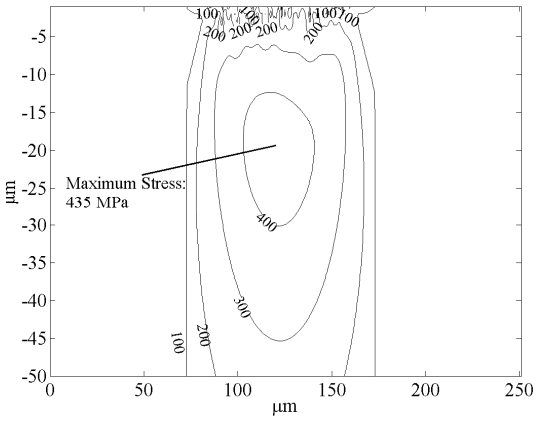

(a)

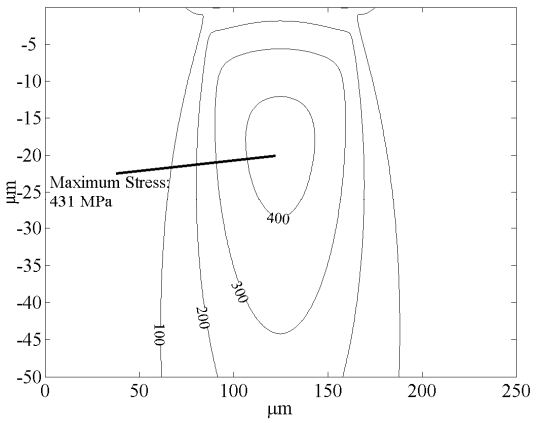

(b)

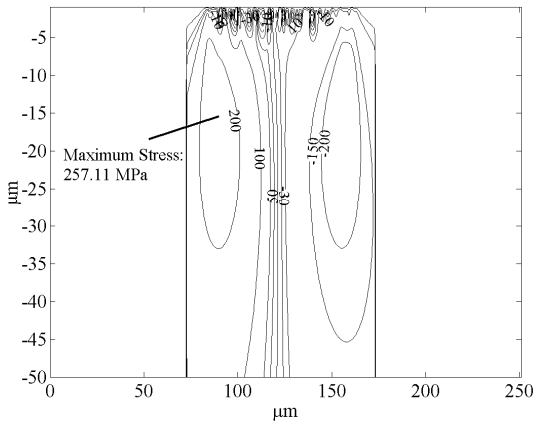

(c)

Figure 5.4. von Mises stresses for (a) experimental surface and (b) ideal flat surface. (c) τ_{xz} distribution beneath the contact for the 1st cycle.

After 50 cycles the average pressure on the asperities is reduced to 0.7 GPa. This value is far below the pressure on the initial yield and the contact is elastic.

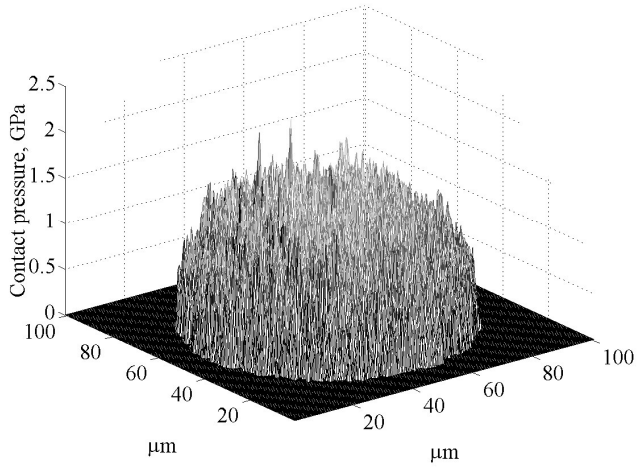

(a)

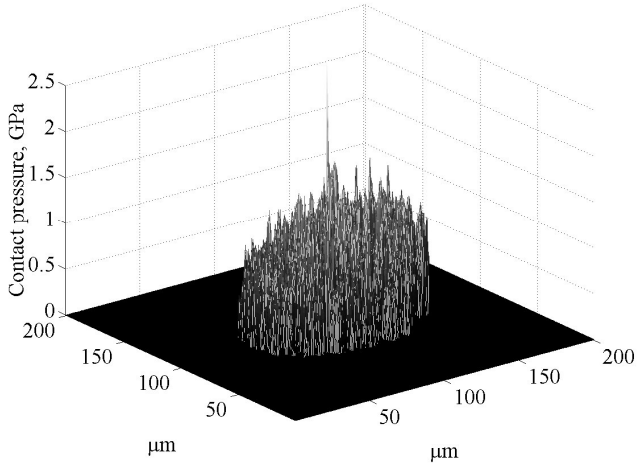

(b)

Figure 5.5. Contact pressures for the 1st (a) and the 50th cycles (b).

The subsurface von Mises stress distribution for the 50th cycle is shown in figure 5.6. It is seen that the magnitude of the von Mises stresses is slightly reduced in the subsurface region compared to the first cycle (figure 5.4.a). In addition, a high stress concentration develops near the surface at a depth of 1 μm because of the high pressure spike at the center as seen in figure 5.5. Note that this spike is an artifact of the experiment.

As a summary,

- When the surface roughness is low then the stresses under the contact are very similar to those in a smooth sphere-flat contact situation (figure 5.4). High "global" stress concentration is deep under the surface in such contacts and the deformation is mainly in the form of bulk deformation.

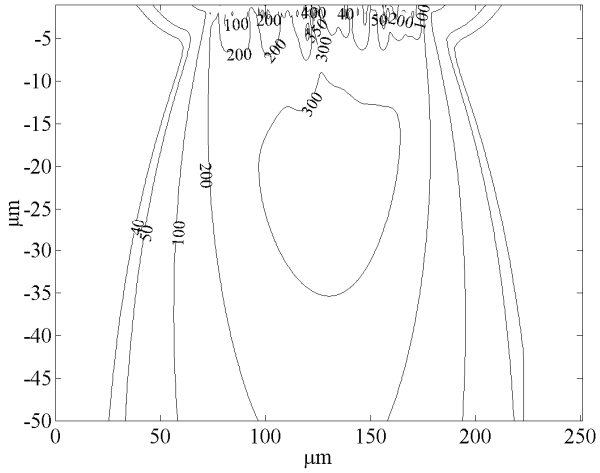

Figure 5.6. von Mises stresses beneath the contact for the 50th cycle.

- After 50 cycles a steady state is achieved.

- When roughness is low, the contact pressure distribution is close to a Hertzian distribution. As conformity increases, the distribution approaches a Kunert type pressure distribution [1].

In the following section, deformation on deformable rough surfaces in a rolling contact with a rigid smooth sphere will be studied.

5.3. Rolling contact of rough surfaces

5.3.1. Roughness effects

In order to analyze the contact of a rigid smooth sphere and a deformable rough surface, rolling contact between a smooth silicon carbide (SiC) ball and a ground steel (EN 1.2510) disk will be presented. The geometrical and material properties of the two contacting bodies are presented in table 5.4. The experimental conditions and Hertzian contact properties are as in tables 5.1 and 5.3 respectively. As a summary, the calculated mean contact pressure (if the contact is assumed to be smooth and elastic) is 0.8 GPa and the maximum contact pressure is 1.2 GPa. The contact radius and approach of the two bodies according to Hertz are 40 μm and 0.5 μm respectively as in the previous example. From equation 2.17, initial yield occurs when the maximum contact pressure is higher than 2.4 GPa (or p_m > 1.6 GPa) and

Table 5.4. Properties of contacting surfaces.

Material	EN1.2510 flat disk	SiC sphere
Radius (mm)	-	3.2
R_q (μm)	0.66	0.01
E (GPa)	210	430
v	0.3	0.17
H (GPa)	4 (z = 2.5 μm)	22
σ_y (GPa)	1.43	3.5 (tensile strength)
k (GPa)	0.83	-
p_0 (initial yield)	2.4	-
p_0 (shakedown)	3.9	-

shakedown is expected below a maximum contact pressure of 3.9 GPa (or p_m < 2.6 GPa) for the contact of smooth surfaces with similar material properties. The experiment covers 50 contact cycles of the ball and the disk. In figure 5.7 the steel disk surface before and after the first cycle is presented. The rolling direction is parallel to the grinding grooves on the surface. The profile marked is across the rolling direction. In order to see the local changes in the micro-geometry, this profile is plotted in figure 5.8 for the first cycle. In figure 5.8 the dotted profile is from the initial (undeformed) surface in figure 5.7. The solid line is the profile of the surface after the first deformation cycle (or the first contact) (see figure 5.7). The direction of rolling in figure 5.8 points out of the page.

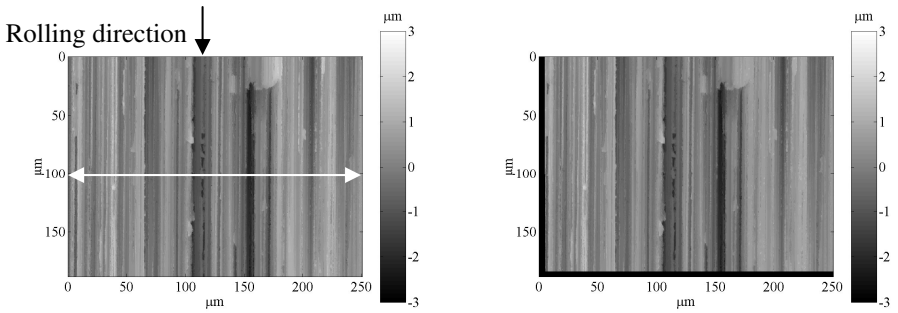

Figure 5.7. Disk surface before (left) and after the first cycle (right).

It is observed from the figure that after the first cycle some of the roughness details are flattened. Looking at the bottom points of the profile, one can say that the bulk deformation is almost negligible compared to the mentioned roughness level deformation. After the first cycle, the contact gradually becomes conforming in 50 cycles, where the profile resembles the shape of the rigid counter-part and the sharp asperities are flattened as shown in figure 5.9. After the 40th cycle there is no change in the surface micro-geometry so shakedown is achieved. The contact radius at this moment was estimated from figure 5.9 as approximately 100 μm. This radius is larger than in the smooth case.

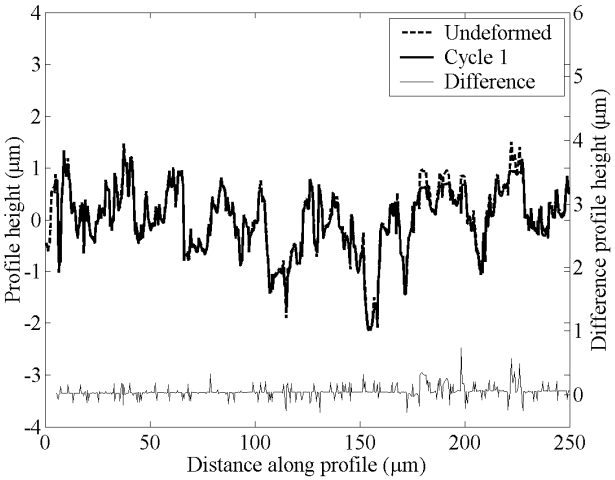

Figure 5.8. Profiles along the rough steel disk surface as marked in figure 5.7 for a single contact.

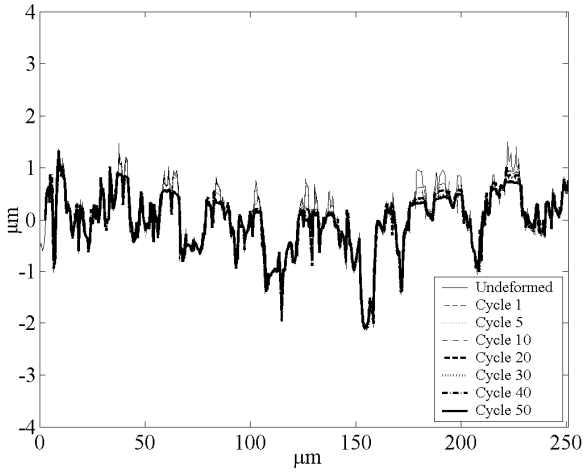

Figure 5.9. Profiles along the steel disk (R_q = 0.66 μm) surface as marked in figure 5.7 for 50 cycles.

For the calculation of the subsurface stresses, the model that was presented in chapter 4 was used again. The contact was assumed to be elastic in the first cycle although the cycle was a plastic cycle, to be able to calculate the stress components. The surfaces were brought into normal loaded contact by centering the sphere surface approximately on the region of contact, determined manually by the last cycle's profile. The initial calculated elastic average contact pressure on the asperities was 12.7 GPa. This high pressure causes the high sloped asperities to deform. The calculated subsurface von Mises stress distribution is plotted in figure 5.10. High stress concentration near the contact is clearly seen. The maximum von Mises stress is approximately 8 GPa just close to the surface and stresses

caused by individual asperities are at a distance from each other, which means that asperities will not "support each other", as discussed in chapter 4.

As mentioned before, after the 40th cycle no plastic deformation takes place. This means that at this stage the contact is elastic. For this reason, elastic calculations can be performed for the last cycles (i.e. the 50th cycle) and the contact pressure and the sub-surface stresses can be calculated using elastic models. The average pressure on the asperities was calculated by the

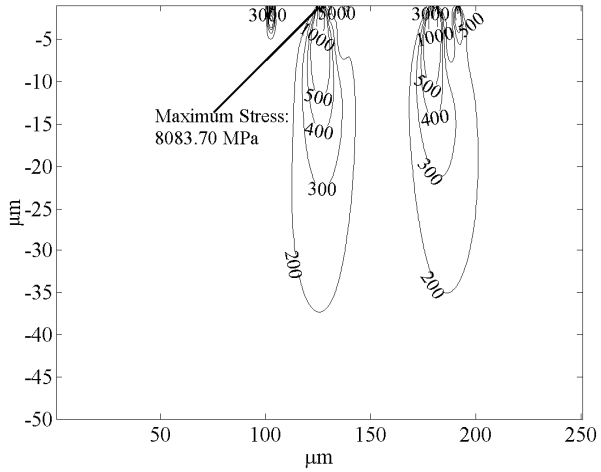

Figure 5.10. Sub-surface von Mises stresses for EN 1.2510 disk with H = 4 GPa and R_q = 0.66 µm, calculated for the first cycle.

elastic contact algorithm as 2.85 GPa. This value is slightly higher than the limiting mean pressure required (which is 2.6 GPa) for shakedown of smooth surfaces. The pressure distribution on the 50th profile in figure 5.9 is seen in figure 5.11. It is seen that there are local areas that have contact pressures higher than 6 GPa. However, these are single points, and may be numerical artifacts resulting from the numerical discretisation of the surface. At the larger microcontacts, the pressures are typically equal to the shakedown pressure.

Finally, the stress distribution below the surface for the 50th cycle at the center of the contact is presented in figure 5.12. The stresses are, compared to the initial situation in figure 5.10, distributed in a wider subsurface region and high stress concentrations are not seen because of the conforming contact. The stresses are mostly below the yield criterion for the material (0.83 GPa), ensuring that this state is elastic, and calculations performed with the elastic contact algorithm are valid.

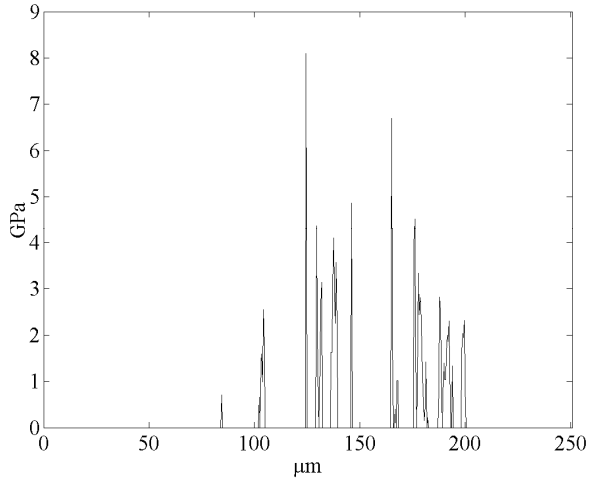

Figure 5.11. Pressure distribution on profile in figure 5.9 for the 50th cycle.

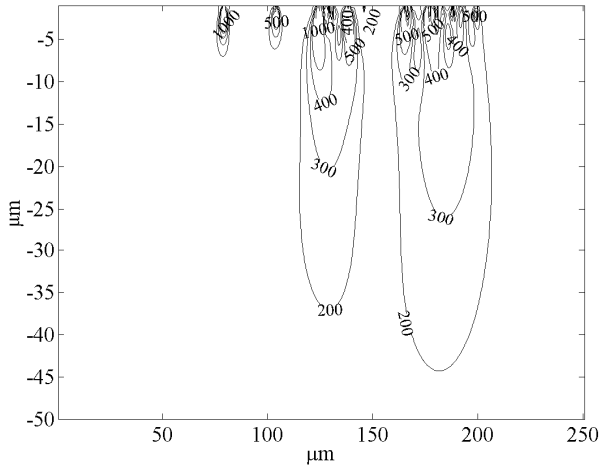

Figure 5.12. Sub-surface von Mises stresses for EN 1.2510 disk with H = 4 GPa and R_q = 0.66 µm, calculated for the 50th cycle.

Summary:

- The deformation is at asperity level.
- Elastic von Mises stresses after 50 cycles are below the yield criterion, ensuring that in this state the contact is elastic.
- The calculated pressure in the last cycle is close to the shakedown pressure.

Up to this point, the shakedown of a rough surface with asperities having high roughness was analyzed. In the second part of this section, the effects

of a reduced roughness will be studied with an experiment. The same materials (SiC ball and EN 1.2510 disk) but this time a disk with lower roughness (R_q = 0.3 µm) will be used. The disk surface before and after the first cycle is presented in figure 5.13. During the experiment in total 50 cycles were performed.

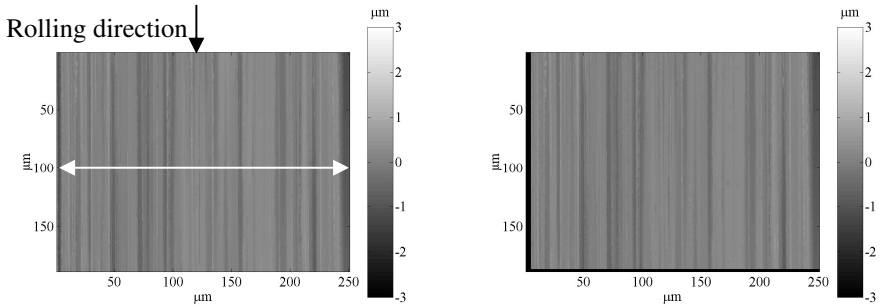

Figure 5.13. Disk surface before (left) and after the first cycle (right).

The marked profile in figure 5.13 at the first cycle is presented in figure 5.14. In contrast to the previous experiment, roughness details are not flattened in the first cycle. The asperities are pushed down together with the bulk material. This can be clearly seen from the bottom points (valleys) of the profile which is pushed down with the roughness details. At first sight, this might be explained by a non-concentrated pressure distribution on the surface. The calculated average contact pressure on the asperities is 6.5 GPa. This value is approximately half of the pressure value in the previous experiment with a rougher surface, however, it is still much higher than the shakedown pressure that was calculated for a smooth contact couple (2.6 GPa). These two different forms of deformation mechanisms, namely asperity deformation in the previous example and combined deformation of asperities and the bulk seen in this case can be explained by the distribution of the stresses below the surface. The subsurface von Mises stresses for the first cycle can be seen in figure 5.15. Compared to the stress field seen in figure 5.10 for the first cycle of the previous case where R_q = 0.66 µm, the stresses are lower, less concentrated and the stress fields of the individual asperities form a combined global stress zone in the subsurface. Stresses are close to the yield criterion which is 0.83 GPa. It could be that when asperities are close to each other it is more difficult to deform them plastically, and higher pressures may be required. The reader is referred to section 4.6 where plastic deformation of rough surfaces is discussed. As a recommendation the sub-surface stresses should be calculated using a plastic model instead of an elastic model, for a better understanding of the phenomena.

In figure 5.16, deformation during 50 cycles at the same profile (see figure 5.13) is presented. There is small scale change in the topography after the

40th cycle to the left of the contact. However, topography changes after the 50th cycle are only minor.

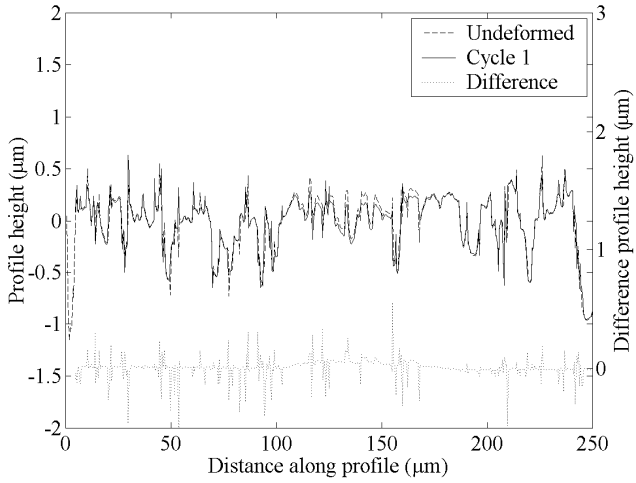

Figure 5.14. Profiles along the rough steel disk surface as marked in figure 5.13 for a single contact.

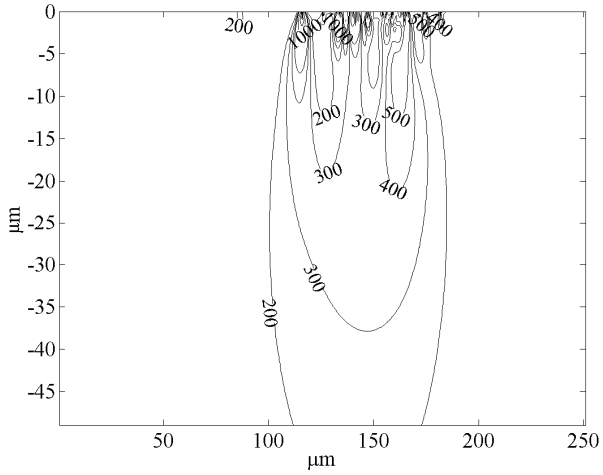

Figure 5.15. Sub-surface von Mises stresses for EN 1.2510 disk with H = 4 GPa and R_q = 0.3 μm, calculated for the first cycle.

After the 50th cycle an elastic analysis was used to calculate the contact pressures and the von Mises stresses. The von Mises stresses under the contact are shown in figure 5.17. The average contact pressure on the asperities was calculated to be 3.43 GPa. This value is larger than the previous case with the rough disk (R_q = 0.66 μm) after 50 cycles. This is expected as the asperities are not flattened completely, and the real contact area is smaller because the asperities are pushed down. Additionally, this value is also higher than the mean shakedown pressure of 2.6 GPa (or p_0 = 4 GPa). An elastic steady state is achieved globally, tough this comparably

high contact pressure in the steady state explains the small scale deformation on the surface. Transition from shakedown to ratchetting might be occurring at this pressure.

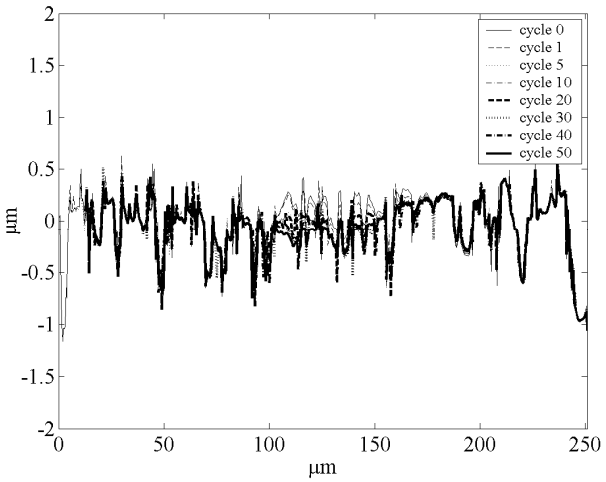

Figure 5.16. Profiles along the steel disk (R_q = 0.25 µm) surface as marked in figure 5.13 for 50 cycles.

Below the surface, the von Mises stress distribution at the 50th cycle was calculated as presented in figure 5.17. The distribution of the stress field gets larger compared to the initial calculation for the first cycle (see figure 5.15) and less points are above the yield criterion for the material.

Summary:

- Deformation is in the form of a combination of asperity deformation and bulk deformation and the asperities are pushed down together with the bulk material. This is not only because of the non-concentrated pressure distribution close to the surface. When asperities are close to each other, it is more difficult to deform them plastically, and higher pressures may be required.

- The calculated pressures are comparable to the shakedown pressures.

- The pressure distribution is very sensitive to the "outliers" on a measured surface.

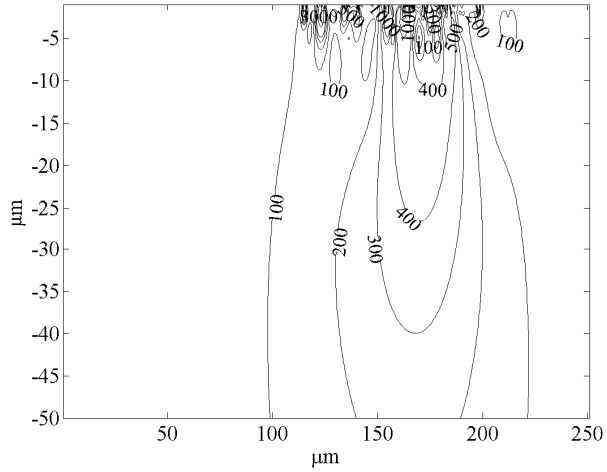

Figure 5.17. Sub-surface von Mises stresses for EN 1.2510 disk with H = 4 GPa and R_q = 0.3 µm, calculated for the 50th cycle.

5.3.2. Asperity layout

In section 2.4.3 it was already discussed that in a lubricated sliding contact, layout of the asperities affects the shakedown limit. The outcome of [6] revealed that lateral asperities might still be in the ratchetting region at contact pressures where longitudinal asperities shakedown to an elastic steady state. In this section the effect of asperity layout will be studied in a rolling contact. For this, experiments with the contact couple seen in table 5.5 were conducted. The applied normal load was 4 N. The calculated

Table 5.5. Properties of contacting surfaces.

Material	EN1.2510 flat disk	SiC sphere
Radius (mm)	-	5
R_q (µm)	0.66	0.01
E (GPa)	210	430
v	0.3	0.17
H (GPa)	4 (z = 2.5 µm)	22
σ_y (GPa)	1.43	3.5 (tensile strength)
k (GPa)	0.83	-
p_0 (initial yield)	2.4	-
p_0 (shakedown)	3.9	-

Hertzian mean contact pressure if the contact is assumed to be smooth and elastic was 0.6 GPa and maximum contact pressure is 0.9 GPa. With the same assumption, the contact radius and approach of the two bodies can be calculated as 46 µm and 0.43 µm respectively. Again from equation 2.17, initial yield occurs when the maximum contact pressure is higher than 2.4 GPa or the mean pressure p_m > 1.6 GPa. Shakedown is expected below a

maximum contact pressure of 3.9 GPa (or $p_m < 2.6$ GPa) for the contact of smooth surfaces with similar material properties.

The duration of the experiment was 20 cycles. The rotational table was stopped at two locations at 90 degrees from each other so that roughness measurements can be made on the grinding patterns which are longitudinally and laterally oriented to the track of the ball. The spots with lateral asperities are shown in figure 5.18 before and after the 20th cycle. In figure 5.18, the change in the marked profile is also shown. It is seen that for lateral asperities plasticity is seen after the first cycle and as the conformity increases the trend for a steady state is observed. Despite the large scale deformation, small scale roughness details are recognizable even after 20 cycles. The area with longitudinal asperities is plotted in figure 5.19 showing the surface before and after the 20th cycle, as well as changes in the marked profile. For longitudinal asperities two hills at the center supported the load. The elastic steady state after 20 cycles is clearer for longitudinal asperities than for the lateral asperities.

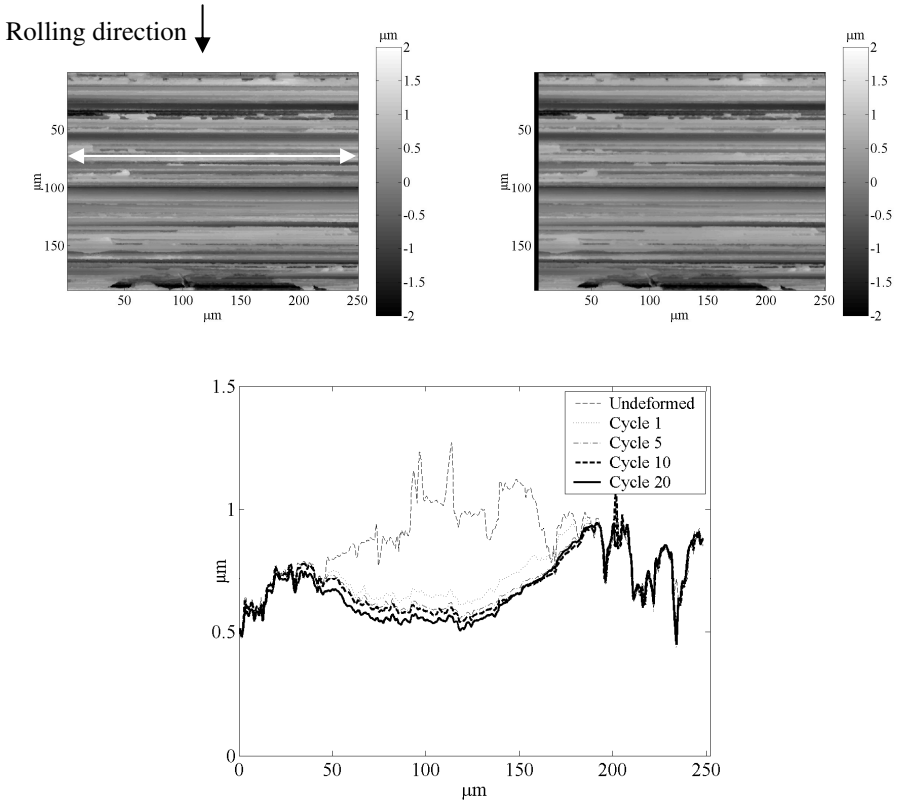

Figure 5.18. Original surface with lateral asperities (top left) and surface after 20 cycles (top right) and change in the marked profile during 20 cycles (bottom).

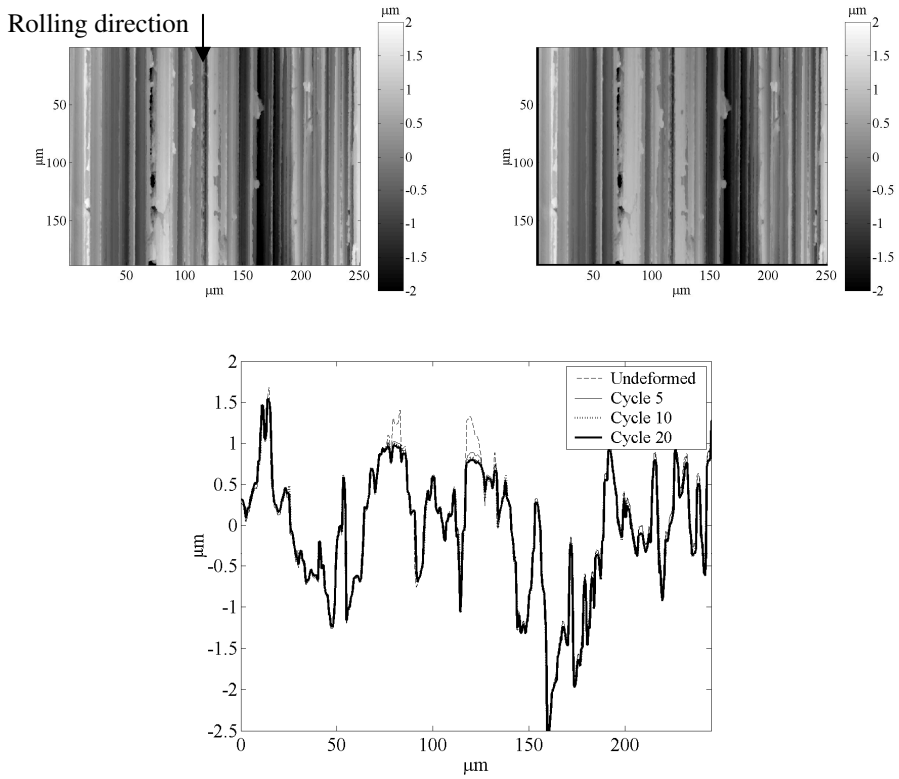

Figure 5.19. Original surface with longitudinal asperities (top left) and surface after 20 cycles (top right) and change in the marked profile in 20 cycles (bottom).

5.3.3. Hardened materials

In this section, two experiments with two hardened EN1.2510 disks with different R_q (0.28 µm and 0.66 µm) will be presented. The experimental conditions were same as those in table 5.1, but this time the disks were much harder with a hardness of 8.3 GPa. The yield strength of the disks was again calculated according to the relation $\sigma_y = H/2.8$ as 2.96 GPa. The rotational velocity of the freely rolling ball (with a radius of 3.2 mm) was approximately 7 mm/sec and the applied normal load was 4 N. The mean Hertzian contact pressure (with the assumption that the contact is smooth and elastic) was 0.8 GPa and the maximum contact pressure was 1.2 GPa. The contact radius and approach of the two bodies was found to be 40 µm and 0.5 µm respectively. The initial yield was expected when the maximum contact pressure is higher than 4.98 GPa (or $p_m > 3.32$ GPa) and shakedown was expected below a maximum contact pressure of 8.04 GPa (or $p_m < 5.36$ GPa) for the contact of smooth surfaces with similar material properties. So, for a smooth disk of this hardness, an elastic contact situation and therefore no surface deformation would be expected. The duration of the experiment was 50 loading cycles. In figure 5.20 the steel disk surface (with $R_q = 0.66$ µm) before and after the first cycles are presented. The rolling direction is

parallel to the grinding direction of the surface. The arrow is marked across the longitudinal roughness profile. The change in this profile is plotted in figure 5.20 for the first cycle.

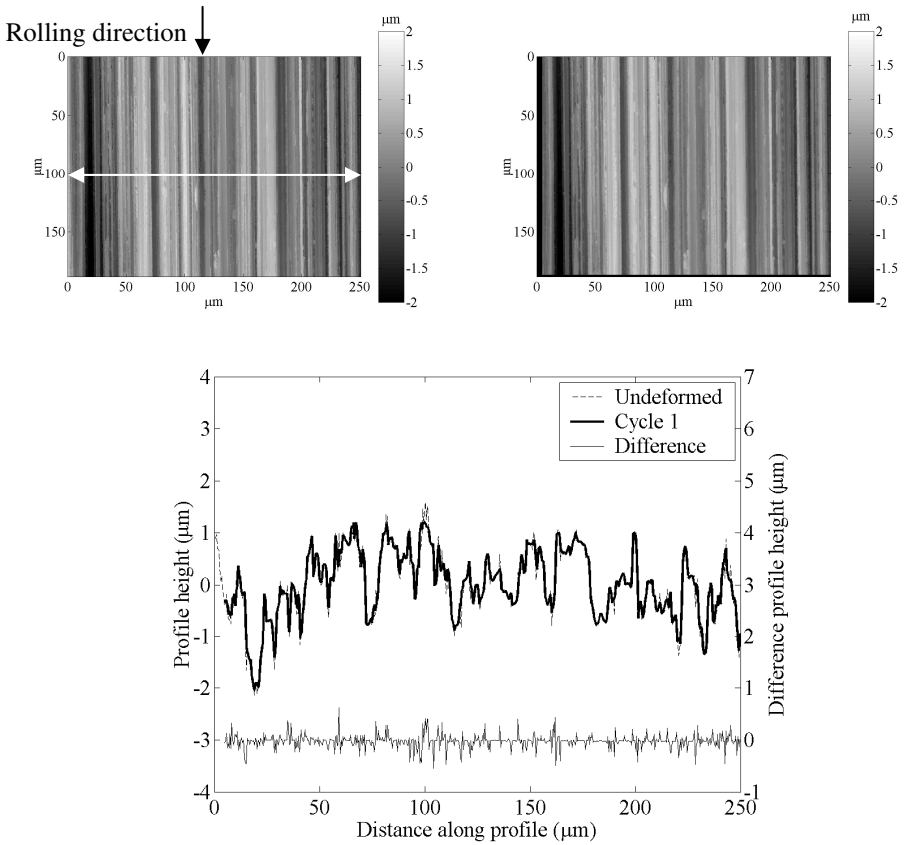

Figure 5.20. Disk surface before (top left) and after the first cycle (top right). The changes in the marked profile (on undeformed surface) are seen on the bottom.

Only the two asperities at the center are deformed in the first cycle and bulk deformation is not observed. After the 5th cycle (figure 5.21) the asperities do not deform further. Note that conformity is not obtained this time as the material is hard enough to carry the load elastically by the contacting asperities only. However, it is also more difficult to estimate the exact contact position of the ball for the calculations. For a numerical analysis, it is assumed that the deformed region is at the center of the contact. The average contact pressure on the asperities was calculated as 20.6 GPa. Initially, these high pressure values cause the highly sloped asperities to deform easily. The calculated subsurface von Mises stress distributions is plotted in figure 5.22.

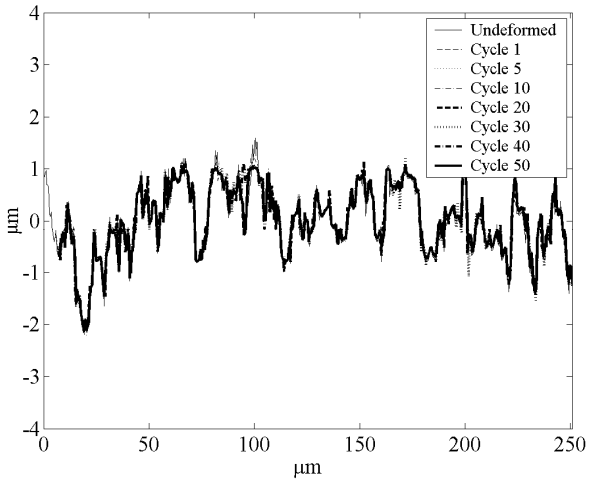

Figure 5.21. Profiles along the steel disk (R_q = 0.66 µm) surface as marked in figure 5.20 for 50 cycles.

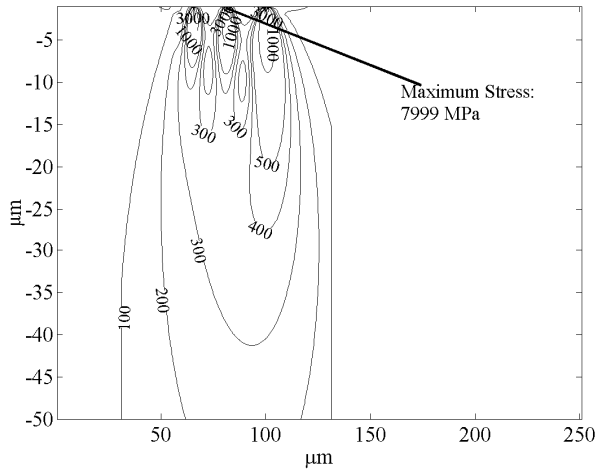

Figure 5.22. Sub-surface von Mises stresses for EN 1.2510 disk with H = 8.3 GPa and R_q = 0.66 µm, calculated for the 1st cycle.

High stress concentration near the contact is clearly seen. The maximum von Mises stress is approximately 8 GPa close to the surface and much lower than the yield criterion (1.71 GPa) for the material in the subsurface. After the 5th cycle, no plastic deformation takes place according to the measurements, see figure 5.21. An elastic contact analysis was carried out for the 50th cycle. The average pressure on the asperities was calculated by the elastic contact algorithm as 6.5 GPa. This value is higher than the mean pressure on the initial yield which was 3.32 (or p_0 = 4.98 GPa) and the limiting mean pressure on shakedown which was 5.36 GPa (or p_0 = 8.04 GPa). In this example the contact size is very small compared to the previous examples with softer surfaces and the contact is not conforming.

As the average pressure on the asperities was calculated through all the contacting points, the mean pressures are possibly not comparable with the values obtained with the conforming contacts.

The stress distribution below the surface for the 50th cycle is presented in figure 5.23. It is seen again that concentrated high stress fields near the surface are reduced in magnitude and expand into a larger region.

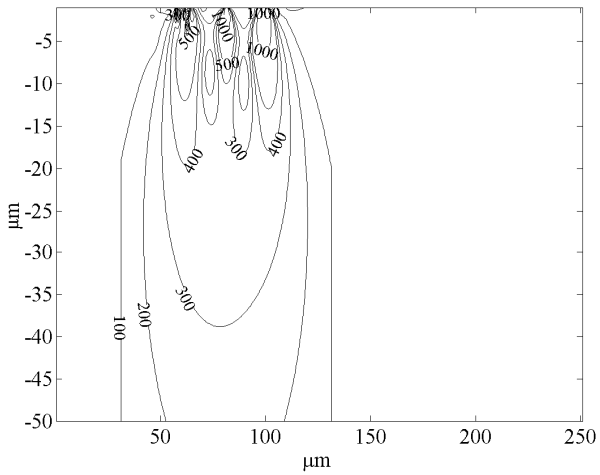

Figure 5.23. Subsurface von Mises stresses for EN 1.2510 disk with H = 8.3 GPa and R_q = 0.66 μm, calculated for the 50th cycle.

In the next experiment, the same disk, but, with a lower roughness (R_q = 0.28 μm) was used. The counter-surface was the SiC ball of radius 3.2 mm and the experimental conditions were the same as in the previous experiment. In figure 5.24, the surface before and after the first cycle as well as the change in the marked profile during a single cycle is presented. It is observed from the figure that after the first cycle few asperities are flattened and there is no bulk deformation. In the first cycle, the calculated elastic average contact pressure on the asperities was 14.9 GPa. Such high pressures lead to a subsurface von Mises stress distribution as seen in figure 5.25. The maximum von Mises stress was around 9.8 GPa near the surface. As the asperities in contact are very sharp, the stress is concentrated near the surface within the first few micrometers.

Shakedown is seen within 10 cycles (figure 5.26). Like the previous example, the contact is not conforming and compared to the softer disks in section 5.3.1, high contact pressures are expected during the final cycle. The numerical calculation led to an average contact pressure of 10.2 GPa at the 50th cycle calculated over all the contacting asperities. This value is much higher than the mean shakedown pressure of 5.36 GPa (or p_0 = 8.04 GPa). As in the previous example, deviation from the shakedown interval

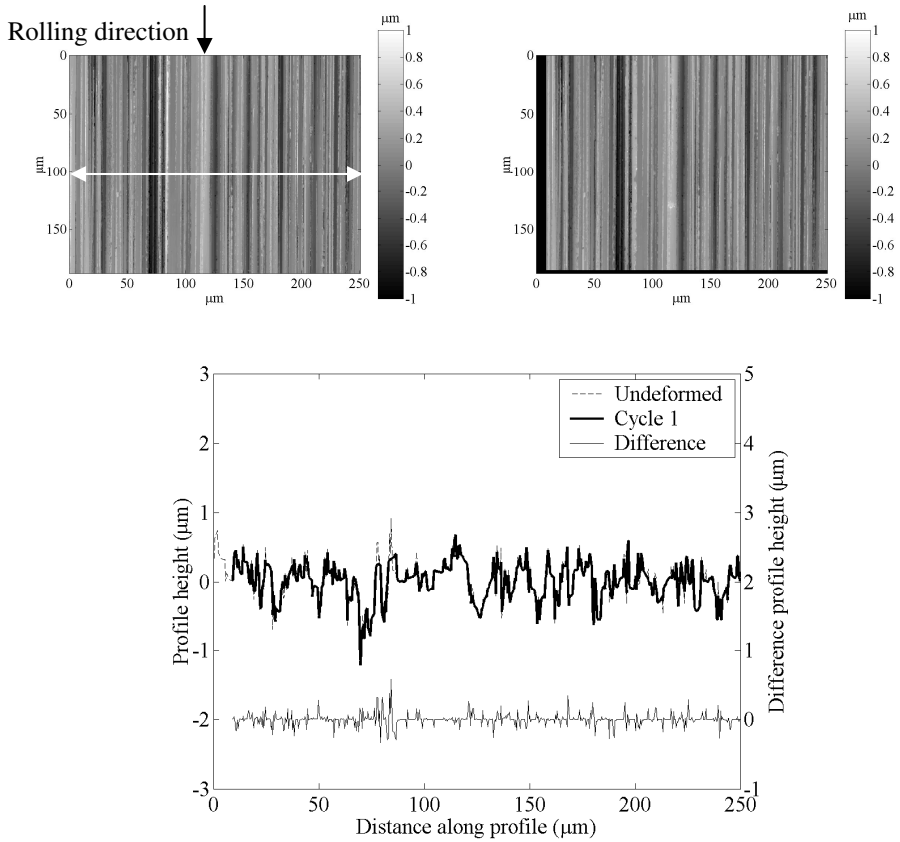

Figure 5.24. Disk surface (R_q = 0.28 µm) before (top left) and after the first cycle (top right). The changes in the marked profile (on undeformed surface) are seen on the bottom.

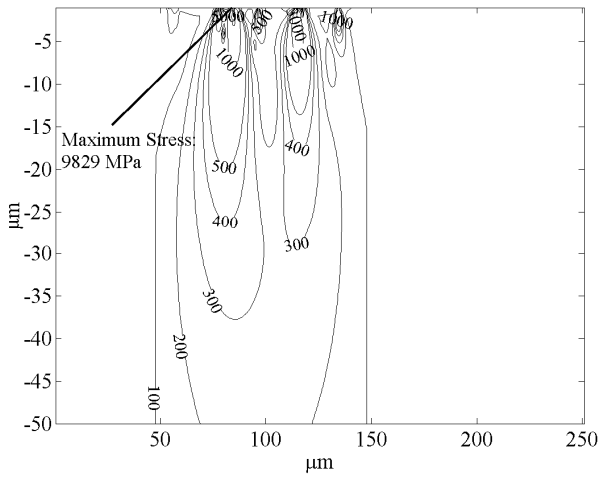

Figure 5.25. Subsurface von Mises stresses for EN 1.2510 disk with H = 8.3 GPa and R_q = 0.28 µm, calculated for the 1st cycle.

formulated for flat surfaces can be explained by the small real area of contact between the contacting surfaces which are non-conforming.

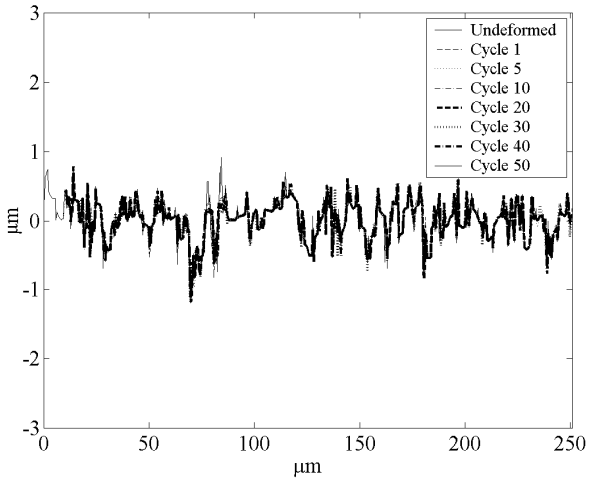

Figure 5.26. Profiles along the steel disk (R_q = 0.28 µm) surface as marked in figure 5.24 for 50 cycles.

The subsurface von Mises stresses are shown in figure 5.27. The maximum stress was calculated to be approximately 9.3 GPa, but the contact is more relaxed as the concentrated stress field widens and decreases in magnitude.

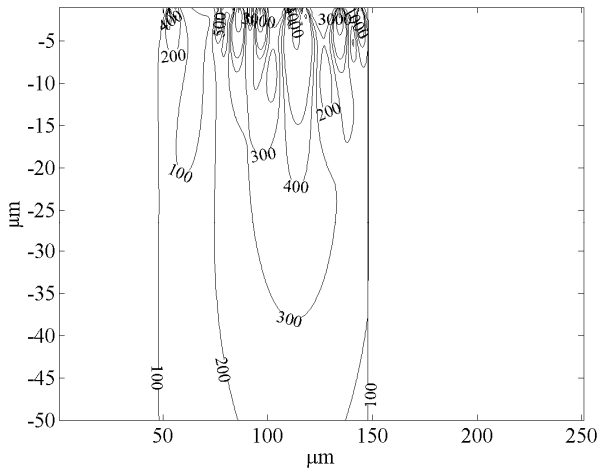

Figure 5.27. Subsurface von Mises stresses for EN 1.2510 disk with H = 8.3 GPa and R_q = 0.28 µm, calculated for the 50th cycle.

Summary:

- Deformation is at the level of asperities this time. Conformity is not obtained with the two surfaces with different roughness, as the

material is hard enough to carry the load elastically by the contacting asperities only.

- Deviation from the shakedown interval as formulated in [1] for smooth surfaces increases if the real area of contact decreases.

In this section, hard and rough surfaces were analyzed. In the following part, an experiment with a non-work hardening material will be presented.

5.3.4. Non-work hardening materials

In this experiment a smooth SiC sphere is in rolling contact with a rough aluminum (AL000790) disk with a purity of 99.999%. The geometrical and material properties of the two contacting bodies are presented in table 5.6.

Table 5.6. Properties of contacting surfaces.

Material	AL000790 disk	SiC sphere
Radius (mm)	-	3.2
R_q (μm)	0.85	0.01
E (GPa)	70	430
v	0.33	0.17
H (GPa)	0.28 (z = 8 μm)	22
σ_y (GPa)	0.1	3.5 (tensile strength)
k (GPa)	0.06	-
p_0 (initial yield)	0.17	-
p_0 (shakedown)	0.27	-

The yield strength of the aluminum disk was 0.1 GPa. The initial yield was expected when the maximum contact pressure exceeded 0.17 GPa. The shakedown limit was 0.27 GPa. In the experiments the rotational velocity of the ball was approximately 7 mm/sec and the normal load was 4 N. The calculated Hertzian mean contact pressure was 0.46 GPa and the maximum contact pressure was 0.7 GPa. This pressure is much higher than the shakedown pressure and the material was expected to be in cyclic plastic deformation or ratchetting [7], see figure 2.10, during the experiment. The Hertzian contact radius and approach of the two bodies can be calculated as 52 μm and 0.86 μm respectively.

The experiment was composed of 50 load cycles. In figure 5.28 the aluminum disk surface before and after the first cycle is presented. The heights along the marked profile before and after the first and fifth cycles can be seen in figure 5.29.

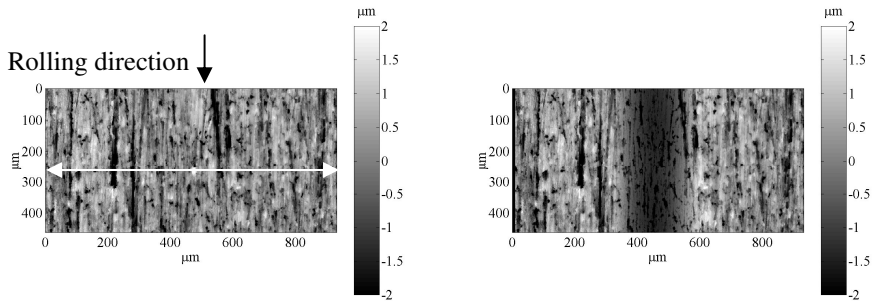

Figure 5.28. Disk surface before (left) and after the first cycle (right).

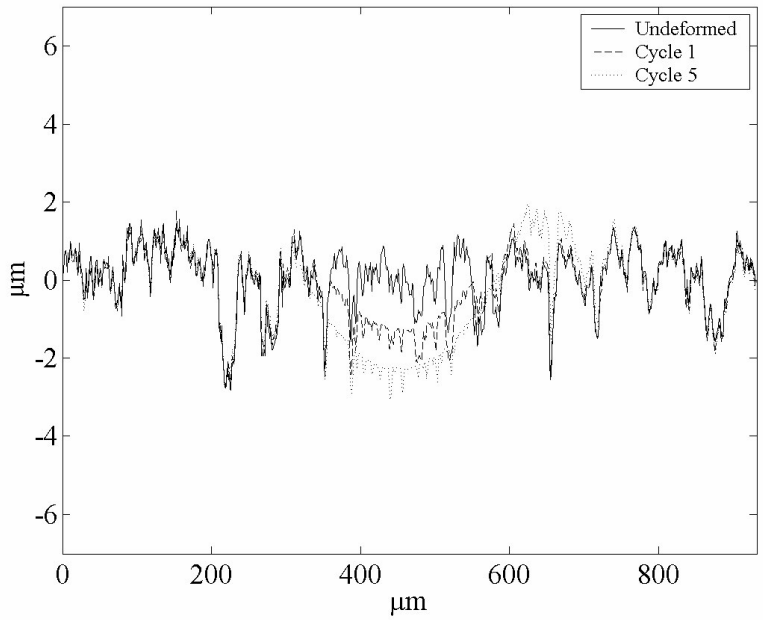

Figure 5.29. Profiles along the rough aluminum disk surface as marked in figure 5.28 for 5 cycles.

In figure 5.29, it is possible to see two mechanisms together, i.e. asperities are flattened and pushed down. Asperity persistence [8] is therefore clearly seen in the figure. The contact diameter was approximately 125 µm. After the 5th cycle (figure 5.30) there are critical changes on the surface not related to surface deformation as studied in this chapter. Visible grooves and hills are formed in the track. A reason could be the ploughing of wear particles. In this state, the system deforms plastically at each cycle and is not in a steady state after 50 cycles. The subsurface von Mises stresses for the first cycle are shown in figure 5.31. The two combined deformation mechanisms can be explained by the fact that the stresses are higher than the yield criterion (57.7 MPa) for the material not only close to the surface but also in the subsurface.

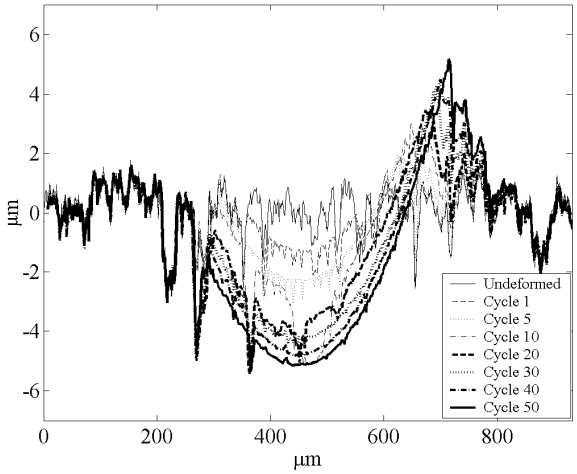

Figure 5.30. Profiles along the aluminum disk surface as marked in figure 5.28 for 50 cycles.

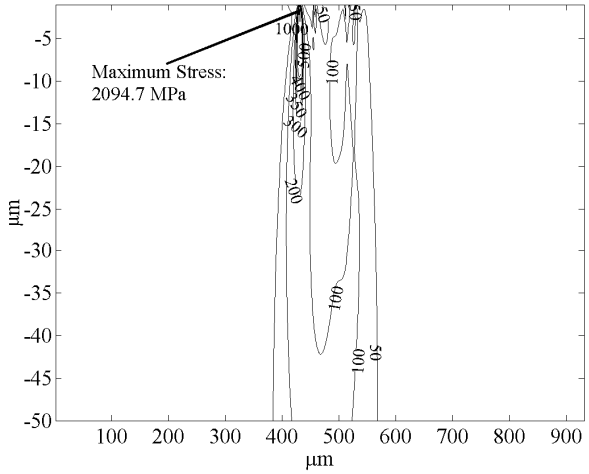

Figure 5.31. Subsurface von Mises stresses for the aluminum disk with H = 0.28 GPa and R_q = 0.85 µm, calculated for the 1st cycle.

Initially, the average pressure on the asperities was 5.5 GPa. After 50 cycles the average pressure on the asperities was calculated as 1.1 GPa and both close to the surface and in the subsurface, stresses (see figure 5.32) are lower compared to those during the first cycle. However, although the contact is more conformal, the pressures are still very high and ongoing plastic deformation was expected from calculations as was also measured in the experiment.

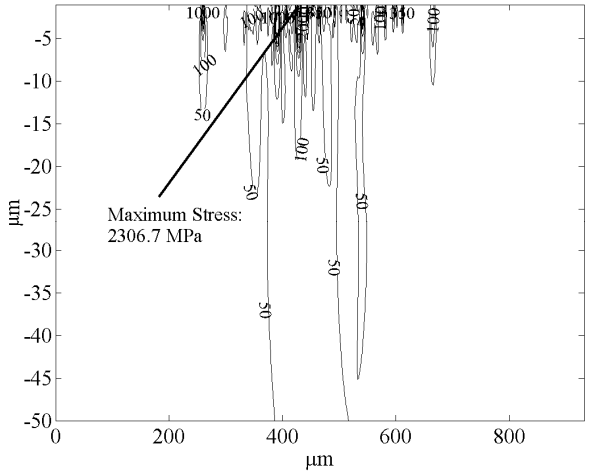

Figure 5.32. Subsurface von Mises stresses for the aluminum disk with H = 0.28 GPa and R_q = 0.85 µm, calculated for the 50th cycle.

5.4. Summary and conclusions

- Deformation and shakedown mechanisms relating to geometrical and material properties of surfaces were investigated in this chapter. It was shown that deformation phenomena seen in rolling contacts can be studied with the existing setup in combination with the elastic contact algorithm introduced in chapter 4.

- In rolling contact experiments it is seen that different deformation types can be present;

  1. Flattening of the asperities, see figure 5.9.
  2. Bulk deformation where asperities are "pushed down" without much change in their shapes, see figures 5.14 and 5.16.
  3. A combination of 1 and 2 as seen in figure 5.29.

  The deformation mechanism depends on geometrical factors (such as roughness, slopes of the asperities, the distance between the asperities) which affect the pressure distributions and hence the stresses at the contact. The position of the major plastic deformation can be predicted fairly well by the elastic calculation of the subsurface von Mises stresses, to indicate whether bulk deformation or asperity deformation will take place. Same calculations can be done for sliding contacts in the next chapter, where friction is involved and stresses are expected to be concentrated close to the surface.

- When rough surfaces are in contact initial stress distributions at a contact are highly concentrated close to the surface. When such a

contact is loaded with a rigid sphere conformity is obtained if the deforming surface is soft enough. In this case, the stresses decrease and the distribution relaxes.

- Recalling that the shakedown pressures based on the derivations presented in chapter 2 takes into consideration only the residual stresses and a smooth sphere-flat contact, the shakedown intervals calculated by this assumption can still give a good estimation for rough surfaces as well, provided that conformity is achieved. Deviation is much greater when conformity is lower, as discussed in section 5.3.3.

- In contact of smooth surfaces, as the conformity increases the pressure distribution changes from a Hertzian-like distribution to a Kunert distribution [1], as seen in figure 5.5.

- Based on [6], it is shown that in rolling contacts the elastic steady state is more clear for longitudinal asperities than for the lateral asperities after a certain number of cycles, see figures 5.18 and 5.19.

- It is shown that in micro-contacts, ratchetting [7] may occur if the pressures involved are much higher than the shakedown pressures, see figure 5.30. Asperity persistence [8] is seen in the initial cycles for such contacts. In such a case, it is observed that asperities are not fully flattened.

- The calculated pressure distribution is very sensitive to the “outliers” and other artifacts on a measured surface. These artifacts can cause pressure spikes of high magnitude that may introduce artificially high local stresses close to the surface.

References

[1] A. Kapoor and K.L. Johnson, Effect of changes in contact geometry on shakedown of surfaces in rolling/sliding contact, Int. J. Mech. Sci. 34 (1992), pp. 223-239.
[2] D. Tabor, The Hardness of Metals, Oxford University Press, Oxford, 1951.
[3] R.S. Sayles, Basic principles of rough surface contact analysis using numerical methods, Tribology International 29 (1996), pp. 639-650.
[4] L. Chang and Y. Gao, A simple numerical method for contact analysis of rough surfaces, Journal of Tribology 121 (1999), pp. 425-432.
[5] A.E.H. Love, The stress produced in a semi-infinite solid by pressure on part of the boundary, Philosophical Transactions of the Royal Society of London, Series A, 228 (1929), pp. 377-420.
[6] K.L. Johnson and H.R. Shercliff, Shakedown of two-dimensional asperities in sliding contact, Int. J. Mech. Sci. 34 (1992), pp. 375-394.
[7] A. Kapoor, K.L. Johnson and J.A. Williams, A model for the mild ratchetting wear of metals, Wear 200 (1996), pp. 38-44.
[8] J.B.P. Williamson and R.T. Hunt, Asperity persistence and the real area of contact between rough surfaces, Proc. R. Soc. Lond. A. 327 (1972), pp. 147-157.

Chapter 6. Changes in the micro-geometry of sliding contacts

6.1. Introduction

Contrary to the free-rolling studies, sliding contacts are characterized by higher coefficients of friction. As a result, tangential components are introduced in the contact, while in rolling contacts they may be neglected. In the previous chapter rolling contacts were studied, in this chapter the changes in the micro-geometry of sliding contacts will be discussed by experimental results and the 3D B.E.M. introduced in chapter 4. By this model, it is possible to analyze the effects of the increased coefficient of friction on the elastic subsurface stress distribution.

In section 6.2, the sliding contact of a smooth rigid sphere and a deformable smooth flat surface will be discussed. Then in sections 6.3 and 6.4, the sliding contact of a smooth sphere against several rough surfaces will be presented.

The experimental conditions are as presented in table 6.1.

Table 6.1. Standard experimental conditions.

Number of cycles	50
Normal load	4 N
Sliding velocity	7 mm/s
Temperature	24 °C
Relative humidity	50 %
Lubrication	None

6.2. Sliding contact of a smooth sphere against a smooth disk

In this experiment, a smooth SiC sphere slides against a smooth EN1.2510 disk. The friction force is also measured in the wear experiment. The geometrical and material properties of the contacting surfaces are presented in table 6.2. Hardness measurements were performed with a Vickers type micro-indentation apparatus. The measured hardness of the disk surface was approximately 1.3 times higher at a depth of 2.5 μm than at a depth of 6 μm. As the maximum stresses are expected for this smooth disk in the subsurface below 2.5 μm, the value for the hardness at 6 μm will be used for the calculation of the pressure for initial yield and the limiting shakedown pressure.

The experimental conditions for the experiments presented in this chapter are given in table 6.1. These conditions are constant through all sliding contact experiments in this chapter. Similar to the rolling contact experiments discussed in chapter 5, the sliding contact experiments cover 50 cycles with an applied load of 4 N in all cases. For a Hertzian contact,

Table 6.2. Properties of contacting surfaces.

Material	EN1.2510 flat disk	SiC sphere
Radius (mm)	-	3.2
R_q (μm)	0.02	0.01
E (GPa)	210	430
v	0.3	0.17
H (GPa)	2.9 (z = 2.5 μm)	22
	2.3 (z = 6 μm)	
σ_y (GPa)	0.82	3.5 (tensile strength)
k (GPa)	0.47	-
p_0 (initial yield) (GPa)	1.31 (μ = 0.11)	-
p_0 (shakedown) (GPa)	1.96 (μ = 0.11)	-

Table 6.3. Hertzian contact properties.

Contact radius	40 μm
Contact approach	0.5 μm
Mean contact pressure (p_m)	0.8 GPa
Maximum contact pressure (p_0)	1.2 GPa

the contact radius, the approach of bodies and the mean contact pressure were calculated as 40 μm, 0.5 μm and 0.8 GPa respectively (Table 6.3). So the maximum contact pressure is close to the initial yield but lower than the shakedown pressure. So, shakedown is expected for the smooth case. The experiments were conducted at room temperature and a relative humidity of 50 %. The sliding velocity was 7 mm/s.

The surface before and after the first cycle is shown in figure 6.1. The groove formed is deeper (≈ 0.13 μm) than the roughness level (0.02 μm) and thus clearly visible. The coefficient of friction as presented in figure 6.2, is equal to 0.11 in the first cycle. During 50 cycles there is a steady increase in the coefficient of friction to a value of 0.2. For μ = 0.11 and from figure 2.10, the shakedown region is estimated as 1.31 GPa < p_0 <1.96 GPa, as follows from the initial yield pressure and the shakedown pressure.

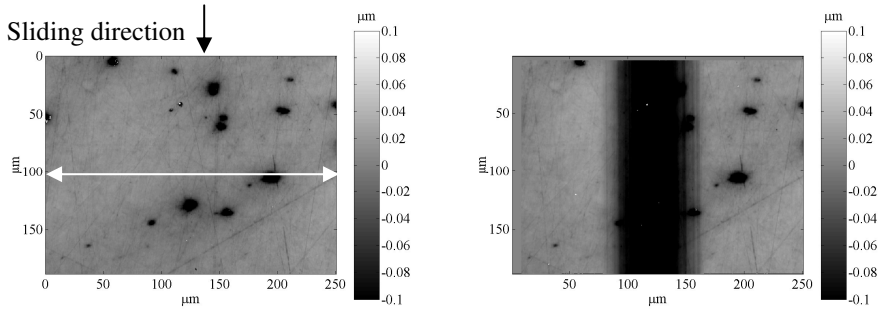

Figure 6.1. Disk surface before (left) and after the first cycle (right).

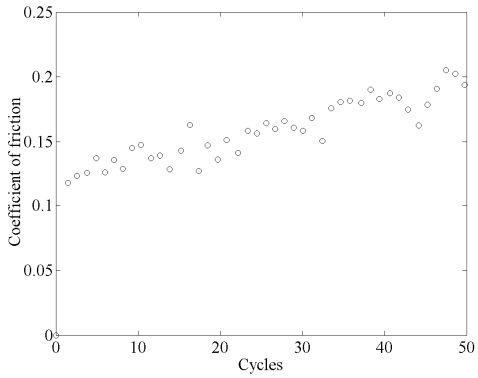

Figure 6.2. Coefficient of friction as a function of the number of cycles.

The change in the profile (as marked in Figure 6.1) for 50 cycles is presented in figure 6.3.a together with the changes in the profile of the rolling contact example with the same contacting material couple and experimental conditions in figure 6.3.b. Initial normal deformation in the sliding contact (≈ 0.13 μm) is larger than the deformation in the rolling contact experiment (≈ 0.1 μm) with the same disk surface. As follows from the figure, a steady state is achieved in 5 cycles in the sliding case. This is in contrast with the small scale cyclic deformation seen before shakedown in the rolling contact example. The final tracks at 50 cycles are about equal for the rolling and sliding contact situation.

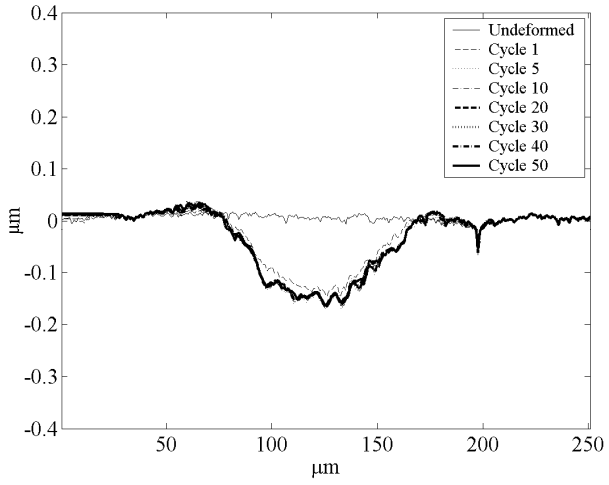

(a)

Figure 6.3. Profiles along the steel disk surface (R_q = 0.02 μm) during 50 cycles for (a) a sliding and (b) a rolling contact.

(continued)

(continued)

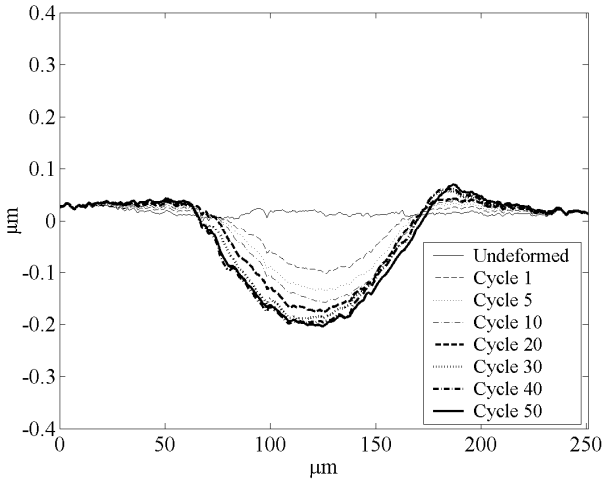

(b)

Figure 6.3. Profiles along the steel disk surface (R_q = 0.02 µm) during 50 cycles for (a) a sliding and (b) a rolling contact.

In order to understand these mechanisms better, the von Mises stress distributions for the first cycle of the sliding and rolling case will be used. The results are shown in figure 6.4.a for sliding and 6.4.b for the rolling contact case. According to the von Mises yield criteria, the yield is expected to be greater than 0.47 GPa. For both cases, the maximum stress is close to this value. The differences in the initial deformation seen in figure 6.3 can be explained by the fact that in the sliding contact the highly stressed kernel

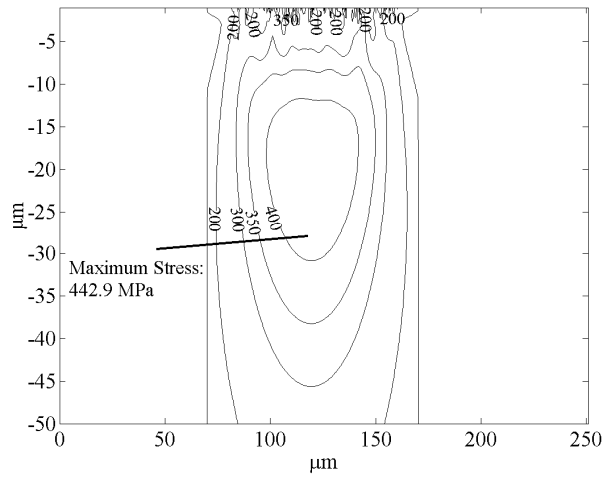

(a)

Figure 6.4. von Mises stresses for (a) sliding and (b) rolling contact of smooth surfaces after the first cycle.

(continued)

(continued)

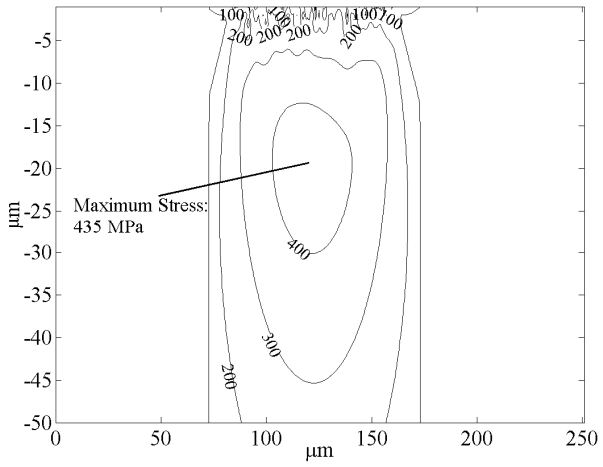

(b)

Figure 6.4. von Mises stresses for (a) sliding and (b) rolling contact of smooth surfaces after the first cycle.

covers a larger subsurface domain compared to that of the rolling contact, so deformation on a larger scale is expected in the sliding case. In this case, friction causes a slightly higher deformation.

The average pressure on the asperities in the first cycle was 0.86 GPa. This value does not change much for the 50th cycle where it is equal to 0.87 GPa. As the pressure is not decreased due to the conformity, the steady state can not be explained by a decrease in contact pressures for this sliding case. Strictly speaking, no yield would be expected at these pressures if the surface was perfectly smooth. However, given the variation (see table 6.2) in the measured hardness value on the higher subsurface stresses due to roughness and tangential load, some plasticity may occur. The stress situation can be characterized as very close to the initial yield. To study the situation further, the von Mises stresses for the last cycle are calculated.

The result is shown in figure 6.5 for the experimental condition (μ = 0.2) and an ideal condition where there is no tangential component (or μ = 0). Because of the increased coefficient of friction (μ = 0.2) and changes in the micro-geometry, the stress distribution that was close to the ideal Hertzian case of contacting smooth surfaces (see figure 6.4) changes after 50 cycles. The most important change is that the high stress zone comes close to the surface. In the subsurface, stresses are low and compared to the zero friction case, stress kernels are more “separated” from each other.

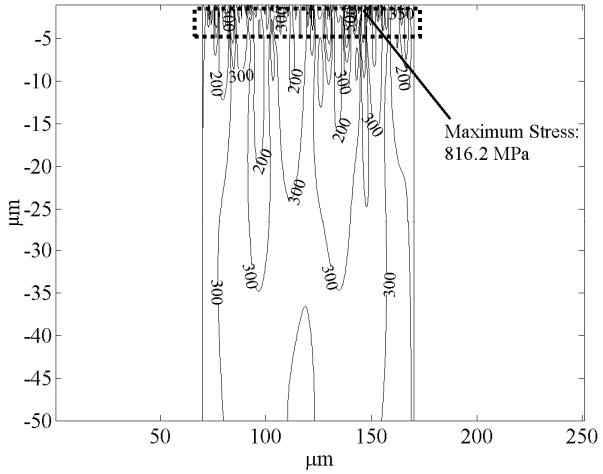

(a)

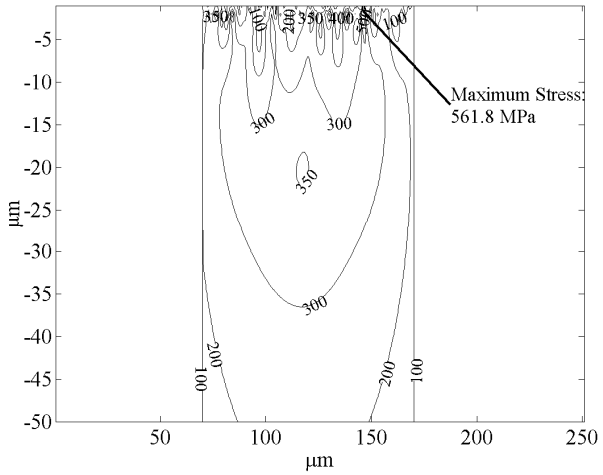

(b)

Figure 6.5. von Mises stresses beneath the contact for the 50th cycle. The coefficient of friction is 0.2 in (a) and 0 in (b).

The high stress region near the surface as marked in figure 6.5 is enlarged in figure 6.6. It is seen that the stresses exceeding 0.47 GPa are distributed down to a depth of approximately 5 µm. There are individual stress fields which do not have any connection to the surface. Even when the coefficient of friction is 0.2, for most of the time the stresses are lower than the yield criterion as can be seen from figure 6.6.a, except for a few points. If the

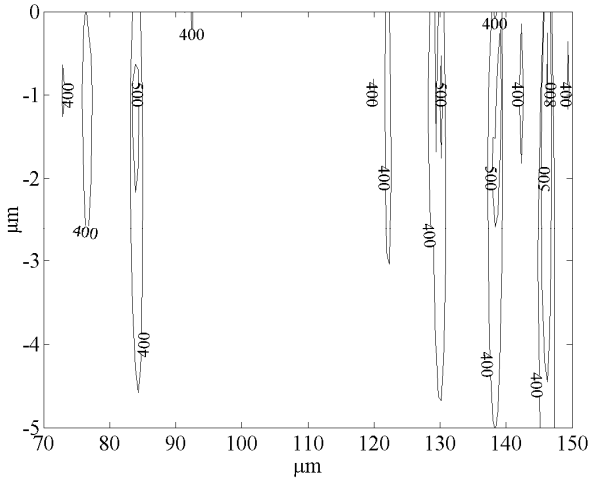

(a)

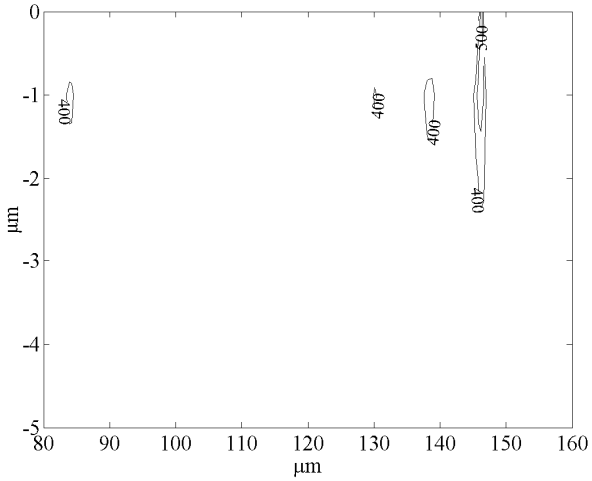

(b)

Figure 6.6. (a) von Mises stresses (μ = 0.2) very close to the surface for the 50th cycle, (b) same region if μ = 0.

coefficient of friction is assumed to be equal to zero (see figure 6.6.b), then the stresses decrease even further below the yield criteria at almost every point of the contact. This shows that the friction force gives rise to higher stresses close to the surface. However, this increase is not large if the coefficient of friction is low. Smooth sliding with low friction is similar to the rolling contact situation, only based on the calculated subsurface von Mises stress distributions. It is also seen that the deformation behavior is very similar to the rolling case.

In this section, the sliding contact of smooth surfaces was discussed. In the next two sections the focus will be on the sliding contact of rough surfaces.

6.3. Sliding contact of rough surfaces-I

The first example is a sliding contact of a smooth SiC sphere (R_q = 0.01 μm) and a rough EN1.2510 disk (R_q = 0.78 μm). The geometric and material properties of the contacting couple are listed in table 6.4. The experimental conditions are again as given in table 6.1. The hardness measurement was now conducted at lower loads, i.e. closer to the surface at a depth of 2.5 μm, where the high stress regions are expected to be.

Table 6.4. Properties of contacting surfaces.

Material	EN1.2510 flat disk	SiC sphere
Radius (mm)	-	3.2
R_q (μm)	0.78	0.01
E (GPa)	210	430
v	0.3	0.17
H (GPa)	4 (z = 2.5 μm)	22
σ_y (GPa)	1.43	3.5 (tensile strength)
k (GPa)	0.83	-
p_0 (initial yield)	2.3 (μ = 0.12)	-
p_0 (shakedown)	3.3 (μ = 0.12)	-

The measured surface topography before and after the first cycle is seen in figure 6.7. The measured coefficient of friction in the first cycle was 0.12 as seen in figure 6.8. In the initial cycles there is an increase in the friction signal, and in the 10th cycle this value rises to 0.14. At approximately the 35th cycle the coefficient of friction becomes constant at 0.35. From figure 2.10, at μ = 0.12 shakedown is expected between 2.3 GPa < p_0 < 3.3 GPa. In 50 cycles, the changes in the profile as marked in figure 6.7 can be seen in figure 6.9.

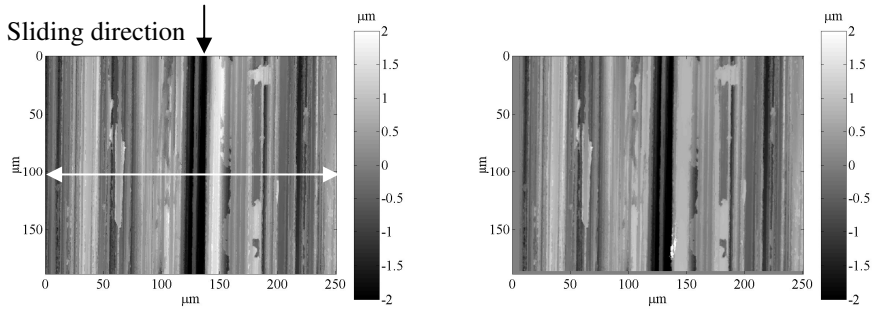

Figure 6.7. Disk surface before (left) and after the first cycle (right).

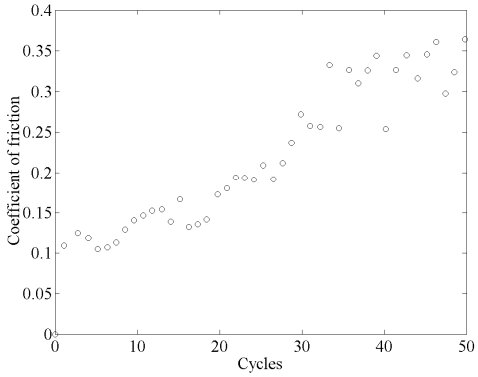

Figure 6.8. Coefficient of friction as a function of number of cycles.

In the first 10 cycles, the high asperity at the center deforms in a cyclic manner. Note that deformation per cycle decreases gradually and there is little difference in the surface micro-geometry between the 5th and 10th cycles. After the 10th cycle there are severe changes on the surface. Wear mechanisms such as adhesion and abrasion, for example due to entrapped abrasive particles ploughing through the softer surface, could be responsible for such severe wear and high friction.

Initially, the elastic average pressure on the asperities was calculated as 26.9 GPa. In the 10th cycle it drops to 2.2 GPa as the high sloped asperity at the center is flattened and neighboring asperities are also involved in the contact carrying the load. The pressure distributions after the 10th cycle are not comparable with the initial cycles, as the roughness details are removed

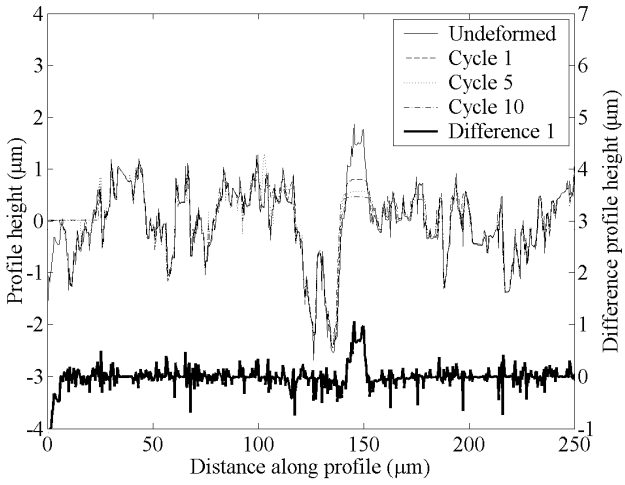

(a)

Figure 6.9. Profiles along the steel disk surface (R_q = 0.78 μm) for the (a) initial 10 cycles and (b) final 40 cycles.

(Continued)

(Continued)

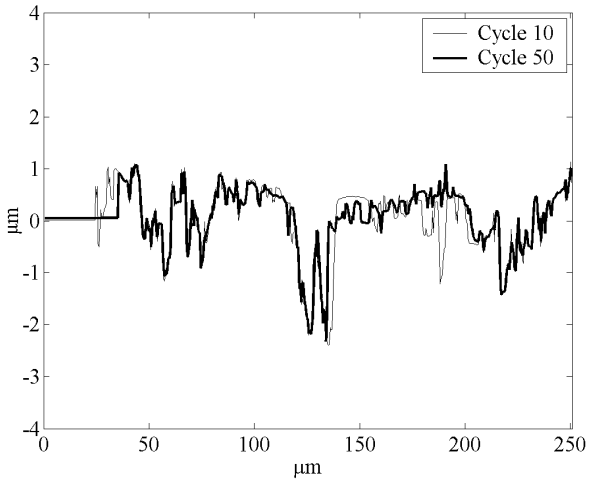

(b)

Figure 6.9. Profiles along the steel disk surface (R_q = 0.78 µm) for the (a) initial 10 cycles and (b) final 40 cycles.

and wear mechanisms (adhesion and abrasion) are involved, see figure 6.9.b for a comparison between the 10th and the 50th cycle. The subsurface von Mises stresses in the 1st and the 10th cycles are shown in figure 6.10. In the first cycle stress concentration on the surface is found at the contacting asperity in the center. In the 10th cycle the high stress concentration is still close to the surface. The maximum stress was calculated as approximately 4.8 GPa for the case after 10 cycles.

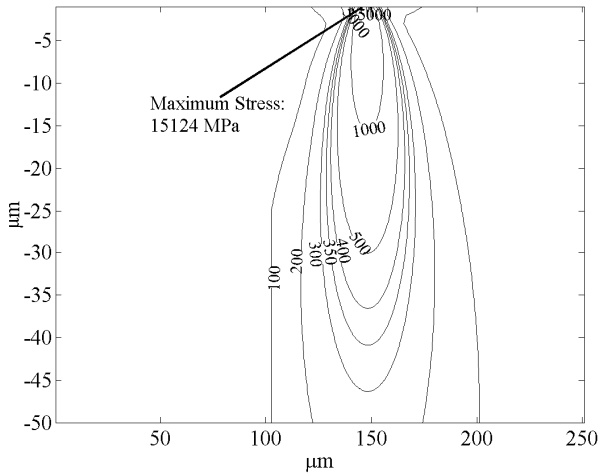

(a)

Figure 6.10. von Mises stresses beneath the contact for (a) the initial and (b) the 10th cycles. The coefficient of friction is 0.12 at (a) and 0.14 at (b).

(Continued)

(Continued)

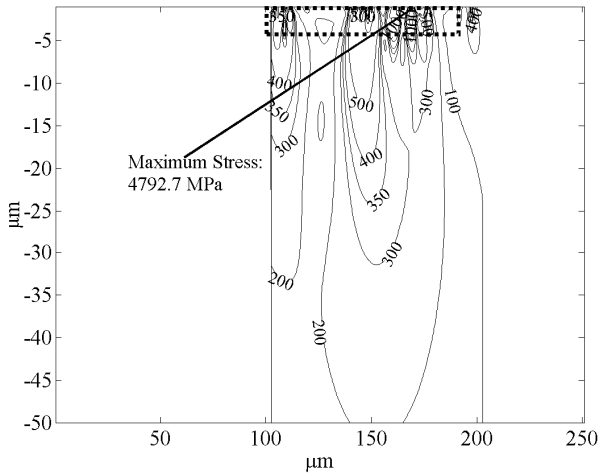

(b)

Figure 6.10. von Mises stresses beneath the contact for (a) the initial and (b) the 10th cycle. The coefficient of friction is 0.12 at (a) and 0.14 at (b).

Figure 6.11 gives detailed information on this high stress concentration region. Note that the yield is expected at 0.83 GPa. It is seen that stresses above this value are positioned closer to the surface at a depth of approximately 3 µm. There is not much change in the distribution if zero friction is assumed (see figure 6.11.b) as this time the normal stresses caused by the higher contact pressures, compared to the contact of smooth surfaces seen in section 6.2, are the more dominant components of the von Mises stresses. Also in this case a high stress zone is concentrated close to the surface as was the case in the previous section.

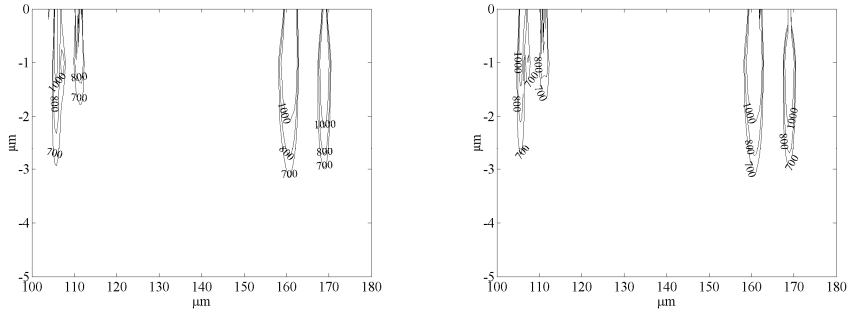

(a) (b)

Figure 6.11. (a) von Mises stresses (μ = 0.14) very close to the surface for the 10th cycle, zoomed in from the marked region in figure 6.10.b. (b) The von Mises stresses when μ = 0.

As a summary,

- For the rolling and sliding contact of rough surfaces, in the initial cycles a highly stressed and finally hardened layer is formed close to the surface. This causes a steady state in the contact.

- It is observed that the deformation mode in sliding contact is not primarily due to the tangential components but instead due to normal stress components, when the friction force is low. This is shown in figures 6.11.a and 6.11.b where distributions are very close for $\mu = 0.14$ and $\mu = 0$.

- Surface changes are much more severe when the coefficient of friction rises above 0.3. In such a state, changes of the surface are seen at every cycle, and the steady state is lost.

6.4. Sliding contact of rough surfaces-II

In the third experiment, a disk specimen with lower R_q (0.25 μm) is used. The properties of the contacting pair are given in table 6.5. The hardness of the disk is the same as in section 6.3. The experimental conditions are as listed in table 6.1.

Table 6.5. Properties of contacting surfaces.

Material	EN1.2510 flat disk	SiC sphere
Radius (mm)	-	3.2
R_q (μm)	0.25	0.01
E (GPa)	210	430
v	0.3	0.17
H (GPa)	4 (z = 2.5 μm)	22
σ_y (GPa)	1.43	3.5 (tensile strength)
k (GPa)	0.83	-
p_0 (initial yield)	2.3	-
p_0 (shakedown)	3.2	-

The surface before and after the first cycle is shown in figure 6.12. In 50 cycles the coefficient of friction increases continuously. Initially it is very low (≈ 0.15). At the 10^{th} cycle the coefficient of friction is 0.2 and after 25^{th} cycle it stabilizes at a value of 0.38, see figure 6.13. With the initial coefficient of friction, the interval for shakedown of a smooth ball against a smooth disk is calculated as 2.3 GPa < p_0 < 3.2 GPa. Compared to the previous example, initially the number of asperities in contact is higher as shown in figure 6.14. In 10 cycles, there is a gradually decreasing plastic deformation similar to the previous case.

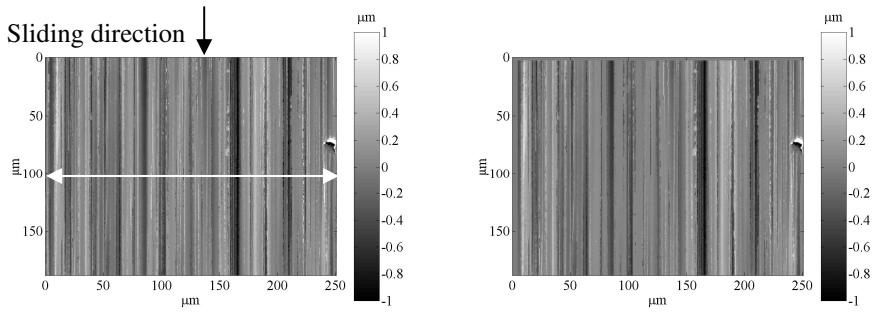

Figure 6.12. Disk surface before (left) and after the first cycle (right).

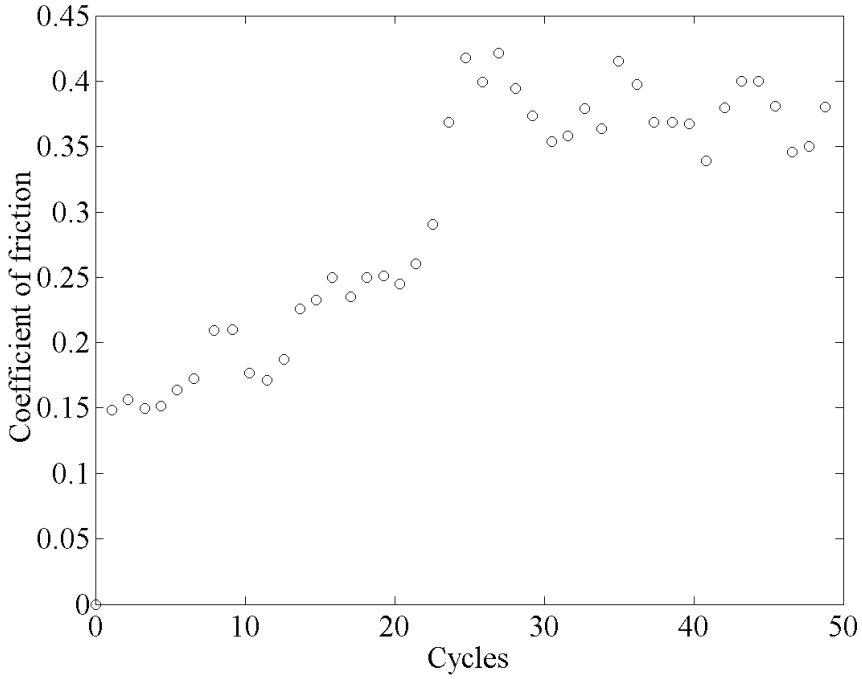

Figure 6.13. Coefficient of friction as a function of the number of cycles.

After the 10^{th} cycle, severe wear is seen based on the mentioned mechanisms, see figure 6.14.b. For comparison purposes, the equivalent rolling contact example that was presented in chapter 5, see figure 5.16, is also shown in figure 6.14.c. Note that the properties of the contact are the same except that friction is involved for the sliding case. It is seen that, for the sliding contact, deformation is concentrated at the surface whereas the rolling contact involves a combination of asperity and bulk deformations. Initially, the average pressure on the asperities is 14.3 GPa. Within 10 cycles this value is gradually reduced to 1.49 GPa with increased conformity. This value is lower than the calculated mean shakedown pressure for a smooth case, which is equal to 2.1 GPa.

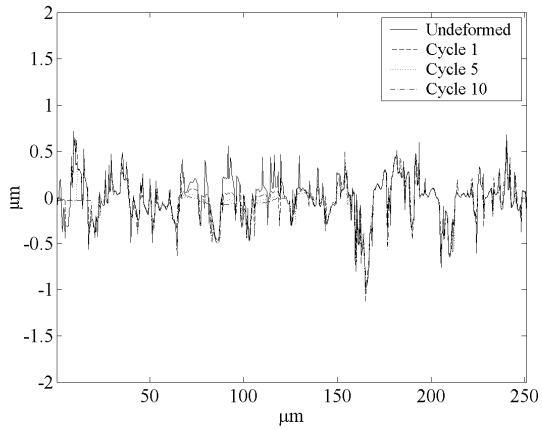

(a)

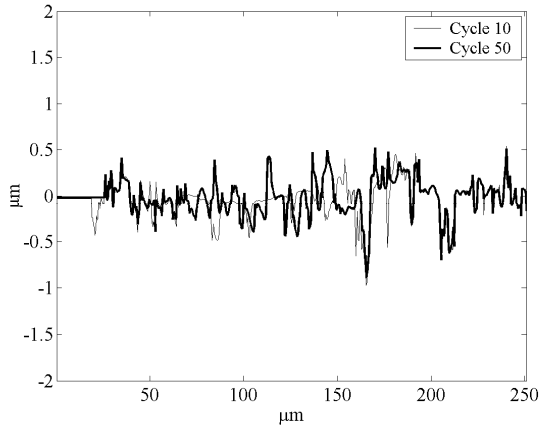

(b)

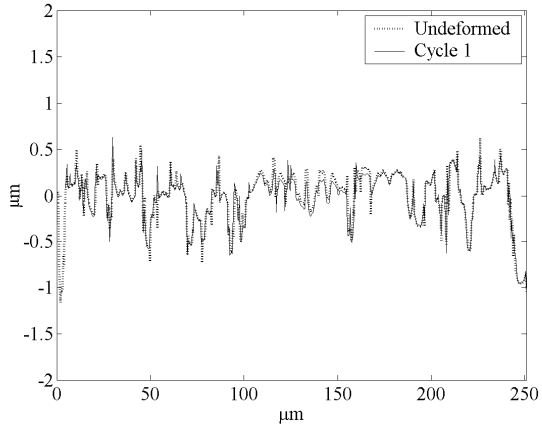

(c)

Figure 6.14. Profiles along the steel disk surface (R_q = 0.25 µm) for the initial 10 cycles (a) and final 40 (b) cycles. (c) are the profiles across the wear track for a rolling contact with same properties in the initial cycle.

The von Mises stress distribution in the contact for the 1st and the 10th cycles are shown in figure 6.15. In 10 cycles, the stresses reduce and the stress kernel becomes wider.

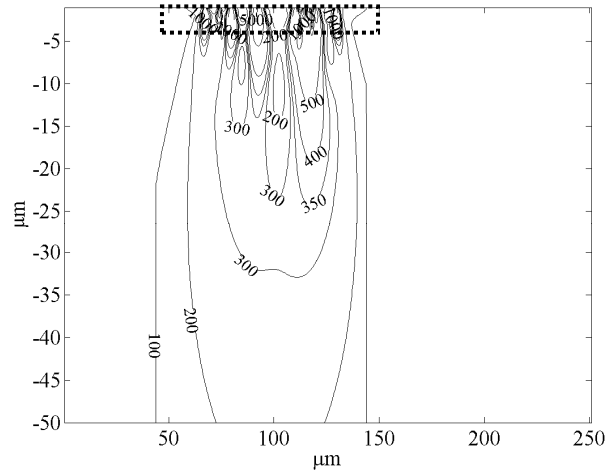

(a)

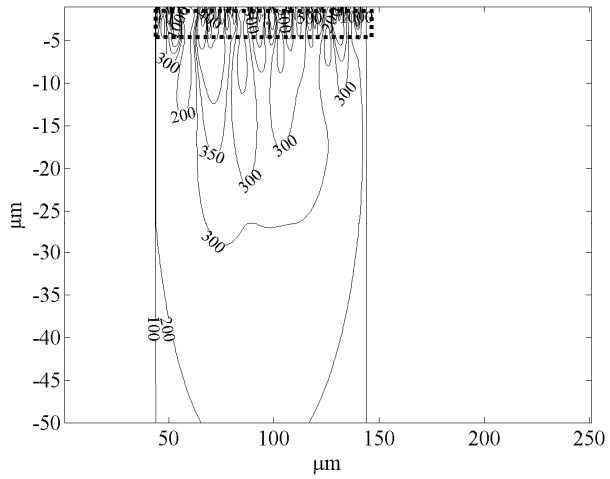

(b)

Figure 6.15. von Mises stresses beneath the contact for (a) the initial cycle and (b) the 10th cycle. The coefficient of friction is 0.15 in (a) and 0.2 in (b).

In figure 6.16, the region marked in figure 6.15.a is plotted on a larger scale for three cases. These are a) the sliding contact in the initial cycle for μ = 0.15, b) μ = 0 and c) the corresponding rolling contact case that was presented in figure 5.15 in the previous chapter. Initially very high contact

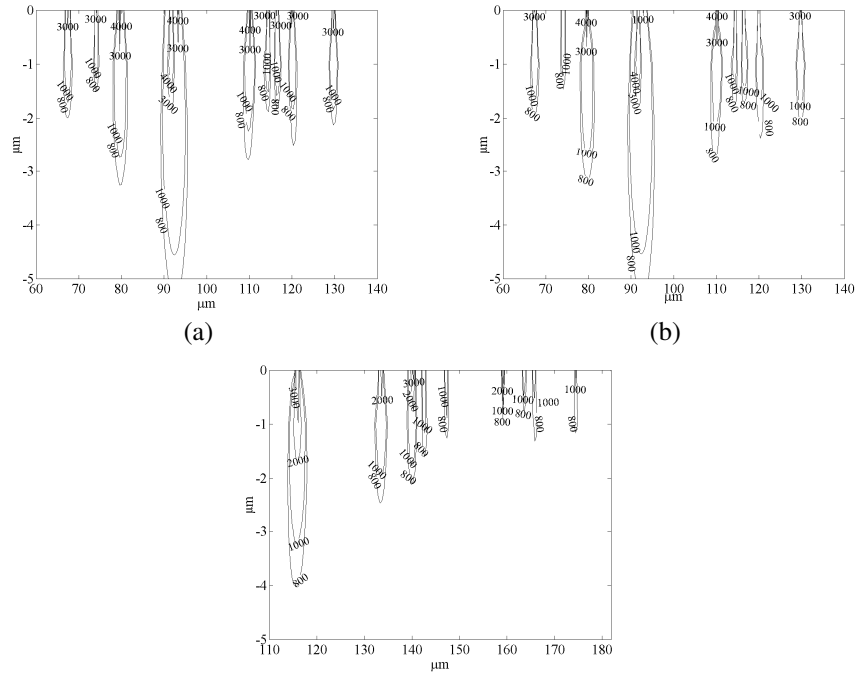

Figure 6.16. von Mises stresses for (a) $\mu = 0.15$, (b) $\mu = 0$ and (c) in rolling contact for the initial situation (Figure 5.15).

pressures causes stress concentration close to the surface. For a few points, the stresses are slightly higher near the contact for sliding with the $\mu = 0.15$ case in figure 6.16.a compared to the frictionless contact calculation in figure 6.16.b but this difference is not too large. For these two cases the subsurface stress distributions are similar again because of the low friction in the initial cycles as was the case in the previous sliding contact example. The calculation performed with the rolling contact surface (a profile can be seen in Figure 6.14.c) is given in figure 6.16.c. In this calculation the coefficient of friction is again taken as zero. It is seen that stresses are comparably less concentrated and lower in magnitude compared to the sliding contact situation with $\mu = 0.15$, but again this difference is not very large.

Note that the deformation for the sliding case was on the asperity level (as seen in figure 6.14.a) and as a combination of a small scale asperity deformation and bulk deformation in the rolling contact case (as seen in figure 6.14.c). It is clear that the von Mises stress distributions discussed in the previous paragraph for the sliding and rolling contact situations are not sufficient to explain the two different deformation modes. This is probably because the changes in the micro-geometry in sliding cannot be explained by plasticity caused by static loading only. Wear mechanisms are probably more dominant. Therefore, it is difficult to predict changes in the micro-

geometry in the sliding contact case by using the 3D B.E.M. in a normally loaded contact analysis in which friction is involved. However, for smooth surfaces such an approach is a better approximation as asperity interaction (i.e. crushing of asperities, abrasion etc.) is reduced in the case of a smooth surface.

In figure 6.17.a, the region marked with a dashed rectangle of the 10th cycle in figure 6.15.b is plotted. As in the first cycle, the difference between the stress distributions for the sliding situations with $\mu = 0$ and $\mu = 0.2$ is again almost insignificant (Figure 6.17.a and 6.17.c). It is also seen that the highly stressed region is close to the surface and extends to a depth of approximately 2 to 3 μm. For a corresponding rolling contact (figure 5.16) with the same properties, the stress distribution is seen in figure 6.17.b. A highly stressed region that withstands deformation starts from the surface and extends to a depth approximately 3.5 μm. So a strain hardened layer characterized by a higher yield strength (σ_y) has to protect the surface to keep the stresses elastic.

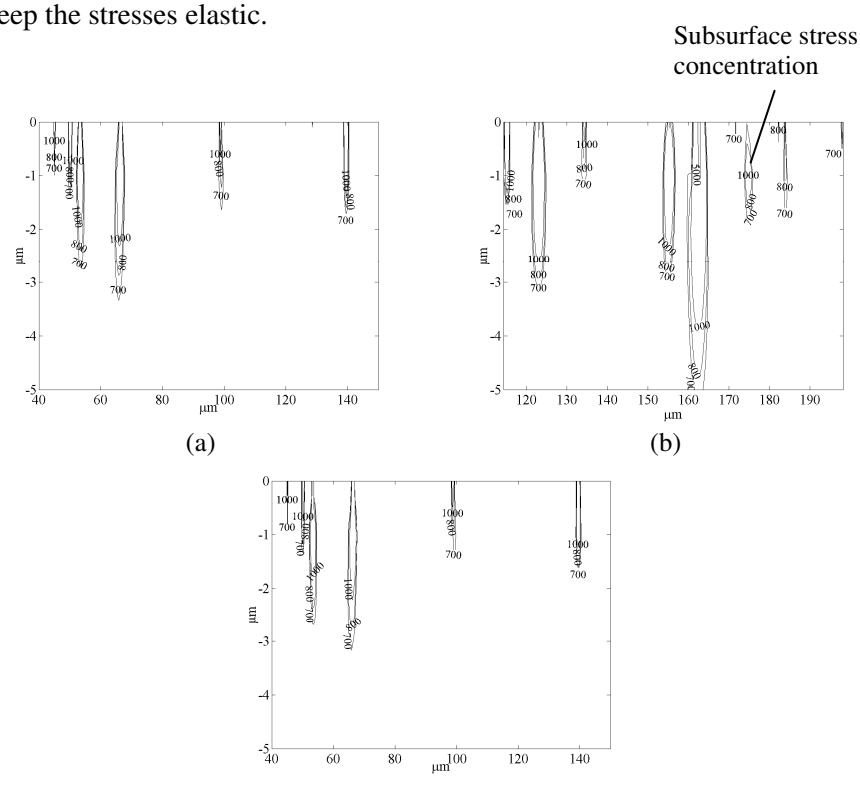

Figure 6.17. (a) von Mises stresses ($\mu = 0.2$) very close to the surface for the 10th cycle, zoomed in from the marked region in figure 6.15.b. (b) Stresses correspond to the rolling contact cycle 50 as represented in figure 5.16. (c) the sliding contact in (a) if $\mu = 0$.

6.5. Summary and conclusions

- For low roughness values (see section 6.2) at the initial cycles, the subsurface stresses are concentrated far below the contact. Such a stress kernel is similar to the one for a perfectly smooth sphere-flat contact except that roughness introduces small scale stress fields close to the surface. Hence, the shakedown is very close to the rolling case.

- Both in sliding and rolling contacts as the contact is close to a steady state there is a strained layer formation close to the surface, which increases the load that can be carried elastically.

- Compared to the rolling contacts, dry sliding contacts involve higher friction in the contact interface. The friction component is high after certain number of cycles, and in such a case topography is changing significantly, see figures 6.9.b and 6.14.b.

- It is observed that initially the friction coefficient is low for the sliding contacts for both smooth and rough surfaces, see Figures 6.2, 6.8 and 6.13. It is first assumed that a sliding contact can be modeled by normally loading the surface including the tangential stress components. It is shown that during the initial cycles when the coefficient of friction is low the stress kernels and the magnitudes of the stresses are not very different for low coefficients of friction, i.e. the distributions for $\mu = 0.15$ and $\mu = 0$ in figures 6.16.a and 6.16.b respectively. One reason is that the effect of roughness induced normal stress components is much higher than the tangential stresses. Comparing the sliding and rolling contact experiments for the same disk surface where respectively asperity and bulk deformations were seen, it is concluded that such an assumption is not sufficient for understanding the asperity deformation seen in a sliding contact as wear mechanisms such as interaction and crushing of asperities probably have a more dominant effect on the changes in the micro-geometry in sliding contacts. So the surface deformation in sliding contacts cannot be predicted at higher roughness.

References

[1] A. Kapoor and K.L. Johnson, Effect of changes in contact geometry on shakedown of surfaces in rolling/sliding contact, Int. J. Mech. Sci. 34 (1992), pp. 223-239.
[2] D. Tabor, The Hardness of Metals, Oxford University Press, Oxford, 1951.
[3] R.S. Sayles, Basic principles of rough surface contact analysis using numerical methods, Tribology International 29 (1996), pp. 639-650.
[4] L. Chang and Y. Gao, A simple numerical method for contact analysis of rough surfaces, Journal of Tribology 121 (1999), pp. 425-432.
[5] A.E.H. Love, The stress produced in a semi-infinite solid by pressure on part of the boundary, Philosophical Transactions of the Royal Society of London, Series A, 228 (1929), pp. 377-420.
[6] K.L. Johnson and H.R. Shercliff, Shakedown of two-dimensional asperities in sliding contact, Int. J. Mech. Sci. 34 (1992), pp. 375-394.
[7] A. Kapoor, K.L. Johnson and J.A. Williams, A model for the mild ratchetting wear of metals, Wear 200 (1996), pp. 38-44.

Chapter 7. Models and experiments

In chapter 4, a model for normally loaded elastic and elastic-plastic contact of rough surfaces was introduced. Later in chapters 5 and 6 experiments for the deformation and wear in rolling and sliding cyclic loaded contacts were studied. These experiments were performed by the semi-online wear measurement system introduced in chapter 3. In the previous chapter, it was shown that the subsurface stresses, where the contact was normally loaded and friction induced tangential stresses were involved, were not sufficient to explain the deformation in a sliding contact during the initial cycles. The reason for this is that the dynamic effects (i.e. ploughing and crushing of asperities in interaction) and wear are the primary mechanisms for the changes in the micro-geometry. Therefore in this section sliding contact experiments will not be studied. The rolling contact experiments which were presented in chapter 5 have shown that deformation of a rough surface in rolling contact with a smooth surface can be in three different forms. These are:

- Asperity deformation where only the asperities are flattened and there is no bulk deformation;
- Bulk deformation where asperities are pushed down, without much change in their shape;
- A combination of asperity and bulk deformation.

The occurrence of the deformation mode could be explained by the subsurface stress field. In this chapter, these experimental results introduced in chapter 5 are combined with the elastic-plastic contact algorithm described in chapter 4.

It was shown in chapter 5 that when the roughness is low, the von Mises stress distribution and its magnitude beneath the contact is very similar to the case where ideally smooth surfaces are in contact, as was presented in figure 5.4. Such a case of relatively smooth surfaces is characterized by bulk deformation. At first, bulk deformation that is seen in surfaces with low roughness will be studied in section 7.1 by comparison of the elasto-plastic contact model of Kogut and Etsion [1] and the experimental results. Later in section 7.2, elastic-plastic normally loaded contact results by 3D B.E.M. will be compared with the experimental solutions for surfaces with comparably high roughness. In section 7.3, an approach for modeling a rolling contact by multiple indentation of the deformation track will be introduced. Finally, in section 7.4, a study of the deformation zones under a contact will be presented. In this final analysis, artificial surfaces with a Gaussian distribution and with different roughness, autocorrelation length and material properties will be used and compared with the experimental results. Note that in all the experiments a rough surface is in contact with a

smooth SiC sphere. The properties of the deforming surfaces are presented in table 7.1.

Table 7.1. Properties of the deforming surfaces

	Properties of the deforming surfaces					
Experiment	R_q (μm)	H (GPa)	E (GPa)	v	σ_y (GPa)	k (GPa)
Experiment 1 (section 5.2)	0.03	2.3	210	0.3	0.82	0.47
Experiment 2 (section 5.3)	0.3	4	210	0.3	1.43	0.83
Experiment 3 (section 5.3.2)	0.66	4	210	0.3	1.43	0.83
Experiment 4 (section 5.3.1)	0.66	4	210	0.3	1.43	0.83
Experiment 5 (section 5.3.3)	0.66	8.3	210	0.3	2.96	1.71
Experiment 6 (section 5.3.3)	0.28	8.3	210	0.3	2.96	1.71
Experiment 7 (section 5.3.4)	0.85	0.28	70	0.33	0.1	0.06

7.1. Bulk deformation

Elastic-plastic contact analysis of a sphere and a rigid flat surface was studied by Kogut and Etsion in [1]. In their model, the authors used a deformable sphere and a rigid flat surface where the sphere is normally loaded by the rigid flat and unloading is not involved. The material model used by the authors is based on an elastic-perfectly plastic assumption as presented in figure 4.7. In chapter 4, calculations with the same contact situation were made and the relation between the dimensionless interference and dimensionless mean pressure was presented in figure 4.9. In [1], the relations between dimensionless contact area, dimensionless load and dimensionless interference were also presented. By curve fitting, based on their finite element calculations, the authors obtained the following equations:

$$\omega_c = \left(\frac{\pi KH}{2E}\right)^2 R \tag{7.1}$$

For $1 \le \omega / \omega_c \le 6$,

$$\left(\frac{F}{F_c}\right) = 1.03\left(\frac{\omega}{\omega_c}\right)^{1.425} \tag{7.2}$$

$$\left(\frac{A}{A_c}\right) = 0.93\left(\frac{\omega}{\omega_c}\right)^{1.136} \tag{7.3}$$

For $6 \le \omega / \omega_c \le 110$,

$$\left(\frac{F}{F_c}\right) = 1.40\left(\frac{\omega}{\omega_c}\right)^{1.263} \tag{7.4}$$

$$\left(\frac{A}{A_c}\right) = 0.94\left(\frac{\omega}{\omega_c}\right)^{1.146} \tag{7.5}$$

where ω_c is the critical interference defined as the interference at the end of elastic regime, ω is the interference of the contacting bodies, R is the radius of the deformable sphere, K is the hardness coefficient defined by $K = 0.454 + 0.41\nu$, F is the applied load, F_c is the load at the critical interference ω_c, A is the contact area and A_c is the critical contact area again defined at ω_c, H is the hardness and E is the elastic modulus.

In section 5.2, an experiment presenting the rolling contact of a smooth sphere against a smooth disk was introduced. The change on the surface can be seen through the profile presented in figure 7.1.a where it is clear that the deformation is in the form of bulk deformation because the roughness details in the track remain. The idea is that the loaded track in the case of bulk deformation can be simulated by subtraction of a groove with contact radius a, according to equation 7.3. The average contact pressure on the contacting asperities calculated initially by the 3D B.E.M. was 0.84 GPa. This value is lower than the hardness of the disk which is 2.3 GPa and thus the contact situation is elastic for the 3D B.E.M. Therefore, for comparison with the model introduced by Kogut and Etsion [1], cycle 1 shown in figure 7.1.a was used. At first, using the 3D B.E.M, this deformed profile was elastically loaded by the same load used in the experiments (4 N). In this way, the nominal contact area was calculated in the loaded situation, and the rolling contact experiment that was presented in section 5.3.1 was analyzed. For this surface with a roughness of 0.3 μm and hardness of 4 GPa, bulk deformation takes place as seen in figure 7.1.b.

The calculated nominal contact areas for the two experimental results in the loaded situation are compared to those of Kogut and Etsion ($\omega / \omega_c \approx 1.5$). The results are presented in figure 7.2. The contact area for the contact of a smooth deformable sphere and the rigid-flat calculated by using equations 7.1 to 7.3 reads 0.004 mm^2. For experiment 1 where the roughness is 0.03 μm this value is 0.006 mm^2 and for experiment 2, where the roughness is 0.3 μm, the nominal contact area is ten times the one estimated by the model in [1] as 0.04 mm^2. It is seen that the deviation from the model in [1] increases with the increasing roughness. This means that, for a surface with low roughness, bulk deformation and the resulting contact shape could be approximated by subtraction of a groove from the surface with contact radius a from equation 7.3. However, when the roughness is high, the deviation from the real ball-on-flat approximation increases. Although the

contact is in the elasto-plastic regime, the trend of increase represented by a curve fit through the three points shows resemblance with the elastic calculations of Greenwood and Tripp that was presented in [2]. Their calculations were for the contact of two surfaces with similar elastic modulus and geometry. It is seen from the figure that also when the contact is elasto-plastic, the nominal contact area increases with the increasing roughness.

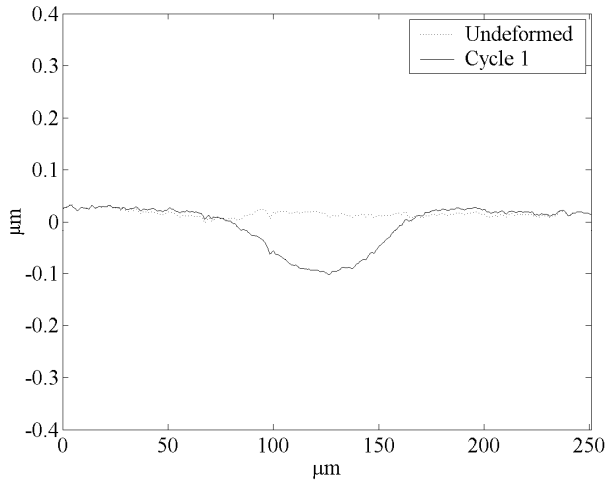

(a)

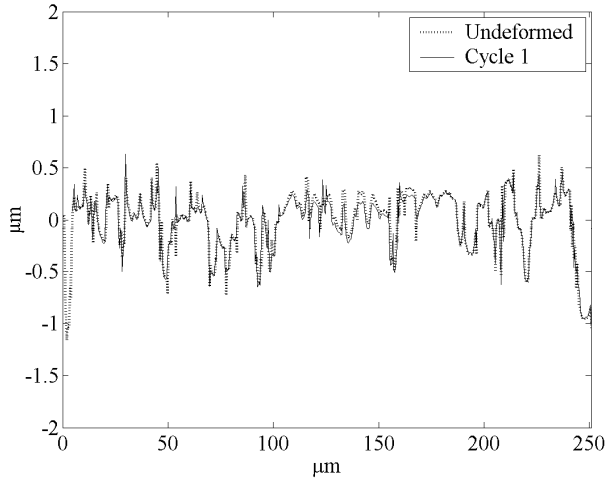

(b)

Figure 7.1. Measured profiles along (a) the smooth steel disk (R_q = 0.03 µm, H = 2.3 GPa) and (b) the steel disk (R_q = 0.3 µm, H = 4 GPa) surface for a single cycle.

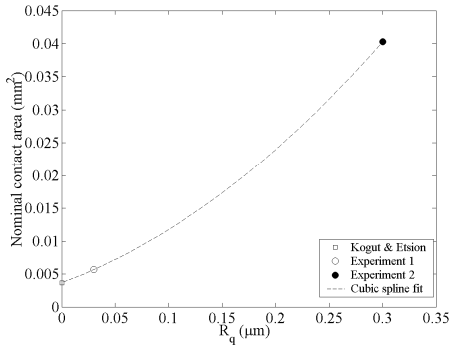

Figure 7.2. The nominal contact area versus the roughness. The properties of the surfaces in experiments 1 and 2 can be found in table 7.1.

In this section, bulk deformation in rough surfaces is studied with an elasto-plastic model [1]. On the other hand with 3D B.E.M. introduced in chapter 4, it is possible to model the plastic asperity deformation seen in rough surfaces and bulk deformation cannot be modeled, see for instance figure 7.3. In the next section, normally loaded contact of rough surfaces will be studied with the use of the 3D B.E.M.

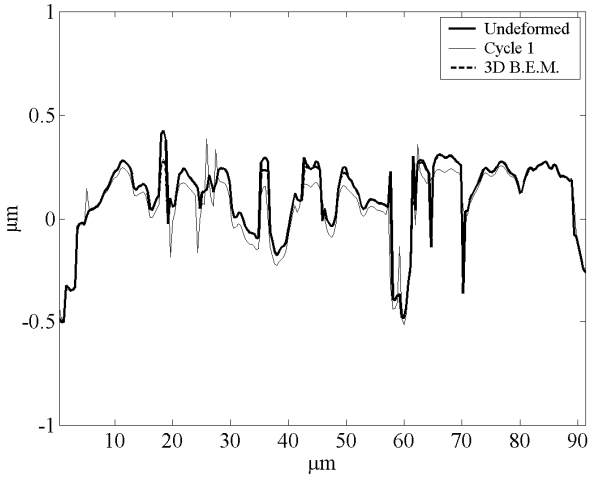

Figure 7.3. Profiles along the steel disk (R_q = 0.3 μm, H = 4 GPa) for a single cycle experiment and a numerical solution by 3D B.E.M. This experimental result is the zoomed version of figure 7.1.b.

As a summary,

- Bulk deformation of surfaces cannot be modeled by the elastic-plastic contact algorithm that was presented in chapter 4 because this model describes surface deformation. However, if the roughness is very low, bulk deformation can be approximated. So, for a limiting case, bulk deformation can be approximated by

subtraction of a groove with a calculated radius from a measured surface micro-geometry.

- For rough surfaces, the calculated nominal contact areas deviate by a larger amount from the results obtained by such models and are not applicable for modeling bulk deformation. However, at high roughness, the deformation mode will switch to surface deformation.

7.2. Surface deformation

Plastic deformation of asperities in normally loaded contacts can be modeled by the elastic-plastic contact method that was described in chapter 4. In this section, numerical calculations will be compared with three rolling contact experiments that were presented earlier in chapter 5. These experiments will be denoted as experiments 3, 4 and 5 for simplicity. The EN1.2510 samples in experiments 3 and 4 have similar hardness (H = 4 GPa) and surface roughness (R_q = 0.66 μm). However, the SiC balls used in experiments 3 and 4 had radii of 5 mm and 3.2 mm respectively. In experiment 5, the hardness and the roughness of the hardened EN1.2510 disk are 8.3 GPa and 0.66 μm respectively. Note that in all the experiments an elastic steady state was obtained within 50 cycles. The experimental and numerically calculated deformed profiles across the deformation track are shown in figure 7.4. Note that in contrast to the experiments of the previous section, in all the three experiments, the deformation was at asperity level due to increased roughness of the surfaces. Secondly, in all the cases the numerically calculated normal deformations are within good agreement with the ones obtained by the experiments, but the pressures that can be carried by the surface are slightly lower than the measured hardness values. In experiments 3 and 5 presented in figures 7.4.a and 7.4.c respectively it is also seen that the deformation is not only in the normal direction, but the material flow also results in asperity enlargement to the sides.

As a summary,

- The results show that in three different rolling contact experiments where the deformation is at asperity level, the calculated normal deflections are in a fairly good agreement with the experimental results.

In this section, the rolling experiments were compared with the numerical method introduced where the contact is normally loaded. In the following section, instead of a single indentation of the surface, multiple indentations at different positions using 3D B.E.M. are performed for a simplified rolling contact simulation of a whole surface instead of the central profile only.

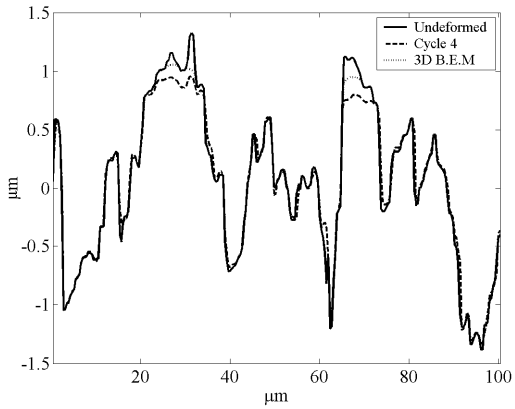

(a)

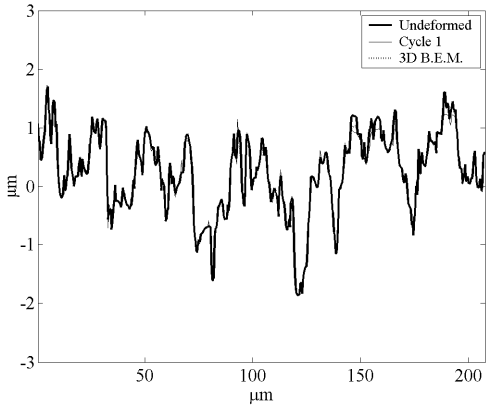

(b)

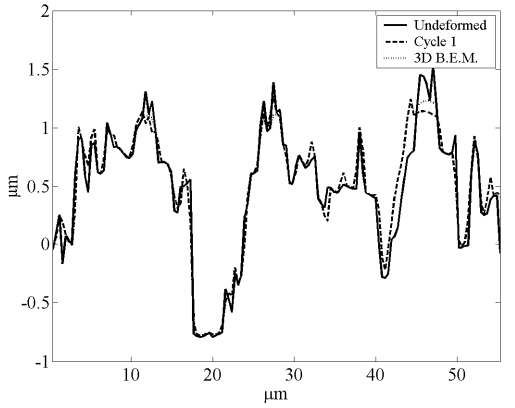

(c)

Figure 7.4. The deformations calculated by the 3D B.E.M. and as a result of (a) Experiment 3, (b) Experiment 4, and (c) Experiment 5. The rolling direction is normal to the page and towards the reader. For experiments 3 to 5 see table 7.1.

7.3. A rolling contact simulation

In the previous section it was shown that the elastic-plastic 3D B.E.M. where a single indentation takes place can be used as a fairly good approximation for the determination of surface deformation in a rolling contact. The compared profiles in the previous section were the central profiles under normal loading where the maximum deformation at a single indentation was expected. A better approximation of the track formed by a rolling contact can be made by multiple indentations along the rough surface. This is realized by:

Step 1: Normally loading the rough surface by a rigid smooth sphere and calculating the deformed surface.

Step 2: Re-positioning the sphere so that it is positioned one pixel size further.

Step 3: Normally loading the deformed rough surface which was the output of step 1.

Step 4: Returning to step 1 and continuing until the desired rolling distance is achieved.

The numerical calculations will be compared with experiment 3 that is presented in table 7.1 for the longitudinal and lateral shaped asperities. These experiments were presented in section 5.3.2. The roughness and the hardness of the surfaces were 0.66 μm and 4 GPa respectively. The longitudinal asperities before and after cycle 4 and the resulting surface after a numerical rolling simulation are presented in figure 7.5. The experimental and numerically calculated topographies after deformation are seen in figures 7.5.b and 7.5.c respectively. As expected, the profile at the center is exactly the same as the profile calculated by normal loading that was presented in 7.4.a. It is also seen that again the deformations provide a good approximation. For the lateral asperities (figure 7.6) it is observed that small scale roughness details are preserved in the experiment. This is due to a small scale bulk deformation, where micro-contacts are pushed down. On the other hand, in the simulated rolling simulation a similar conformity is obtained but the roughness details are completely flattened. As a summary,

- A simple numerical rolling simulation method is introduced. For this purpose, the 3D B.E.M. is used in multiple normal indentation cycles. The results show that a rolling contact can be simulated with

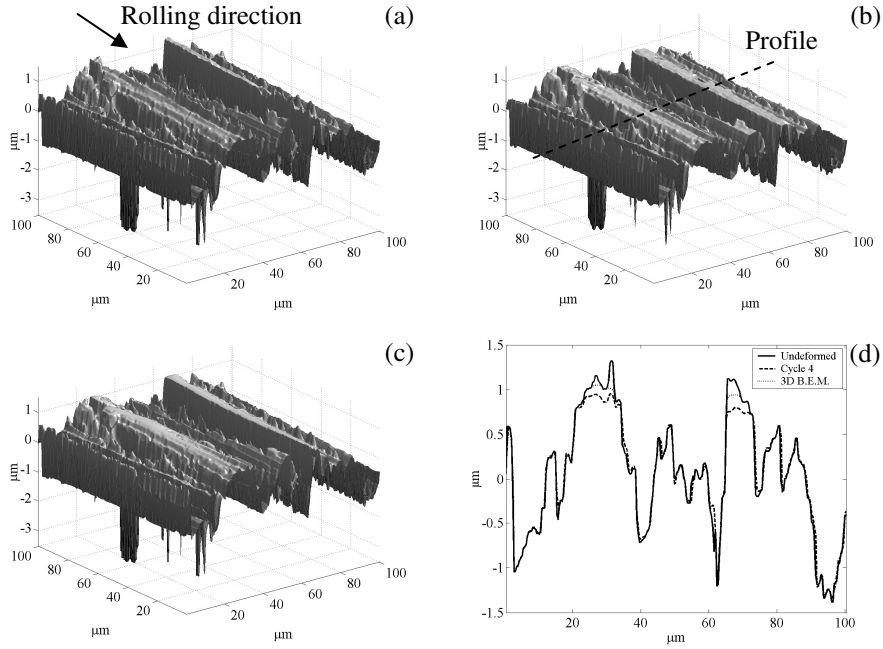

Figure 7.5. The longitudinal asperities in experiment 3, (a) initially, (b) after 4 cycles, (c) after rolling simulation with 3D B.E.M and (d) across the deformation track in marked profile in (b).

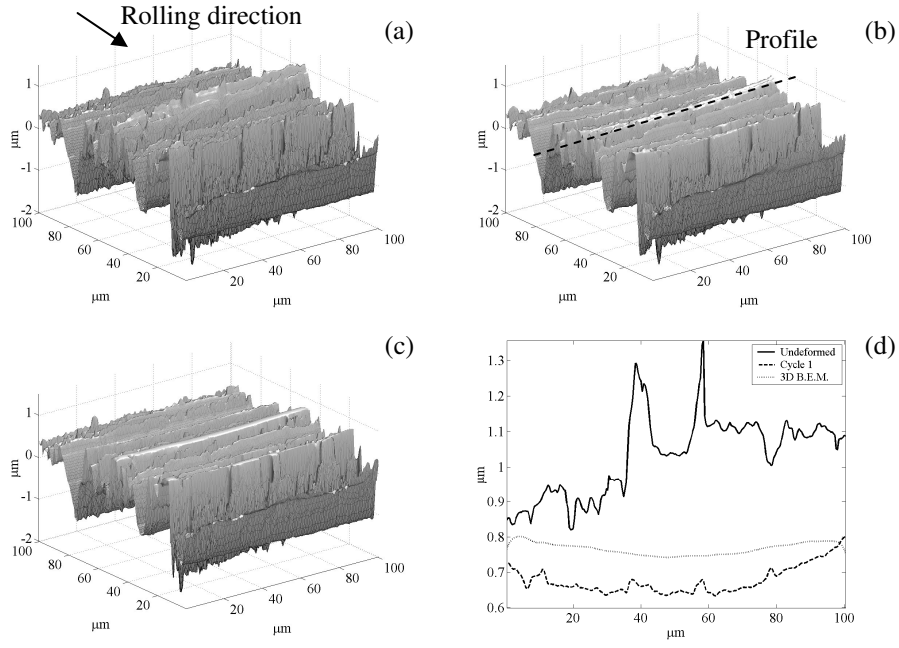

Figure 7.6. The lateral asperities in experiment 3, (a) initially, (b) after 1 cycle, (c) after rolling simulation with 3D B.E.M and (d) across the deformation track in marked profile in (b).

a reasonably good approximation by this approach.

- The numerically calculated profiles shows that in all the analyses up to now, the deformations calculated by the numerical technique are slightly smaller than the experimental results. As mentioned before in the previous section, one reason could be that the measured hardness values that determine the deformation criteria in the 3D B.E.M are slightly higher than the real pressure that can be carried by the surface.

7.4. A study on deformation modes

In the previous sections and chapters, it was shown that changes in the micro-geometry of a rolling contact can be measured, modeled and analyzed by the experimental and the numerical techniques developed. In addition, in chapter 5, experimental results were analyzed by the use of stress distributions under the rolling contact. As mentioned in the beginning of this chapter, it was shown that three deformation mechanisms can be distinguished in rolling contacts. These are asperity deformation, bulk deformation and a combination of asperity and bulk deformation. It was shown that the von Mises stresses in the sub-surface show the position of the initial yield. It was also shown that if the stresses are high and concentrated in the subsurface, then bulk deformation is favored, as in the case of contact of surfaces with low roughness. On the other hand, if the surfaces are rough, then high magnitude stresses are concentrated close to the surface, which leads to asperity level deformation.

In this final section of this chapter, a study on the prediction of the deformation mode is carried out. For this purpose, numerically generated surfaces with 7 different roughness, 4 different material properties and 3 different autocorrelation lengths ($A(\tau)$) and additionally the experiments presented in table 7.1 are used. As an example, an artificial surface with R_q = 0.5 μm, $A(\tau)$ = 3.5 μm and a Gaussian height distribution is presented in figure 7.7. The R_q roughness values of the artificial surfaces were 0.01, 0.05, 0.1, 0.3, 0.5, 0.7 and 0.9 μm. The three different correlation lengths were 2.2, 3.5 and 5 μm. The material properties used in the calculations can be seen in table 7.2. In the analysis a ball radius of 3.2 mm and a normal load of 4 N was used as in the experiments.

Table 7.2. Material properties of the artificial surfaces

	E (GPa)	ν	H (GPa)	σ_y (GPa)	k (GPa)
Material 1	70	0.33	0.28	0.1	0.06
Material 2	210	0.3	1.94	0.69	0.4
Material 3	210	0.3	4	1.43	0.83
Material 4	210	0.3	8.3	2.96	1.71

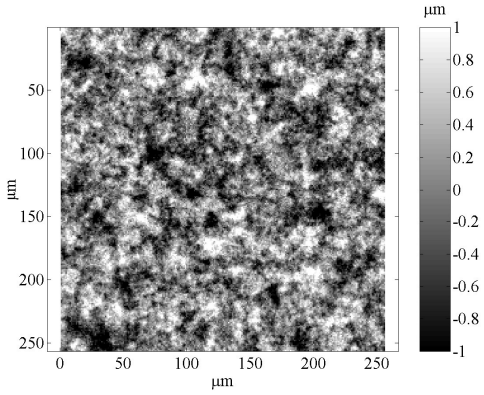

Figure 7.7. Artificial surface with R_q = 0.5 µm, $A_x(\tau)$ = 3.5 µm. The height distribution is Gaussian.

In section 7.4.1, the effect of material properties and roughness on the position of the initial yield will be discussed. Next, in section 7.4.2, the effect of the correlation distance, or in other words the distance between the asperities on the subsurface stress distributions, will be presented. Finally, in section 7.4.3 a map for determining the mode of deformation will be introduced and discussed.

7.4.1. Material properties, roughness and deformation modes

In this analysis, four different materials and seven different roughnesses were used in the numerical analysis with artificial surfaces. The 3D von Mises stress distribution under the contact was calculated using the 3D B.E.M technique and the methods described in chapter 4. At first, within the calculated 3D stress distribution, the yielding points where the stresses exceed the yield criterion (k) were found. Next, the mean and the standard deviation at the depth below the surface of these "yield spots" were calculated. The calculated mean depth represents the depth where stresses are concentrated and larger than the yield limit, and the standard deviation represents the boundaries of the regions with stresses above the yield limit around the average. The combination of the mean and standard deviation defines the yield region.

The results are plotted in figure 7.8 for both the artificial surfaces and the experimental surfaces. From the figure it is seen that for surfaces with low hardness the yield region is in the subsurface and increasing roughness results in an initial yield closer to the surface. When the material is harder, the yield region is close to the surface because of the high concentrated pressures for contacting rough surfaces. The measured surfaces give similar results for the calculated depths. It is also seen from figure 7.8 that, for the hard surfaces, the yield region is closer to the surface for smooth surfaces than for the rough surfaces. However, the number of points above the yield

for the smooth case is very small, so the statistical average is not so accurate.

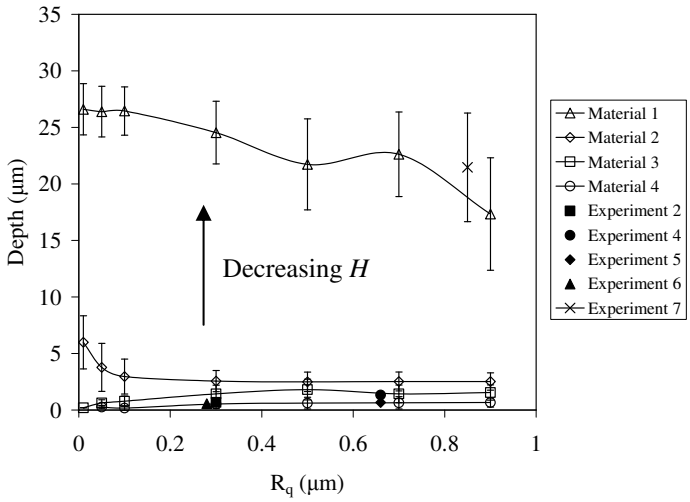

Figure 7.8. Depth of the initial yield for different material properties and roughness.

As a summary,

- Analyses with artificial and experimental surfaces are carried out. Yield regions for surfaces with different material properties and roughness values are determined for a constant load. It is seen that, when hardness and roughness is low, the yield region is in the subsurface. Conversely, if hardness and roughness are high, yield occurs closer to the surface.

7.4.2. Distance between asperities and deformation modes

In this section the artificially generated surfaces with the properties of material 3 (table 7.2) is considered. Note that these material properties are similar to those of the disks used in experiments 2 and 4 which will also be included in this analysis. In experiment 2 the deformation mode was bulk deformation and in experiment 4 asperity deformation. The artificial surfaces had different correlation lengths which were; 2.2 μm, 3.5 μm and 5 μm whereas the surfaces in experiments 2 and 4 had correlation lengths of 2.3 μm and 3.5 μm respectively. As the experimental surfaces were anisotropic, $A(\tau)$ was calculated perpendicular to the direction of the grinding grooves.

In figure 7.9 the relation between the yield depth and R_q is presented for artificial surfaces as well as for experimental surfaces. From the figure it is seen that the increase in the correlation length $A(\tau)$ leads to a deeper location for the initial yield. In addition, given a constant roughness, the

yield region is slightly larger for a higher $A(\tau)$, but both effects are not very significant. A much wider span can be used for further studies. A more dominant effect on the yield region is again the roughness of the deforming surface. When the roughness increases, the yield region moves closer to the surface and becomes more concentrated. Comparing experiments 2 and 4, it is seen that in experiment 2 the yield depths are close to each other, however the yield region is more concentrated for experiment 2. This could be an explanation for the bulk deformation seen in experiment 2 and the asperity deformation seen in experiment 4.

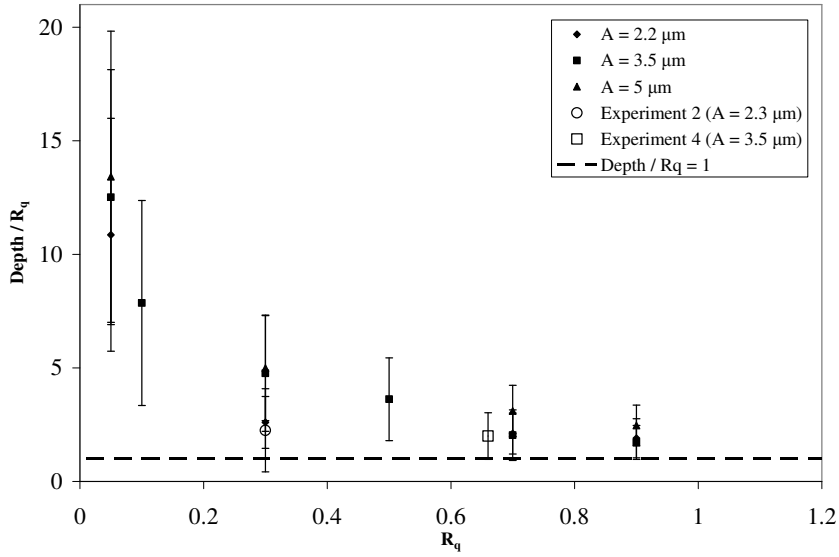

Figure 7.9. Yield region for different correlation lengths ($A(\tau)$). The material properties for the artificial and experimental surfaces are H = 4 GPa, E = 210 GPa, v = 0.3, σ_y = 1.43 GPa and k = 0.83 GPa.

As a summary,

- A parametric study was carried out to understand the effect of correlation distance on the yield depth. It was seen that increasing distance between the asperities, i.e. increasing the autocorrelation length, leads to a slightly deeper yield region. A much wider span for the autocorrelation length can be used in further studies.

In the next section, a deformation map based on the findings of the previous sections will be presented.

7.4.3. A deformation map

Findings in the preceding sections show that roughness and hardness are the two main parameters in the deformation mode. In this section, a

deformation map based on roughness (R_q) and hardness will be presented. The four materials presented in table 7.2 are used at seven different roughnesses. For a determination of whether asperity deformation or bulk deformation is expected, again at first the subsurface von Mises stresses are calculated. Here an assumption is made. If the yield depth (calculated as in the previous sections) is larger than five times the standard deviation of the surface height distribution (or simply $5R_q$), then the deformation is considered to be in the bulk. If the yield depth is smaller than $5R_q$ then the deformation is assumed to be at the asperity level.

The other parameter in the map will be the normalized mean contact pressure (p_m / H) which is roughness independent. The mean Hertzian contact pressure p_m is calculated for a corresponding smooth surface with the same material properties as the rough surface in the analysis using:

$$p_m = \frac{2}{3}\left(\frac{6 \cdot F \cdot E^{*2}}{\pi^3 \cdot R^2}\right)^{1/3} \tag{7.6}$$

In figure 7.10 the results are presented. The dark symbols represent predicted asperity deformation and the open symbols represent cases where bulk deformation is predicted. A dominant asperity level deformation can be seen for hard and rough surfaces. When the surface is smooth and soft, surfaces experience bulk deformation. The marked circle represents the analysis point for the artificial surface having the same properties as experiment 2 where bulk deformation was seen. This point is at the

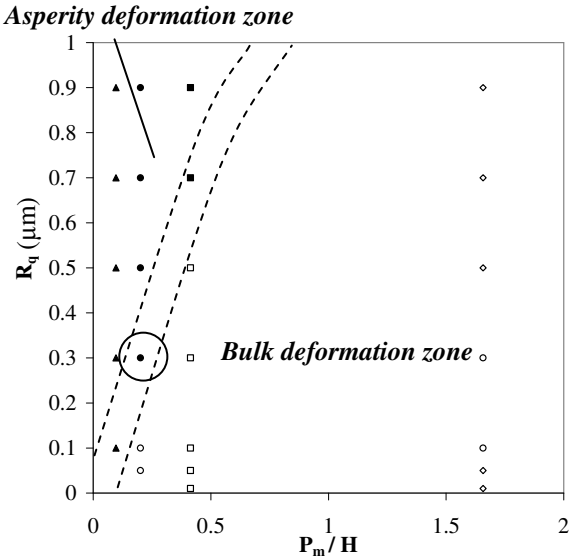

Figure 7.10. A map for different modes of deformation.

transition between the two different modes of deformation. As a recommendation, further experiments could be done in this regime. Experimental observation of the deformation mode can be compared with the estimated values and as a result the transition regime could be estimated much more accurately.

7.5. Summary and Conclusions

- Asperity deformation can be modeled very well by the elastic-plastic contact algorithm that was presented in chapter 4. For bulk deformation the model is less suitable. For this reason, bulk deformation was analyzed using the available elasto-plastic contact models such as the one presented in [1]. When the roughness is low, bulk deformation can be approximated by such approaches, see section 7.1.

- It was shown that 3D B.E.M. can be used with a reasonably good accuracy in modeling roughness level deformation in rolling contacts. The normally loaded contact model is extended to a rolling simulation which is composed of multiple shifted indentations on a surface. The results are consistent with the experimental findings. However, the deformations calculated by the numerical technique are still slightly smaller than the experimental results. The pressures that can be carried by the surface are slightly lower than the measured hardness values.

- Analyses with artificial and experimental surfaces were carried out to obtain the yield regions for surfaces with different material properties and roughness values. A conclusion is that when hardness and roughness is low the predicted yield region is in the subsurface. Conversely, if hardness and roughness are high, yield occurs closer to the surface, see section 7.4.1.

- Increasing the distance between the asperities characterized by a higher autocorrelation length $A(\tau)$ leads to a slightly deeper yield region but within the range of the parameters studied, the dominant factor is roughness. A much wider span for the autocorrelation length can be used in further studies.

- The different deformation modes are presented as a deformation map. It was shown that a dominant asperity level deformation can be seen in the case of hard and rough surfaces. When the surface is smooth and soft, bulk deformation is dominant.

References

[1] L. Kogut and I. Etsion, Elastic-plastic contact analysis of a sphere and a rigid flat, Journal of Applied Mechanics 69 (2002), pp. 657-662.
[2] J.A. Greenwood and J.H. Tripp, The elastic contact of rough spheres, Journal of Applied Mechanics 34 (1967), pp. 153-159.

Chapter 8. Conclusions and recommendations

In this chapter, conclusions from the preceding chapters and additional recommendations will be presented respectively in sections 8.1 and 8.2.

8.1. Conclusions

Chapter 3: Measurement of changes in the surface micro-geometry

- A measurement method and system for measuring the 3D local changes in the surface topography with 1 nm height resolution was developed. This system makes it possible to conduct 3D roughness measurements on a certain area of a disk during rolling and sliding experiments with a ball specimen. Different modes of deformation such as asperity or bulk deformation can be measured and phenomena like running-in or deformation in single or repeating contacts can be studied.

- A repositioning algorithm based on previous studies was developed. This algorithm is a very accurate "repositioning" tool that can compensate the repositioning inaccuracies of the positioning system and effects of wear and outliers on the measured surface. If larger areas are of interest, images with a percentage of overlap can be stitched together.

Chapter 4: Modeling contact of rough surfaces

- A 2D F.E.M. and a 3D B.E.M. were introduced. 3D B.E.M. can be used for the 3D elastic-plastic contact problem with a fairly good approximation and is much faster and memory efficient than the finite elements technique.

- The general material assumption of having fully plastic deformation with $p_m = 2.8\sigma_y$ holds very well for the single asperity case. However, when rough surfaces are considered, this value (p_m) increases due to the interaction of neighboring asperities.

- When a rough surface is in contact with a rigid counter-surface, different deformation mechanisms of asperities are seen for elastic and elastic-plastic contacts. If the contact is elastic, the asperities are mainly pressed down together with a little change in their shape. If the contact is elastic-plastic then the change in the shape of the asperities is larger because of flattening effects.

Chapter 5: Changes in the micro-geometry of rolling contacts

- In a rolling contact different deformation types can be present. The two main mechanisms are flattening of the asperities and bulk deformation where asperities are “pushed down” without much change in their shape. Besides this, a combination of asperity deformation and bulk deformation may occur.

- The position of the major plastic deformation can be calculated fairly well by the calculation of the subsurface von Mises stresses. In this way, the occurrence of bulk deformation or asperity deformation can be calculated. Rough surfaces are characterized by surface deformation whereas smooth surfaces are characterized by bulk deformation.

- In contact of nearly smooth surfaces the pressure distribution is initially Hertzian. As the conformity increases due to plastic deformation, the pressure distribution changes to a Kunert distribution.

- For surfaces with a low roughness, the subsurface stress distribution is very close to the one for the contact of perfectly smooth surfaces. When the roughness increases, initial stress distributions under a contact are highly concentrated close to the surface. As the conformity increases in cyclic loading, the stresses decrease and the distribution relaxes.

- The shakedown intervals calculated by the smooth surface assumption can also give a good estimation for rough surfaces, provided that conformity is achieved. The shakedown pressures deviate much more when the conformity is lower.

- It was shown that in micro-contacts, with contact pressures much higher than the calculated shakedown pressures, ratchetting occurs. In such contacts, asperity persistence is seen in the initial cycles where asperities cannot be completely flattened. This asperity persistence in fully plastic contacts is different from the bulk deformation mechanism in elastic-plastic deforming contacts.

- The calculated pressure distribution is very sensitive to the “outliers” and other artifacts on a measured surface.

Chapter 6: Changes in the micro-geometry of sliding contacts

- At low roughness values and at the initial cycles, high values for the subsurface stresses are concentrated far below the sliding contact. This state is similar to the one for a perfectly smooth sphere-flat contact except that small scale concentrated stresses due to the roughness are close to the surface. Hence, shakedown in sliding contacts is very close to the rolling case for this situation, i.e. low roughness.

- When the contact is close to the steady state, a strained layer is formed close to the surface, both in sliding and rolling contacts. In this way, the load that can be carried elastically increases.

- The friction force in the contact increases after a certain number of cycles. At values of a coefficient of friction higher than about 0.3, the topography changes significantly.

- It is seen that for rough surfaces, asperity level deformation in a sliding contact cannot only be explained by a normally loaded contact model where frictional effects are involved. Wear mechanisms such as ploughing and crushing of asperities have a more dominant effect on the changes in the micro-geometry in sliding contacts.

Chapter 7: Models and experiments

- For roughness level deformations seen in rolling contacts, 3D B.E.M. can be used with reasonably good accuracy. The experimental results agree well with the results obtained with 3D B.E.M. for normally loaded and simulated rolling contacts with multiple indentations. The pressures that can be carried by the surface are slightly lower than the measured hardness values.

- 3D B.E.M does not predict bulk deformation. However, for surfaces with low roughness, bulk deformation can be approximated by using available elasto-plastic contact models describing the contact between a flat and a sphere.

- In rough surfaces, when hardness and roughness is low, the yield region is in the subsurface. If both the hardness and roughness are high, the yield region is close to the surface.

- When the distance between the asperities is high, yield occurs at a slightly higher depth. This distance can be characterized by the

autocorrelation length. However, within the range of surface parameters studied, the dominant factor is roughness.

- The different deformation modes are presented in a deformation map. Accordingly, when the surface is smooth and soft, bulk deformation occurs and when it is rough and hard asperity deformation can be expected.

8.2. Recommendations

On the experimental setup

- In this study the measurements were performed in a semi-online manner in which the ball stays in contact with the disk, where a wear or deformation experiment is stopped before each roughness measurement. There are optical techniques under investigation that makes it possible to measure surface roughness on moving surfaces. An interference microscope with an inclined lens is a good option. Here a surface scan is not performed by a PZT movement of the lens but instead by the movement of the surface.

- Phenomena involving changes in the surface micro-geometry such as running-in, transfer film formation in plastic metal systems, oxide layer formation in ceramics can be studied with the developed measurement system.

- The Linnik option of the interference microscope allows measurement of the underlying surface through a lubricant film. This option can be used for measuring semi-online or if possible online measurement of changes in the micro-geometry of lubricated rolling and sliding contacts.

- The repositioning algorithm for matching and stitching can be used in in-situ quality control systems, where topography of a sample can be compared with the designed surface topography or shape. Difference images can be used for this purpose.

On the experimental work

- Long cycle experiments could be conducted for a study on rolling contact fatigue.

- Lubricated sliding experiments could be conducted and the available models compared with the experimental results.

Shakedown and running-in of lubricated sliding contacts could be studied.

- For the deformation map, more experiments with different surface roughness and hardness can be conducted, so that the transition region from asperity deformation to bulk deformation can be determined more precisely.

- To extend the deformation map to more "types" of roughness, a study with the different autocorrelation lengths could be performed. This could be included in the map as a design criterion.

On the contact model

- Using 3D B.E.M., the contact of contacting coated rough surfaces could also be calculated with a similar approach. In this way, a coated surface can be designed in terms of desired hardness and coating thickness.

- The algorithm could be improved so that plastic stresses under the contact can also be calculated. This would increase the accuracy in prediction of the deformation mechanisms on the level of asperities and bulk material.

Appendix A: Stresses

A.1. Stresses beneath a sliding/rolling point contact

The equations for the stresses beneath a sliding spherical contact were given in [1].

Stresses due to a normal load *F*

$$\sigma_{x,F} = \frac{3F}{2\pi\pi^3}\left[(1+\nu)z\varphi + \frac{1}{r^2}\left\{\frac{y^2-x^2}{r^2}\left[(1-\nu)N\cdot z^2 - \frac{1-2\nu}{3}\left(N\cdot S + 2A\cdot N + a^3\right) - \nu M\cdot za\right] - N\left(x^2+2\nu y^2\right) - \frac{Mx^2za}{S}\right\}\right] \tag{A.1}$$

$$\sigma_{y,F} = \frac{3F}{2\pi a^3}\left[(1+\nu)z\phi + \frac{1}{r^2}\left\{\frac{x^2-y^2}{r^2}\left[(1-\nu)Nz^2 - \frac{1-2\nu}{3}\left(N\cdot S + 2\cdot A\cdot N + a^3\right) - \nu M\cdot za\right] - N\left(y^2+2\nu x^2\right) - \frac{My^2za}{S}\right\}\right] \tag{A.2}$$

$$\sigma_{z,F} = \frac{3F}{2\pi a^3}\left[-N + \frac{azM}{S}\right] \tag{A.3}$$

$$\tau_{xy,F} = \frac{3F}{2\pi a^3}\left[\frac{xy(1-2\nu)}{r^4}\left\{-Nr^2 + \tfrac{2}{3}N(S+2A) - z(zN+aM) + \tfrac{2}{3}a^3\right\} + \frac{xyz}{r^4}\left\{-\frac{aMr^2}{S} - zN + aM\right\}\right] \tag{A.4}$$

$$\tau_{yz,F} = \frac{3F}{2\pi a^3}\left[-z\left\{\frac{yN}{S} - \frac{yzH}{G^2+H^2}\right\}\right] \tag{A.5}$$

$$\tau_{zx,F} = \frac{3F}{2\pi a^3}\left[-z\left\{\frac{xN}{S} - \frac{xzH}{G^2+H^2}\right\}\right] \tag{A.6}$$

With,

$$r^2 = x^2 + y^2 \tag{A.7}$$
$$A = r^2 + z^2 - a^2$$
$$S = \sqrt{A^2 + 4a^2 z^2}$$
$$M = \sqrt{\frac{S + A}{2}}$$
$$N = \sqrt{\frac{S - A}{2}}$$
$$\phi = tan^{-1}\left(\frac{a}{M}\right)$$
$$G = M^2 - N^2 + zM - aN$$
$$H = 2MN + aM + zN$$

If $r = 0$ (so, at the axis through the center of the contact), the equations need to be rewritten to:

$$\sigma_{x,F} = \sigma_{y,F} = \frac{3F}{2\pi a^3}\left[(1+v)\left(z\,tan^{-1}\left(\frac{a}{z}\right) - a\right) + \frac{a^3}{2\left(a^2 + z^2\right)}\right] \tag{A.8}$$

$$\sigma_{z,F} = \frac{3F}{2\pi a^3}\left[\frac{-a^3}{a^2+z^2}\right] \tag{A.9}$$

$$\tau_{xy,F} = \tau_{zx,F} = \tau_{yz,F} = 0 \tag{A.10}$$

On the surface $z = 0$, the stresses outside the contact for $r \geq a$, are given by:

$$\sigma_{x,F} = \frac{3F}{2\pi a^3}\left[\frac{(1-2v)(x^2-y^2)a^3}{3r^4}\right] \tag{A.11}$$

$$\sigma_{y,F} = \frac{3F}{2\pi a^3}\left[\frac{(1-2v)(y^2-x^2)a^3}{3r^4}\right] \tag{A.12}$$

$$\tau_{xy,F} = \frac{3F}{2\pi a^3}\left[\frac{2a^3xy(1-2v)}{3r^4}\right] \tag{A.13}$$

$$\sigma_{z,F} = \tau_{yz,F} = \tau_{zx,F} = 0 \tag{A.14}$$

On the surface $z = 0$, the stresses inside the contact for $r < a$, are given by:

$$\sigma_{x,F} = \frac{3F}{2\pi a^3}\left[\frac{1}{r^2}\left\{\frac{y^2-x^2}{r^2}\left[\frac{1-2v}{3}\left\{\left(a^2-r^2\right)^{\frac{3}{2}}-a^3\right\}\right]-\left(x^2+2vy^2\right)\left(a^2-r^2\right)^{\frac{1}{2}}\right\}\right] \tag{A.15}$$

$$\sigma_{y,F} = \frac{3F}{2\pi a^3}\left[\frac{1}{r^2}\left\{\frac{y^2-x^2}{r^2}\left[\frac{1-2v}{3}\left\{\left(a^2-r^2\right)^{\frac{3}{2}}-a^3\right\}\right]-\left(x^2+2vy^2\right)\left(a^2-r^2\right)^{\frac{1}{2}}\right\}\right]\left[\left(-r^2-\frac{2}{3}\left(a^2-r^2\right)\right)+\frac{2}{3}a^3\right] \quad \text{(A.16)}$$

$$\sigma_{z,F} = \frac{3F}{2\pi a^3}\left[-\left(a^2-r^2\right)^{\frac{1}{2}}\right] \quad \text{(A.17)}$$

$$\tau_{xy,F} = \frac{3F}{2\pi a^3}\left[\frac{xy(1-2v)}{r^4}\left\{\left(a^2-r^2\right)^{\frac{1}{2}}\left[-r^2-\frac{2}{3}\left(a^2-r^2\right)\right]+\frac{2}{3}a^3\right\}\right] \quad \text{(A.18)}$$

$$\tau_{yz,F} = \tau_{zx,F} = 0 \quad \text{(A.19)}$$

Stresses due to a tangential load *Q*

$$\sigma_{x,Q} = \frac{3Q}{2\pi a^3}\left[\begin{array}{l} -x\left(\frac{v}{4}+1\right)\phi+\frac{axM}{r^4}\left\{\left(\frac{3}{2}-\frac{2x^2}{r^2}\right)\left(Sv-2Av+z^2\right)+\frac{x^2z^2}{S}+\frac{7vr^2}{4}-2vx^2+r^2\right\}+ \\ \frac{xzN}{r^4}\left\{\left(\frac{3}{2}-\frac{2x^2}{r^2}\right)\left[-\frac{S}{6}(1-2v)-\frac{A}{3}(1-2v)-\frac{1}{2}\left(z^2+3a^2\right)\right]+\frac{a^2x^2}{S}-\frac{vr^2}{4}-\frac{7r^2}{4}\right\}+ \\ \frac{4a^3xz}{3r^4}\left(\frac{3}{2}-\frac{2x^2}{r^2}\right)(1-2v) \end{array}\right] \quad \text{(A.20)}$$

$$\sigma_{y,Q}=\frac{3Q}{2\pi a^3}\left[\begin{array}{l}-\frac{3vx\phi}{4}+\frac{axM}{r^4}\left\{\left(\frac{1}{2}-\frac{2y^2}{r^2}\right)\left[v\left(S-2A+r^2\right)+z^2\right]+\frac{y^2z^2}{S}+\frac{3}{4}vr^2\right\}+\\ \frac{xzN}{r^4}\left\{\left(\frac{1}{2}-\frac{2y^2}{r^2}\right)\left[-\frac{S}{6}(1-2v)-\frac{A}{3}(1-2v)-\frac{z^2}{2}-\frac{3}{2}a^2\right]+\frac{a^2y^2}{S}-\frac{3}{4}vr^2-\frac{r^2}{4}\right\}+\\ \frac{4a^3xz}{3r^4}\left(\frac{1}{2}-\frac{2y^2}{r^2}\right)(1-2v)\end{array}\right] \tag{A.21}$$

$$\sigma_{z,Q}=\frac{3Q}{2\pi a^3}\left[\frac{zxN}{2r^2}\left\{1-\frac{r^2+z^2+a^2}{S}\right\}\right] \tag{A.22}$$

$$\tau_{xy,Q}=\frac{3Q}{2\pi a^3}\left[\begin{array}{l}\frac{y}{2}\left(\frac{v}{2}-1\right)\phi+\frac{ayM}{r^4}\left\{\frac{x^2z^2}{S}+v\left[(S-2A)\left(\frac{1}{2}-\frac{2x^2}{r^2}\right)-2x^2+\frac{r^2}{4}\right]+\frac{r^2}{2}+z^2\left(\frac{1}{2}-\frac{2x^2}{r^2}\right)\right\}+\\ \frac{yzN}{r^4}\left\{\left(\frac{1}{2}-\frac{2x^2}{r^2}\right)\left[(2v-1)\left(\frac{S}{6}+\frac{A}{3}\right)-\frac{z^2}{2}-\frac{3a^2}{2}-\frac{r^2}{2}\right]+\frac{r^2v}{4}+\frac{a^2x^2}{S}-\frac{y^2}{2}-\frac{3x^2}{S}\right\}+\\ \frac{4a^3yz}{3r^4}\left(\frac{1}{2}-\frac{2x^2}{r^2}\right)(1-2v)\end{array}\right] \tag{A.23}$$

$$\tau_{yz,Q}=\frac{3Q}{2\pi a^3}\frac{xyz}{2r^4}\left[aM\left\{\frac{1}{2}+\frac{1}{S}\left(\frac{z^2}{2}-\frac{3a^2}{2}-\frac{r^2}{2}\right)\right\}+\frac{zN}{2}\left\{-3+\frac{1}{S}\left(5a^2+z^2+r^2\right)\right\}\right] \tag{A.24}$$

$$\tau_{zx,Q} = \frac{3Q}{2\pi a^3}\left[\frac{3z\phi}{2} + \frac{azM}{r^2}\left\{1 + \frac{x^2}{r^2} - \frac{x^2}{S}\right\} + \frac{N}{r^2}\left\{-\frac{3}{4}(S+2A) + z^2 - \frac{3}{4}a^2 - \frac{1}{4}r^2 + \frac{z^2}{2}\left(\frac{1}{2} - \frac{2x^2}{r^2}\right)\right\}\right] \quad \text{(A.25)}$$

At the axis $r = 0$ all stresses are non-existent except τ_{zx}:

$$\tau_{zx,Q} = \frac{3Q}{2\pi a^3}\left[-a + \frac{3}{2}z\,tan^{-1}\left(\frac{a}{z}\right) - \frac{az^2}{2\left(a^2 + z^2\right)}\right] \quad \text{(A.26)}$$

On the surface $z = 0$, the stresses outside the contact for $x \geq a$, are given by:

$$\sigma_{x,Q} = \frac{3Q}{2\pi a^3}\left[-x\left(1 + \frac{v}{4}\right)\phi + \frac{axM_0}{r^4}\left\{-vM_0^2\left(\frac{3}{2} - \frac{2x^2}{r^2}\right) + \frac{7vr^2}{4} - 2vx^2 + r^2\right\}\right] \quad \text{(A.27)}$$

$$\sigma_{y,Q} = \frac{3Q}{2\pi a^3}\left[-\frac{3}{4}vx\phi + \frac{axM_0}{r^4}\left\{va^2\left(\frac{1}{2} - \frac{2y^2}{r^2}\right) + \frac{3}{4}vr^2\right\}\right] \quad \text{(A.28)}$$

$$\tau_{xy,Q} = \frac{3Q}{2\pi a^3}\left[\frac{y}{2}\left(\frac{v}{2} - 1\right)\phi + \frac{ayM_0}{r^4}\left\{-vM_0^2\left(\frac{1}{2} - \frac{2x^2}{r^2}\right) - 2vx^2 + \frac{1}{4}vr^2 + \frac{1}{2}r^2\right\}\right] \quad \text{(A.29)}$$

$$M_0 = \sqrt{r^2 - a^a} \quad \text{(A.30)}$$

$$\sigma_{z,Q} = \tau_{yz,Q} = \tau_{zx,Q} = 0$$

On the surface $z = 0$, the stresses inside the contact for $x < a$, are given by:

$$\sigma_{x,Q} = \frac{3Q}{2\pi a^3}\left[-\frac{\pi x}{2}\left(\frac{v}{4}+1\right)\right] \tag{A.31}$$

$$\sigma_{y,Q} = \frac{3Q}{2\pi a^3}\left[-\frac{3\pi v x}{8}\right] \tag{A.32}$$

$$\tau_{xy,Q} = \frac{3Q}{2\pi a^3}\left[\frac{\pi y}{4}\left(\frac{v}{2}-1\right)\right] \tag{A.33}$$

$$\tau_{zx,Q} = \frac{3Q}{2\pi a^3}\left[-\sqrt{a^2-r^2}\right] \tag{A.34}$$

$$\sigma_{z,Q} = \tau_{yz,Q} = 0 \tag{A.35}$$

A.2. The von Mises yield parameter

The von Mises yield parameter J can be calculated from the principal stresses as:

$$J = \frac{1}{6}\left\{\left(\sigma_x - \sigma_y\right)^2 + \left(\sigma_y - \sigma_z\right)^2 + \left(\sigma_z - \sigma_x\right)^2\right\} + \tau_{xy}^2 + \tau_{yz}^2 + \tau_{zx}^2 \qquad \text{(A.36)}$$

References

[1] G.M. Hamilton, Explicit equations for the stresses beneath a sliding spherical contact, Proc. Instn. Mech. Engnrs. 197C (1983), pp. 53-59.

Appendix B. The experimental setup

B.1. The interference microscope

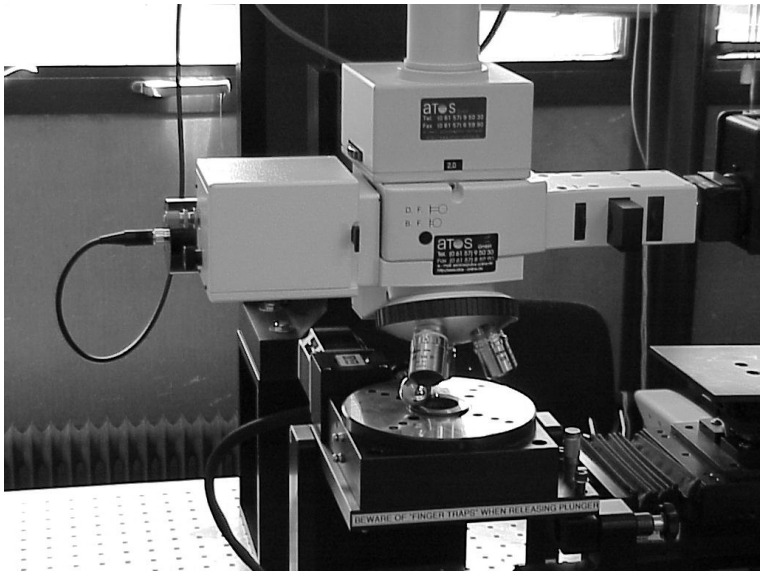

B.2. The wear and friction tester (in a sliding contact experiment)

B.3. The wear and friction tester

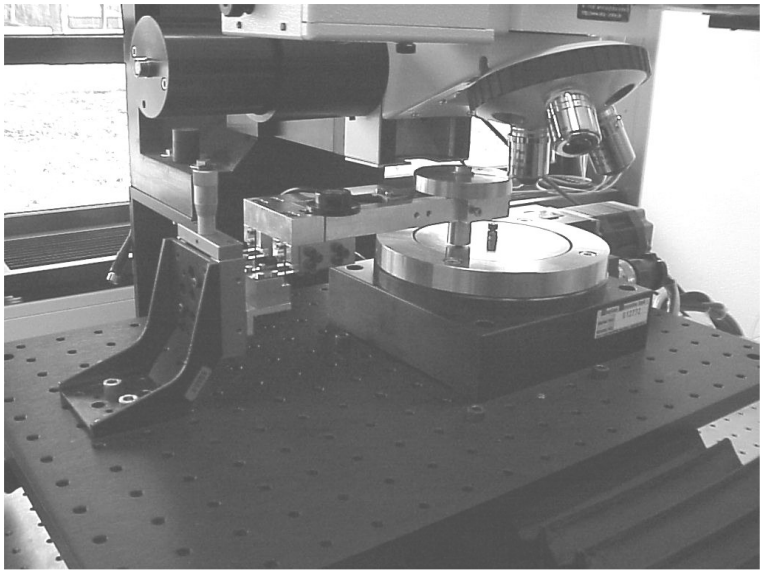

B.4. The rolling contact adaptor

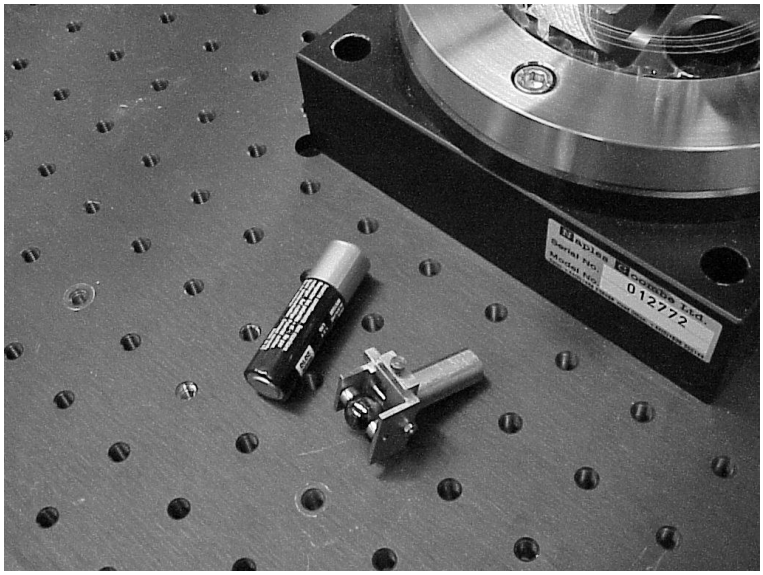

Appendix C. Matching and stitching solver

C.1. The method

The solver used to obtain the minimum value of the cost function was the global optimizer by Huyer and Neumaier [1]. The minimization procedure was done by combining:

- Global search
- Local search

The "global search" is defined as splitting the search space with boxes for large unexplored areas, and the "local search" is the splitting of the areas near the good candidate function values. Figure C.1. shows the six-hump camel function and the boxes (or search windows) for the search. In the figure, the asterisk denotes the global minimum of the function. Each window is split into smaller windows of a "multilevel" nature. The number of times a box has been processed forms this multilevel nature. The large boxes which are not yet split have a small level, and the boxes considered to be too small for further splitting have the highest level. After initialization (section C.2), series of search through levels are done. The global part of the algorithm is the search performed in the boxes with small level. The local search is the selection of the boxes with lowest function value and further search within these boxes.

For every window, base points (black dots in Figure C.1) are determined and function values for these base points are stored for the local search. After that, local search is performed near good values for base points. In the local search, the local search space is minimized by splitting of the search area into smaller areas. The user can adjust the amount of local/global search. For example if the amount of local search is set to zero then only the base points are selected to the so-called "shopping basket" containing useful points. On the other hand, if also the local search is introduced, the algorithm starts local searches from these points and looks for local minima near them before putting them into the shopping basket. The aim in this integration of methods is to accelerate convergence while avoiding local minima problems. In the case of highly varying functions, the global search should be increased.

Another important aspect of searching a large space and number of independent variables is the initialization of the search. The solver has different initialization choices that will be discussed in the next section.

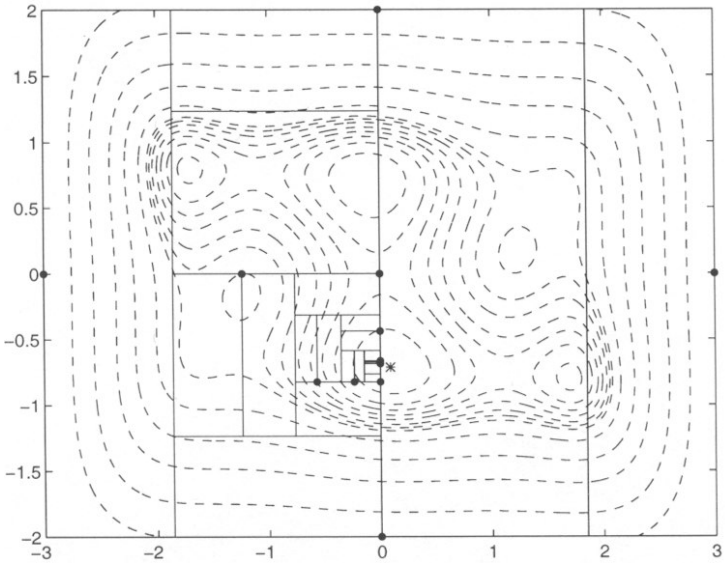

Figure C.1. Splitting for the six-hump camel function. Black dots are bases for each level and the asterisk is the global minimum. The figure is taken from [1].

C.2. Initialization of the global search

The base points in each search window are on the boundaries of the window, but shared by a number of windows. Each box is also assigned an opposite vertex, so two of them define a box. u_i and v_i are the boundaries of the search and points defining box frame at each level is denoted as x. The initialization structures in the solver that determine the initial splitting points are three in number:

- Initialization with the mid and boundary points of the search interval so that:

$$x_i^1 = u_i, \qquad x_i^2 = \frac{1}{2}(u_i + v_i), \qquad x_i^3 = v_i \tag{C.1}$$

- Initialization with:

$$x_i^1 = \frac{5}{6}u_i + \frac{1}{6}v_i, \quad x_i^2 = \frac{1}{2}(u_i + v_i), \quad x_i^3 = \frac{1}{6}u_i + \frac{5}{6}v_i \tag{C.2}$$

  where $i = 1, \ldots, n$ are the points in or along the search windows.

- Initialization with the aid of line searches, a Matlab file *gls.m* was used for this type of search

Splitting criteria and selection of the additional splitting points are given in detail in [1].

At the moment the line search method is being used as an initialization step. However more focus on the cost function characteristics for different surfaces would give more idea of which type of initialization could be selected. On the other hand from [1] it can be concluded that increasing the number of levels used increases the convergence chance. However as can be expected, the number of levels used also affects the calculation time significantly as the number of points in the shopping basket increases. Up to now, the solver converged in all cases to the correct solution.

C.3. The shopping basket

The shopping basket involves candidate points for the minimum of a function which are local minima. When a local search is not selected, the shopping basket involves the base points and the corresponding function values. When local search is involved, the convergence is accelerated by local searches around the base points before putting them in the shopping basket.

Before introducing the steps of shopping basket evaluations it is necessary to define the variables. Letter x is used for the candidates for the shopping basket (and their updates), $f(x)$ is the function to be minimized and w is used for points already in the shopping basket. Note that the lowest function value at a certain w is the real global minimum. The steps are as follows:

- Step 1: It is first checked whether a local search for the x has already been performed. This is because many points belong to multiple windows. If it is the case that a search had already been performed, the next x is taken. If this is not the case or in other words, x is a new point in the basket then w in the basket are sorted by their distances to x starting from the nearest point. Then, for each w for which $f(w) \leq f(x)$ the following is performed:

- Step 2: Calculate:

$$x' = x + \frac{1}{3}(w - x) \qquad \text{(C.3)}$$

  If $f(x')$ > $f(x)$ then x is not in the "domain of attraction" of w. Take another w and go to step 2. For points that pass step 2, so for points which x is in the domain of attraction:

- Step 3: Calculate:

$$x'' = x + \frac{2}{3}(w - x) \qquad \text{(C.4)}$$

If $f(x'') > max(f(x'), f(w))$, then $x = x'$. Take the next w and return to step 2. Else if $min(f(x'), f(x'')) < f(w)$, then all four points seem to be in the same valley. x is set the value of either x' or x'' (with the smaller function value) and the next w is taken and go to step 2. Else take next x and go to step 1.

- **Step 4:** If x survives from step 2 and 3 a local search is started. After the local search (steps similar to step 2 and 3) if a new point is found then it is put in the basket as an extra point w, so an extra potential global minimum.

From experience the number of points in the shopping basket (or candidate points giving the best cost function value) is dependent on the amount of time spent on the global search. The solver has a built in structure to manipulate this ratio between the local and the global search, and these parameters can be used to change the convergence behavior of the process.

References

[1] W. Huyer, A. Neumaier, Global optimization by multilevel coordinate search, Journal of Global Optimization 14 (1999), 331-355.

Appendix D. The elastic contact algorithm

Consider a rigid flat surface in contact with an elastic rough surface. A 2D profile of such a contact is schematically shown in figure D.1. If the *x*-*y* plane is assumed to be the plane of the flat-rigid surface and *z* is the direction normal to the plane, then the numerical penetration ($z(x, y) > 0$) or separation ($z(x, y) < 0$) between the two surfaces (upon convergence $z(x, y) = 0$) in the *z*-direction can be defined as:

$$z(x,y) = -\delta + g(x,y) + r(x,y) + d(x,y) \qquad \text{(D.1)}$$

as introduced in [1]. In equation D.1, δ is the normal approach of the flat surface to the rough surface, *g(x, y)* is the underlying geometry of the nominally flat surface (i.e. sphere, cylinder etc.), *r(x, y)* is the surface roughness and *d(x, y)* is the deformation of the rough surface. The approach is defined as the distance of the flat surface is to a specific point on the rough surface. In [1], the deformation of the rough surface is calculated from the contact pressures by:

$$d_i = \sum_{j=1}^{N} C_{ij} p_i \qquad i = 1,2,...,N \qquad \text{(D.2)}$$

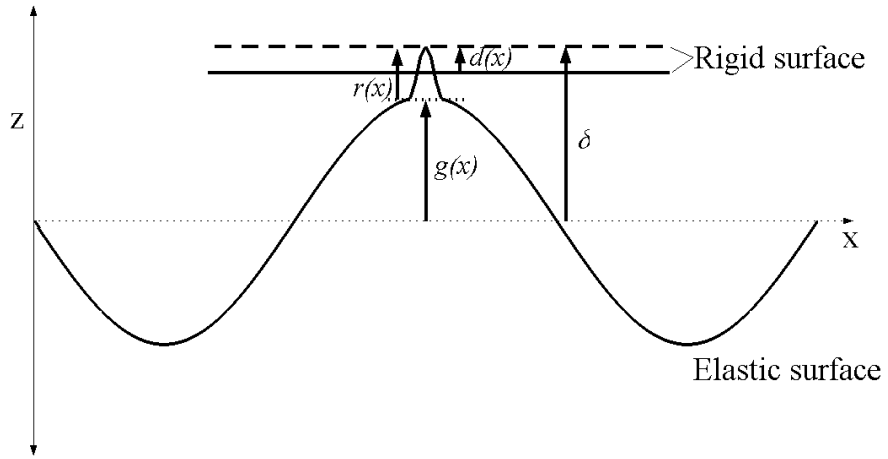

Figure D.1. Contact of a rigid flat and a rough elastic surface.

where d_i is the deformation of each surface patch, C_{ij} is the surface compliance matrix and is a function of distances between points *i* and *j*, p_i is the pressure at each element and *N* is the total number of surface patches on the surface. So a deformation of a certain point *i* is influenced by all pressures acting on the surface. The surface compliance matrix C_{ij} represents the influence of pressure p_i on the deformation d_i. Chang et al.

pointed out that, in a 3D problem, the use of a uniform grid for the surface reduces the size of the surface compliance matrix C_{ij} from NxN to N as C_{ij} is a function of the distances between points i and j. Equation D.1 can be re-written in the same numerical form as:

$$z_i = -\delta + g_i + r_i + d_i \qquad i = 1,2,...,N \tag{D.3}$$

Because both the pressures and the deformations are not known beforehand, an iterative procedure has to be used. The flow diagram of the method is shown in figure D.2.

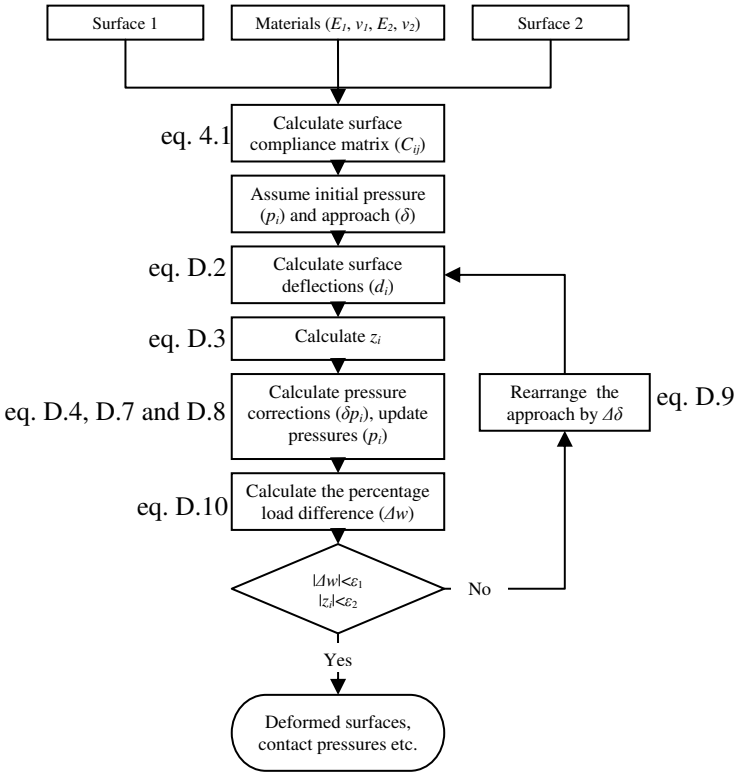

Figure D.2. Elastic contact algorithm.

Initially, a pressure distribution p_i and an initial normal approach δ are assumed. Initial p_i is assumed so that the pressure distribution is Hertzian for i.e. contact of a rough elastic sphere and rigid flat body, and zero for the contact of nominally flat surfaces. Surface deflections d_i are calculated from the pressures p_i by equation D.2. It is determined whether the contact is in separation ($z_i < 0$) or penetration ($z_i > 0$). The assumed initial pressure p_i is corrected using a pressure correction factor δp_i^k . This factor is calculated by:

$$\delta p_i^k = -\frac{z_i^k}{C_{ii}} \qquad i = 1,2,...,N \qquad k = 1,2,.... \tag{D.4}$$

where C_{ii} has the same value for each grid location and k is the current iteration number.

The deflection at a point is not only a result of the pressure element at that point but also effected by the surrounding pressure distribution. Equation D.4 leads to an over-estimated corrected pressure. So, a reduction factor λ is calculated iteratively. δp_i^k will be multiplied with this λ. The initial value of the reduction factor is calculated as:

$$\lambda^0 = \frac{p^0 C_{ii}}{z^0} \tag{D.5}$$

p^0 is chosen as a percentage of the nominal contact pressure and z^0 is chosen to be of the order of the initial geometrical overlap of the contacting bodies. The reduction factor is modified during the iterations. It is increased if there is rapid convergence and decreased if not. The reduction factor was defined by Chang et al. as:

$$\lambda^k = \lambda^{k-1} + \Delta\lambda^k \qquad k = 1,2,..... \tag{D.6}$$

The change of the reduction factor is defined by the following three logical conditions:

1. $If \ \max\left(\delta p_i^k\right) > 2 \cdot \max\left(\delta p_i^{k-1}\right) \Rightarrow \lambda = 0.5\lambda$

2. $If \ \max\left(\delta p_i^k\right) > 1.05 \cdot \max\left(\delta p_i^{k-1}\right)$
   $or \ mean\left(\delta p_i^k\right) > mean\left(\delta p_i^{k-1}\right) \Rightarrow \lambda = 0.9\lambda$

3. Every three iterations if:

$$If \ \max\left(\delta p_i^k\right) > 1.01 \cdot \max\left(\delta p_i^{k-1}\right)$$
$$and \ mean\left(\delta p_i^k\right) < mean\left(\delta p_i^{k-1}\right) \Rightarrow \lambda = 1.1\lambda$$

In order not to have too large pressure corrections in one step, a maximum pressure correction value (Δp_{max}) is set. Value of Δp_{max} is set to a percentage of the nominal contact pressure. The pressure correction then is defined as:

$$\Delta p_i^k = sign\left(\delta p_i^k\right) \cdot \min\left(\Delta p_{\max}, \lambda^{k-1}\left|\delta p_i^k\right|\right) \qquad i = 1,2,...,N \quad k = 1,2,... \tag{D.7}$$

With the corrected pressure in equation D.7, the pressure at the grid points is calculated as:

$$p_i^k = \max\left(0,\, p_i^{k-1} + \Delta p_i^k\right) \qquad i = 1,2,...,N \qquad k = 1,2,... \tag{D.8}$$

Three criteria are used for convergence. The first criterion is that the penetration of the surfaces should be lower than a certain given value ε which is a small percentage of the roughness. The second criterion is that there be no pressure at the non-contacting points and the last criterion is that the total reaction load calculated from the estimated pressures should be equal to the applied normal load. The approach is increased or decreased if the third criterion is not satisfied. This is handled by the change in the approach $\Delta\delta$ by:

$$\Delta\delta = \begin{cases} sign(\Delta w)\cdot c_w \cdot |\Delta w| & |\Delta w| \geq \varepsilon \\ 0 & |\Delta w| \leq \varepsilon \end{cases} \tag{D.9}$$

where Δw is percentage load error defined by:

$$\Delta w = \left| \frac{applied\ \ load - calculated\ \ reaction\ \ force}{applied\ \ load} \right| \tag{D.10}$$

and c_w is a positive valued factor that is set equal to applied load over equivalent elastic modulus for Hertzian contacts. For contact of nominally flat surfaces the value of c_w was initially 0.1 times the R_q roughness value, and it is changed during the iterations with the two logical conditions:

1. $If \left|\Delta w^k\right| < \left|\Delta w^{k-1}\right|$
   $and \ \ \Delta w^k \cdot \Delta w^{k-1} > 0 \Rightarrow c_w = 1.05 c_w$

2. $If \left|\Delta w^k\right| > 0.01$
   $and \ \ \Delta w^k \cdot \Delta w^{k-1} < 0 \Rightarrow c_w = 0.7 c_w$

Chang et al. recommend that in order to have the pressure distribution develop at a given approach, the value of c_w should not be changed every iteration except when:

($h_{max} < 200h_{tol}$ and $Iter > 40$) or ($h_{ma\,x} < 60h_{tol}$ and $Iter > 30$) or ($h_{max} < 30h_{tol}$ and $Iter > 20$) or ($h_{max} < 15h_{tol}$ and $Iter > 10$) or ($h_{max} < 5h_{tol}$ and $Iter > 5$) or ($h_{max} < h_{tol}$).

where h_{max} is the maximum penetration, h_{tol} is the penetration tolerance and $Iter$ is the number of iterations after the last normal approach adjustment presented in equation D.9.

In order to have a faster convergence, the problem is solved in multiple levels. This approach is similar to the one used in the re-positioning algorithm presented in chapter 3. The criterion for switching to a finer grid is when:

$$|\Delta w| < 0.1 \quad and \quad \max(|z_i|) < \alpha \tag{D.11}$$

where α is a certain percentage of the R_q and the finer the level, the smaller the value of α. At each level C_{ij} is recalculated with the new pixel size a and b (see figure 4.1).

References

[1] L. Chang and Y. Gao, A simple numerical method for contact analysis of rough surfaces, Journal of Tribology 121 (1999), pp. 425-432.